PROTON INDUCED X-RAY EMISSION (PIXE) AND APPLICATIONS TO ELEMENTAL ANALYSIS

by

Robert Dalton Willis

Department of Physics
Duke University

Date: July 31, 1977

Approved:

Richard L. Walter
Richard L. Walter, Supervisor

James A. Fox

Mod Young Han

Thomas L. Ogley

William R. Dunkmeht

A dissertation submitted in partial fulfillment of the requirements for the degree of Doctor of Philosophy in the Department of Physics in the Graduate School of Arts and Sciences of Duke University

1977

ABSTRACT

(Physics)

PROTON INDUCED X-RAY EMISSION (PIXE) AND

APPLICATIONS TO ELEMENTAL ANALYSIS

by

Robert Dalton Willis

Department of Physics
Duke University

Date: _____

Approved:

_____
Richard L. Walter, Supervisor

_____

_____

_____

_____

An abstract of a dissertation submitted in partial fulfillment of the requirements for the degree of Doctor of Philosophy in the Department of Physics in the Gracuate School of Duke University

1977

PROTON INDUCED X-RAY EMISSION (PIXE) AND APPLICATIONS TO ELEMENTAL ANALYSIS

by

Robert Dalton Willis

A Proton Induced X-Ray Emission (PIXE) system has been developed at Duke University with application to elemental analysis of biological, medical, and environmental samples. The system utilizes a 3-MeV beam of protons to excite characteristic X-ray emission from the bombarded sample. A solid-state Si(Li) detector is used to detect a fraction of the emitted X-rays. The present system provides moderately low detection limits, typically 1-100 ppm on a dry weight basis in a five minute irradiation, for elements heavier than sulphur. Numerous analyses of calibration standards yield an estimated accuracy better than 14% and an estimated precision of 12% or better for determining concentrations greater than 10 ppm.

The production of characteristic X-rays and the generation of background radiation are considered for both proton bombardment and excitation by heavier ions. Background contributions arising from secondary electron bremsstrahlung constitute the limiting factor to sensitivity in the X-ray

region below 10 keV, while primary bremsstrahlung and/or Compton scattering of nuclear gamma rays limit sensitivity for the X-ray region above 15 keV. The choices of bombarding ion and energy are examined with regard to optimizing the analytical capabilities of particle-induced X-ray emission. Protons of 2 to 4 MeV are generally considered to provide optimal sensitivity.

A number of techniques are described for sample preparation. These include solution deposits, wet ashing, fabrication of pellets, and analysis of the sample in its original state. The use of thin targets ($\lesssim$ 1 mg/cm^2) is generally recommended for best quantitative results; however, it is shown here that thick targets can in many cases also provide adequate quantitation with the added advantage of minimal sample preparation. Our varied experiences with wet ashing suggests that the problems inherent in this technique may outweigh the benefits to be derived from this procedure.

The applicability of PIXE for multielemental analysis is demonstrated for a wide variety of sample types. Particular emphasis has been placed at Duke on the analysis of biological and environmental samples. Major studies conducted include: (1) an investigation of metal uptake in plants and soils located near a source of pollution; and (2) a comparative study of toxic metals in marine fauna collected from clean and polluted environments. Results of such studies indicate the need for large sample sets because of the vari-

bility naturally present among such specimens. PIXE is demonstrated to be well suited for rapid and quantitative analysis of large numbers of samples.

Two computer programs are described which facilitate the analysis of PIXE data. Program TRACE is a semi-automatic peak-fitting program which provides elemental abundances for 10-20 elements in a time of 1-2 minutes. Program FUDGE calculates factors to correct for the reduced X-ray yield in thick targets due to X-ray absorption and proton energy loss.

A comparison of the PIXE technique with the X-ray Fluorescence method indicates similar detection limits for the two methods. The choice between the two techniques will therefore be determined by practical and economic considerations.

Future improvements are described for optimizing and extending the analytical capabilities of the present system. Advantages and disadvantages of the PIXE technique are summarized in the concluding section.

ACKNOWLEDGMENTS

I would like to express my deep appreciation to the many people who have contributed to this research effort and who have shaped my life during these last six years.

I am indebted to my advisor, Dr. R. L. Walter, for his support and guidance during my graduate career, and for his innumerable contributions in all areas of this research.

It has been a pleasure to work with Dr. W. F. Gutknecht who provided invaluable assistance throughout the course of these studies; without his enthusiastic participation, this work would not have been possible.

The collaboration with numerous people within and from outside the Duke community has been an especially rewarding aspect of this work. In particular I would like to acknowledge contributions from the following people: Dr. J. Joyce was instrumental in initiating this research project and also provided our data taking program; Dr. J. Antonovics contributed to the botanical and soil studies; Dr. B. Fowler provided samples and support for the marine life studies; and Dr. T. G. Dzubay provided valuable assistance on numerous occasions during this research. The collaboration with Dr. R. W. Shaw, Jr. during the past two years has been a most valuable and rewarding experience.

The assistance of numerous graduate and undergraduate students during all phases of this research is gratefully acknowledged. I am particularly indebted to Janette Stanford, Rudy Baum, and Mauri Ditzler. Mr. A. B. Baskin deserves particular mention for the initial development of the basic data analysis code which has served us so well for the last four years.

The expertise of Mr. S. E. Edwards and Mr. R. L. Rummel of the laboratory technical staff, and Mr. A. W. Lovette of the Duke University Instrument Shop, are gratefully acknowledged.

The figures enclosed were expertly drafted by Mrs. Joseph Bailey, and the manuscript was admirably typed by Mrs. Bonnie Farrell.

I shall always be indebted to my parents for their unfailing support, encouragement, and love throughout my life. The patience and understanding of my wife, Diane, during this past year has been very much appreciated and admired.

This work was supported in part by the U. S. Energy Research and Development Administration, the U. S. Environmental Protection Agency, and the National Institute for Environmental Health Sciences.

R.D.W.

CONTENTS

LIST OF FIGURES

LIST OF TABLES

PROTON INDUCED X-RAY EMISSION (PIXE) AND APPLICATIONS TO ELEMENTAL ANALYSIS

Chapter I

INTRODUCTION

Elements present at low levels in living organisms have long been the subject of scientific investigation (Bowen, 1966; Underwood, 1971). During the past one hundred years major efforts have been and continue to be devoted to several fundamental questions: (1) Which elements are "essential" to the organism's existence and which are not? (2) What biochemical functions do these trace elements perform? (3) At what concentration level does an element become toxic to the organism? and (4) Do the metabolic responses of certain elements exhibit interrelationships?

Adding to this continuing interest in trace elements has been the growing awareness in recent years of the complex interdependence of man and his surroundings. Scientists are only now beginning to accumulate evidence linking the geochemistry of the environment with certain disease states of man (Freedman, 1975). Some of the major environmental concerns which have been recently brought into focus involve experimental investigations of the pathways of trace elements between humans and their environment, uncovering correlations between the external environment and man's internal biochemistry, and

also identifying, quantifying, and monitoring man's impact on the environment.

This continuing interest in trace elements and the recent concern over the quality of the environment have provided the impetus for the development of a number of new analytical techniques. The goal of the analysts was to find a method which would combine some or all of the following desirable features: high sensitivity (ppm level or better) with good accuracy and precision; simultaneous multielement capability; rapid sample throughput with minimal sample preparation; non-destructive analysis which would permit previously analyzed samples to be either rechecked later or reanalyzed by other methods; and low cost per analysis.

In 1970, Johansson et al. described a new analytical technique utilizing characteristic X-ray emission induced by proton bombardment and suggested the capability of this method to detect many elements simultaneously at the 10^{-12} g level (Johansson, 1970). The new technique fulfilled most, if not all of the analytical requirements listed above and promised to become a valuable addition to existing methods. The enthusiastic report of Johansson et al. spurred efforts at a number of accelerator laboratories to develop their own PIXE (Proton-Induced X-ray Emission) systems in response to growing environmental concerns. The interest was additionally stimulated in many cases by the sharp reductions in funding during the early 1970's for the traditional areas of nuclear research.

In the years since Johannson's report, scientists have demonstrated that the PIXE method has impressive capabilities in the areas of biological and environmental analysis, pollution monitoring, and materials research. Articles by Walter et al. (1974), Folkmann (1975), Deconninck et al. (1975), and Johansson et al. (1976) provide excellent reviews of the applications of PIXE, and the capabilities as well as the limitations of PIXE. It is estimated that nearly thirty laboratories in the United States, Canada, Europe and Japan have contributed to the development of the PIXE technique.

It is interesting to briefly recount the steps leading up to Johansson's paper in 1970. The ability to detect the presence of an element via its characteristic X-ray emissions dates back to 1914 when Moseley first related the atomic number of an element with the wavelengths of the element's characteristic X-ray emissions, thus opening the door to wavelength dispersive X-ray spectrometry. This analytical technique continues to play a dominant role in X-ray spectroscopy, providing good sensitivity and unsurpassed resolution. The wavelength dispersion technique suffers however from a low detection efficiency, and until the advent of efficient multi-wavelength (i.e., multicrystal) spectrometers (Birks and Gilfrich, 1976), routine multielemental analyses using wavelength dispersive techniques were impractical for environmental samples.

Rapid advances during the 1960's in the development of high-resolution semiconductor detectors (Bowman et al., 1966) constituted a technological breakthrough in gamma ray and X-ray spectroscopy. The high resolution of the new solid-state detectors enabled the analyst to resolve X-ray emissions from adjacent elements on the periodic table (for $Z \gtrsim 10$) while the fundamental nature of the detection process (in which incoming X-rays are analyzed on the basis of their energies rather than their wavelengths) permitted the detection of up to thirty elements simultaneously.

The dramatic success of the solid-state detectors and the demand for new techniques applicable to environmental analysis stimulated a renewal of interest in X-ray spectroscopy. One topic of debate which developed early in this new period of activity and persists today concerns the relative merits of ion-induced X-ray spectrometry (employing protons or heavier ions as the excitation source) and energy-dispersive X-ray fluorescence (utilizing X-rays to excite the sample). Most of the work in ion-induced X-ray spectrometry utilizes proton beams (Walter, 1974; Campbell, 1975; Johansson, 1976) except for a major program at Davis, California, where alpha beams are employed (Perry and Brady, 1973 and Cahill, 1975). An excellent review of the status and prospects of energy-dispersive X-ray fluorescence is given by Goulding et al. (1973).

This dissertation describes the development at Duke University and the Triangle Universities Nuclear Laboratory

(located on Duke's campus) of a Proton-Induced X-ray Emission system. The work was initiated in 1972 while many questions still remained concerning the practical potential of the PIXE method. During the first two years, the emphasis of our research was twofold: (1) to develop and calibrate the PIXE system, and (2) to assess the potential and limitation of the technique. In the past three years modifications to the system have been minor and the emphasis has shifted toward applications of the system to a number of interdisciplinary studies involving the analyses of biological, clinical, and environmental samples.

The material which follows is divided into six chapters. Chapter II examines theoretical aspects of particle induced X-ray emission, including a discussion of background sources and facts determining the selection of beam ion and energy. Chapter III discusses experimental aspects: the experimental arrangement, system calibration and data analysis, methods of sample preparation, and considerations of sensitivity, accuracy, and precision. Chapter IV presents a general survey of applications of the Duke PIXE system to the analysis of environmental, biomedical, and botanical specimens. Chapter V discusses in detail two in-depth studies undertaken at Duke: (1) a series of studies concerned with correlating elemental abundances observed in plants with those observed in the soils which nourished the plants; and (2) an investigation of metal accumulation in marine

life collected from clean and contaminated environments. Chapter VI concludes with a summary highlighting the strengths and weaknesses of PIXE, suggestions for future improvements, and a comparison of the relative merits of PIXE and X-ray fluorescence analysis (XRF).

Chapter II

THEORY

IIA. Introduction to PIXE

Before proceeding with a discussion of the theoretical basis for the PIXE technique, a brief introduction to Proton-Induced X-ray Emission analysis is in order.

PIXE is an analytical technique for studying a wide variety of environmental, biological, and clinical specimens. For such samples it is capable of determining concentrations of approximately twenty elements simultaneously with sensitivities typically between 1 and 100 ppm for atomic numbers $Z \gtrsim 14$. The method usually employs a beam of protons with an energy around 3 MeV to irradiate the sample. The proton beam interacts with atoms in the sample with some probability for ejecting electrons from the inner atomic shells. Atoms thus excited return to their ground states via a series of electron transitions from outer-lying orbitals to inner-shell vacancies. Each of these transitions may be accompanied by the simultaneous emission of an X-ray whose energy is equal to the difference in binding energies of the two electron orbitals participating in the transition. Since each element of the periodic table possesses a unique and characteristic set of

atomic energy levels, these X-ray emissions -- known as characteristic X-rays -- serve as "fingerprints" which uniquely identify the atomic species giving rise to them, thus providing the basis for elemental analysis via X-ray spectroscopy.

A representative spectrum obtained by PIXE analysis of a section of crab muscle is shown in Figure 2.1. Approximately sixteen elements in the sample can be identified by their characteristic X-ray lines. These lines are always superimposed on a broad and smoothly varying X-ray continuum. The origins of this background radiation -- which represents a fundamental limitation to PIXE sensitivity -- will be examined in Section IIE.

The X-ray data is collected during a PIXE analysis by means of a solid state detector (Section IIIA.3) which converts the incoming X-ray emissions into voltage pulses such that the voltage of a given pulse is linearly related to the corresponding X-ray energy. These analog signals are sorted by pulse height into discrete energy channels of a multichannel analyzer, thus generating a spectrum of X-ray counts versus channel location (or equivalently, X-ray energy) as shown in Figure 2.1. Elemental concentrations (ppm) or absolute abundances (ng) can be immediately obtained from the corresponding X-ray peak areas if one knows the total amount of proton charge that impinged on the sample, and the system's efficiency calibration (Section IIIC).

Figure 2.1 PIXE spectrum obtained from a thick section of crab muscle in approximately 10 min. A polyethylene filter, inserted between the sample and the detector to absorb excess low-energy X-rays, was used to obtain the data. The solid line through the data points is a computer-generated fit to the data. Elemental abundances are extracted from the integrated peak areas and a calibrated efficiency curve. Vertical bars through the data points represent the statistical uncertainty in the data.

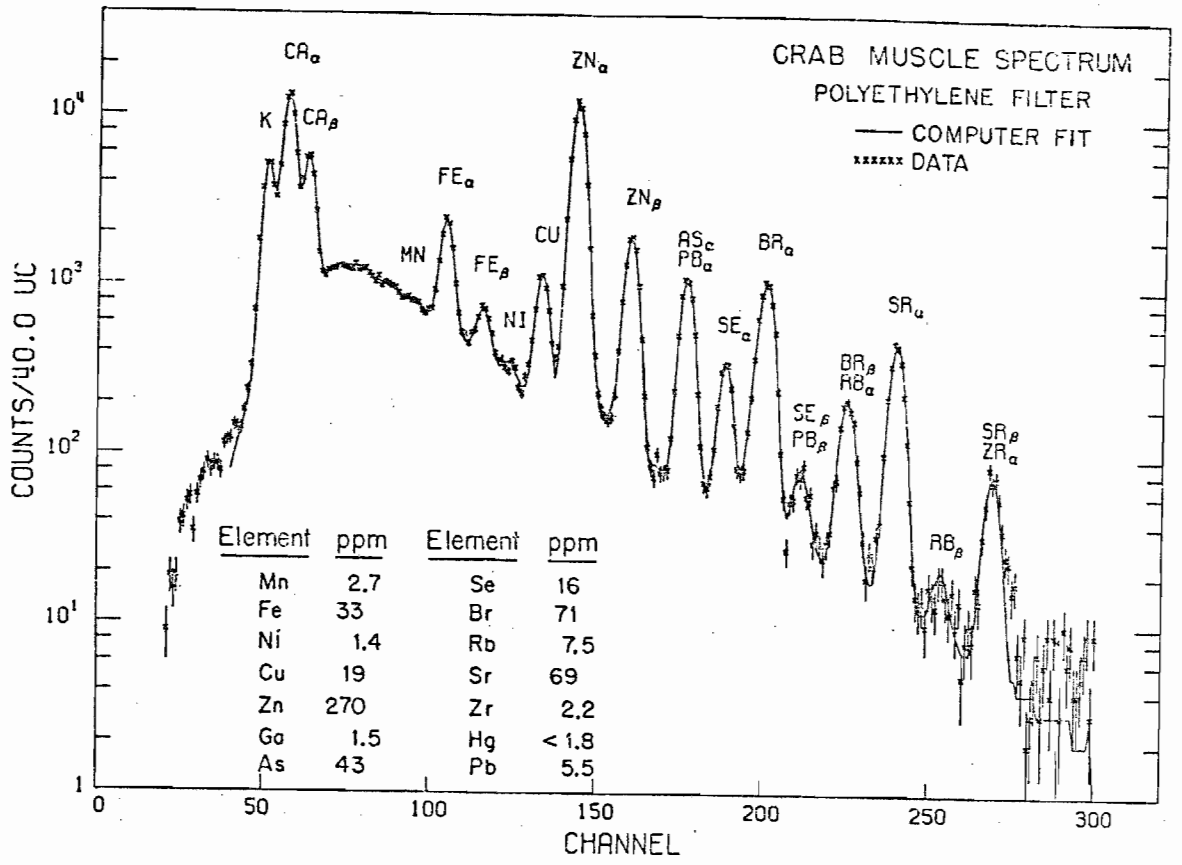
CRAB MUSCLE SPECTRUM
POLYETHYLENE FILTER
COMPUTER FIT
DATA
COUNTS/40.0 UC
CHANNEL
CA$_\alpha$
K
CA$_\beta$
MN
FE$_\alpha$
FE$_\beta$
NI
CU
ZN$_\alpha$
ZN$_\beta$
AS$_c$ PB$_\alpha$
SE$_\alpha$
BR$_\alpha$
SE$_\beta$ PB$_\beta$
BR$_\beta$ RB$_\alpha$
SR$_\alpha$
RB$_\beta$
SR$_\beta$ ZR$_\alpha$
Element ppm Element ppm
Mn 2.7 Se 16
Fe 33 Br 71
Ni 1.4 Rb 7.5
Cu 19 Sr 69
Zn 270 Zr 2.2
Ga 1.5 Hg < 1.8
As 43 Pb 5.5

As a final comment concerning the display of PIXE spectra it should be noted that in Figure 2.1 and in spectra to follow, the vertical axis represents the log of the X-ray counts. As a consequence, the background and regions of few counts are visually enhanced relative to the characteristic X-ray peaks, suggesting a poorer signal-to-noise ratio than is in fact obtained.

The mechanism of X-ray production can be viewed as a two step process involving first the creation of inner-shell vacancies by proton bombardment, and second the emission of characteristic X-rays as outer-shell or free electrons drop in to fill the inner-shell vacancies. Details of each of these processes are discussed in the following sections.

IIB. Fundamentals of X-ray Emission

Characteristic X-ray line spectra result from the de-excitation of atoms which have been excited to higher energy states by the removal of one or more electrons from the inner atomic shells. The mechanism for producing inner-shell vacancies can be either charged particle bombardment (using electrons, protons, or heavier ions) or excitation by energetic photons (X-rays or gamma rays). In the process of returning to its ground state, the excited atom may emit characteristic X-rays. This process is shown schematically in Figure 2.2a for an atom having vacancies in the two innermost (K and L) atomic shells. The excited atom returns to its ground state via a

Figure 2.2a Simplified schematic of the X-ray production process showing the dominant K-shell and L-shell transitions giving rise to the K and L X-ray series.

Figure 2.2b Atomic model showing electron transitions giving rise to the K, L, and M X-ray emissions. Transitions are labeled with conventional notation for the associated emission lines. Transitions occurring with highest probability are indicated by heavier lines (from Woldseth, 1973).

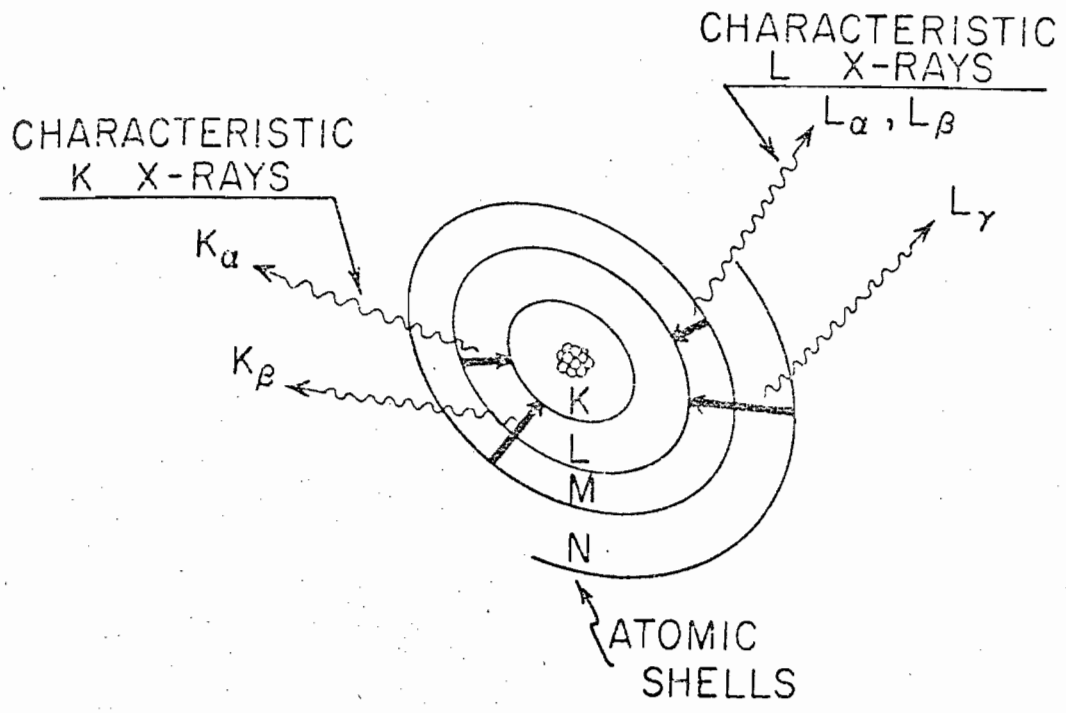
CHARACTERISTIC
L X-RAYS
L_α , L_β
L_γ
CHARACTERISTIC
K X-RAYS
K_α
K_β
K
L
M
N
ATOMIC
SHELLS

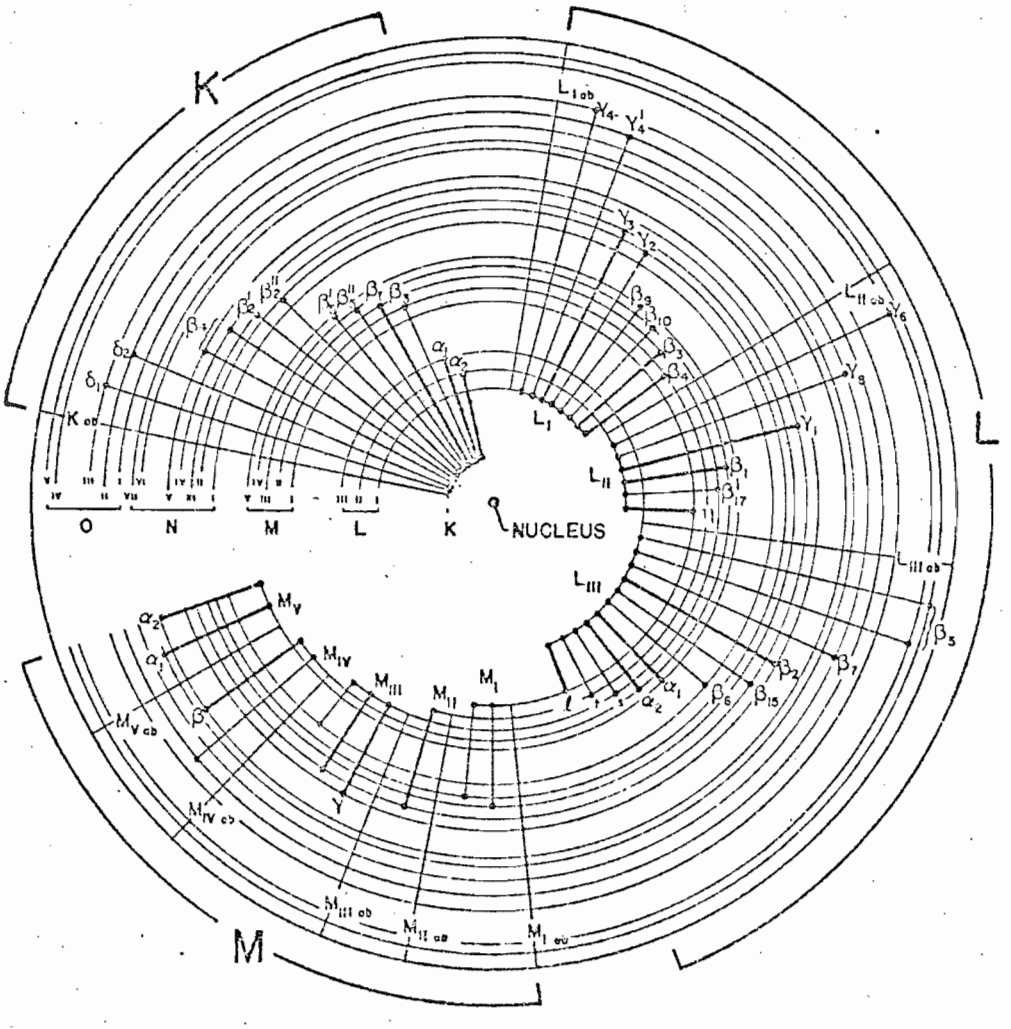
K
L
M
O
N
M
L
K
NUCLEUS

succession of electron transitions (subject to transition selection rules) which is initiated by the primary transition of one electron from a higher shell (or subshell) to the original inner-shell vacancy. The transition leaves a vacancy in the outer shell which is subsequently filled by a second electron transition, and so forth, until the electron configuration of the ground state atom is reproduced.

Figure 2.2b (from Woldseth, 1973) shows a more detailed model of the atom indicating with radial lines the electron transitions to inner-shell (K, L, or M) vacancies which occur with reasonable probabilities. The transitions are labeled with the conventional notation used for the associated emission lines. Thus, vacancies in the K-shell which are filled by electrons originating in outer atomic shells give rise to the K series of X-ray lines comprised mainly of the K_α and K_β series (Figure 2.2a). Similarly, the series of L X-ray emissions of which the most dominant are (in decreasing probability) the L_α, L_β, and L_γ series, results from the filling of L-shell vacancies by electrons from the outer-lying M, N, and O shells. Individual lines within a series are labeled with a subscript (e.g., K_{α_1} or L_{α_1}) according to the transition scheme shown in Figure 2.2b.

Each transition in the de-excitation process of an atom returning to its ground state lowers the energy of the excited atom by a discrete amount ΔE equal to the difference

in binding energies of the two electron orbitals participating in the transition. Conservation of energy demands that this energy loss be accounted for elsewhere in the system. Three mechanisms exist to satisfy the requirement that energy be conserved: (1) radiative transitions resulting in the emission of characteristic X-rays of energy ΔE; (2) radiationless transitions leading to the emission of Auger electrons, and (3) radiationless Coster-Kronig transitions (for the L-shell and higher shells) in which the primary inner-shell vacancy is filled by a transition from a subshell within the same atomic shell. Energy is conserved as in the Auger process by the simultaneous ejection of an outer-shell electron. The relative probabilities governing these three modes of de-excitation will be discussed in Section IIC. The remainder of the present section will deal with the mechanism of characteristic X-ray emission, as this process provides the basis for both PIXE and XRF (X-ray Fluorescence analysis).

The X-ray emissions accompanying inner-shell electron transitions are characterized by several noteworthy features:

1. Every element possesses a unique set of X-ray emission lines which serves as a "fingerprint" for elemental identification. The energies of the characteristic X-ray emissions are simply related to the atomic number Z, and the relative intensities of the X-ray lines are governed by the fixed probabilities of the corresponding electron transitions.

2. Energy-dispersive X-ray analysis provides elemental information only; the very small energy shifts (tens of eV or less) in the X-ray emission lines due to different chemical states of the same atom (i.e., different vacancy distributions in the outer shells) are not resolved using energy-dispersive detectors.

3. The X-ray emission spectrum for a single element is relatively simple when studied with a comparatively poor resolution energy-dispersive system, thus facilitating rapid, quantitative analysis.

The characteristic nature of X-ray emissions was first observed by Moseley (1913, 1914) who related the energies of K and L X-rays to the square of the atomic number Z according to the following empirical formulae:

for K-line emissions, $E_K \simeq C_K (Z-\sigma_K)^2$;

for L-line emissions, $E_L \simeq C_L (Z-\sigma_L)^2$.

These results can be understood in terms of the simple Bohr model of the atom in which the binding energy of an electron is given by

$$E_n \simeq -\frac{\mu Z^2 e^4}{(4\pi\varepsilon_o)^2 2\hbar^2} \cdot \frac{1}{n^2} = -(13.6)\left(\frac{Z}{n}\right)^2 \text{ eV},$$

where n represents the principle quantum number of the atomic shell (n=1 and 2 for the K- and L- shells, respectively). The energy E_x of the X-ray associated with an electron transition from an initial shell ($n=n_i$) to the primary vacancy in the

final shell ($n=n_f$) is equal to the difference in binding energies of the two shells:

$$E_x = E_{n_f} - E_{n_i} \simeq 13.6Z^2\left(\frac{1}{n_i^2} - \frac{1}{n_f^2}\right)\text{eV}.$$

In order to obtain reasonable agreement with experimental results, screening of the nuclear charge due to electrons in inner shells must be accounted for by replacing Z in Bohr's formula with an effective nuclear charge,

$Z_{eff} = Z - \sigma$ where σ is the appropriate screening constant. Then,

$$E_x \simeq 13.6\left(\frac{1}{n_i^2} - \frac{1}{n_f^2}\right)(Z-\sigma)^2$$

in agreement with the functional form of Moseley's laws.

The efficiency for X-ray detection in a typical PIXE system which utilizes a lithium-drifted silicon detector (Si(Li)) is such that reasonable sensitivities are obtained for X-ray energies between approximately 1.5 keV and 25 keV. This energy window corresponds to K-line emissions for $13 \lesssim Z \lesssim 50$, L-line emissions for $Z \gtrsim 35$ and M-line emissions for $Z \gtrsim 74$. Tables of X-ray energies for K and L-line emissions including ionization energies for the K shell and L_1, L_2, and L_3 sub-shells are provided in Appendix C (Table C.1). The M-line emissions are rarely observed in trace element analysis and have not been included in the table of X-ray energies. Table C.2 provides another representation of the dominant K,

L, and M X-ray emissions (up to 20 keV) which is useful in identifying potential line interferences given a typical system resolution of roughly 200 eV. Familiar examples of X-ray line interferences are the Co K_α - Fe K_β interference and the Pb L_α - As K_α interference. These interelement interferences pose potential problems for quantitative analysis of PIXE spectra and are treated in more detail in Section IIID.

Some additional features of characteristic X-ray spectra can be discussed with reference to Figure 2.3 showing a PIXE spectrum of a calibration standard for the elements Pb and V. The V K_α and K_β lines and the Pb L_α, L_β, and L_γ lines are in fact multiplets of two or more individual lines as Figure 2.3 indicates. (Only those transitions occurring with reasonably high probability have been included in Figure 2.3.) This fine structure can contribute to line broadening as seen for example in the Pb L_β and L_γ peaks, but cannot be resolved with the energy-dispersive detectors commonly used in PIXE analysis (i.e., with detector resolutions of approximately 170-200 eV (FWHM) for the Mn K_α line). For purposes of obtaining quantitative analysis of PIXE spectra, it is sufficient in most cases to treat K-line emissions as two lines (K_α and K_β) and L-line emissions as composed of three to five major lines. This relative simplicity facilitates rapid interpretation and analysis of PIXE spectra. More typical PIXE spectra (Figure 2.1 for example) are obtained from samples containing fifteen or more elements of interest,

Figure 2.3 PIXE spectrum of calibration standards for the elements V and Pb showing V K-lines and Pb L-lines. Fine structure of the line shapes is indicated below the peaks. Intrinsic intensity ratios for the individual lines (relative to the K_{α_1} and L_{α_1} lines for V and Pb, respectively) are also shown. (Adapted from Folkmann, 1977).

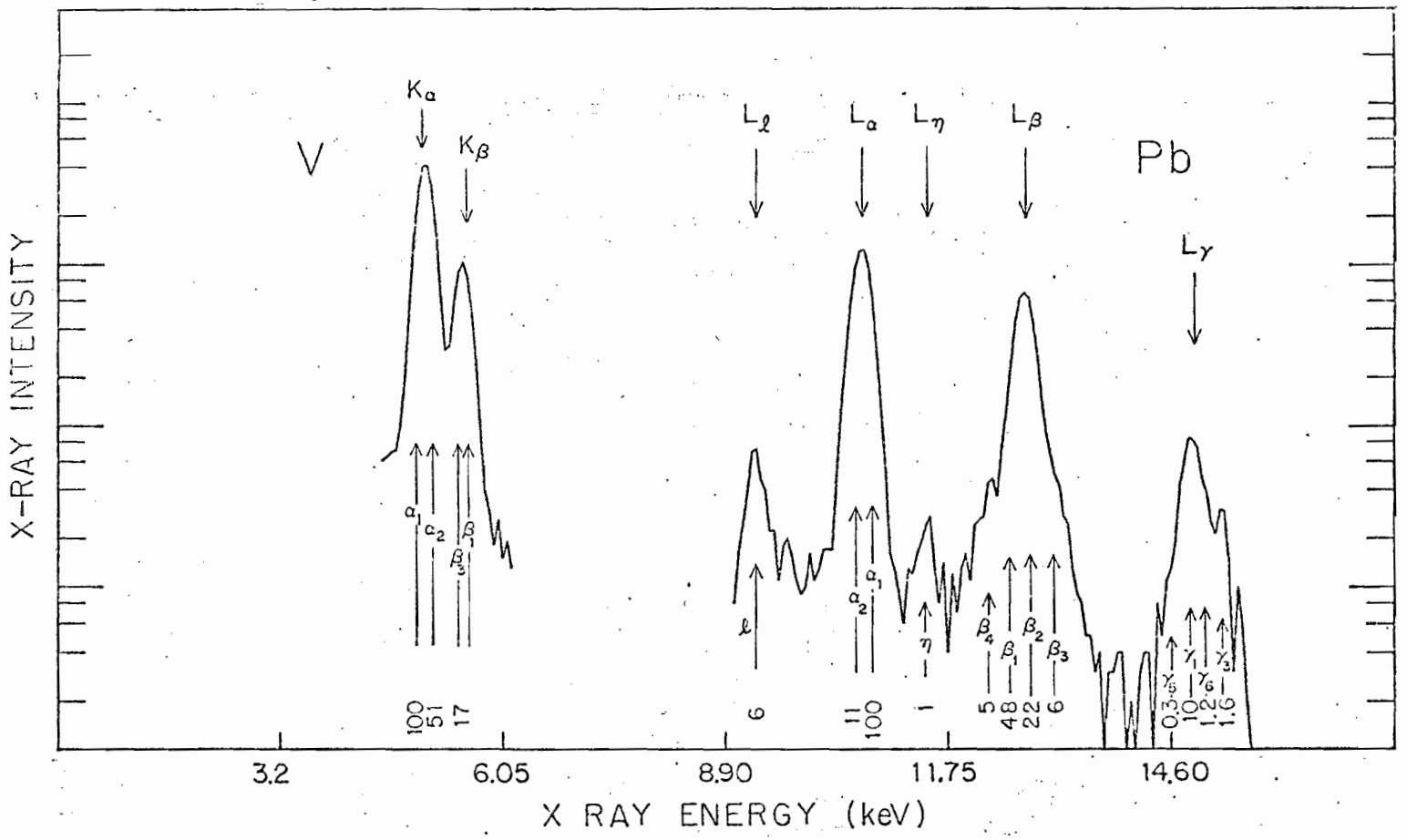
V
Pb
K_α
K_β
L_ℓ
L_α
L_η
L_β
L_γ
X-RAY INTENSITY
X RAY ENERGY (keV)
3.2
6.05
8.90
11.75
14.60
100
51
17
6
11
100
1
5
48
22
6
0.3
10
1.2
1.6

generating thirty or more X-ray lines. Rapid, accurate analysis of such spectra requires sophisticated computer techniques as described in Section IIID.

Each transition corresponding to the X-ray emission lines in Figure 2.3 occurs with an intrinsic probability which is constant for a given Z and which determines the relative intensities of the emission lines observed for a given element. (In Figure 2.3, the probabilities of the various emission lines are indicated relative to the K_{α_1} and L_{α_1} lines which are arbitrarily assigned a value of 100.) "Best fit" values for these relative emission rates have been collected by Salem et al. (1974) for K-shell and L-subshell transitions. It is customary to express these probabilities relative to the emission rate for the dominant line within a subshell's emission spectra. The intensity ratios are important because they determine an element's unique "fingerprint" and are essential in being able to resolve interferences due to overlapping X-ray lines. Figure 2.4 plots K_β/K_α intensity ratios versus Z using values calculated by Scofield (1974). The actual intensity ratios observed in a PIXE spectrum differ somewhat from the intrinsic intensity ratios due to the fact that the efficiency for X-ray detection is not uniform over the usable X-ray energy region. Hence, peak-fitting routines used to analyze PIXE spectra employ experimentally determined intensity ratios or stored sets of elemental emission lines.

Figure 2.4 Plot of K_β/K_α intensity ratios versus atomic number. Values are taken from Scofield (1974).

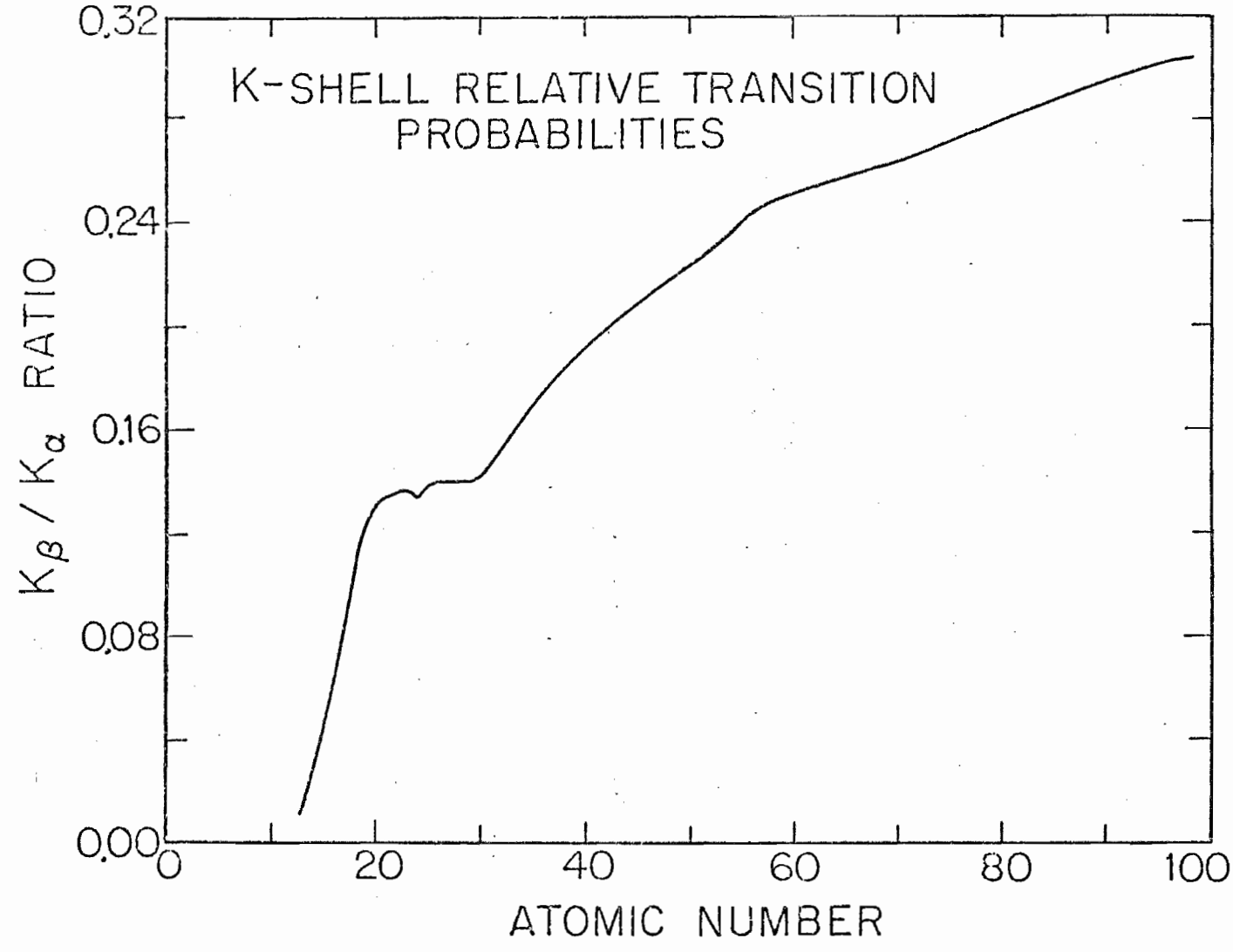
K-SHELL RELATIVE TRANSITION PROBABILITIES
K_β / K_α RATIO
0.32
0.24
0.16
0.08
0.00
0
20
40
60
80
100
ATOMIC NUMBER

IIC. Radiationless Transitions

Not all inner-shell vacancies result in radiative electron transitions; for certain regions of the periodic table radiationless transitions, i.e., Auger and Coster-Kronig transitions, occur with much greater probability than characteristic X-ray emission.

A measure of the relative probabilities for X-ray emission and radiationless transitions is given by the fluorescence yield factor ω_s defined as the ratio of X-ray quanta emitted per primary s-shell vacancy created (s = K or L). While this definition is adequate for K-shell transitions, for all higher shells the fluorescence yield will in general depend on how the shell vacancies are distributed among the subshells (Bambynek et al., 1972). For the L shell and all higher shells, an average fluorescence yield $\bar{\omega}_s$ can be defined which takes into account the subshell vacancy distribution including primary vacancies shifted to each subshell by Coster-Kronig transitions. Figure 2.5 plots values for the K-shell fluorescence yield ω_K, and the mean L-shell fluoresence yield $\bar{\omega}_L$, versus Z. (Values for ω_K are empirical "best fit" values calculated by Bambynek et al. (1972). The values of $\bar{\omega}_L$ are average experimental values from the same reference.). The K- and L-shell fluorescence yields are seen to be smoothly increasing functions of Z. This behavior has important consequences for analytical techniques using X-rays, contributing

Figure 2.5 K-shell fluorescence yield ω_K and average L-shell fluorescence yield $\bar{\omega}_L$ versus atomic number. Values for ω_K are "best fit" values to experimental data (Bambynek et al., 1972). Values for $\bar{\omega}_L$ are average experimental values from the same reference.

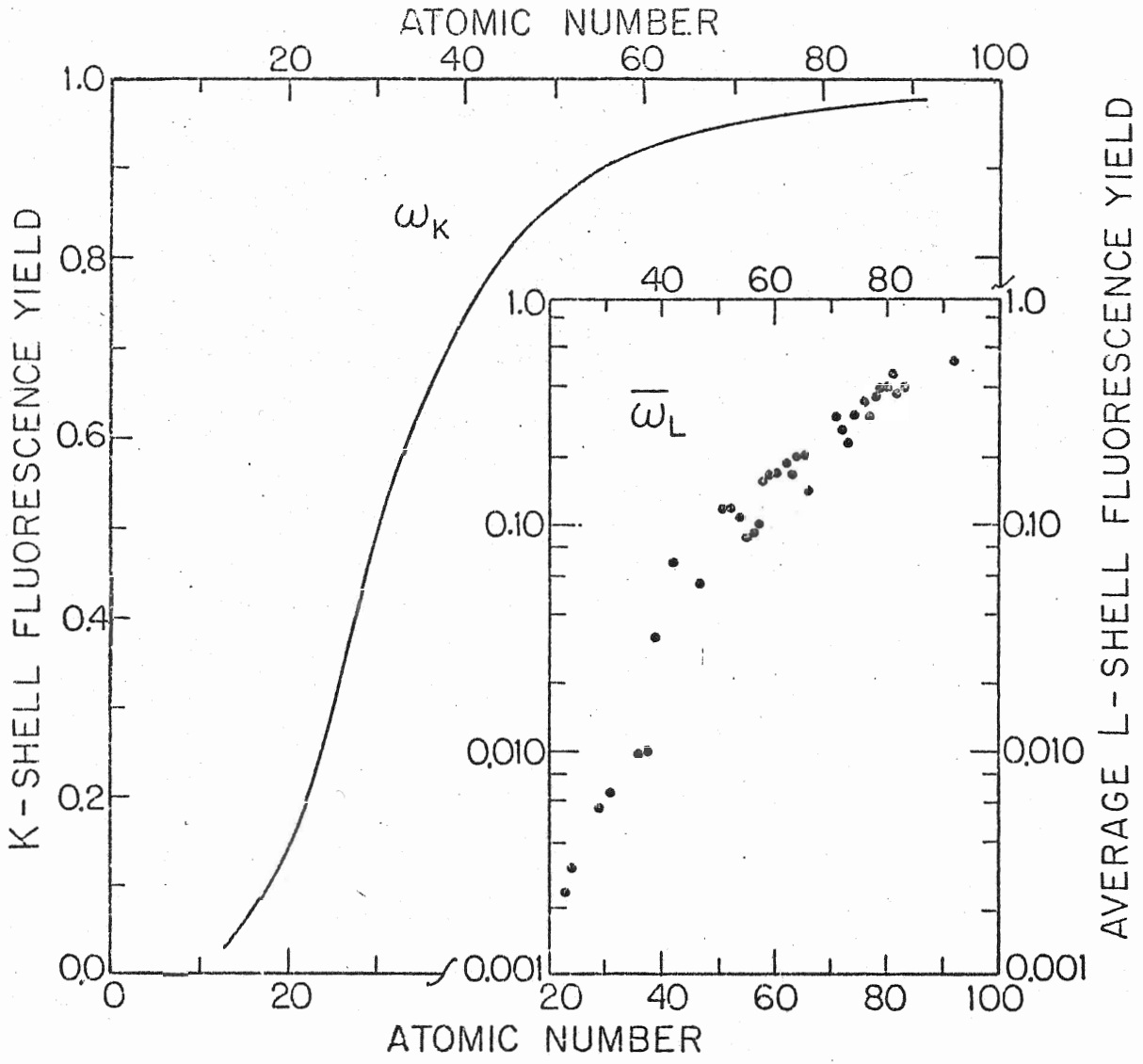
ATOMIC NUMBER
20
40
60
80
100
1.0
0.8
0.6
0.4
0.2
0.0
K-SHELL FLUORESCENCE YIELD
ω_K
$\overline{\omega}_L$
0.10
0.010
0.001
AVERAGE L-SHELL FLUORESCENCE YIELD
0
ATOMIC NUMBER

significantly to a reduced efficiency for the detection of K and L X-ray emissions from low and medium Z elements. For example, less than 20 percent of K-shell vacancies (for $Z_K < 22$) and L-shell vacancies ($Z_L < 68$) are filled by radiative transitions.

IID. Inner-Shell Vacancy Production

The low levels of detection (~1 ppm) attainable with PIXE are largely a consequence of the relatively large probabilities or cross sections for inner-shell ionization by charged particle bombardment. The behavior of these ionization cross sections as a function of projectile energy and target atomic number is understood quite well for protons and light ion projectiles in general. The study of collision phenomena using heavy ions as projectiles is currently an area of much interest, but a comprehensive theoretical understanding of heavy ion phenomena is still lacking, due to the much more complex nature of heavy ion interactions. The present section describes the major features of inner-shell vacancy production by light ions and the consequences for PIXE analysis. The potential use of heavy ions for trace element analysis will be commented upon in Section IIF.

Several different theoretical approaches have been used with considerable success in understanding the main features of inner-shell vacancy production by light ions (protons and He ions). These include the Plane Wave Born

Approximation (PWBA) (Merzbacher and Lewis, 1958; Madison and Merzbacher, 1975), the Binary Encounter Approximation (BEA) (Garcia, 1970), and the Semiclassical Approximation (SCA) (Bang and Hansteen, 1959). The starting point for each of these models is to treat the ion-atom interaction as essentially a perturbation of the atomic state by a point charge. In PWBA calculations, the incident charged particles are treated as plane waves impinging on inner-shell target electrons described by hydrogenic wave functions. The Binary Encounter Approximation considers the ionization process in terms of a classical impact between the projectile and a free target electron. The role of the target nucleus is simply to provide the electron in its initial state with a momentum distribution. The Semiclassical Approximation attempts to treat the Coulomb deflection of the incident projectile (which becomes important at low projectile velocities) by means of an impact parameter formulation in which appropriate deflection corrections are inserted. Refinements of these basic approaches continue to yield improved agreement with experiment as various second-order effects are treated -- e.g., increased electron binding due to the formation of molecular orbitals, polarization of the electron distribution by the incident ions, inner and outer-shell screening effects, and relativistic effects (for heavy target atoms). (See, for example, recent modifications to the Born Approximation by

Basbas et al. (1973) which treats Coulomb deflection and increased binding effects.) For more detailed discussions of these various models, the reader is referred to current reviews by Garcia et al. (1973), Madison and Merzbacher (1975) and Hansteen (1975).

The physical quantity of interest to the PIXE analyst is the X-ray production cross section, or in other words, the probability that exposure of a target atom to the excitation source will result in the emission of a characteristic X-ray. The production cross section $\sigma_s^{prod}(Z_2)$ for the s th atomic shell or subshell and for target atom Z_2, depends on the probability for vacancy production in the s-shell through the ionization cross section σ_s^{ion}, and on the fluorescence yield ω_s which measures the number of X-ray quanta emitted per s-shell vacancy. Accordingly,

$$\sigma_s^{prod}(Z_2) = \omega_s(Z_2) \cdot \sigma_s^{ion}(Z_2).$$

The behavior of $\sigma_s^{prod}(Z_2)$ as a function of excitation source (protons, electrons, heavy ions and photons) and excitation energy has important consequences in terms of detection sensitivity (Section IIF) and it is worthwhile to consider some of the major features of the production cross section. Figure 2.6 (from Folkmann, 1977) shows the K-shell X-ray production cross section versus Z_2 via proton, electron, and photon excitation at several different energies. It is interesting to note in Figure 2.6 that $\sigma_K^{prod}(Z_2)$ is a sharply

Figure 2.6 K X-ray production via protons, electrons, and photons versus target atomic number. The energies for electron and photon excitation represent an upper limit for the K-shell binding energy. Note the difference in the behavior of the emission cross section versus Z for particle excitation and photon excitation (from Folkmann, 1977).

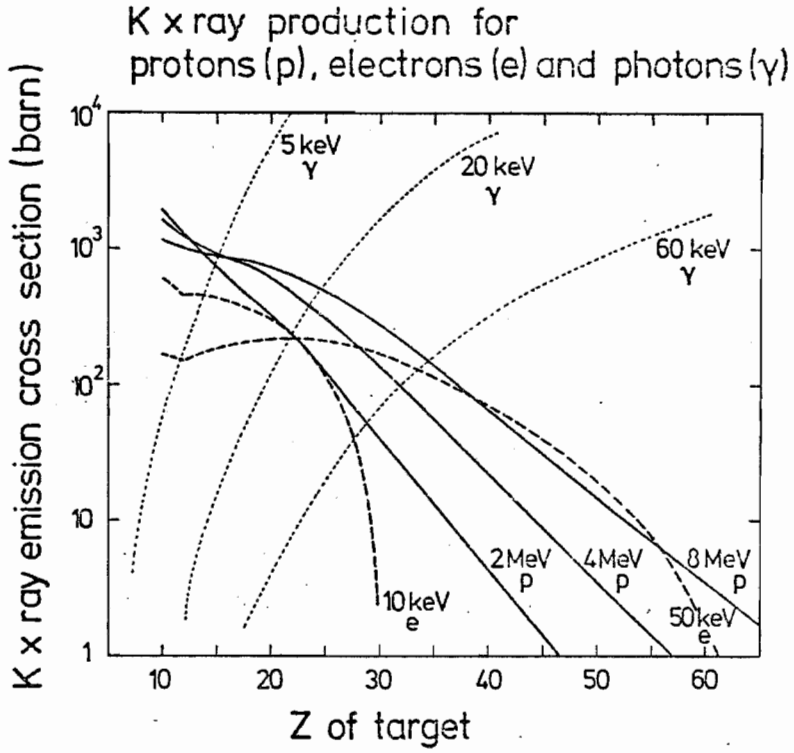
K x ray production for
protons (p), electrons (e) and photons (γ)
K x ray emission cross section (barn)
10⁴
10³
10²
10
1
5 keV γ
20 keV γ
60 keV γ
2 MeV p
4 MeV p
8 MeV p
10 keV e
50 keV e
10
20
30
40
50
60
Z of target

increasing function versus Z_2 for photon excitation, and a sharply decreasing function for particle excitation. While this behavior suggests advantages in using proton excitation for light element analyses and X-ray excitation for the analysis of medium to high Z elements, it should be pointed out that the accompanying background radiation (Section IIE) shows similar behavior to the dependences exhibited in Figure 2.6 -- that is, the background intensity peaks in the low Z region for particle excitation, whereas for XRF, it reaches its maximum intensity at X-ray energies immediately below the photon energy of the excitation source.

The behavior of the K- and L-shell emission cross section for proton excitation is plotted in Figure 2.7 for proton energies between 1.0 and 5.0 MeV which includes the energy range of interest for optimum analytical sensitivity. The data for Figure 2.7 was generated from a semiempirical formula which was developed by Johansson (1976) and which is described below. For a given proton energy E_p, the emission cross sections are observed to decrease approximately exponentially as a function of Z_2 (for $Z_2 \gtrsim 25$):

$$\sigma_K^{prod}(Z_2) \sim \exp\left[-AZ_2 + B\right],$$

where A and B are constants. This precipitous decline in both the K- and L-shell emission cross sections, folded in with a decreasing detector efficiency above 18 keV X-ray energy,

Figure 2.7 Calculated K and L X-ray production cross sections versus Z for proton energies between 1.0 and 5.0 MeV. Calculations are from Equation 2.2 and Table 2.1.

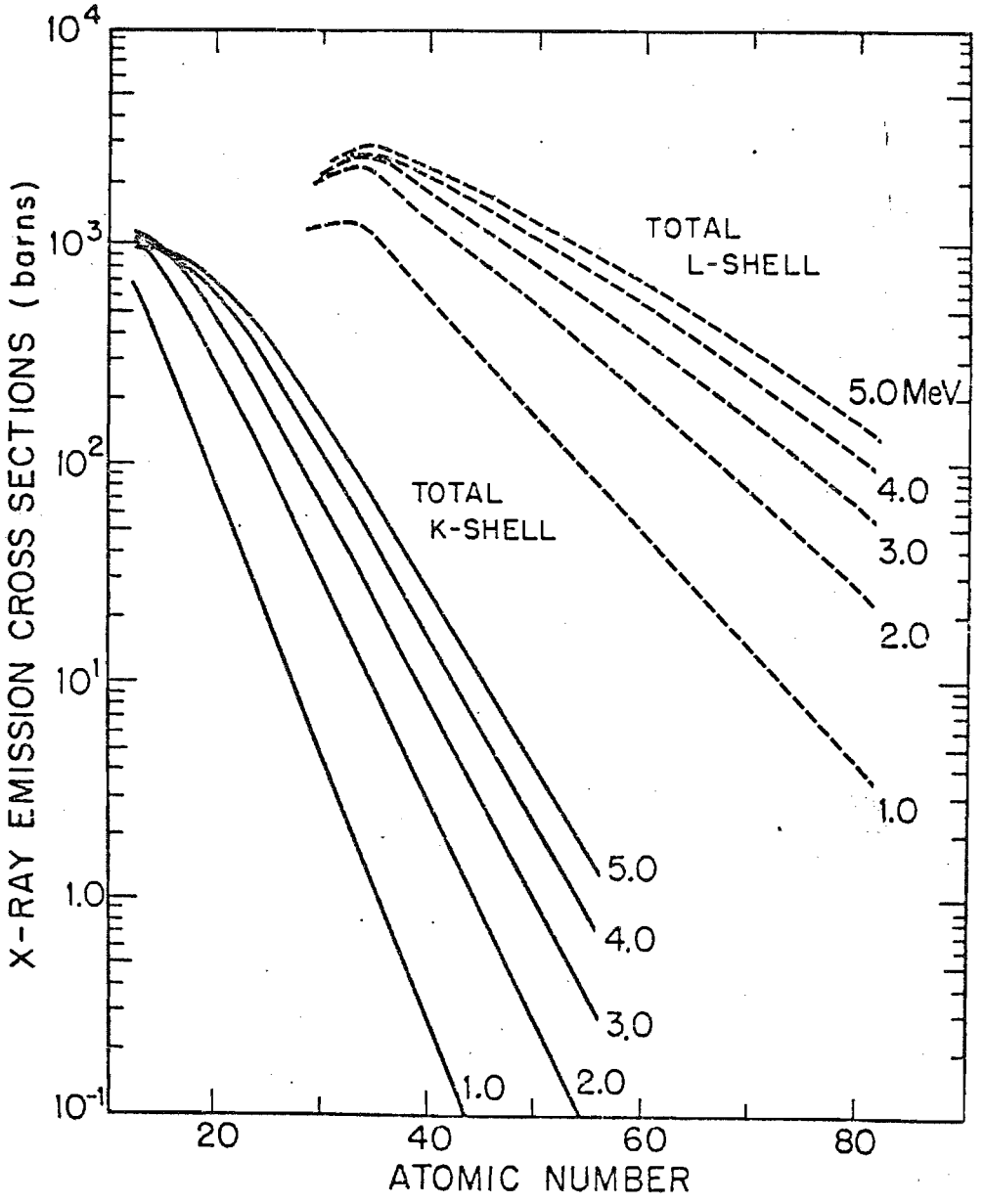
X-RAY EMISSION CROSS SECTIONS (barns)
ATOMIC NUMBER
TOTAL
L-SHELL
TOTAL
K-SHELL
5.0 MeV
4.0
3.0
2.0
1.0
5.0
4.0
3.0
2.0
1.0
10^4
10^3
10^2
10^1
1.0
10^{-1}
20
40
60
80

establishes an upper limit of approximately 25 keV as the maximum X-ray energy for which an element can be detected by PIXE with reasonably high sensitivity.

The behavior of $\sigma_s^{prod}(Z_2)$ as a function of the projectile energy E_p is important in optimizing the experimental parameters for maximum sensitivity in the elemental region of interest. Calculations in PWBA predict that given a target atom Z_2, the s-shell ionization cross section (hence also the s-shell production cross section) will increase rather slowly with projectile energy and will reach a maximum at an energy E_p such that the projectile velocity is approximately equal to the average velocity of the inner-shell electron (Madison and Merzbacher, 1975). This region of the maximum is known as the "velocity-matching" peak. For Z_2 = 13 (the lightest element observable with PIXE), the maximum in the production cross-section curve occurs at $E_p \sim 3.0$ MeV, and as Z_2 increases the cross section peak shifts to higher E_p. As Figure 2.7 shows, for proton energies between 1.0 and 5.0 MeV, the emission cross section displays a rather weak dependence on proton energy, varying approximately as $(E_p)^y$ where $1.0 \lesssim y \lesssim 2.5$ depending on the value of Z_2.

An important feature of the production cross section is the scaling property predicted by PWBA and BEA calculations: for projectile charge Z_p and energy E_p, the production cross section for target atoms Z_2 should scale as $(Z_p)^2$ for equal-velocity projectiles. That is,

$$\sigma_{Z_p}^{prod}(E_p, Z_2) = (Z_p)^2 \cdot \sigma_{Z=1}^{prod}(E_p/M_p, Z_2) \qquad (2.1)$$

where M_p is the projectile mass expressed in atomic mass units (amu). Folkmann et al. (1974b) measured production cross sections for six target elements using beams of protons, ^4He and ^{16}O ions at energies of 3 and 5 MeV/amu. These results are presented in Figure 2.8 and compared to calculated values based on the Born Approximation (solid line) and the Binary Encounter model (dashed line). (Figure 2.8 is adapted from Figures 2 and 3 of Folkmann, 1974b. The calculated curves are from the same reference.) The calculated curves shown for the ^4He and ^{16}O ions were obtained from the proton calculations by assuming the simple scaling property above (Equation 2.1). The scaled results agree reasonably well with the ^4He-induced data and to a lesser degree with the ^{16}O data. In general, the situation for vacancy production by heavy ions is considerably more complex than the scaling property above suggests (Section IIF).

Johansson et al. (1976) developed a semiempirical formula for ionization cross sections based on available thin-target measurements. The K- and L-shell cross section data were fitted using fifth degree polynomial curves given by:

$$\log_e(\sigma_s^{ion} U_s^2) = \sum_{n=o}^{5} b_n x^n \qquad (2.2)$$

where s = K or L. Here, $x = \log_e (10^{-3} E_p/\lambda U_s)$

Figure 2.8 K and L X-ray production cross sections for 3 MeV/amu and 5 MeV/amu ^{1}H (triangles), ^{4}He (squares) and ^{16}O ions (circles). Calculated values based on the Born approximation (solid lines) and the Binary Encounter Approximation (dashed lines) are also shown (from Folkmann et al., 1974b).

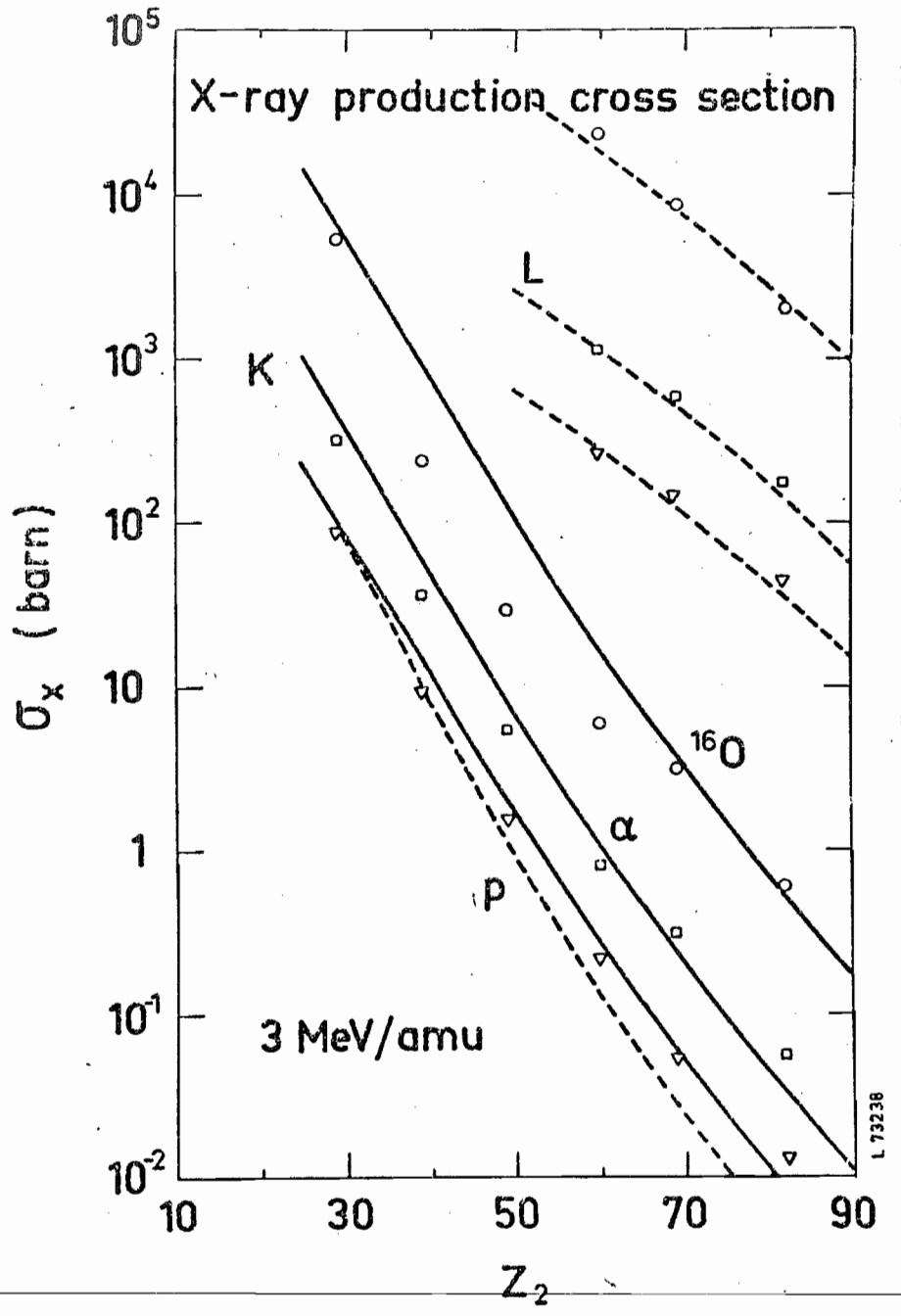
X-ray production cross section
σ_x (barn)
10^5
10^4
10^3
10^2
10
1
10^{-1}
10^{-2}
K
L
^{16}O
α
p
3 MeV/amu
10
30
50
70
90
Z_2
L 73238

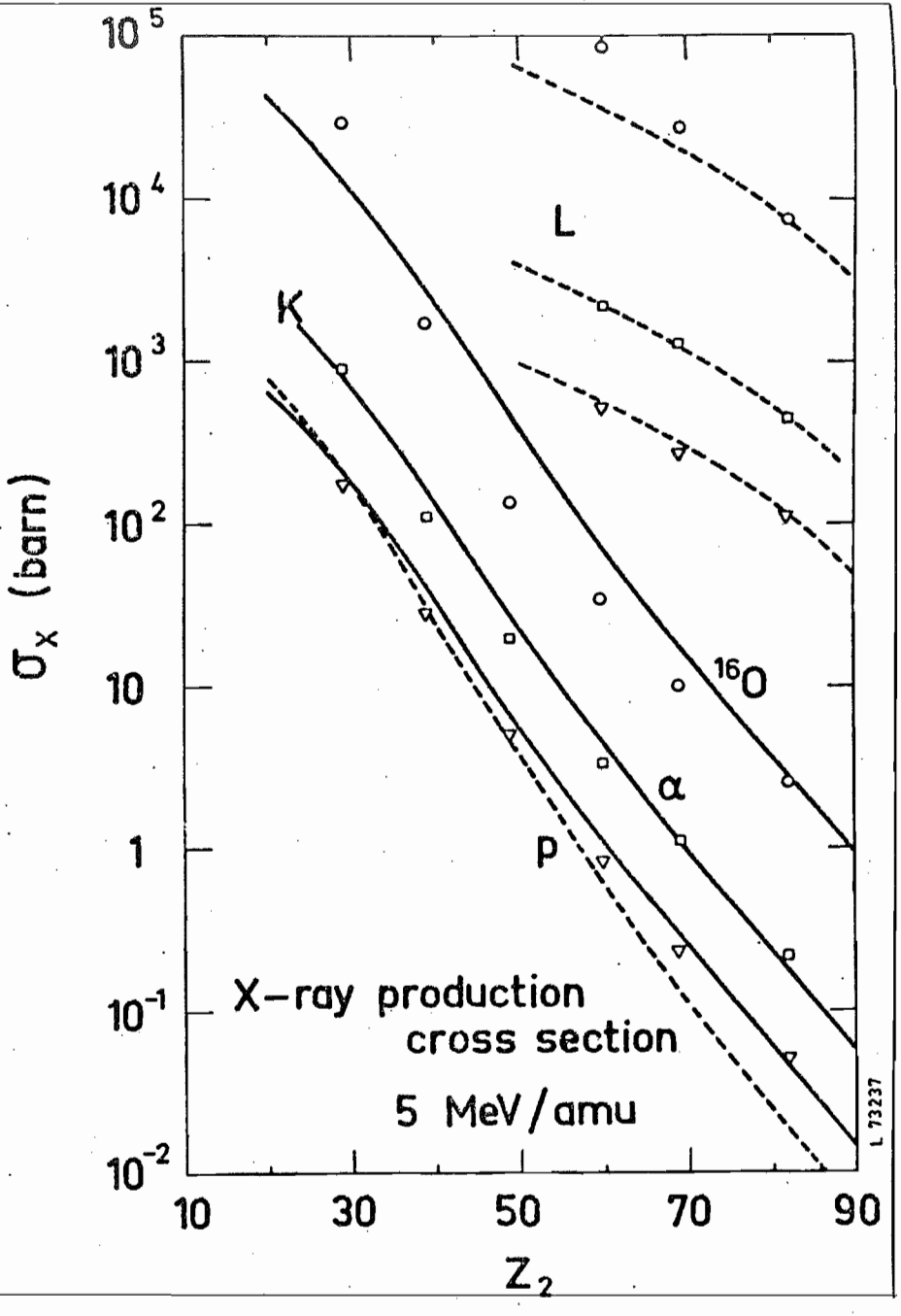
σ_x (barn)
10^5
10^4
10^3
10^2
10
1
10^{-1}
10^{-2}
K
L
^{16}O
α
p
X-ray production
cross section
5 MeV/amu
10
30
50
70
90
Z_2
L 73237

E_p = proton energy (eV)

λ = 1836 = ratio of proton mass to electron mass

U_K = K-shell ionization energy (eV)

U_L = L-shell ionization energy (eV)

$U_L = 1/4\ (U_{L1} + U_{L2} + 2U_{L3})$

where U_{L_i} is the ionization energy (eV) of the i th L-subshell. Also, σ_s^{ion} is the s-shell ionization cross section ($10^{-14} cm^2$). The fitting constants b_n are listed in Table 2.1.

Expression (2.2) is particularly useful in calculating ionization (or production) cross sections at arbitrary projectile energies E_p. For example, in order to obtain quantitative results for PIXE analyses of "thick" samples (i.e., samples in which the incident proton beam loses a significant fraction of its initial energy) corrections must be applied to the observed X-ray yields to account for the changing X-ray emission cross sections as the proton beam loses energy in the sample. These calculations are included in a computer program FUDGE (Section IIIC.4 and Appendix A) developed at this laboratory in order to calibrate the PIXE system for thick-target analyses. Tables C.3 and C.4 in Appendix C contain values calculated from expression 2.2 for the K- and L-shell X-ray production cross sections for selected elements and proton energies between 0.5 MeV and 10.0 MeV. These values generally agree with measured data within experimental uncertainties. Numerous references to experimental cross section data are provided in Johansson (1976) and Deconninck (1975).

Table 2.1

Coefficients for Calculating σ_s^{ion} Using Equation 2.2 (See Text)

X-ray	b_0	b_1	b_2	b_3	b_4	b_5
K	2.0471	-0.65906(-2)[a]	-0.47448	0.99190(-1)	0.46063(-1)	0.60853(-2)
L	3.6082	0.37123	-0.36971	-0.78593(-4)	0.25063(-2)	0.12613(-2)

a) Numbers in parentheses are powers of 10 multiplying the coefficient--e.g., -0.65906×10^{-2}.

IIE. Background Production Processes

The PIXE spectrum shown in Figure 2.1 indicates a series of characteristic X-ray peaks superimposed on a broad continuum background which characteristically peaks in the low energy region and includes a slowly rising tail extending through the high energy end of the spectrum. The sources of this background radiation exist primarily in physical processes that are intimately related to the production of characteristic X-rays. The background contribution can be minimized but never eliminated and therefore constitutes a fundamental limitation to PIXE sensitivity. The following paragraphs present a discussion of the major contributions to background radiation. The actual background level observed experimentally depends on a number of considerations -- choice of the excitation particle and energy, and the particular experimental arrangement. The optimum choices for these parameters which yield the best sensitivity are discussed in Sections IIF and IIIF.

The background illustrated in Figure 2.1 can be attributed primarily to three sources:

1. bremsstrahlung due to secondary electrons ejected from target atoms by the primary ion beam;
2. bremsstrahlung due to the primary ions themselves; and
3. Compton scattering in the X-ray detector of gamma rays produced in nuclear reactions. These background sources are the subject of the next two sections. Additional sources of

background associated with the detector and the pulse-processing electronics are discussed in Section IIIB.3.

IIE.1 Bremsstrahlung Radiation

Bremsstrahlung literally means "braking radiation" and results from the acceleration (or deceleration) of charged particles in the presence of electric fields. During charged particle bombardment of a target, bremsstrahlung is generated via two mechanisms: (1) the interaction between the primary ions and the local electric fields produced by the target nuclei, and (2) the radiative collisions between target nuclei and electrons which have been ejected from target atoms by the primary ion beam. The expected contribution of these two bremsstrahlung sources for bombardment of a thin carbon matrix by 3-MeV protons is shown by the solid lines in Figure 2.9. (This figure has been adapted from Folkmann et al. (1974b). The calculations and experimental data are from the same reference.) Also shown in Figure 2.9 are the measured background levels obtained for a carbon matrix using 3 MeV/amu protons, ^{4}He ions, and ^{16}O ions. The experimental results have been scaled by $1/Z_p^2$ where Z_p is the atomic number of the projectile. The reason for this scaling factor is discussed below. The deviation observed at higher X-ray energies between the measured background levels and the calculated bremsstrahlung level is attributed primarily to contributions from Compton scattering of gamma rays produced in nuclear reactions (Section IIE.2).

Figure 2.9 Experimentally observed background levels for 3 MeV/amu ^{1}H, ^{4}He, and ^{16}O ions incident on a thin carbon matrix. The experimental data have been scaled by $1/Z_p^2$ where Z_p is the projectile atomic number for comparison with calculated bremsstrahlung levels (solid lines) for incident proton beams. (Adapted from Folkmann et al., 1974b.)

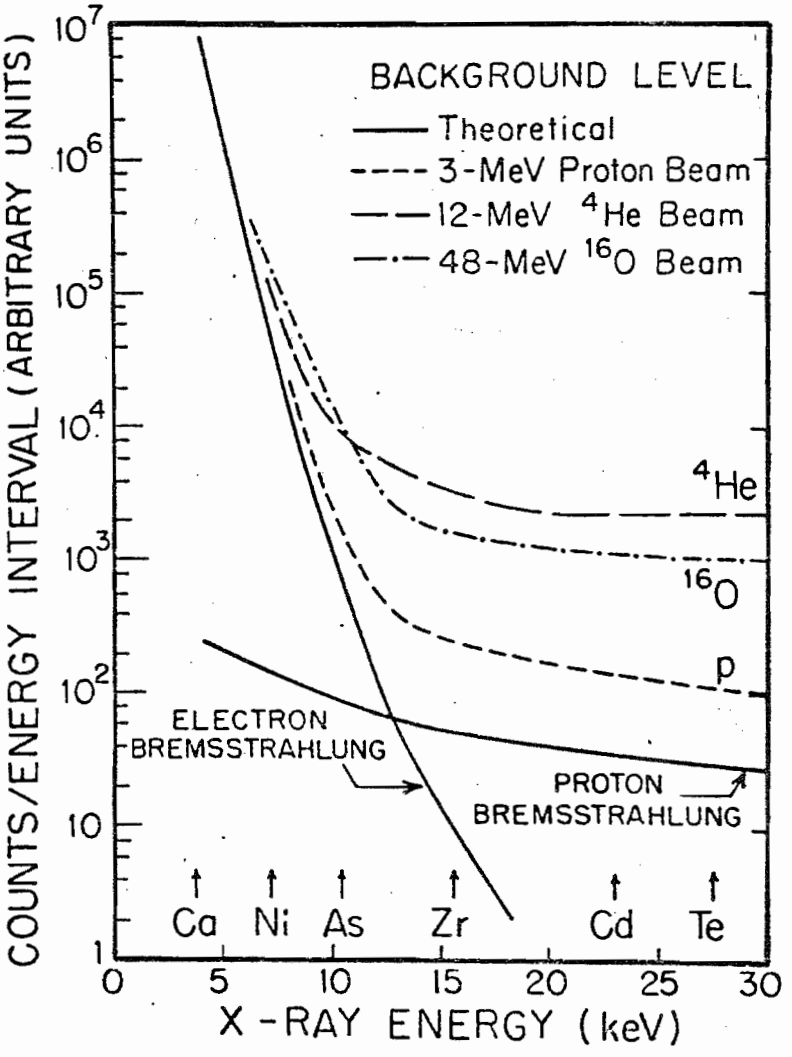
BACKGROUND LEVEL
Theoretical
3-MeV Proton Beam
12-MeV ^{4}He Beam
48-MeV ^{16}O Beam
^{4}He
^{16}O
p
ELECTRON BREMSSTRAHLUNG
PROTON BREMSSTRAHLUNG
Ca
Ni
As
Zr
Cd
Te
COUNTS/ENERGY INTERVAL (ARBITRARY UNITS)
X-RAY ENERGY (keV)
10^7
10^6
10^5
10^4
10^3
10^2
10
1
0
5
10
15
20
25
30

Comparison of the calculated bremsstrahlung curve in Figure 2.9 with the measured background levels indicates that below approximately 10 keV in X-ray energy, the scaled background data is reasonably well approximated by the secondary electron bremsstrahlung, with best agreement obtained for the proton-induced data. The production of bremsstrahlung by secondary electrons is essentially a two-step process consisting first of the ejection of electrons from matrix atoms by the incident projectiles, and secondly, of the radiative collision of these ejected electrons with the nuclei of matrix atoms resulting in bremsstrahlung. The bremsstrahlung produced by a single electron yields an energy spectrum featuring a broad, smoothly varying continuum extending from zero energy up to the energy of the ejected electron.

In order to estimate the intensity of this radiation, one must consider the probabilities associated with both mechanisms of the two-step process described above. The probability that a projectile of energy E_p and mass M will eject an electron of energy E_e and mass m is characterized by a sharp decline for $E_e \geq T_m$ where T_m represents the maximum kinetic energy transferred from the incident projectile to a free electron. It is easily shown that $T_m \sim 4 \frac{m}{M} E_p$. For 3 MeV protons, $T_m \sim 6.5$ keV which falls in the region of the Fe K_α X-ray (6.403 keV). The probability for ejection of a secondary electron with $E_e > T_m$ decreases dramatically -- approximately as E_e^{-10} (Folkmann, 1974a). Folkmann also

points out that the dominant contribution to secondary electron bremsstrahlung produced in the energy interval E_x to (E_x+dE_x) can be traced to secondary electrons having energies in the range 0% to 20% above E_x. Consideration of these facts leads to the following conclusions: (1) the region of minimum secondary electron bremsstrahlung (therefore the region of interest for trace element analysis) occurs for X-ray emissions $E_x > T_m$, and (2) it is advantageous in terms of minimizing electron bremsstrahlung to make T_m as small as practically possible. This can be accomplished by reducing the projectile energy E_p, but one suffers a corresponding decrease in the characteristic X-ray yield. It will be shown in Section IIF that the optimum choice of E_p for proton beams is between 2.0 and 4.0 MeV depending upon the elemental region of interest.

In an earlier section it was pointed out that the ionization cross sections scale approximately as Z_p^2 for equal-velocity projectiles of charge Z_p. Since the generation of secondary electrons is an immediate consequence of the ionization process, it is not surprising that the probability for secondary electron bremsstrahlung should also scale as Z_p^2. In the X-ray region in which the background contribution from secondary electron bremsstrahlung is dominant, i.e., below approximately 10 keV, the scaled ^4He and ^{16}O data plotted in Figure 2.9 are in fair agreement with the proton data and the calculated bremsstrahlung curve. To the extent that this

scaling property is observed for both characteristic X-ray emission and secondary electron bremsstrahlung (for $E_x \lesssim 10$ keV), the signal to background ratio is independent of the type of ion employed. The validity of this result will be examined in Section IIF.

Aside from the consequence of one's choice of particle and projectile energy, there is little that can be done to yield a significant reduction in the secondary electron bremsstrahlung. One might attempt to use extremely thin targets so that the secondary electrons have a relatively high probability for escaping from the sample before suffering any radiative collisions with target nuclei. Folkmann (1976a) and Johansson et al. (1976) have concluded that the thicknesses required to realize any significant gains are impractically small. (Folkmann calculates critical escape thicknesses for several matrices and radiation energies E_r, for which secondary electrons will escape and radiate only half the bremsstrahlung at energy E_r that would be generated in a thick sample. For a carbon matrix, and 1 keV $\leq E_r \leq$ 20 keV, the critical thickness varies from 1.3 to 260 $\mu g/cm^2$ (Folkmann, 1976a)).

Some reduction in the background intensity at low energies can be achieved by exploiting the angular distributions of the secondary electron bremsstrahlung. Measurements of these angular distributions have been made by Kaji et al. (1977) for 1.5 and 4 MeV protons incident on an aluminum target. This data clearly shows that the secondary electron

bremsstrahlung is anisotropic, being peaked in the direction of the proton beam, i.e., at forward angles. From these results it appears that a factor of 2 reduction in the background intensity for X-ray energies less than 10 keV may be possible by moving the detector to backward scattering angles.

In addition to bremsstrahlung generated by ejected electrons, the projectiles themselves also undergo radiative collisions in penetrating the target. This projectile bremsstrahlung can represent a significant and perhaps dominant contribution to the background intensity for the X-ray region above approximately 15 keV (Figure 2.9).

For a projectile (Z_1, M_1, E_p) incident on a target matrix (Z_2, M_2) the cross section for the production of projectile bremsstrahlung in the energy interval E_x to $E_x + dE_x$ is given as

$$\frac{d\sigma}{dE_x} = \frac{CM_1 Z_1^2 Z_2^2}{E_p E_X} \left(\frac{Z_1}{M_1} - \frac{Z_2}{M_2} \right)^2 \qquad (2.3)$$

where C is approximately constant. The intensity of the projectile bremsstrahlung is thus a slowly decreasing function of the projectile energy E_p and the X-ray energy E_x (in contrast to the very rapid decrease in secondary electron bremsstrahlung with E_x). The presence of the dipole radiation term $\left(\frac{Z_1}{M_1} - \frac{Z_2}{M_2} \right)^2$ in Equation (2.3) is very interesting and suggests that the projectile bremsstrahlung can be made to vanish by employing

projectiles whose charge to mass ratio is the same as that of the target matrix. Taking carbon (Z/M = 1/2) to be a typical matrix for analytical applications, this term would appear to be an important factor which would favor the use of ^{4}He or ^{16}O ions as an excitation source rather than protons. Watson et al. (1975) have experimentally verified this effect using 1.7 MeV/amu ions incident on a mylar foil. For higher velocity projectiles, however, the amount of gamma rays produced in the sample increases significantly due to high cross sections for nuclear excitation via energetic heavy ions. The resulting Compton scattered photon background and other background processes unique to heavy ions may nullify any reductions in the projectile bremsstrahlung gained by using heavy ions (Section IIF).

IIE.2 Compton Scattering of Nuclear Gamma Rays

Adding significantly to the projectile bremsstrahlung in the energy region above 15 keV is a broad, relatively flat continuum which can be attributed to Compton scattering of nuclear gamma rays. These gamma rays ($E_{\gamma} \gtrsim 70$ keV) accompany the de-excitation of nuclei (in the sample being analyzed) which have been excited by collisions with the bombarding projectiles. In addition, gamma rays will also be produced in the nuclei of any other material that the beam strikes. Such "targets" would be beam collimators, sample housing (if the

beam scatters from the sample or collimators) and the material in which the beam eventually stops (in the case of thin-target irradiations).

For low Z materials, and for gamma ray energies $\gtrsim 70$ keV, the dominant mechanism of interaction of gamma rays with matter is Compton (or "inelastic") scattering from the electrons in the matter. Hence, there is a high likelihood that gamma radiation produced in the bombarded sample will undergo Compton scatterings in the detector volume (and in the sample itself, though this contribution to the background intensity is difficult to estimate). Typically, a gamma ray of energy E_o incident on the detector volume will lose energy via multiple "inelastic" scatterings with the loosely bound electrons of the detector material. The recoil (Compton) electrons thus generated build up an amount of free charge in the detector which is linearly related to the energy deposited in the detector by the incident radiation, and which signals the "detection" of an event. Although there is a finite probability that the incident gamma ray will deposit its full energy in the detector volume, for the typical size of Si(Li) X-ray detectors employed, it is far more likely that the Compton scattered gamma ray will exit the detector with an energy E_f during one of its multiple scatterings. This leaves a net energy deposit in the detector of $(E_o - E_f)$.

The energy lost by a gamma ray in a single inelastic scattering is governed by the kinematics of the scattering

Figure 2.10 Illustration of the Compton scattering process. Nuclear gamma rays of with an energy of 100 keV undergo inelastic scattering in the detector giving rise to an escape continuum extending from zero energy up to approximately 28 keV (the Compton edge).

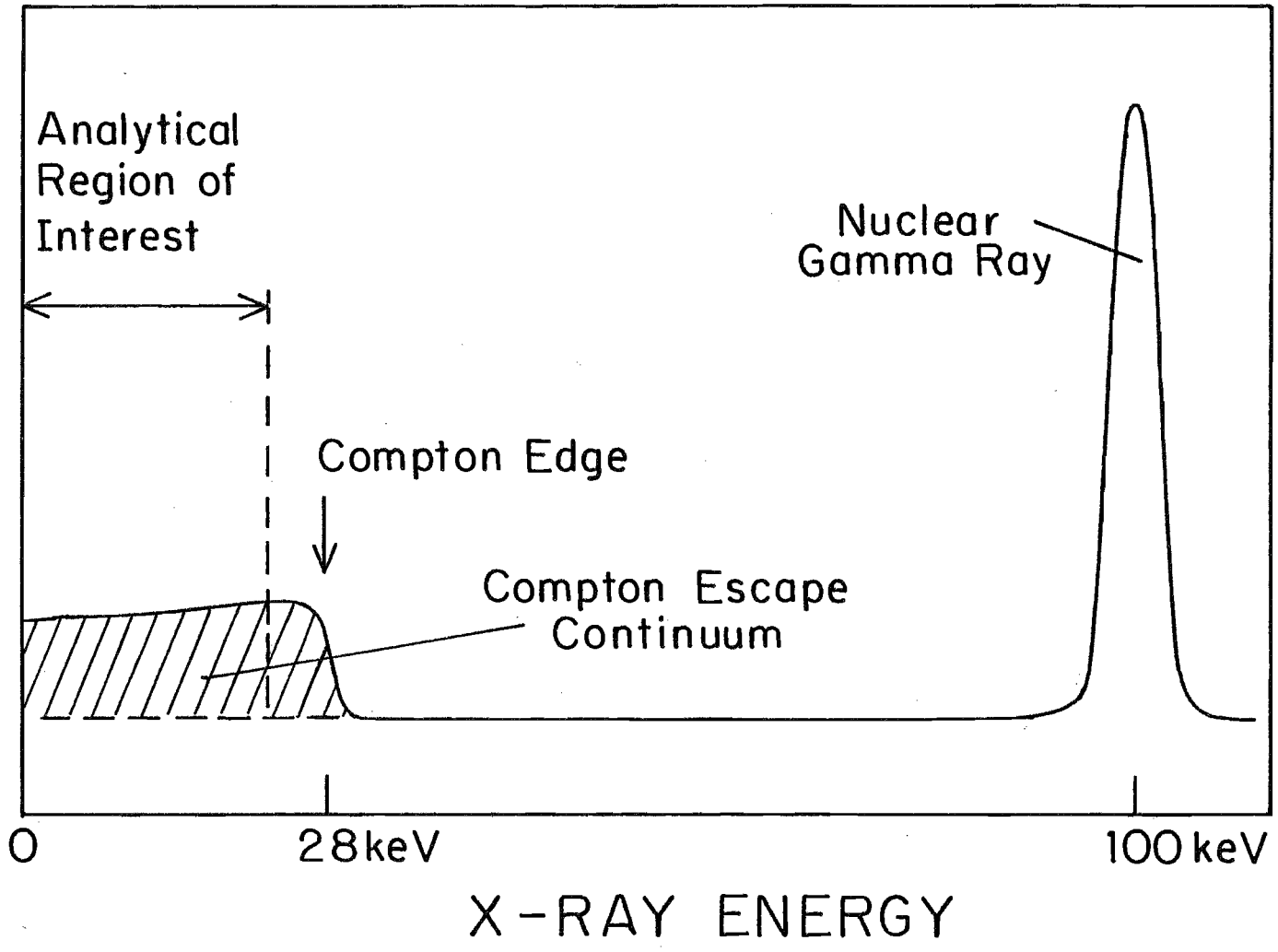
Analytical
Region of
Interest
Nuclear
Gamma Ray
Compton Edge
Compton Escape
Continuum
0
28keV
100keV
X-RAY ENERGY

process, and is a maximum for backscattering and decreasing continuously to zero as the scattering angle approaches 0°. Over a large number of scatterings of monoenergetic gamma rays (and a full range of scattering angles), a broad continuum, called the Compton escape continuum, is built up extending from zero energy up to a maximum energy corresponding to the energy of the Compton electron in a backscattering event (Figure 2.10). If gamma rays of other energies are included, the summed background contributions normally result in a flat continuum extending throughout the X-ray region of interest to the analyst.

Estimates of the intensity of the Compton background are in general difficult to make. The probability for nuclear excitation is sensitive to such factors as the choice of projectile and energy, and the particular target composition; and the probability for Compton scattering in the detector is a function of the detector composition and geometrical configuration.

Several studies have been made in an effort to gauge the significance of the Compton background under different experimental conditions (Folkmann et al., 1974b; Cahill et al., 1974; Herman et al., 1973). The following conclusions result from these studies:

1. In comparing the high energy (>20 keV) background induced by equal-velocity projectiles, proton excitation is superior to excitation by heavier ions (even with the backgrounds

scaled as $1/Z_p^2$); heavy ions, because of their higher energies have a much greater probability for producing nuclear gamma rays. The relative advantage in using protons however will depend on the particular experimental arrangement. (Cahill's comparison of 4 MeV/amu ^1H and ^4He ions incident on an aerosol filter showed a factor of 2 reduction in the high energy background level by using protons; Folkmann's results for 3 and 5 MeV/amu ^1H, ^4He, and ^{16}O ions incident on a carbon matrix indicated a factor of 10 reduction in high energy background using protons.)

2. The Compton tail will dominate the background radiation above $\sim$ 15 keV for energetic ions. Measurements by Folkmann indicate that Compton scattering of nuclear gamma rays is much more important than projectile bremsstrahlung in determining the high energy background level. For proton energies below approximately 2 MeV, the Coulomb barrier of carbon and heavier nuclei cannot be penetrated (Folkmann et al., 1974b), so that projectile bremsstrahlung constitutes the limiting factor at these low energies.

IIF. Choice of Ion and Energy

The analytical capabilities of ion-induced X-ray spectrometry systems are determined by a number of experimental parameters, e.g. -- choice of ion and energy, beam handling, target-detector geometry, sample type and preparation, use of filters, etc. In general one seeks to optimize the

sensitivity of the system (expressed in terms of "detection limits" for the elements of interest) by proper selection of these experimental parameters. Any improvements in the system's sensitivity are likely to have a cost which may be in the form of added time or economic costs, more elaborate sample preparation, or beam damage to the target. The following paragraphs discuss a number of considerations relating to the optimum choice of ion and energy. In particular, the potential use of heavy ions for analytical applications is discussed.

IIF.1 Heavy Ions

According to the scaling property predicted in the PWBA, BEA, and SCA formulations (Section IID), the cross section for Coulomb ionization of inner shells by equal-velocity projectiles of charge Z_p should scale as Z_p^2. The prospect of ionization cross sections two to three orders of magnitude greater for heavy ion excitation (relative to proton excitation) has prompted interest in the analytical potential of heavy ions. Experimental results accumulated since 1970 demonstrate that the situation for heavy ions is considerably more complicated than simple application of the scaling property. It is convenient to discuss the additional complexities of heavy ions in terms of (1) the X-ray production process, and (2) background-producing processes. For

thorough reviews of the current state of knowledge regarding heavy ion collision phenomena, the reader is referred to articles by Garcia et al. (1973) and Richard (1975).

The dominant features of X-ray production via heavy-ion excitation are summarized below:

1. Ionization cross sections

At high collision energies ($\gtrsim$1 MeV/amu) measured cross sections scale roughly as Z_p^2 as predicted by direct Coulomb ionization. Deviations from scaling do occur however, reflecting contributions from additional excitation mechanisms (see Item 3).

For low energy collisions ($\lesssim$1 MeV/amu), the measured cross sections are enhanced as much as three orders of magnitude above predicted values based on scaling. This enhancement is attributed to electron promotion in the Molecular Orbital (MO) model (Fano and Lichten, 1965).

Figure 2.11 displays K-shell ionization cross section data (scaled by $1/Z_p^2$) in both the low energy and high energy regimes. The quantity $(E/\lambda u)$ is the square of the ratio (V_p/V_e) where V_p is the projectile velocity and V_e the mean orbital electron velocity.

2. Resonance structure in ionization cross sections

Ionization cross sections for heavy ions display relative maxima for target-ion combinations in which the inner-shell binding energies are nearly the same or overlapping,

Figure 2.11 K-shell ionization cross sections for heavy ions versus the reduced energy parameter ($E/\lambda u$) where λ = ratio of proton mass to electron mass and u = K-shell binding energy. The data are compared to calculations in the Binary Encounter Approximation (from Garcia et al., 1973).

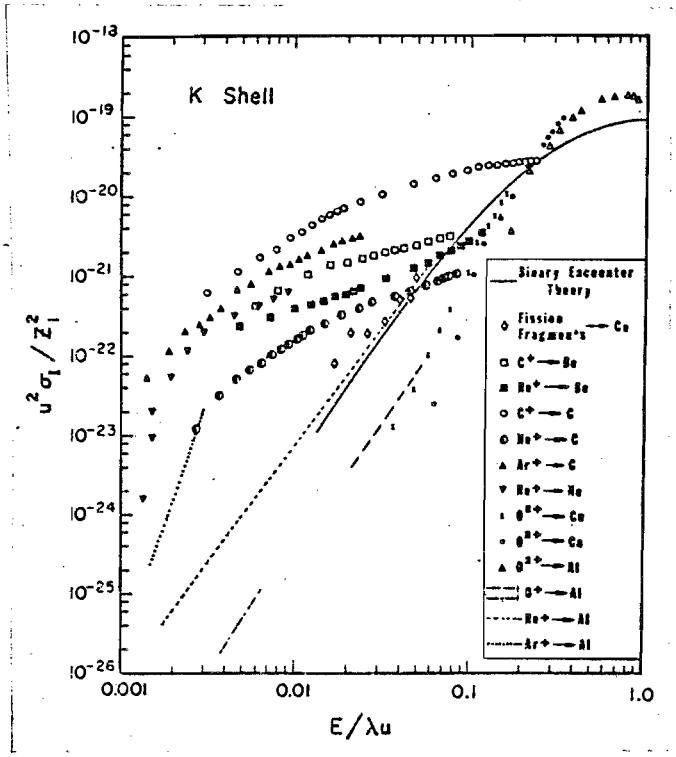
K Shell
Binary Encounter Theory
Fission Fragments — Cu
C+ — Be
Ne+ — Be
C+ — C
Ne+ — C
Ar+ — C
Ne+ — Ne
O2+ — Cu
O2+ — Cu
O2+ — Al
O+ — Al
Ne+ — Al
Ar+ — Al
10^-18
10^-19
10^-20
10^-21
10^-22
10^-23
10^-24
10^-25
10^-26
0.001
0.01
0.1
1.0
u^2σ_1 / Z_1^2
E/λu

e.g., near-symmetry collisions for which $Z_p \sim Z_2$. This oscillatory behavior due to MO excitation cannot be explained in terms of direct Coulomb ionization which increases monotonically with Z_2.

3. Charge state dependence of X-ray production

X-ray production cross sections measured for gas targets display a strong dependence on the projectile charge state; vacancies brought into the collision by the projectile can capture inner-shell electrons from the target resulting in enhanced X-ray production cross sections.

4. X-ray spectra

X-ray spectra obtained from heavy-ion excitation are in general more complicated than proton-induced spectra. The increased ionization cross sections for heavy ions applies to outer-shell ionization as well as inner-shell ionization, resulting in a much greater probability for single K-shell, multiple outer-shell ionization in a single collision. These multiple vacancies created in outer shells result in small but detectable shifts in inner-shell binding energies, and in the appearance of X-ray satellite lines associated with different vacancy configurations. The degree of multiple ionization (and therefore the relative intensities of the satellite lines) is highly sensitive to the projectile, its charge state and its energy. Figure 2.12 demonstrates the growing complexity of the K-line spectra for ^{1}H, ^{4}He, and

Figure 2.12 K-line X-ray spectra of ^{1}H, ^{4}He, and ^{16}O ions incident on Ti, demonstrating the variation in multiple ionization with increasing projectile charge (from Moore et al., 1972).

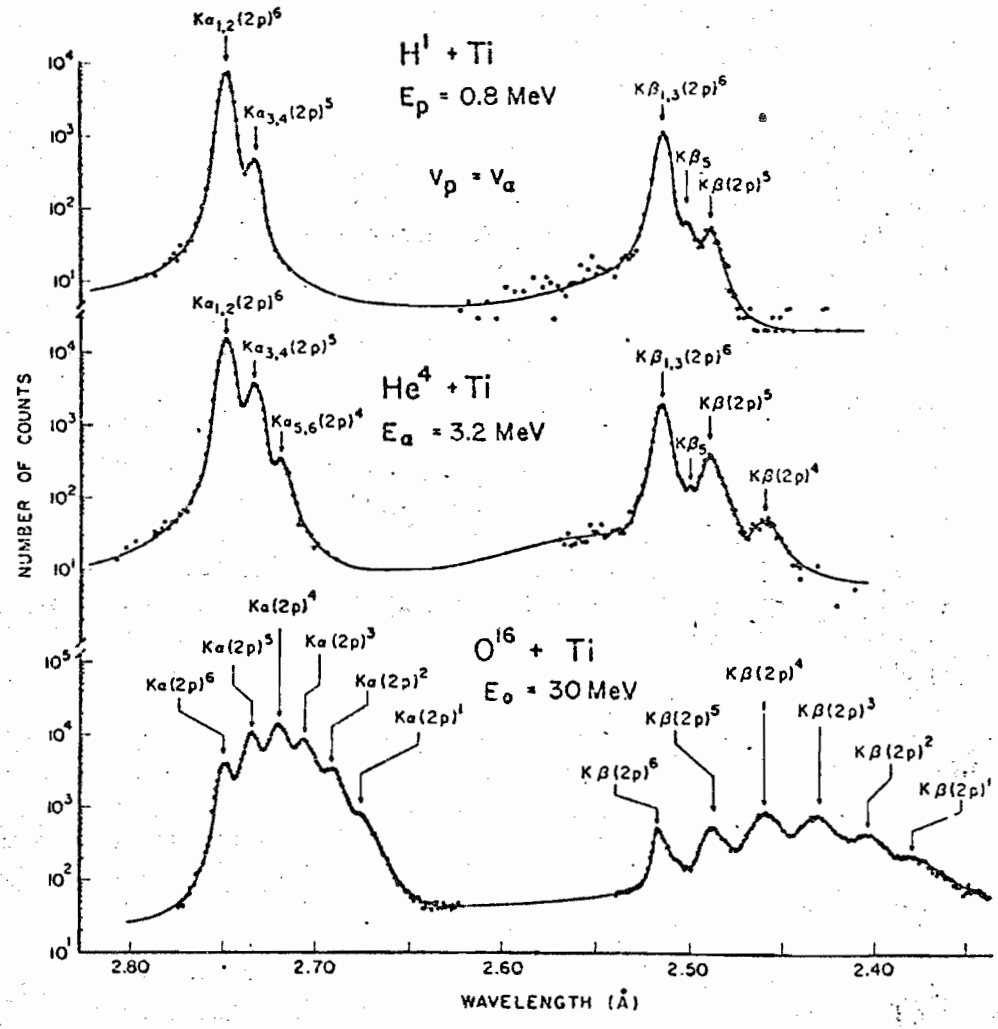
H^1 + Ti
E_p = 0.8 MeV
$V_p = V_\alpha$
He^4 + Ti
E_α = 3.2 MeV
O^{16} + Ti
E_o = 30 MeV
NUMBER OF COUNTS
WAVELENGTH (Å)
2.80
2.70
2.60
2.50
2.40

^{16}O ions incident on a titanium target. (These spectra were obtained with a high-resolution crystal spectrometer. The same data taken with an energy-dispersive detector would show a shift of the characteristic X-ray lines to higher energy, a broadening of the X-ray peaks, and a change in the relative intensity ratios.)

The analysis of heavy-ion spectra is further complicated because the fluorescence yield, which determines the probability for X-ray emission for a particular vacancy state, is a function of the outer-shell vacancy distribution and is therefore sensitive to the projectile charge state and energy -- increasing as one would expect for more extensive ionization of the target orbitals.

Much of the experimental data in the low energy region can be explained in terms of the Molecular Orbital (MO) model (Fano and Lichten, 1965). In this model, the ion-atom collision is viewed as the formation of a transient molecular system in which the electron orbitals of the separated atoms can intersect the quasimolecular orbitals as the separation between the colliding atoms decreases and then increases following the collision. If a filled orbital crosses an unfilled molecular orbital, there is some probability that an electron will be transferred to the molecular orbital. This contributes to the X-ray production cross section and is most effective for nearly symmetric collisions at low energies.

The enhanced cross sections for K-shell excitation at low energies due to molecular orbital excitation were previously shown in Figure 2.11.

Background processes in heavy ion excitation:

1. Bremsstrahlung and Compton scattering

Bremsstrahlung due to secondary electrons scales as Z_p^2. For heavy ions incident on low Z targets, the dipole radiation term in the cross section for projectile bremsstrahlung (Equation 2.3) may be non-zero because of the neutron excess in the projectile, and some direct bremsstrahlung may occur.

As mentioned in Section IIE.2, heavy ions having greater energies than equal-velocity protons have a greater probability for inducing gamma radiation via nuclear excitation. The resulting Compton tail for X-ray energies $\gtrsim$15 keV may be a serious limitation for heavy ions, possibly offsetting the Z_p^2 gain in X-ray emission cross sections.

2. Radiative electron capture (REC)

For fast, heavy ions there is some probability that loosely-bound electrons in the target will be captured into inner-shell vacancies of the projectile with the simultaneous emission of radiation. The energy of the REC photons will be slighly higher than the projectile binding energy by an amount equal to the electron kinetic energy relative to the

projectile; and the width of the resulting X-ray band is determined by the projectile velocity and the velocity distribution of the target electrons.

3. Quasi-molecular radiation

During slow collisions in which molecular orbitals are formed, it is possible (if the lifetime of the vacancy is shorter than or comparable to the collision time) for radiative decay processes to take place. The X-ray energies in such events would be characteristic of the transient molecular system rather than the separated collision partners, and as the MO levels depend on the internuclear distance, the resulting spectrum averaged over the duration of the collision would appear as a continuous band with an endpoint energy given by the binding energy of the united atom orbital at the distance of closest approach.

A clear-cut choice between excitation by heavy ions and protons or ^{4}He ions is difficult to make; certain features of heavy-ion excitation (the resonance in the ionization cross section for near-symmetry collisions, for example) can be exploited in a particular analytical application making heavy ions advantageous. Heavy-ion analysis can provide chemical state information, not possible with light ions, in addition to element composition analysis (Folkmann, 1977). Low energy heavy ions because of their low penetrating power and relatively high cross sections have found numerous applications in the analysis of surface layers (Cairns, 1973;

Chemin et al., 1974). While the low penetrating powers of heavy ions can be advantageous, the higher energy loss of heavy ions can be a source of concern in terms of beam heating effects, i.e., target damage and volatilization of certain elements. The critical parameter relating to the relative energy losses of different ions in the same target matrix is the projectile charge Z_p, and for energetic ions ($\gtrsim$ 1 MeV/amu) the stopping power of the ion scales approximately as Z_p^2 times the stopping power of protons. If target damage and beam heating are to be kept at the same levels found tolerable for proton excitation, the beam current (or integrated charge) must be scaled down by a factor of $1/Z_p$ for heavy ions. But this scaling has the effect of cancelling the Z_p^2 gain in the heavy-ion X-ray yield (Cahill et al., 1974).

In summary, it would seem at the present time that the additional complexities in X-ray emission and background processes for heavy-ion excitation, and the additional potential for beam heating effects outweigh the possible advantages of heavy ions from the point of view of quantitative multielemental analysis for a wide variety of targets.

IIF.2 Light Ions; Definition of Detection Limits

Most of the applied work in ion-induced X-ray spectrometry has utilized 1-4 MeV proton beams. A notable exception is the work of Cahill and co-workers (1975) at the

Table 2.2
Recent Studies Evaluating Relative Merits of Different Projectiles and Energies

Reference	Summary
Folkmann et al. (1974b)	Compared analytical sensitivities for 3 and 5 MeV/amu ^{1}H, ^{4}He, and ^{16}O ions incident on C, Al, and V matrices.
Barrette et al. (1976)	Evaluated relative capabilities of 2.25, 3, and 6 MeV protons, and 6, 9, 12, and 16 MeV ^{4}He ions.
Watson et al. (1975)	Examined signal-to-noise ratios for element analysis ($Z \leq 30$) using 1.7 MeV/amu ^{1}H, ^{4}He, ^{12}C, and ^{20}Ne ions.
Flocchini et al. (1972)	Examined sensitivity of ^{4}He excitation for various target backings.
Cahill et al. (1974)	Compared sensitivities for equal-velocity proton and ^{4}He excitation of aerosol samples.
Herman et al. (1973)	Evaluated ^{1}H (2-10 MeV), ^{4}He(6-25 MeV), and ^{16}O (6-40 MeV) beams with respect to background levels and potential for beam heating.
Umbarger et al. (1973)	Determined sensitivities for 1.0, 2.25, and 3.0 MeV proton excitation.
Zeisler et al. (1976)	Compared ^{16}O excitation (0.5-7 MeV/amu) and proton excitation (1.6-7 MeV).
Willis et al. (1974-1977)	Compared sensitivities for 1.5-3.4 MeV protons; results reported in this thesis.

University of California at Davis who employ 18 MeV ^{4}He ions for analysis of atmospheric aerosols. Several investigations exploring the potential use of heavier ions have been reported (Watson et al., 1975; Zeisler et al., 1976) but no laboratories are currently known to be using ions heavier than ^{4}He for routine multielemental analysis. A summary of recent studies evaluating the relative capabilities of various projectiles and projectile energies is listed in Table 2.2.

Based on these studies it appears that the optimum range of bombarding energies is 1-5 MeV/amu. Within this range, the particular choice of projectile and bombarding energy will be influenced by a number of considerations: analytical sensitivity requirements, target damage and beam heating, practical limitations (accelerator facilities, analysis time and cost limitations, etc.), and constraints imposed by the particular analytical application (what type of sample is to be analyzed? what is the nature of the analysis: bulk? surface? microanalysis?). The premise for the PIXE work at Duke was to develop a system capable of quantitative, rapid multielemental analysis while retaining the flexibility to analyze a wide variety of sample types. This is in contrast for example with Cahill's system at the University of California at Davis which is optimized for automatic analysis of atomospheric aerosols (Cahill, 1975). Although our original decision in 1972 to use 3.0 MeV protons for the Duke PIXE

system was based in part on practical circumstances, our own studies as well as the recent investigations summarized above generally support this choice of particle and energy.

For purposes of evaluating and comparing the capabilities of different projectiles and energies, a commonly employed "figure of merit" is the analytical sensitivity of the system defined in terms of "detection limits". As pointed out by Currie (1968), the concept of the detection limit has been given a variety of different and often erroneous interpretations in the literature. The following discussion of detection limits follows Currie's thorough treatment of the subject.

The question of sensitivity is concerned with two basic aspects: qualitative detection, and quantitative analysis. The first aspect relates to: (1) deciding whether a "true" signal has been detected, and (2) estimating the minimum "true" signal which will lead to reliable detection for the particular measuring process. Qualitative detection is to be distinguished from quantitative analysis which relates to the question of what is the minimum elemental concentration which can be quantitatively determined to a desired level of precision. A complete discussion of sensitivity requires that specific levels be defined to correspond to each of the three aspects distinguished above. Using the notation of Currie, these levels are designated as: (1) the "decision limit" L_C, (2) the "detection limit" L_D, and (3) the

Table 2.3

Limits for Qualitative Detection and Quantitative Determination [2)]

Criterion	Notation	Definition	Working expression[b)]
Decision Limit	L_C	Net signal level (X-ray counts above background) above which an observed signal is reliably recognized as detected	$L_C(\text{counts}) = 1.64\sqrt{N_B}$ where N_B = background counts within one fwhm beneath the X-ray signal of interest
Detection Limit	L_D	Minimum "true" net signal which may be expected to lead to detection	$L_D(\text{counts}) = 2.71 + 3.29\sqrt{N_B}$
Determination Limit	L_Q	Minimum "true" net signal at which the measuring process is sufficiently precise to yield a quantitative determination	$L_Q(\text{counts}) = 50\{1+[1+\frac{N_B}{25}]^{\frac{1}{2}}\}$[c)]

(70)

a) Reference: Currie (1968)

b) Assumptions: (1) Poisson statistics apply;

(2) $\alpha = \beta = 0.05$, where $(1-\alpha)$ = probability that a "true" net signal of zero yields the correct decision "not detected";

$(1-\beta)$ = probability that a non-zero "true" net signal yields the correct decision "detected."

(3) The background blank is assumed to be well known--i.e., $\sigma_B^2 = 0$ where σ_B^2 represents the variance of the mean blank.

c) The expression guarantees a relative standard deviation of 10% or less in the measuring process.

"determination limit" L_Q. Definitions of these quantities, and working formulas applicable to the case of X-ray analysis are summarized in Table 2.3. As indicated by the working expressions, the values of L_C, L_D, and L_Q are intimately related to the variance of the background ($\sqrt{N_B}$). Implicit in the formulas chosen for Table 2.3 are the selected values of α, corresponding to the error in deciding that an element is present when in fact it is not, and β, corresponding to the error in failing to detect an element when it is present. For $\alpha = \beta = 0.05$ as in Table 2.3, L_D is to be interpreted as the minimum "true" (net) signal which will result in detection 95% of the time. The expression given for L_Q is based on assuming a maximum permissible value of 10% for the relative standard deviation of the measuring process. This guarantees a <u>precision</u> of 10% or better in the measured elemental abundances. Nothing has yet been implied about the <u>accuracy</u> of the results which is determined by systematic errors entering in to the calibration factor relating L_Q to the physical quantity of interest (i.e., the minimum determined mass M_Q or concentration T_Q corresponding to L_Q counts).

A number of authors have employed a less rigorous criterion for the detection limit given by:

$$L_D' = 3\sigma_B = 3\sqrt{N_B}$$

where σ_B is the standard deviation of the measured back-

ground. Although this "three sigma" criterion is in common usage, and is a convenient figure of merit for intercomparison of results, the interpretation of L_D' as the "detection limit" is not strictly valid, and is in fact often misleading.

The quantities L_C, L_D, L_Q (expressed as X-ray counts above background), are related to the physical quantities of interest T_C, T_D, T_Q (elemental concentrations expressed in ppm) by the factor F:

$$T_i(\text{ppm}) = F\, L_i(\text{counts}) \quad , \quad i = C, D, Q$$

where $F = (\varepsilon \cdot q \cdot \overline{M})^{-1}$

and ε = system efficiency (X-ray counts detected per microgram of element Z irradiated, per microcoulomb of charge collected on the sample)

q = total charge incident on the sample (μC)

$\overline{M}$ = effective mass of the irradiated sample (grams)

(The effective mass is the mass of the sample which is actually effective in producing detected X-rays, i.e., the irradiated mass reduced by a factor representing the decrease in detected X-ray yield due to: (1) energy loss of the projectile as it penetrates the sample, and (2) the attenuation in the sample matrix of X-rays en route to the detector (see Figure 3.16). For thin samples in which these effects are negligible, the effective mass is identical to the irradiated mass.)

The response of the determination limit concentration

T_Q to changes in proton energy E_p has been measured at Duke for protons of 1.4 to 3.35 MeV incident on a thick pellet of homogenized bovine liver, Standard Reference Material 1577 which is available from the National Bureau of Standards. The resulting spectra obtained for six energies E_p are displayed in Figure 2.13, and the response curves for T_Q as a function of atomic number Z and energy E_p are presented in Figure 2.14. The curves for T_Q are semiempirical, based on the measured background levels $N_B(Z)$ (for two different absorbing filters inserted between the detector and the irradiated sample), and values for the effective mass $\bar{M}(Z,E_p)$ and the detection efficiency $\varepsilon(Z,E_p)$ calculated by FUDGE (Appendix A) for selected values of Z and E_p.

Figure 2.15 presents a plot of the relative peak-to-background ratios versus E_p for six selected elements, using the data of Figure 2.13. The peak-to-background ratios are determined relative to those at E_p = 2.94 MeV, the chosen operating energy for the Duke PIXE system.

Several noteworthy features are to be observed in the sensitivity curves of Figure 2.14:

1. All curves share in common a smoothly varying dependence on the atomic number Z, reaching a minimum (corresponding to optimum sensitivity) for Z between approximately 20 and 30, and increasing to maximum values (poorest sensitivity) at the low$-Z$ and high$-Z$ extremes. The relatively poor

Figure 2.13 PIXE spectra of a bovine liver pellet obtained at six different proton energies. Data was taken using both the mylar and polyethylene absorbers.

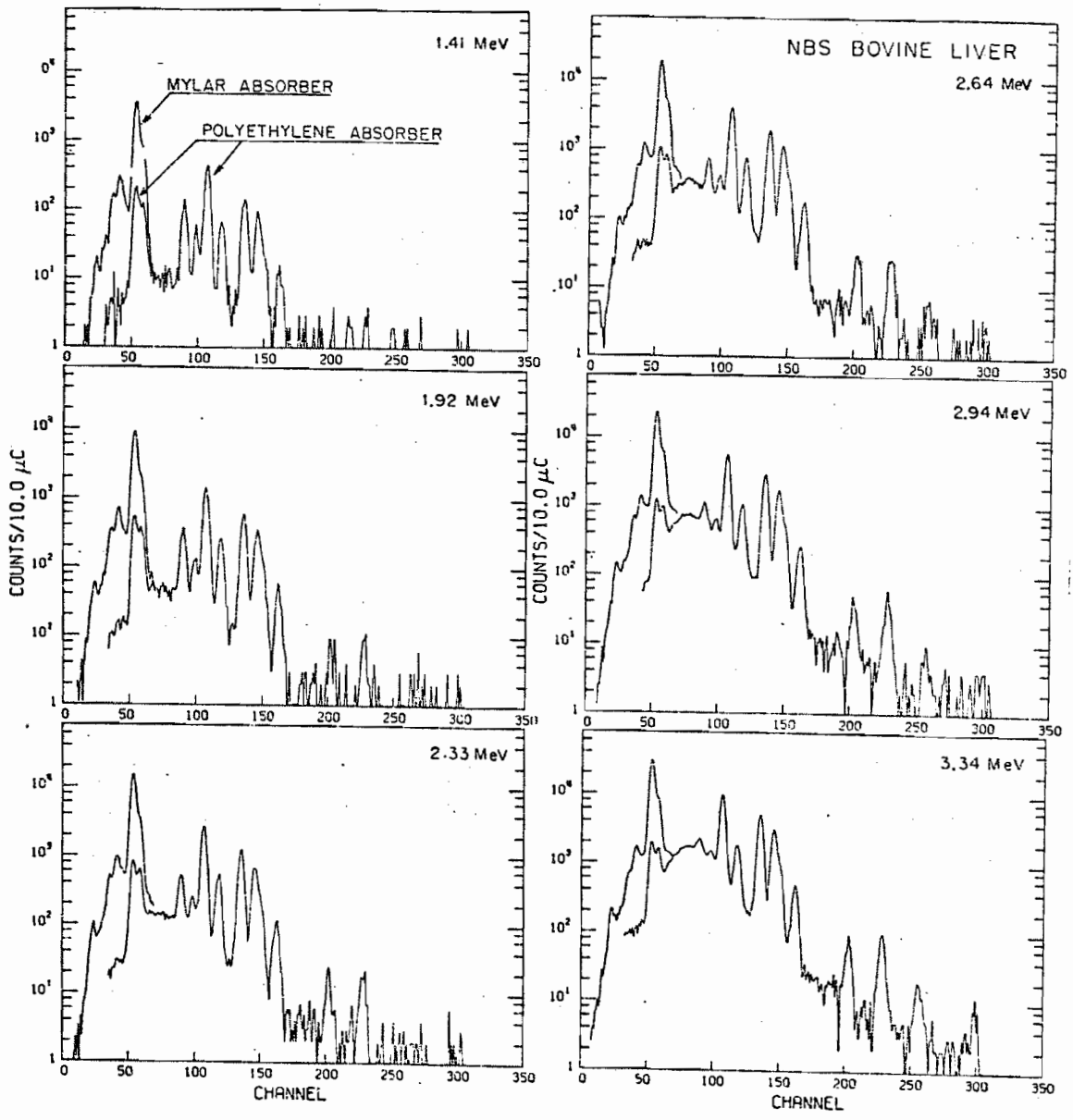
NBS BOVINE LIVER
1.41 MeV
MYLAR ABSORBER
POLYETHYLENE ABSORBER
2.64 MeV
1.92 MeV
2.94 MeV
2.33 MeV
3.34 MeV
COUNTS/10.0 μC
CHANNEL

Figure 2.14 PPM determination levels yielding 10% precision as a function of atomic number Z and proton energy E_p for 10 μC of accumulated charge. The sample is a thick pellet of bovine liver. The curves are based on the measured background levels extracted from the spectra shown in Figure 2.13, and on calculated values of the X-ray production cross sections and effective masses at the various proton energies E_p. Note the minima in the sensitivity curves near Z = 30, and the shift in the minima toward higher Z with increasing proton energy.

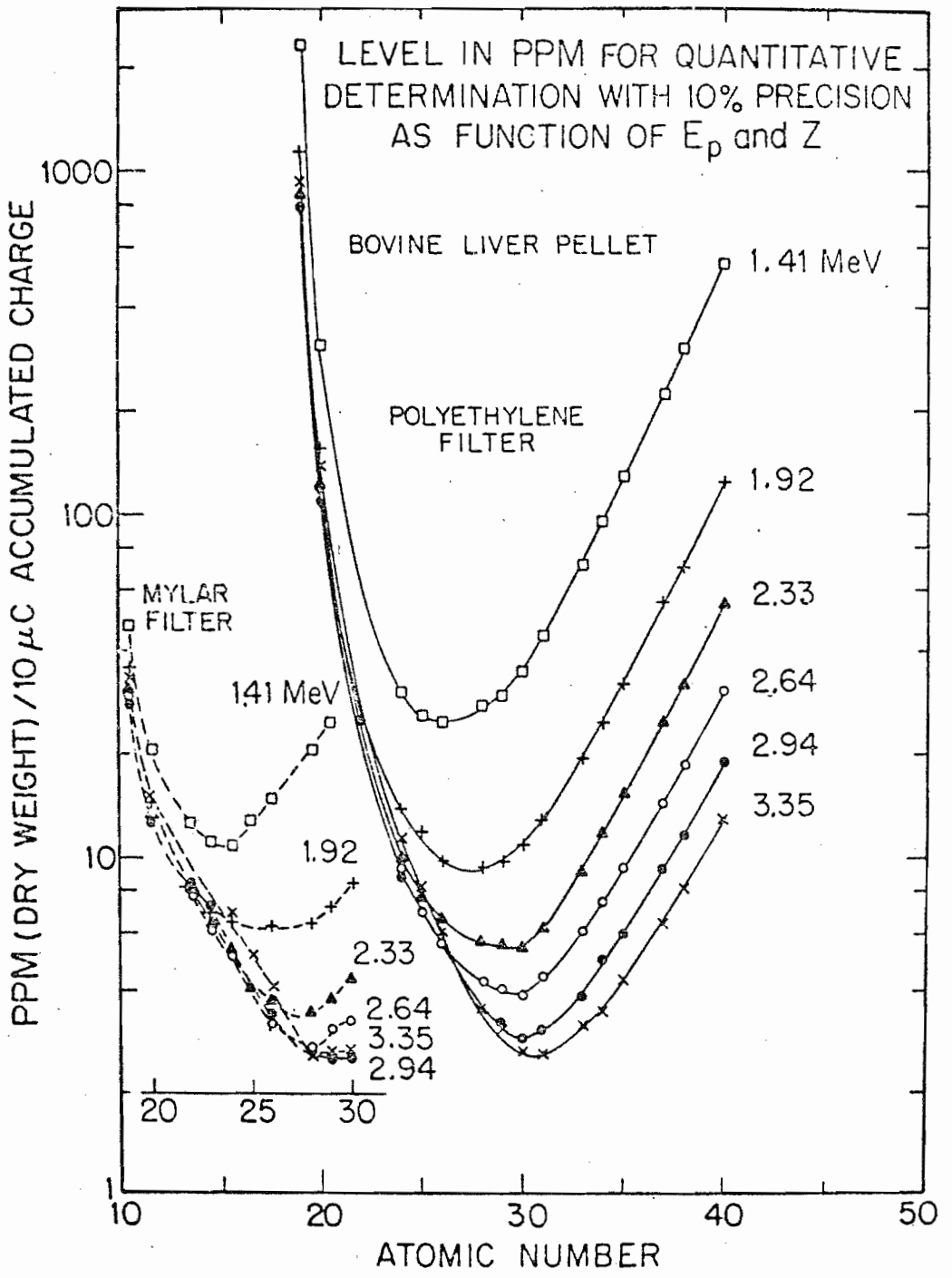
LEVEL IN PPM FOR QUANTITATIVE DETERMINATION WITH 10% PRECISION AS FUNCTION OF E_p and Z
BOVINE LIVER PELLET
POLYETHYLENE FILTER
MYLAR FILTER
1.41 MeV
1.92
2.33
2.64
2.94
3.35
PPM (DRY WEIGHT) / 10 μC ACCUMULATED CHARGE
ATOMIC NUMBER
1000
100
10
1
10
20
30
40
50
20
25
30

sensitivity for low-Z elements is due to small values for the fluorescence yields for light elements, to declining detector efficiency (Figure 3.9), to the attenuation of low-energy X-ray by absorbing filters, transmission windows, and air passages, and lastly, to the relatively large background intensity due to secondary electron bremsstrahlung which reaches maximum intensity in the low-Z region. The falloff in sensitivity at high Z is primarily attributable to decreasing X-ray cross sections (whereas the background level remains relatively constant), and to decreasing detector efficiency (for X-ray energies $\gtrsim$ 20 keV).

2. As E_p increases, the minima in the sensitivity curves T_Q shift to higher values of Z. This behaviour could be exploited in order to optimize the system's sensitivity for a particular elemental region of interest.

3. Sensitivity for low-Z elements is greatly improved by using a thin (mylar) absorbing filter rather than a thicker (polyethylene) filter. The purpose of the filter is to reduce the flux of low energy X-rays into the detector which might otherwise saturate the detection electronics; hence, attempts to improve low-Z sensitivity by employing successively thinner filters, or by placing the Si(Li) detector inside the evacuated target chamber may eventually run up against limitations due to excessive counting rates.

4. For the particular sample and experimental conditions represented in Figures 2.13 and 2.14, the optimum determina-

tion levels are obtained for E_p = 3.35 MeV ($Z \gtrsim 28$) and E_p = 2.94 MeV ($Z \lesssim 28$). Although the use of higher proton energies has the advantage of larger X-ray yields, the background intensity (for medium to low Z elements) increases at a somewhat faster rate resulting in degraded and eventually prohibitive signal-to-noise ratios (Herman et al., 1973 and Figure 2.15). This factor combined with the added potential for beam heating problems, makes the use of more energetic beams unlikely.

5. Figure 2.15 indicates that for $Z \lesssim 30$, the signal-to-noise ratio improves with decreasing E_p, whereas for $Z \gtrsim 35$, just the opposite holds true. This behaviour is understood by consideration of the characteristic X-ray and background production processes described earlier in Sections IID and IIE. The background in the low-Z region is dominated by secondary electron bremsstrahlung for X-ray energies approximately up to the cutoff energy $T_M \simeq \frac{E_p}{500}$ (keV) (Section IIE.1). Beyond T_M, the intensity of the secondary electron bremsstrahlung decreases extremely rapidly and as T_M is reduced to lower energies by lowering E_p, the signal-to-noise ratios are expected to improve substantially in the energy region near and above T_M. For the medium and high-Z region, the sensitivity is limited by direct projectile bremsstrahlung which depends on the projectile energy approximately as $(E_p)^{-1}$ (Equation 2.3). In addition, X-ray pro-

Figure 2.15 Relative signal-to-noise ratios as a function of Z and proton energy E_p for six selected elements, based on the data shown in Figure 2.13 for a bovine liver pellet. The ratios are determined relative to the corresponding ratios observed at E_p = 2.94 MeV. The solid curves drawn through the data indicate the suggested trends.

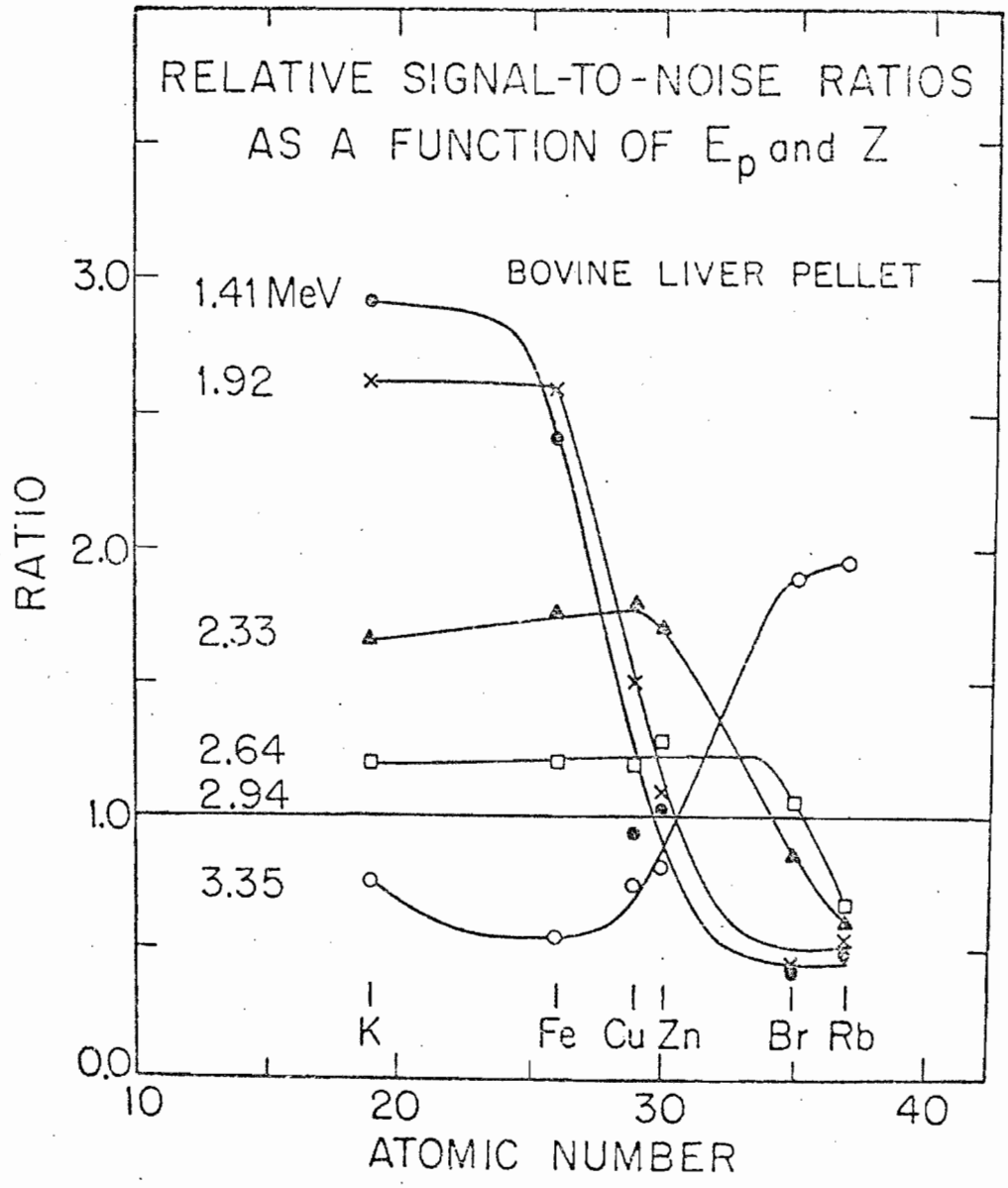
RELATIVE SIGNAL-TO-NOISE RATIOS
AS A FUNCTION OF E_p and Z
BOVINE LIVER PELLET
1.41 MeV
1.92
2.33
2.64
2.94
3.35
RATIO
3.0
2.0
1.0
0.0
K
Fe
Cu
Zn
Br
Rb
10
20
30
40
ATOMIC NUMBER

duction cross sections increase with E_p. Therefore, if nuclear reactions (and the associated Compton tail) do not predominate at higher E_p, one would expect the signal-to-noise ratios to improve with increasing bombarding energy. A reasonable compromise, resulting in moderately good signal-to-noise ratios over the entire elemental range of interest is to use proton energies between 2.0 and 3.0 MeV.

The results above apply to PIXE analysis of an "infinitely thick" sample -- i.e., thick enough to completely stop protons in the energy range considered above. Similar behaviour in the determination levels $T_Q(Z,E_p)$ for a moderately thin target are observed in Figure 2.16, based on PIXE analyses at 2.94 and 2.43 MeV of a condensed tap water sample. (The thickness of the sample plus nuclepore substrate was approximately 3.6 mg/cm^2). The 2.43 MeV beam yielded better sensitivities for $Z \lesssim 26$, while the 2.94 MeV beam provided better sensitivity for the medium and heavy elements.

Johansson et al. (1976) have calculated the variation of the "minimum detectable concentration" based on the 3σ criterion as a function of proton energy and atomic number. These results are shown as a contour plot in Figure 2.17, and the experimental parameters assumed in the calculations are indicated in the figure caption. Note that the results here apply to thin targets. Clearly, the optimal choice for the bombarding energy is determined by the elemental region of

Figure 2.16 Determination levels (ppb wet weight) yielding 10% precision as a function of atomic number for 10 μC of accumulated charge and two different proton energies E_p. The sample is tap water which has been condensed down by a factor of 100 and deposited on a nuclepore membrane.

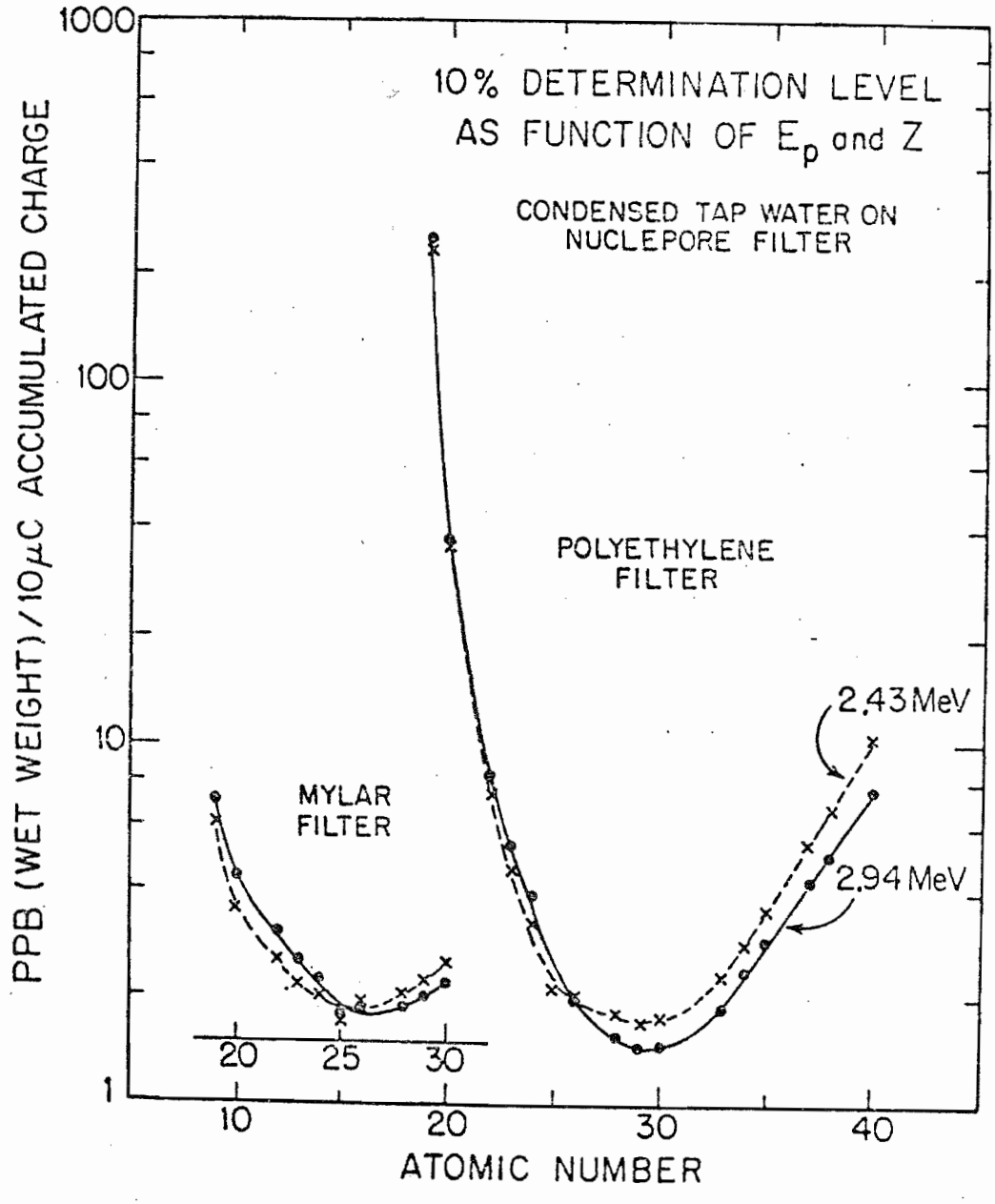
10% DETERMINATION LEVEL
AS FUNCTION OF E_p and Z
CONDENSED TAP WATER ON
NUCLEPORE FILTER
POLYETHYLENE
FILTER
MYLAR
FILTER
2.43 MeV
2.94 MeV
PPB (WET WEIGHT) / 10μC ACCUMULATED CHARGE
ATOMIC NUMBER
1000
100
10
1
10
20
30
40
20
25
30

Figure 2.17 Minimum detectable concentration as a function of atomic number and bombarding energy for a thin target. The calculations are based on the 3σ criterion for detectability and assume the following experimental parameters: detector resolution = 165 eV, solid angle = $.003 \times 4\pi$, accumulated charge = 10 μC, and target thickness = 0.1 mg/cm^2.

(From Johansson et al., 1976)

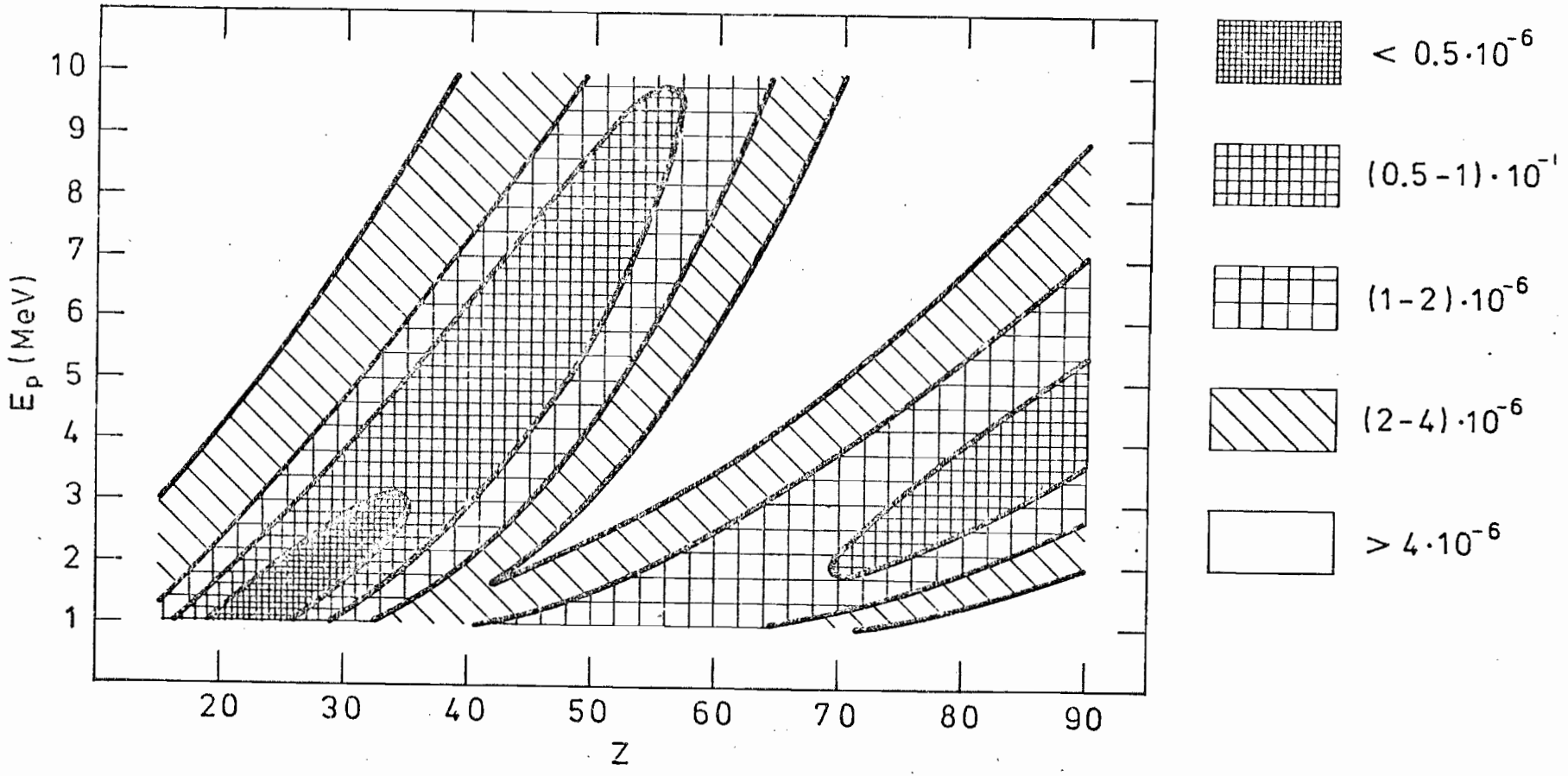
E_p (MeV)
10
9
8
7
6
5
4
3
2
1
20
30
40
50
60
70
80
90
Z
$< 0.5 \cdot 10^{-6}$
$(0.5-1) \cdot 10^{-1}$
$(1-2) \cdot 10^{-6}$
$(2-4) \cdot 10^{-6}$
$> 4 \cdot 10^{-6}$

interest. For many biological and environmental samples, the trace elements of most interest are found in the ranges $20 \lesssim Z \lesssim 40$ and $75 \lesssim Z \lesssim 92$. Sensitivities in these elemental ranges are optimized for thin targets according to Figure 2.17 by choosing E_p between approximately 2.0 and 4.0 MeV in agreement with our own experimental results.

In summary, both theoretical estimates and experimental evidence indicate an optimal energy range of 2.0 to 4.0 MeV for proton excitation.

It remains in this section to evaluate the potential of other light ions for analytical applications. A number of comparisons between ^{1}H, ^{4}He, and ^{16}O ions are reported in Table 2.2. Again these results apply to targets that are considered thin. Because of the scaling property for X-ray cross sections and secondary electron bremsstrahlung, it is convenient to compare ions having equal velocity. Such a comparison is presented in Table 2.4. The sensitivity is defined here in terms of the "minimum detectable mass" based on the 3σ criterion. Clearly from Table 2.4, the scaling factor relating the sensitivities of protons to heavier ions will depend on how the experimental results are normalized, i.e., according to equal accumulated charge, equal X-ray yield, etc. The scaling factors for the minimum detectable mass and the peak-to-background ratio are applicable only in the X-ray region below approximately $T_m \approx \frac{4\ m_e}{M} E_p$. The

Table 2.4

Comparison of Equal-Velocity Ions where Z_p = projectile charge and A_p = projectile mass

Item	Scaling Factor[a]
1. Characteristic X-rays (N_x):	$(Z_p)^2$
2. Background (N_B)	
a. Secondary electron bremsstrahlung:	$(Z_p)^2$
b. Projectile bremsstrahlung:	~ 0 for $Z_p/A_p = Z_M/A_M$ [b]
c. Compton tail:	> 1
2. Minimum detectable mass[c] $(\frac{3\sqrt{N_B}}{\varepsilon Q})$	
a. Equal accumulated charge (Q):	$(Z_p)^{-1/2}$
b. Equal no. of projectiles:	$(Z_p)^{-1}$
c. Equal characteristic X-ray yield (N_x):	1
4. Peak-to-Background Ratio (N_x/N_B):	1

for $E_x \lesssim T_m$ [d]

a) Item (heavy ions) = scaling factor × Item (protons).

b) (Z_M, A_M) = atomic number and atomic mass of target matrix; for light ions heavier than protons incident on a biological matrix, $Z_p/A_p \sim Z_M/A_M \sim 1/2$.

c) Using the 3σ criterion; ε = total detection efficiency = X-ray counts of element Z per unit mass of element Z irradiated, per unit charge accumulated on the sample.

d) The scaling factors shown apply to the energy region $E_x \lesssim T_m$ where T_m = maximum energy transferred by the incident projectile: $T_m \sim \frac{E_p}{500}$ (keV). This is the region for which N_B and N_x scale according to Z_p^2 for equal-velocity ions.

sensitivity and peak-to-background ratio for $E_x \gtrsim T_m$ will be determined by projectile bremsstrahlung and the Compton tail associated with inelastic scattering of nuclear gamma rays. These background processes do not obey a scaling property and depend very much on the particular sample being analyzed, thus making a general comparison of equal-velocity ions impossible in the region $E_x \gtrsim T_m$.

Cahill et al. (1974) compared 4 MeV/amu ^1H and ^4He ion beams incident on thin deposits from aerosol samples. Normalizing the experimental results to the same characteristic X-ray yields, Cahill found that the sensitivities (defined by the 3σ "detection limit") for both ions were essentially identical for X-rays below about 8 keV. This is in agreement with predicted scaling results (Table 2.4). Above 15 keV, the detection limits were approximately 40% higher for ^4He ions primarily because of the more intense Compton background for ^4He excitation.

Barrette et al. (1976) evaluated 2.25, 3.0 and 6.0 MeV protons and 6, 9, 12, and 16 MeV ^4He ions, and concluded that 3.0 MeV protons provided the best overall sensitivity, generated lower backgrounds, and proved less damaging to the sample than equal-velocity ^4He ions. Their criterion was that the peak height be equal to three times the square root of the mean background counts per channel.

Figure 2.18 Minimum detectable concentration yielding a peak to background ratio of 1 for 3 MeV/amu ^{1}H, ^{4}He, and ^{16}O ions incident on a thin carbon matrix. The experimental results indicated by the dashed lines are extracted from Figures 2.8 and 2.9. Theoretical estimates shown in the solid lines are taken from the theoretical background levels of Figures 2.9 and the theoretical cross sections of Figure 2.8.

(From Folkmann et al, 1974b.)

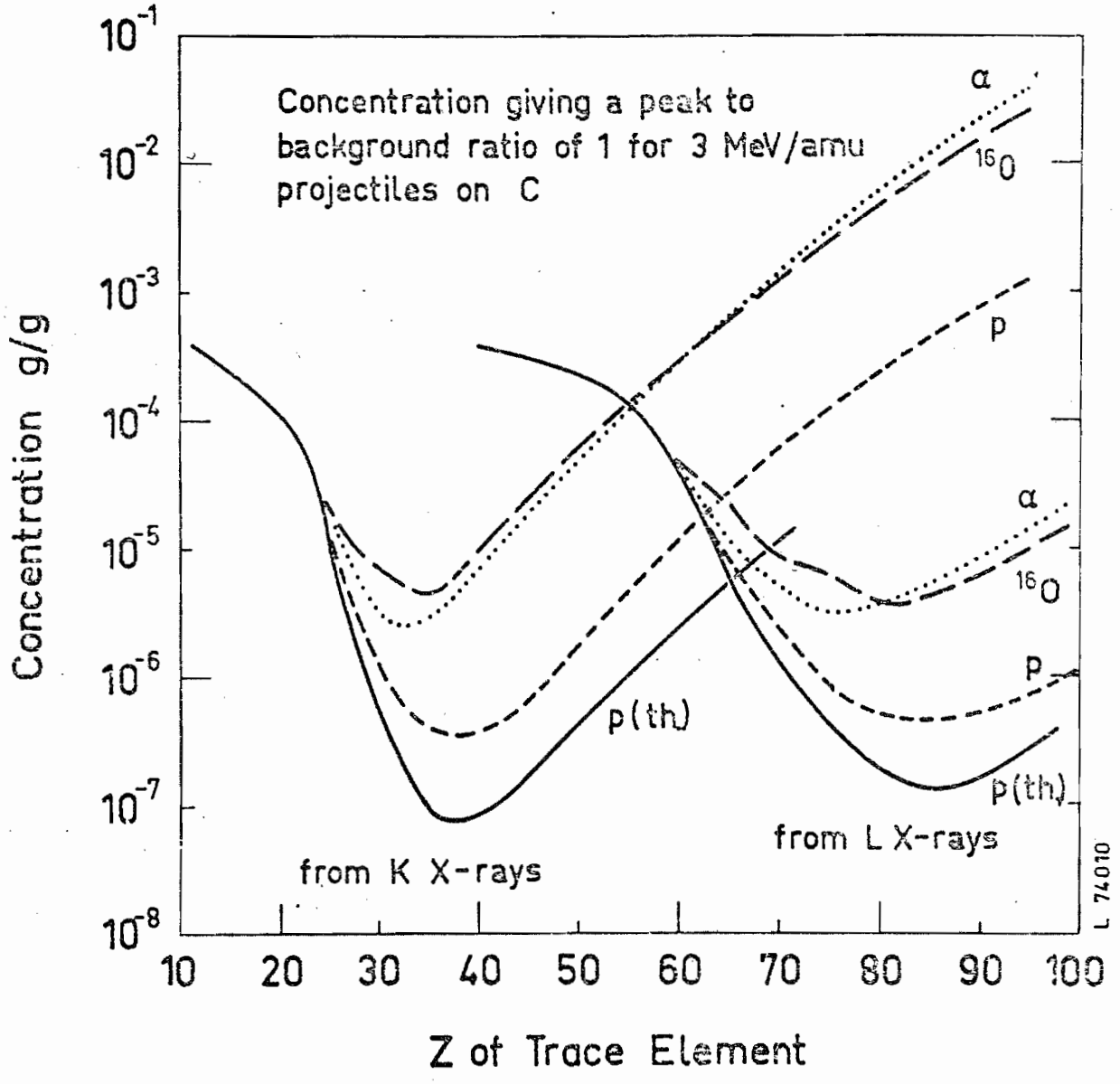
Concentration giving a peak to background ratio of 1 for 3 MeV/amu projectiles on C
α
16O
p
α
16O
p
p(th)
p(th)
from K X-rays
from L X-rays
Concentration g/g
Z of Trace Element
L 74010

Folkmann et al. (1974b) compared the analytical sensitivities for 3 and 5 MeV/amu ^{1}H, ^{4}He, and ^{16}O ions incident on C, Al, and V matrices. Folkmann employed a more conservative criterion for sensitivity requiring that the X-ray peak area be equal to the background counts underlying the peak. The results of Folkmann's studies for 3 MeV/amu projectiles on a thin carbon matrix are displayed in Figure 2.18. The dashed curves represent experimental measurements and the solid curves are calculations for proton bombardment. These results clearly show proton bombardment to be superior for target elements $Z \gtrsim 30$. Folkmann attributes the relatively poor sensitivities of the heavier ions and the deviation of the experimental proton-induced data from the theoretical curve to background induced by nuclear gamma rays (see Figure 2.9). Based on these results, Folkmann concludes that no significant advantages are gained by employing projectiles heavier than protons and bombarding energies greater than 3 MeV.

In conclusion, it is unlikely that significant advantages in terms of sensitivity are gained by employing projectiles heavier than protons, and for the elemental range of interest, protons of 2.0 to 4.0 MeV appear to be the optimal choice for particle and energy.

Chapter III

EXPERIMENTAL

IIIA. Introduction

The present chapter discusses the experimental aspects of PIXE analysis in terms of the following topics: (1) system calibration, (2) sample preparation, (3) data collection, (4) data analysis, (5) sensitivity considerations, and (6) precision and accuracy considerations.

The present PIXE system at Duke University was designed to facilitate the rapid analysis of a wide variety of sample types. The experimental design reflects the desire to retain as much flexibility as possible in the types of samples that can be analyzed and in the kinds of analysis that can be routinely performed. For example, samples are currently positioned manually (rather than automatically) for analysis largely because of the added flexibility which manual positioning provides. The present experimental design is not fully optimized in terms of analytical sensitivity, and design improvements which would provide better sensitivities will be discussed also.

III B. Equipment Needs and System Design

III B.1 Beam generation and beam handling

The proton beam used in the Duke PIXE studies was obtained from the Triangle Universities Nuclear Laboratory (TUNL) 4-MeV Van de Graaff generator. Quantitative analyses were made using a proton energy of 3.0 MeV, determined to approximately $\pm$ 0.02 MeV. The proton beam was deflected through 60° by a bending magnet and directed onto a 1.0 micron thick ultrapure nickel foil located approximately 1 m upstream of the irradiated sample. The purpose of the nickel foil was to diffuse the incident beam while causing negligible loss of proton energy. After collimation, this beam results in a spot on target of approximately uniform intensity. The diffuser foil also reduces the energy of the proton beam from the original value of 3.0 MeV to 2.94 MeV at the sample. Because of the spreading of the beam by the foil, the amount of beam that is passed through the final limiting aperature or collimator is reduced to about 1/100 of its original magnitude.

Figure 3.1 shows a schematic of the experimental beam line employed at Duke. The nickel diffuser foil is mounted on a rotating cylinder which permits any of three pairs of openings to be aligned with the incident beam without breaking vacuum. During normal data collection, the pair of openings labeled as 1 in Figure 3.1 will contain the Ni diffuser

foil (upstream port) followed by a tantalum collimator with a 1/16" diameter opening (downstream port). The second pair of openings consists of a Ni foil diffuser followed by a quartz collimator (1/16"). An eyepiece attached to the collimator box allows one to view the diffused beam on the quartz collimator while fine adjustments in the beam's steering and focus can be made by means of a pair of orthogonal electrostatic steerers and a pair of quadrupole magnets. The third pair of openings on the rotating collimator are usually left vacant, permitting the incident beam to pass unattenuated onto the target. This enables one to selectively analyze small areas (<0.5 mm^2) of the sample when desirable. The set of four graphite collimators preceding the scattering chamber serve to define the diffused beam, selecting out the central and most uniform portion of the beam. The graphite collimators are bevelled as shown in Figure 3.1 to minimize beam scattering. The combination of the nickel diffuser foil and the set of collimators results in a beam spot on target which is approximately 6.5 mm in diameter and which is nearly uniform in intensity over the entire spot. Typical operating currents on target ranged from 1 to 100 nA. For thin targets, the beam was eventually stopped in a thick graphite slab located about 20 cm from the target position.

A uniform intensity distribution of the proton beam spot is essential in obtaining quantitative and reproducible

Figure 3.1 Diagram of the experimental beam line for the Duke PIXE system.

Figure 3.2 Experimentally measured profile of the proton beam under operating conditions. Vertical bars through the data represent the associated statistical uncertainties. The profile was obtained by moving a point monoelement deposit across the proton beam in calibrated steps and measuring the X-ray yields at each position.

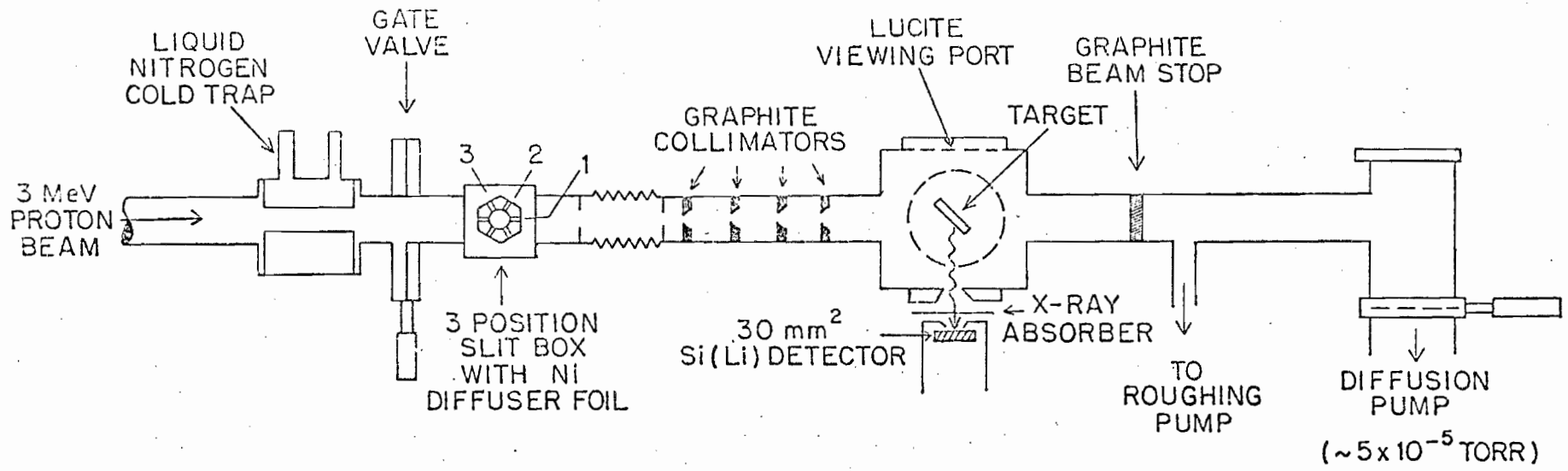

DIAGRAM OF EXPERIMENTAL BEAM LINE

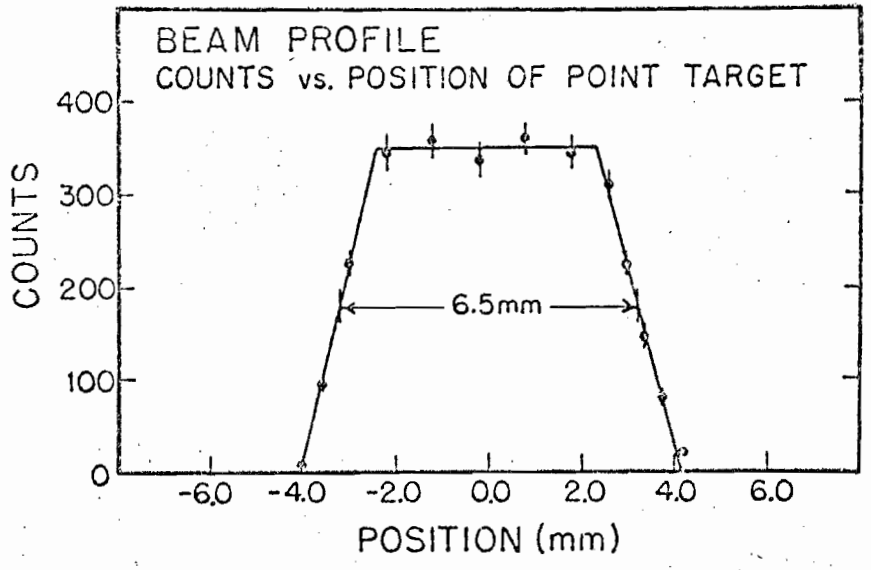

information from (1) samples smaller than the beam spot, and (2) inhomogeneous samples larger than the beam spot. Profiles of the intensity distribution across the diameter of the beam spot were periodically measured in order to monitor changes in the size or uniformity of the beam spot. An example of such a beam profile is shown in Figure 3.2, obtained by moving a pinpoint monoelement deposit across the diameter of the proton beam in calibrated steps and measuring the X-ray yield at each position. Since the beam intensity is linearly related to the X-ray yield, the resulting profile is a direct picture of the intensity variations across the beam spot. The effects of the nickel diffuser foil and the series of graphite collimators are observed respectively in the broad, flat top of the profile, and the sharp falloff in X-ray yield (or beam intensity) at the edges of the beam spot. While we have found the foil diffuser to be a satisfactory method for obtaining a uniform beam spot, one can achieve similar results by sweeping a well-focused beam in the x-y planes across the target face using electrostatic or magnetic sweeping (Cahill et al., 1975; Johansson et al., 1972).

IIIB.2 Sample mounting and target irradiation

PIXE analysis at Duke presently requires that the irradiation of the sample take place in a moderate vacuum (approximately 5×10^{-5} Torr). Most PIXE laboratories analyze

samples in vacuum, although a number of workers have reported success using an external beam to analyze samples in air (Deconninck, 1972; Seaman and Shane, 1975; Horowitz and Grodzins, 1975). The advantages of the external beam approach will be discussed in Section VIC.

Figure 3.3 shows a schematic of the scattering chamber and sample-holder design. Samples to be analyzed are mounted on an aluminum frame which attaches at both ends to cylindrical rods. Extension arms which join to the scattering chamber at 90° relative to the beam axis are fitted at both ends with vacuum seal O-rings allowing the target rod to be moved transversely across the beam path and rotated to any desired target angle without breaking vacuum. The rectangular frame is approximately 5 cm wide by 32 cm long and can accomodate up to 25 1-cm wide samples. A recessed channel 2.5 cm wide and extending the length of the frame is designed to hold up to 12 samples which have been mounted on our standard 2.5 cm diameter fiber washer rings. An open channel approximately 2 cm wide has been cut along the length of the frame allowing the proton beam to exit from thin targets with minimum scattering from the frame itself. A representative collection of samples are shown mounted for analysis in Figure 3.4. These include a collection of self-supporting leaves (top frame), pieces of fish tissue glued to an aluminized mylar strip (middle frame), and a group of

Figure 3.3 Diagram of the target chamber and sample-holder design.

Figure 3.4 A representative collection of samples mounted on aluminum target frames for analysis. Included here are self-supporting leaves (top frame), sections of fish tissue attached to aluminized mylar (middle frame), and a group of samples supported on 2.5 cm diameter fiber washers (bottom frame).

CUT AWAY VIEW OF TARGET CHAMBER

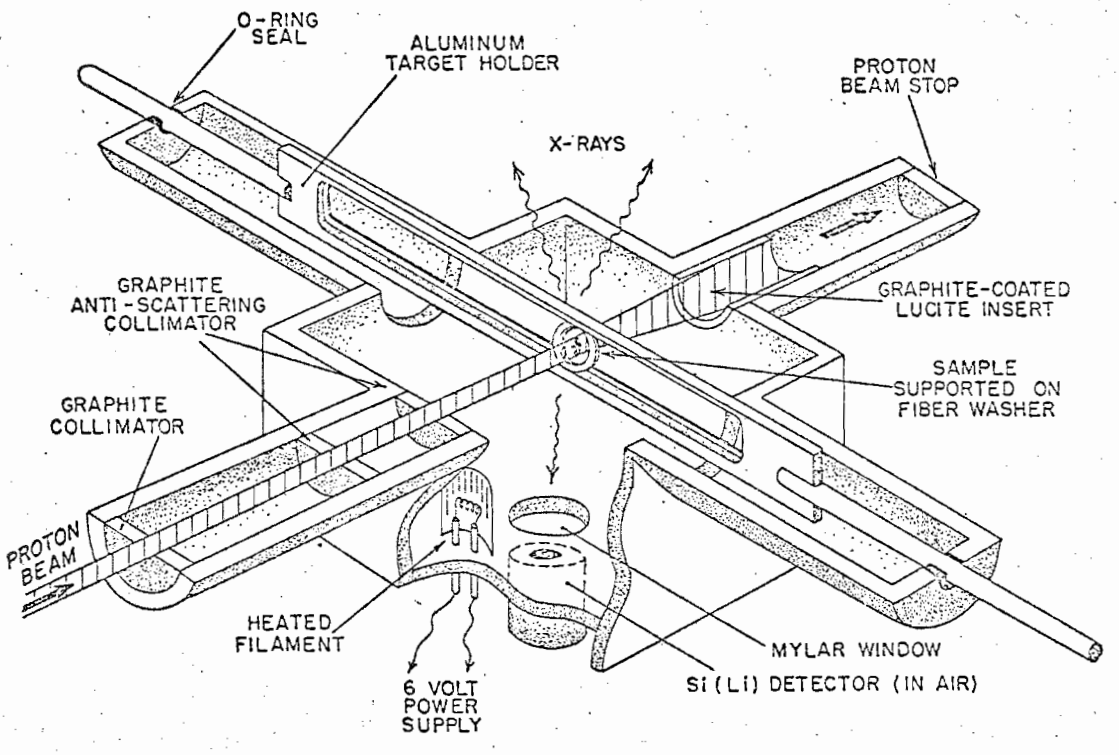

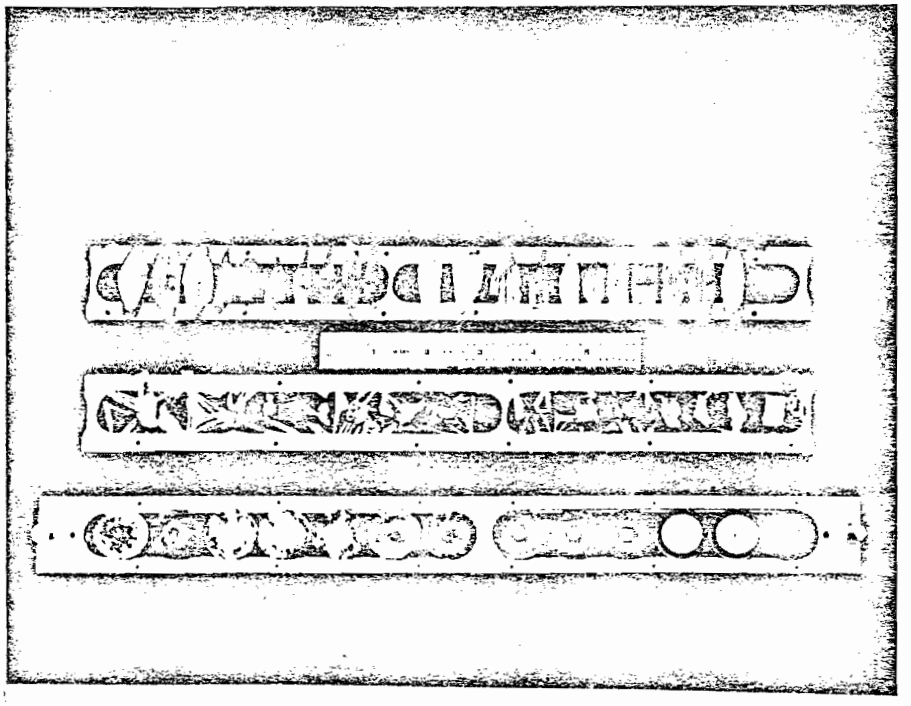

samples supported on 2.5 cm diameter fiber washers (bottom frame). The latter samples include orchard leaf and placenta pellets sandwiched between thin mylar films, and spot deposits of fuel oil and ashed placenta on mylar or nuclepore substrates.

The scattering chamber (Figure 3.3) is constructed of aluminum in order to minimize X-ray background associated with scattered protons striking heavier elements in the vicinity of the X-ray detector. The aluminum X-rays are too low in energy to be detected with the present Duke PIXE system. One must also be concerned with background arising from nuclear gamma rays produced by energetic protons which strike material anywhere in the general vicinity between the diffuser foil and the beam stop. As 3 MeV protons will not generate nuclear gamma rays from ^{12}C bombardment, graphite was used for the collimators and the beam stop, and a lucite cylinder was used to line the beam pipe beyond the target chamber (where scattered beam might impinge). The lucite was coated with a graphite solution to provide a conductive path for such beam. (See also Herman et al., 1973). Background spectra have been measured on the Duke PIXE system under two test conditions. First, the background was measured when the proton beam was stopped about 3 m upstream from the X-ray detector. Second, the beam was brought through the target chamber as usual, except with no target or sample in place. The background levels

were extremely low and, suprisingly, the level in the second test was virtually identical to the background measured in the first test.

A lucite plate on top of the scattering chamber allows visual positioning of the sample. A fraction of the X-rays excited in the sample exit the scattering chamber through a 25 μm mylar window located in the bottom of the chamber immediately above the detector face.

A shielded tungsten filament has been mounted inside the scattering chamber and is connected by vacuum feedthroughs to a battery power supply. The purpose of the filament is to eliminate buildup up positive charge from the proton beam as it is deposited in thick, non-conducting samples. Electrons emitted from the filament are attracted to the sample as it becomes slightly positive. That is, the target-filament system acts in the same way as a common diode. In this way, the potential of the target is maintained near ground potential. Without some type of charge cancellation, a thick insulating sample would continue to accumulate charge until local breakdown potentials were reached. At this point the target would begin to spark generating excessive bremsstrahlung background which can have deleterious effects on the X-ray spectrum. Some contamination of the sample by tungsten ions boiled off of an unshielded filament had been observed, and a cylindrical aluminum shield surrounding the filament was therefore insert-

Figure 3.5 PIXE spectra of an orchard leaf pellet demonstrating the improvement gained by using a hot filament to discharge the target. The dashed curve was obtained with the filament turned off. The solid curve shows the improved spectra obtained with filament turned on.

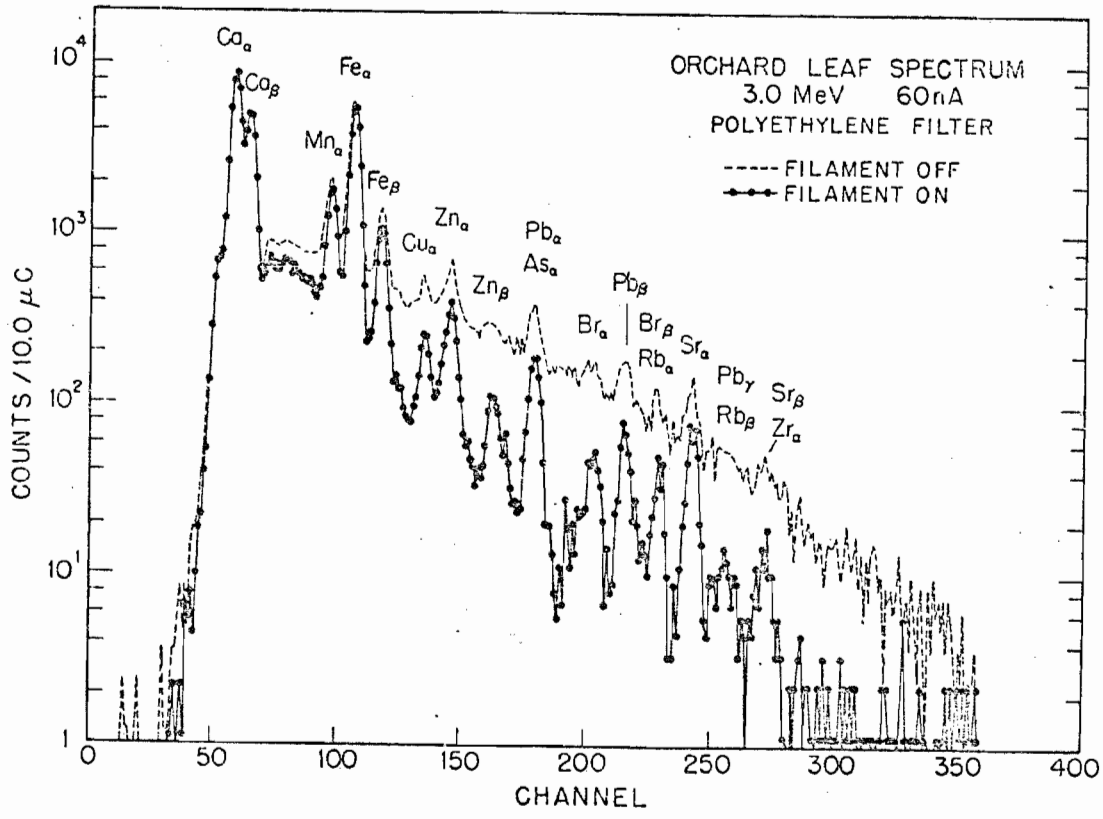
ORCHARD LEAF SPECTRUM
3.0 MeV 60nA
POLYETHYLENE FILTER
FILAMENT OFF
FILAMENT ON
Ca$_\alpha$
Ca$_\beta$
Mn$_\alpha$
Fe$_\alpha$
Fe$_\beta$
Cu$_\alpha$
Zn$_\alpha$
Zn$_\beta$
Pb$_\alpha$
As$_\alpha$
Br$_\alpha$
Pb$_\beta$
Br$_\beta$
Rb$_\alpha$
Sr$_\alpha$
Pb$_\gamma$
Rb$_\beta$
Sr$_\beta$
Zr$_\alpha$
COUNTS / 10.0 μC
CHANNEL
10^4
10^3
10^2
10^1
1
0
50
100
150
200
250
300
350
400

ed in order to prohibit the tungsten ions from reaching the sample. The constructive effect of the tungsten filament is illustrated in Figure 3.5 which shows PIXE spectra obtained from a pellet made from ground orchard leaf (NBS SRM #1571) with the filament turned off (dashed line) and with the filament turned on (solid curve). The dramatic improvement in the spectrum collected with the filament turned on is obvious.

In order to maximize the efficient operation of the PIXE system for large numbers of samples, the time required to change target rods and to attain a working vacuum should be minimal. The vacuum system for the Duke PIXE system is shown in Figure 3.1. A hand operated vacuum lock isolated the scattering chamber from the accelerator vacuum system. A liquid nitrogen cold trap is located immediately upstream of the vacuum gate valve. The isolated system is pumped down initially through a roughing valve and is then opened to the diffusion pump. The time required to replace a target rod and to attain working vacuum is highly dependent on the water content and the size of the targets. It can be as little as 10 min but is typically more like 20 min. Future improvements in the design of the vacuum system and in predrying the targets should reduce this pump-down time to a few minutes.

Quantitative analysis requires that the total amount of proton charge incident on a sample during the course of an analysis be measured. The total integrated charge for the

system shown in Figure 3.1 is comprised of the charge collected on the graphite beam stop plus any charge which may have been collected on the walls of the scattering chamber or the aluminum target rod due to protons which were scattered after interacting with the sample. The scattering chamber, target rod and the graphite beam stop are electrically isolated from the remainder of the apparatus. The total current collected is fed into a current integrator (Ortec model 431) which outputs a voltage pulse (suitable for a scaler) for each unit of charge collected. During normal operation a scaler records these pulses and is interfaced with the data collecting electronics to stop the collection of data once a predetermined proton charge has been accumulated.

IIIB.3 Data acquisition

a. Introduction

Figure 3.6 is a block diagram of the essential components of the data processing system used for PIXE work at Duke. Those X-rays which are emitted by the sample vertically downward are detected with a 30 mm^2 lithium-drifted silicon detector (Si(Li) detector). The X-rays exit the target chamber through a 25 micron mylar window and pass through approximately 2 cm of air before entering the 25 micron thick Be window of the detector. An X-ray filter is usually inserted between the target chamber and the detector in order

Figure 3.6 Block diagram of the X-ray detection and pulse-processing electronics.

BLOCK DIAGRAM OF ELECTRONICS

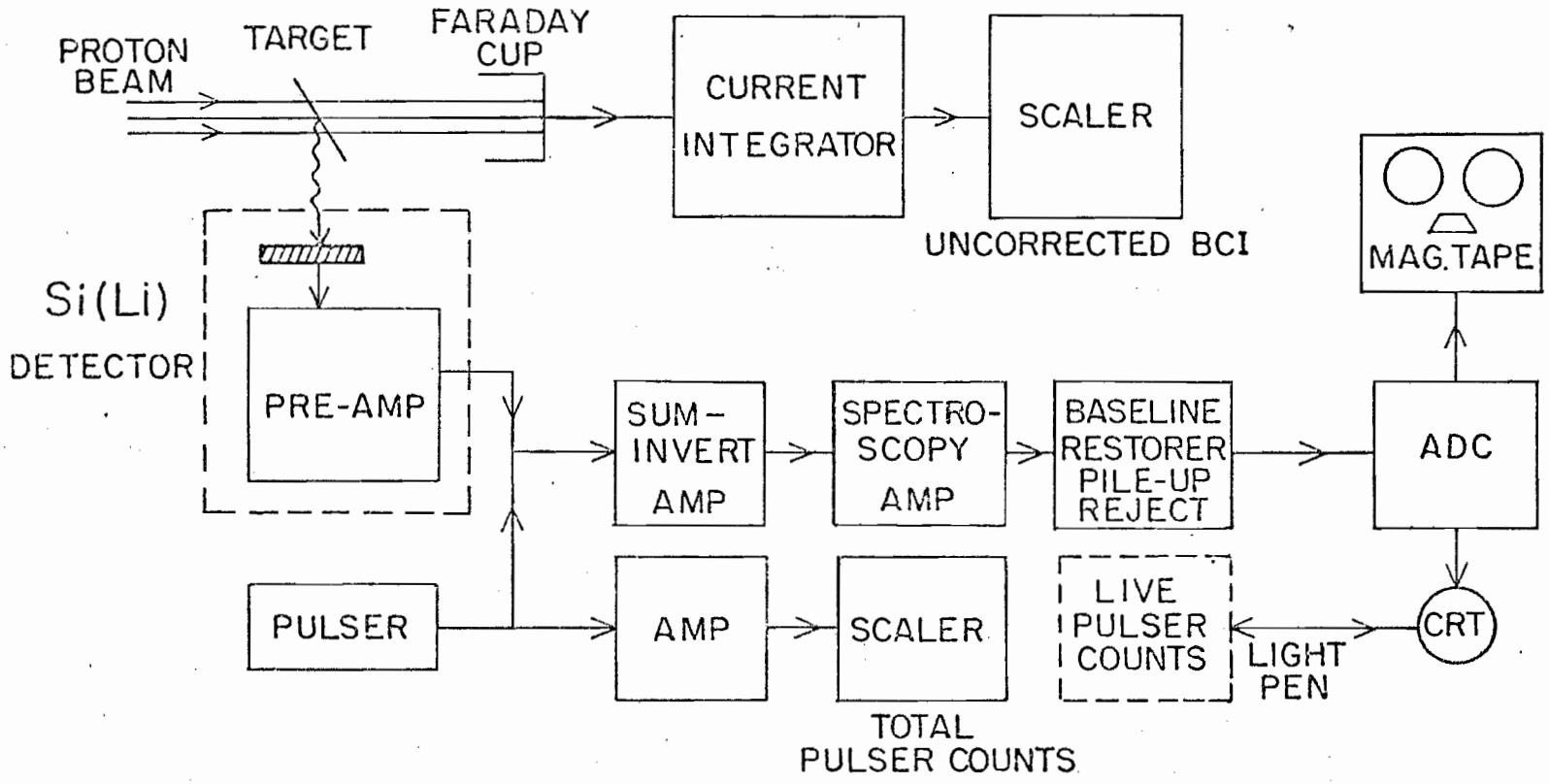

(108)

DEADTIME CORRECTION

$$\text{LIVE BCI} = (\text{UNCORRECTED BCI}) \times \left(\frac{\text{LIVE PULSER COUNTS}}{\text{TOTAL PULSER COUNTS}} \right)$$

to reduce to a tolerable level the flux of low-energy X-rays into the detector. Each X-ray entering the Si(Li) detector gives rise to a number of ion pairs, producing a "free charge" pulse whose amplitude is proportional to the energy deposited in the detector by the incident X-ray. The preamplifier converts the charge pulse into a voltage signal which retains the proportionality between the initial energy deposit and the pulse height. These signals are amplified and passed to a pulse restorer-rejector. The restorer-rejector unit combines base line restoration with pulse pile-up rejection to minimize high counting rate effects and to improve the spectral resolution of the system. Output signals from the restorer-rejector are sent to an analog-to-digital converter (ADC) which is interfaced to the TUNL DDP-224 Honeywell Corporation computer. The ADC sorts the input signals by pulse height or magnitude into 512 channels, thereby building up a spectrum of counts versus channel number, or counts versus X-ray energy, since channel number is proportional to energy. The spectral resolution of the system shown in Figure 3.6 is approximately 190 eV for the 5.89-keV Mn K_{α} line.

For quantitative analysis, the measured quantity of interest is the number of X-ray counts detected (of a given energy) per unit of proton charge accumulated on the sample. As described earlier, the proton current is measured with the current integrator and the output pulses (each corresponding

to one unit of charge) are recorded on the master scaler. This scaler will send a logic pulse to the ADC terminating data acquisition when a preset amount of charge has been collected.

A very short but finite time interval is required by the electronic system shown in Figure 3.6 to process each incoming X-ray signal. During this time interval, known as "deadtime", no other signals can be processed, and any X-rays detected during this time are essentially lost data. The total deadtime losses incurred during an analysis are measured in the following manner. Pulses from a 60 Hz precision pulser are fed, together with the preamplifier output signal, into the amplifier input and simultaneously counted on the pulser scaler (P_i = number of input pulser counts). At the end of an analysis, the number of pulser counts accumulated in the X-ray spectrum (P_f) is determined and the system deadtime is given by:

$$\% \text{ Deadtime} = \left(\frac{P_i - P_f}{P_i} \right) \times 100.$$

Actual analysis time ranges from 1 to 15 min per sample depending upon the nature of the sample, the concentration levels of the elements to be determined, and the accuracy one desires to achieve.

At the end of an analysis the data are stored on

magnetic tape for off-line analysis at a later time, and transferred to another location in memory for further study and/or a modest on-line analysis. The on-line computer program which controls data acquisition provides the capability to extract single peak areas and peak centroids of previously stored data while the next X-ray spectrum is being accumulated. More complete analysis of the X-ray data is provided by the off-line computer code TRACE discussed in Section III.D.

b. The use of X-ray filters

The relatively large cross sections for both characteristic X-ray production and bremsstrahlung production in the low-energy X-ray region, combined with the typically large concentrations of low Z elements (e.g., S, Cl, K, Ca) in biological and environmental samples results in a high flux of low-energy X-rays into the detector. This intense low-energy flux effectively impairs the detection efficiency for more energetic X-rays, reducing the system's sensitivity to the frequently important medium and high-Z elements. For this reason, most PIXE systems employ some type of filtering to reduce the X-ray flux at low energies.

Two basic approaches to filtering have been used, i.e., either the use of multiple filters, or the use of a single "funny filter". By employing filters of different thicknesses, one can effectively optimize the detection

efficiency for a selected region of interest (see Figure 3.12). This is the premise behind the use of multiple filters. However, in order to obtain optimal sensitivity over a broad range of elements, the sample must be analyzed several times, each time using a different filter. The "funny filter" (Cahill, 1975; Johansson et al., 1976) achieves essentially the same results obtained by using multiple filters, but with a single filter. This "funny filter" has a small hole in the center permitting a fraction of the intense low energy flux to pass unattenuated into the detector. This filter provides the advantages that the sensitivity over the full range of elemental interest can be obtained in a single irradiation, and that the detection efficiency of the system needs to be calibrated for only one filter rather than several. A wedge shaped filter is a compromise between using several uniform filters and the "funny filter", but to our knowledge, no PIXE analysts are currently using one of this design.

The Duke PIXE system is presently calibrated for three absorbing filters:
(1) 0.1 mm mylar, (2) 0.8 mm polyethylene, and (3) 0.2 mm of aluminum foil. Typically, a short analysis (1 min or less) for the low-Z elements will be done using the mylar filter and a second, longer analysis (for the medium and high-Z elements) will be done with the thicker polyethylene filter. The aluminum filter is used infrequently--typically

when the sample contains an unusually high concentration of a moderately heavy element such as Fe (as in blood samples or fly ash samples), and when there is interest in observing elements heavier than this dominant one. When analyzing for Al, Mg, P, and S, it is necessary to remove all filters leaving only the 25 micron mylar window of the scattering chamber and the Be window of the detector to attenuate the X-rays. A number of researchers eliminate even these windows by placing the detector inside the evacuated target chamber (Cahill, 1972; Barrette et al., 1976). This step has not yet been taken at Duke primarily because of the potential risk to the detector in the event of a vacuum failure, and the possibility of evaporating some contaminants onto the Be window.

The use of X-ray filters is demonstrated in Figures 3.7a,b and Figure 3.8. Figures 3.7a and 3.7b show the effects of three different absorbers on spectra obtained from a fly ash sample. The effect of the thicker polyethylene filter in the low-Z region is quite dramatic. (Note particularly the absence of Cl in Figure 3.7b which dominates the spectra in Figure 3.7a.) Figure 3.8 illustrates the use of the three standard absorbers in obtaining spectra for a heavily loaded air filter. The mylar spectrum was obtained in approximately 8 minutes of irradiation time, while the polyethylene and aluminum spectra represent 5 minute runs. Over-

Figure 3.7a PIXE spectra of NBS fly ash obtained with two different thicknesses of mylar absorber.

Figure 3.7b PIXE spectrum of NBS fly ash obtained with polyethylene absorber. Note the attenuation of low energy X-rays compared to the spectra in Figure 3.7a. The thicker polyethylene absorber yields improved sensitivity to medium and high-Z elements.

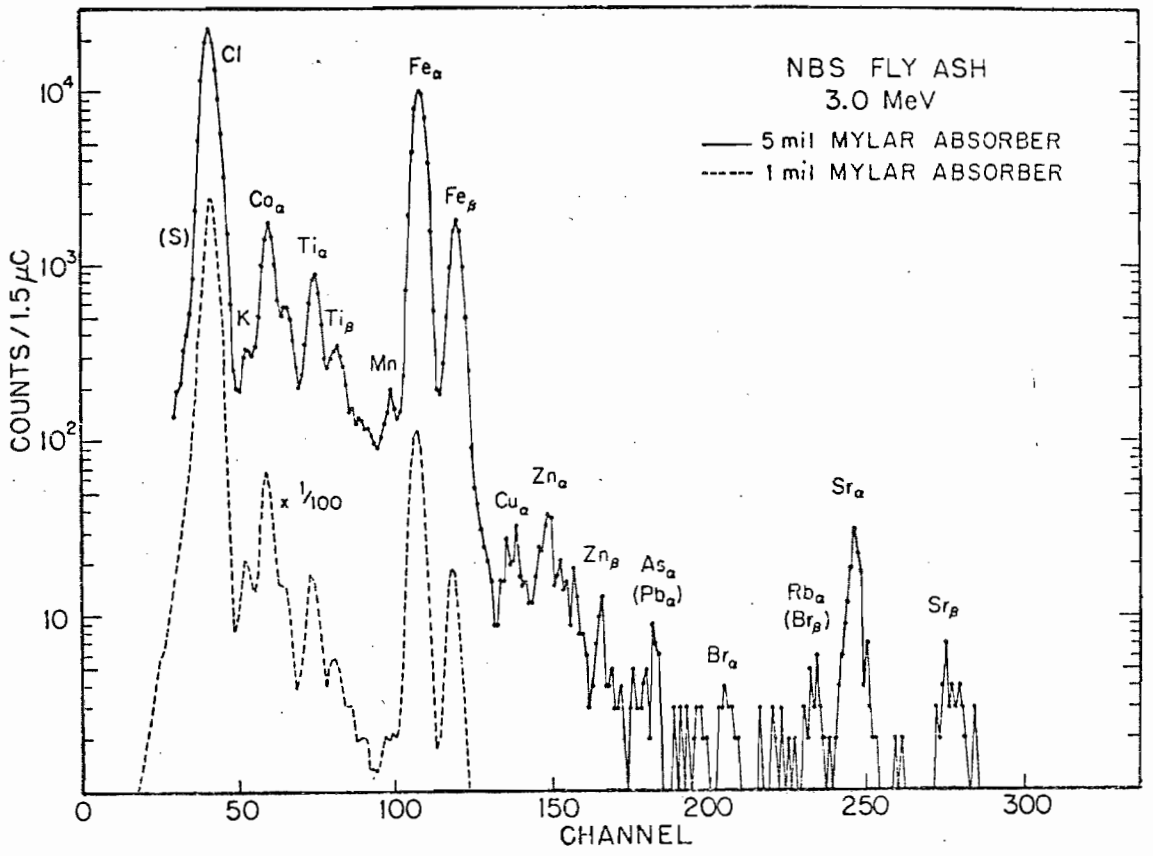
NBS FLY ASH
3.0 MeV
5 mil MYLAR ABSORBER
1 mil MYLAR ABSORBER
COUNTS / 1.5 μC
CHANNEL
Cl
Fe$_\alpha$
Co$_\alpha$
Ti$_\alpha$
Fe$_\beta$
(S)
K
Ti$_\beta$
Mn
x 1/100
Cu$_\alpha$
Zn$_\alpha$
Zn$_\beta$
As$_\alpha$ (Pb$_\alpha$)
Br$_\alpha$
Rb$_\alpha$ (Br$_\beta$)
Sr$_\alpha$
Sr$_\beta$

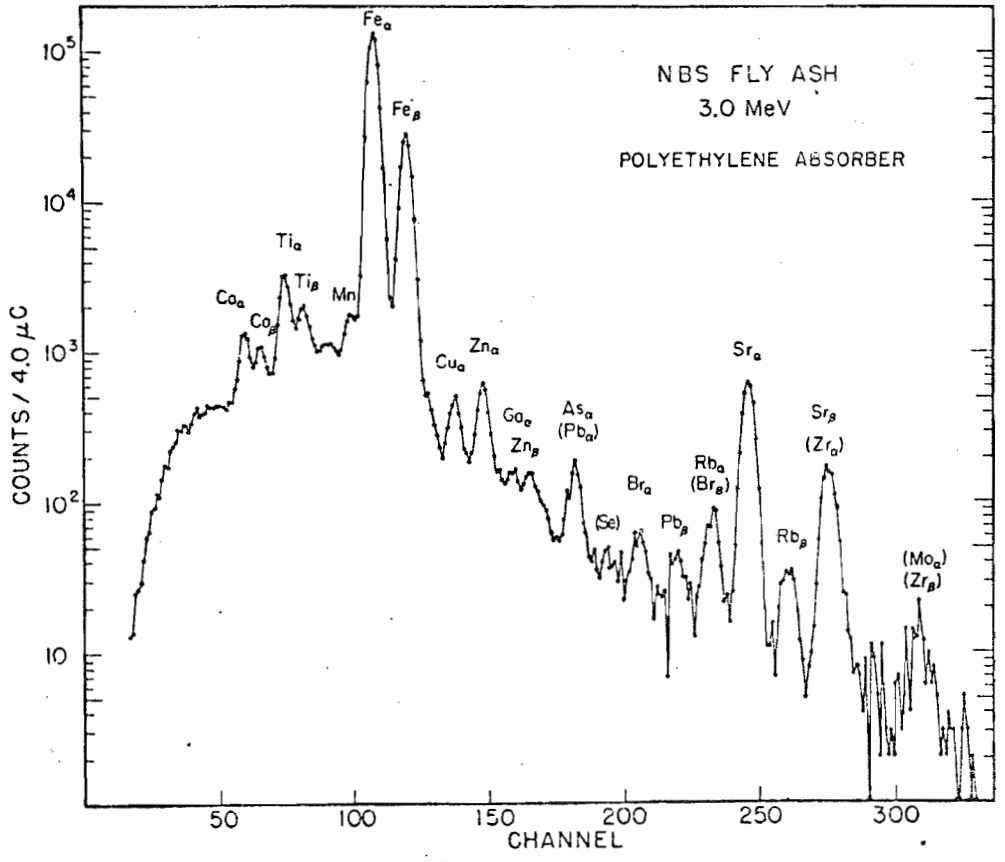
NBS FLY ASH
3.0 MeV
POLYETHYLENE ABSORBER
COUNTS / 4.0 μC
CHANNEL
Fe$_\alpha$
Fe$_\beta$
Ti$_\alpha$
Ti$_\beta$
Co$_\alpha$
Co$_\beta$
Mn
Cu$_\alpha$
Zn$_\alpha$
Ga$_\alpha$
Zn$_\beta$
As$_\alpha$ (Pb$_\alpha$)
Br$_\alpha$
(Se)
Pb$_\beta$
Rb$_\alpha$ (Br$_\beta$)
Sr$_\alpha$
Rb$_\beta$
Sr$_\beta$ (Zr$_\alpha$)
(Mo$_\alpha$) (Zr$_\beta$)

Figure 3.8 PIXE spectra of a nuclepore air filter demonstrating the use of the three standard absorbers. The mylar spectrum was obtained in approximately 8 minutes, while the polyethylene and aluminum spectra each represent 5 minute irradiations.

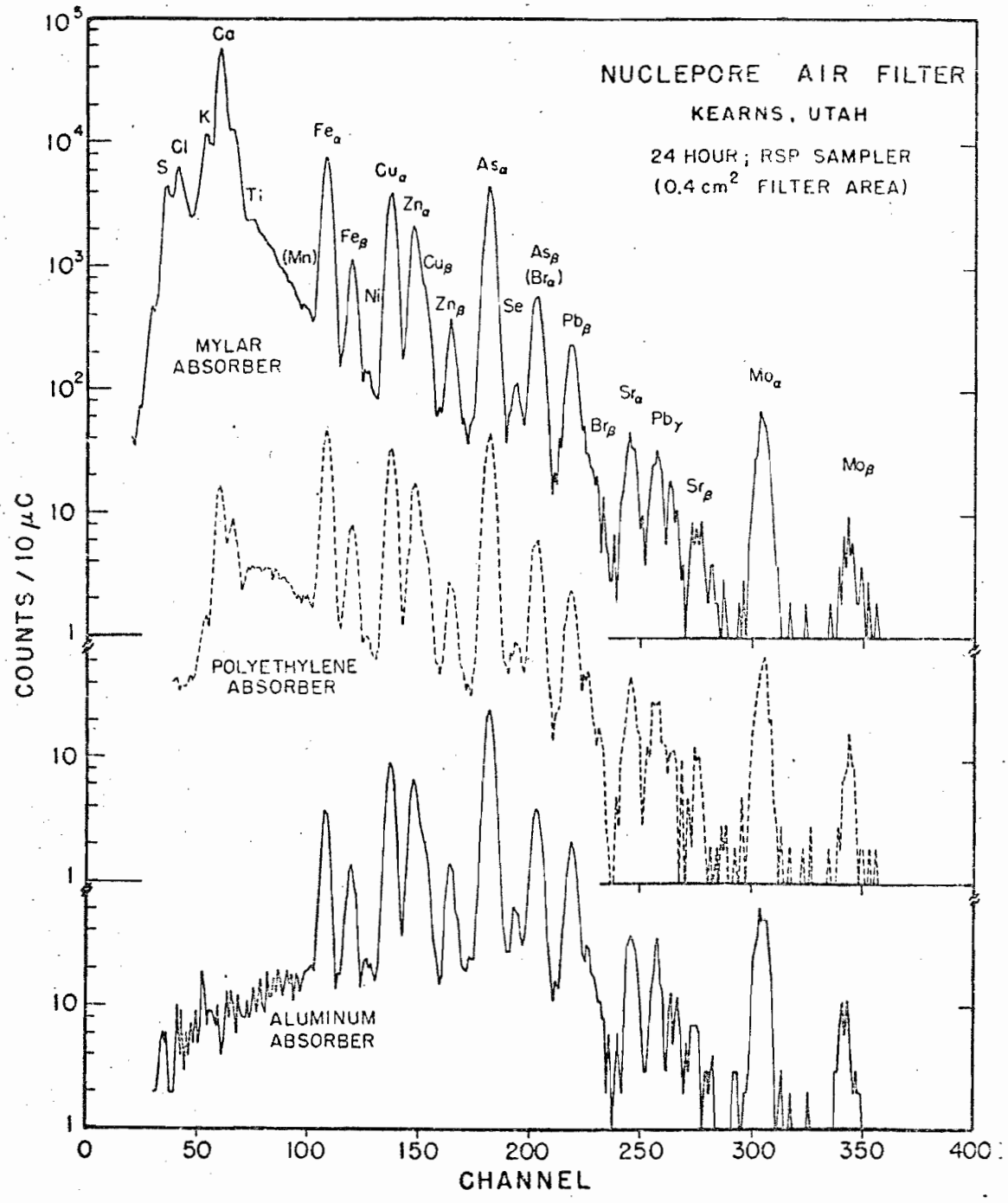
NUCLEPORE AIR FILTER
KEARNS, UTAH
24 HOUR; RSP SAMPLER
(0.4 cm² FILTER AREA)
MYLAR ABSORBER
POLYETHYLENE ABSORBER
ALUMINUM ABSORBER
COUNTS / 10 μC
CHANNEL
S
Cl
K
Ca
Ti
(Mn)
Fe$_\alpha$
Fe$_\beta$
Ni
Cu$_\alpha$
Zn$_\alpha$
Cu$_\beta$
Zn$_\beta$
As$_\alpha$
Se
As$_\beta$ (Br$_\alpha$)
Pb$_\beta$
Br$_\beta$
Sr$_\alpha$
Pb$_\gamma$
Sr$_\beta$
Mo$_\alpha$
Mo$_\beta$

all counting rates were reduced by a factor of 10 roughly in changing from the mylar filter to the aluminum filter, but most of this loss in counting rate is associated with low energy X-rays (compare the background levels below Fe for the two absorbers). The primary benefit gained by X-ray filtering is to reduce the counting rate at low X-ray energies, permitting one to increase the beam current and thus accumulate improved statistics for the heavier elements in a significantly shorter time.

For samples containing unusually large concentrations of a particular element, the detection sensitivity for neighboring elements may be appreciably enhanced by the technique of critical absorption. Here, the filter is chosen so that the X-ray absorption edge of the filter material lies just below the X-ray energy of the dominant element in the sample. The X-rays from the dominant element are strongly attenuated while the X-rays of the neighboring elements of lower Z are relatively unaffected. Sensitivity is particularly improved for those elements immediately below and including the element composing the filter material. By appreciably attenuating the X-rays from a dominant peak, the critical absorber can reduce the background due to low energy tailing and escape peaks (Figure 3.10) which degrade the sensitivity on the low energy side of the dominant peak. Examples of the use of

critical absorbers are given by Deconninck et al. (1975) and Ahlberg et al. (1975).

c. X-ray detection

The ability to detect X-rays of many elements simultaneously is the primary attraction of energy dispersive X-ray analysis, distinguishing this approach from wavelength dispersive techniques which (for single-crystal spectrometers) detect only X-rays of a single wavelength (or energy). The key component of the energy dispersive system at Duke is the solid state Si(Li) detector comprised of (1) a 30 mm^2 silicon chip drifted with lithium impurity atoms to improve the detection characteristics, and (2) a charge sensitive preamplifier.

X-rays entering the Si(Li) detector interact with atoms of the silicon chip primarily via photoelectric and Compton scattering processes. The resulting ionization of the silicon atoms creates an amount of "free charge" which is proportional to the amount of energy deposited in the detector by the X-ray. The preamplifier effectively integrates this charge pulse and converts it to a voltage signal while preserving the proportionality between the initial energy deposit and the level of the output voltage signal.

Two parameters which relate to the performance of the Si(Li) detector are the detector resolution, and the

detector efficiency. Detector resolutions for Si(Li) detectors commonly used in PIXE work, typically range from 160-200 eV fwhm for the 5.9 keV Mn K_α line. The effective resolution is comprised of an intrinsic resolution (determined by the details of the energy transfer process in the detector chip) and an electronic noise contribution and is given as a function of X-ray energy E by (Woldseth, 1973):

$$(\text{FWHM}) = \{\Gamma_N^2 + [2.35(F\ \varepsilon\ E)^{\frac{1}{2}}]^2\}^{\frac{1}{2}} \text{eV}$$

where Γ_N = electronic noise contribution (fwhm)

F = Fano factor (approximately 0.1 for Si)

ε = 3.9 eV (average energy required per electron-hole pair produced in Si)

E = X-ray energy (keV).

This resolution is sufficient to resolve the K_α X-ray lines for adjacent elements in the periodic table for all $Z \gtrsim 10$ and L_α lines for all $Z \gtrsim 55$. Interferences nevertheless occur because of overlapping K and L-lines of widely differing Z or overlapping K_α and K_β lines of neighboring elements.

The detector efficiency as a function of X-ray energy is shown in Figure 3.9. The detector is approximately 100% efficient for detecting incident X-rays with energies between 4 and 18 keV. At lower energies, the rapid decline in ef-

ficiency is attributable to absorption losses primarily in the 25 micron Be window protecting the detector chip. For energies greater than 18 keV, the falloff in efficiency is due to the increasing probability that inelastic scattering will occur. Each incident X-ray which Compton scatters out of the active volume of the detector deposits only a fraction of its full energy in the detector, resulting in decreased efficiency for "full energy" peak detection. The detection efficiency at higher energies therefore is a function of the volume of the detector chip.

Processes in the detector which result in only partial deposition of an X-ray's energy or in incomplete charge collection give rise to undesirable background features in the X-ray spectrum. These features include low energy tailing and Si escape peaks. Examples of both features are shown in the PIXE spectra of a Ni target (Figure 3.10) which also demonstrates the effects of pulse pileup rejection. Low energy tailing is caused primarily by incomplete charge collection in the detector volume and produces the characteristic "tail" on the low-energy side of the Ni K_α and K_β lines of Figure 3.10. Incomplete charge collection can occur for both low and high X-ray energies. At low energies, charge is lost in photoelectric interactions taking place near the detector "deadlayer" (a thin inactive layer of silicon near the detector surface);

Figure 3.9 The X-ray detection efficiency versus X-ray energy for a typical Si(Li) detector. The reduced efficiency at low X-ray energies is primarily due to X-ray absorption losses. At energies greater than 18 keV, the falloff in efficiency is due to the increasing probability of Compton scattering.

Figure 3.10 PIXE spectra of a pure Ni target demonstrating the effects of pulse pile-up rejection at high counting rates. (See text for discussion.)

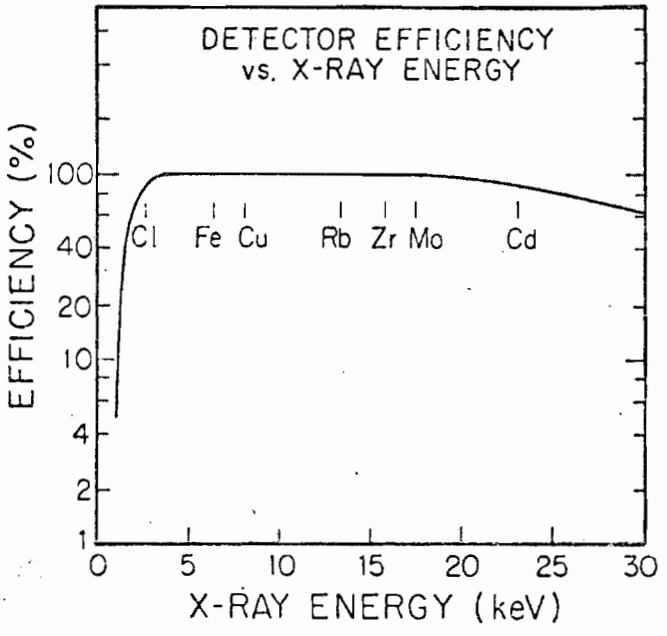
DETECTOR EFFICIENCY
vs. X-RAY ENERGY
EFFICIENCY (%)
100
40
20
10
4
2
1
Cl
Fe
Cu
Rb
Zr
Mo
Cd
0
5
10
15
20
25
30
X-RAY ENERGY (keV)

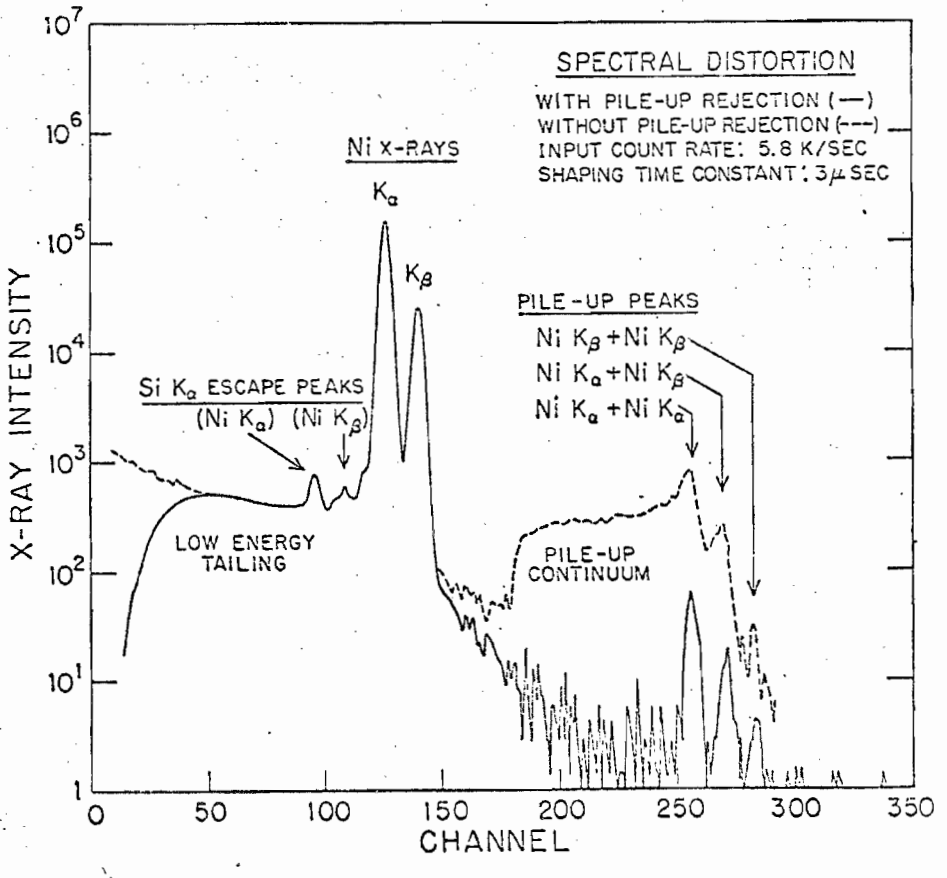
SPECTRAL DISTORTION
WITH PILE-UP REJECTION (—)
WITHOUT PILE-UP REJECTION (---)
INPUT COUNT RATE: 5.8 K/SEC
SHAPING TIME CONSTANT: 3μSEC
Ni X-RAYS
Kα
Kβ
PILE-UP PEAKS
Ni Kβ + Ni Kβ
Ni Kα + Ni Kβ
Ni Kα + Ni Kα
Si Kα ESCAPE PEAKS
(Ni Kα) (Ni Kβ)
LOW ENERGY
TAILING
PILE-UP
CONTINUUM
X-RAY INTENSITY
10^7
10^6
10^5
10^4
10^3
10^2
10^1
1
0
50
100
150
200
250
300
350
CHANNEL

at higher energies charge can escape via photoelectric and Compton scattering processes occurring near the back surface of the detector, or charge may be trapped along the sides of the detector or by impurities in the bulk of the detector resulting in degraded signals collected at the detector electrodes. Techniques can be employed to minimize the loss of ionizing signal due to poor surface characteristics at the sides of the detector, and these are discussed in Section VIC. Some of the background on the low-energy side of the full energy peak can also be attributed to the escape of photoelectron-induced bremsstrahlung from the detector. Low energy tailing impairs sensitivity for the region below large X-ray signals and makes background assignment in this region difficult.

X-rays entering the detector interact with the silicon atoms of the detector primarily via photoelectric absorption--a process in which an X-ray of energy E_0 gives up its full energy in ionizing a Si atom. The excited Si atom returns to its ground state by the emission of a Si X-ray which in general will be reabsorbed by the detector. For such processes occurring near the surface of the detector however, there is a small but non-negligible probability that a Si K_α X-ray (1.74 keV) will escape from the detector leaving a residual energy deposit in the detector of energy $E_1 = (E_0 - 1.74)$keV. If the intensity of the X-ray

line at energy E_0 is great enough, a noticeable peak will accumulate in the spectrum at energy E_1. In Figure 3.10 both the K_α and K_β lines of Ni are sufficiently intense to produce observable escape peaks. The probability for escape of the Si K_α X-ray as a function of the energy of the parent X-ray has been measured (Woldseth, 1973) and increases for decreasing X-ray energies. This behaviour can be understood since the softer X-rays interact nearer the detector surface increasing the probability for Si K_α escape. The PIXE analyst must be aware of the escape peak phenomenon in order to avoid erroneous interpretation of the X-ray spectrum. As an example, pellets pressed from lyophilized blood samples contain large Fe concentrations (approximately 2700 ppm dry weight) sufficient to produce a noticeable escape peak at energy 4.66 keV corresponding to the difference in energies between the Fe K_α and Si K_α X-rays. This escape peak interferes with the Ti K_α peak (4.51 keV) and therefore makes quantitative analysis of Ti in blood samples potentially very difficult. In practice, the elemental concentrations required to generate significant escape peaks are rarely encountered in biological or environmental samples (blood and fly ash are two notable exceptions). Interferences arising between an escape peak and an overlapping X-ray peak can be resolved automatically with the spectrum-analysis code TRACE (Section III.D) but

for routine analysis, the escape peaks have not been included in the list of peaks.

d. Pulse pileup rejection

Because of the high counting rates often encountered in PIXE analysis, and the random nature of the X-ray emission process, there is a reasonable probability that two or more X-ray signals will be detected simultaneously or within a very short time interval of each other. If two or more pulses arrive at the amplifier input within the finite time interval required by the amplifier to process a single pulse, the result is called pulse pileup. The output of the amplifier in this event is a distorted pulse representing the superposition of the overlapping input signals. The pulse height analyzer interprets this signal as the detection of an X-ray whose energy is proportional to the amplitude of the distorted pulse. The energy information of the two original pulses is therefore lost in a pileup event, resulting in a loss of counts in the full energy peaks and the appearance of a pileup spectrum at higher energies. The pileup spectrum typically consists of a pileup continuum and one or more discrete peaks which occur when a relatively large probability exists for coincidence of two signals corresponding to two characteristic X-rays. This probability can be appreciable in samples containing large concentrations

of one or more elements.

The importance of pileup rejection is demonstrated in Figure 3.10 which illustrates spectra obtained from a pure nickel foil. The continuum background in the pileup region beyond channel 175 is virtually eliminated by employing pileup rejection. In addition, the discrete pileup peaks due to coincident Ni X-rays are reduced approximately a factor of 10 with pileup rejection.

Figure 3.11 shows the two types of pileup which can occur: (1) leading edge pileup which distorts both pulse amplitudes, and (2) trailing edge pileup which distorts the amplitude of the trailing pulse only. Ideally the pileup rejector will discriminate between the two types of pileup, rejecting both distorted pulses in the former case and only the trailing pulse in the latter case. The pileup rejector operates by inspecting the time interval T_S between pulses arriving at the amplifier input. If $T_S < T_P$, where T_P is the peaking time of the first pulse (determined by the shaping time constant of the amplifier), then both pulses are rejected (leading edge pileup); if $T_P < T_S < 2T_P$, then only the trailing pulse is rejected (trailing edge pileup). If $T_S = 0$, the pileup rejector is not capable of determining that a pileup event has occurred and therefore passes the pileup pulse. This is the origin of the discrete pileup peaks of Figure 3.10 which are reduced

Figure 3.11 Illustration of leading edge pile-up (top figure) which distorts both incoming pulses; and trailing edge pile-up (bottom figure) which distorts only the trailing pulse.

LEADING EDGE PILE-UP

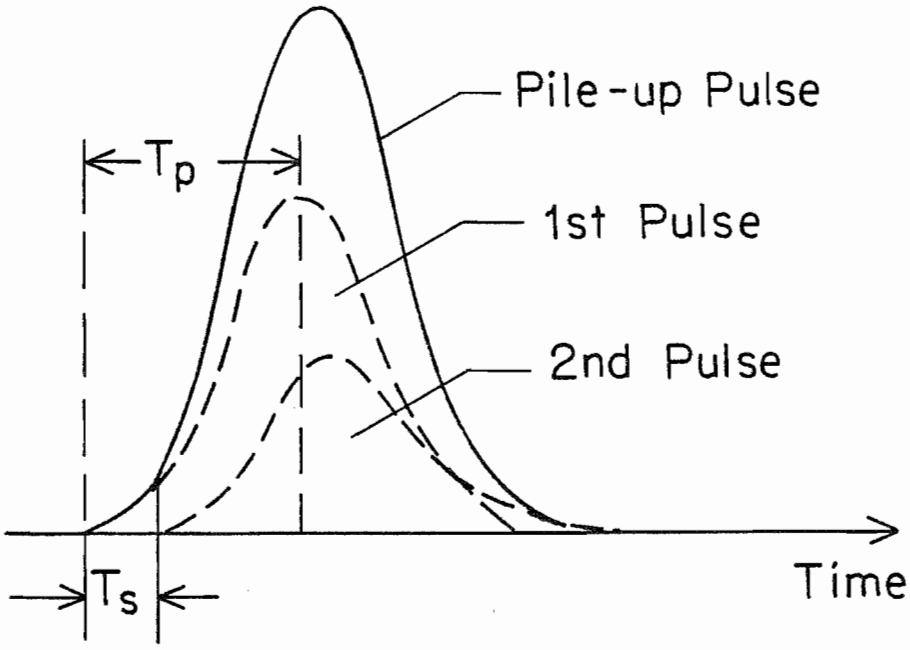

TRAILING EDGE PILE-UP

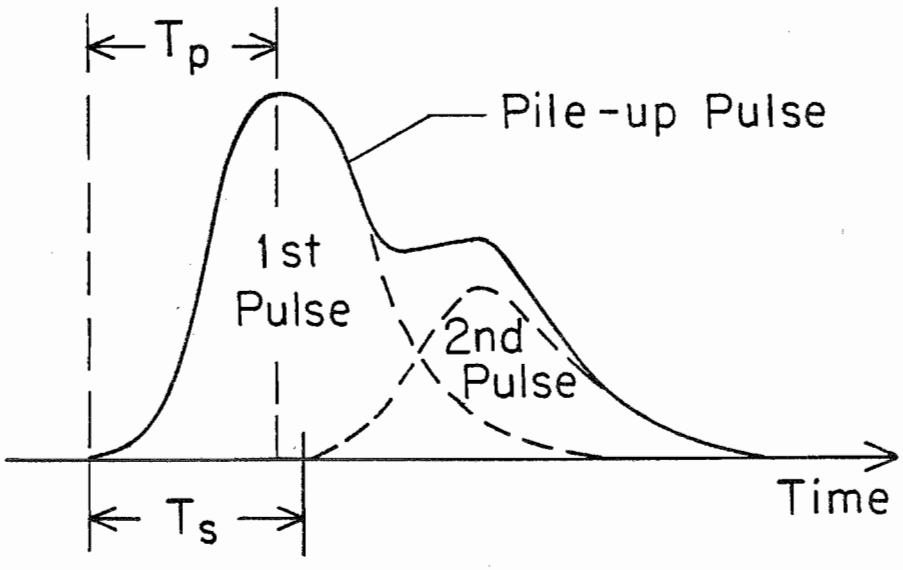

but not entirely eliminated by pileup rejection.

The phenomenon of pulse pileup is important for several reasons: (1) the pileup continuum extending from just above a strong X-ray line to an energy equal to twice the energy of the X-ray line is never entirely eliminated by pileup rejection--this background continuum impairs the analytical sensitivity for elements whose X-ray lines appear in this region; (2) the discrete pileup peaks can interfere with characteristic X-rays of the same energy (for example, the very strong Fe K_{α} line (6.4 keV) in blood samples produces a pileup peak at 12.8 keV which may be misinterpreted as the Pb L_{β} line at 12.61 keV); (3) quantitative analysis based on integration of the full-energy peak area is jeopardized because of the loss of counts to pileup events. Furthermore, this pileup loss depends on the total counting rate in a nonlinear way. The probability of pileup can be diminished by reducing the shaping time constant of the amplifier which is accompanied however by a corresponding loss of resolution, or by reducing the counting rate which thereby increases the analysis time required to obtain the same statistical accuracy. Typical parameters for the Duke PIXE system include a shaping time constant of 4 μs and a counting rate of approximately 1000 counts per second.

IIIC. System Calibration

IIIC.1 Introduction

The objective of quantitative PIXE analysis is in general to determine for an element Z and a given sample, one or more of the following: (1) the absolute mass of element Z in the irradiated fraction of the sample; (2) the mass of element Z per unit area of the sample (g/cm^2); (3) the concentration (ppm) of element Z in the sample. Calibration of a PIXE system requires that the experimentally observed quantity (number of Z X-rays observed (N_Z) per unit of proton charge (Q) collected on the sample) be precisely related to the physical quantity of interest (items (1), (2), or (3) above), for all elements Z of interest. This relation is expressed in the following formula:

$$G_Z(\mu g) = \left\{ \frac{S \cdot AM_Z \cdot 10^6 \cdot e}{\sigma_Z(E_0) \cdot k \cdot \frac{\Omega}{4\pi} \cdot \varepsilon} \right\} \cdot C(Z) \frac{N_Z}{Q} = f^{-1}(Z) \cdot C(Z) \cdot \frac{N_Z}{Q} \quad (3.1)$$

where: G_Z = mass of element Z (μg) in the irradiated region of the sample

N_Z = number of X-ray counts appearing in a selected X-ray line of element Z

Q = total proton charge incident on the sample (μc)

S = cross sectional area of proton beam (cm^2)

AM_Z = atomic weight of element Z ($\frac{\text{grams}}{\text{atom}}$)

$\sigma_Z(E_0)$ = X-ray production cross section for element Z, proton energy E_0, and the atomic shell (K or L) of interest (cm^2/atom)

k = relative transition probability for the particular X-ray line measured

e = unit of charge = 1.6×10^{-13} μC

$\Omega/4\pi$ = solid angle of the detector

ε = detector efficiency including absorption losses in windows, air passages, and X-ray filter

C(Z) = correction factor to account for proton energy loss and X-ray attenuation in thick samples

f(Z) = thin-target response factor for element Z (counts/μg · μC)

It is convenient in the following discussion to distinguish between "thin" targets for which proton energy loss and X-ray absorption effects in the target are negligible, and "thick" targets for which these effects cannot be ignored. For the present discussion, targets which are thick enough to completely stop a 3-MeV beam of protons are considered to be "infinitely thick". (For carbon, this thickness is about 16 mg/cm^2.)

IIIC.2 Thin-target calibration

Equation 3.1 is simplified if $C(Z) \simeq 1$ i.e., if

proton energy losses in the sample and X-ray absorption effects are negligible. This condition will be satisfied approximately for 3-MeV protons if target thicknesses are of the order of 1 mg/cm^2 or less. With $C(Z) = 1$ in Equation 3.1, the thin-target calibration is determined by the response function $f(Z)$ which is matrix-independent. That is, the same calibration is valid for all thin-target analyses regardless of the matrix composition provided that $C(Z) = 1$. (This is not the case for thick targets because the value of $C(Z)$ depends on the chemical composition of the particular target matrix.)

The response functions $f(Z)$ for the Duke PIXE system have been determined experimentally for each of the three X-ray filters (Section IIIB.3) chosen for PIXE work. Two of these curves are shown in Figure 3.12. The data used to generate the response curves were obtained from PIXE measurements of made on calibrated point deposits. Standard solutions for approximately fifteen elements chosen to span the elemental range of interest were prepared from reagent grade metals and/or metal salts using distilled, deionized water. Each standard solution was deposited with a precision micropipette in 10-20 μℓ amounts in the center of a thin membrane. Several substrates were evaluated for this purpose (Section IIIE.2) and two materials--0.15 mil mylar and 1.1 mg/cm^2 nuclepore were chosen for most applications. The solution

deposits were then allowed to dry in open air or vacuum. Care was taken throughout the entire process to ensure that no contamination of the standard deposits occurred.

The dried deposits were typically about 3 mm in diameter guaranteeing excitation of the entire deposit by the larger diameter proton beam (approximately 6.5 mm). The number of detected X-rays per unit of charge of proton beam incident on the sample is then measured to generate the system's response curves shown in Figure 3.12.

The thin-target response curves for the detection of K_α X-rays are seen to peak in the region $22 \lesssim Z \lesssim 30$ depending on the X-ray absorber employed. For a particular absorber, the system response drops rapidly on both the low-Z and high-Z (low-energy and high-energy) sides of the maximum value. The low-energy fall-off is due to the combined effects of: (1) increased absorption losses of soft X-rays in absorbing windows, air passage, and in the X-ray filter, (2) decreasing values for the fluorescence yield (Figure 2.5), and (3) falling detector efficiency (below 4 keV) (Figure 3.9). The high-energy fall-off in system response is due primarily to rapidly decreasing X-ray production cross sections (Figure 2.7). A contributing factor to the decline in the K_α response curves for X-ray energies $\gtrsim 18$ keV ($Z > 42$) is the decreasing Si(Li) detector efficiency.

An important consideration in calibrating the PIXE

Figure 3.12 Measured response curves for two of the three absorbers for the Duke PIXE system. See text for discussion.

Figure 3.13 Linearity of the detected X-ray yield versus deposited mass for selected elements. The system response is linear over a mass range of 5 ng to 40 μg for elements heavier than Ca.

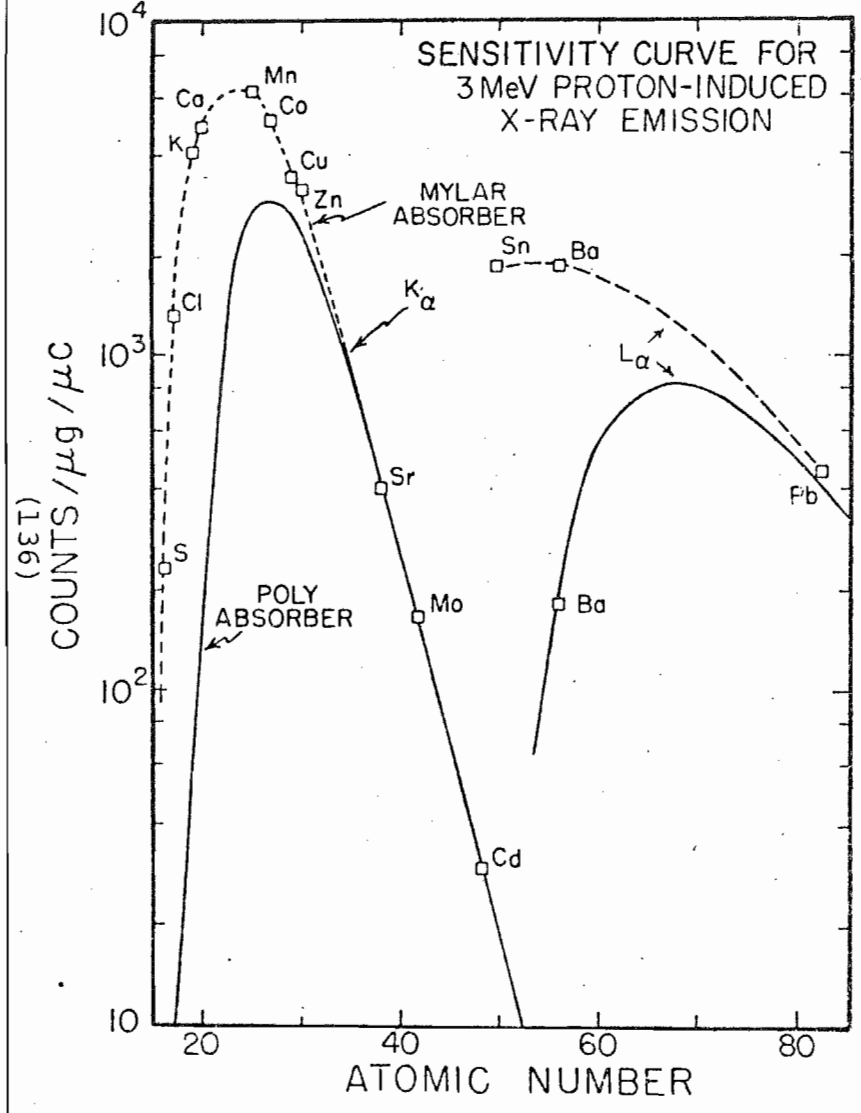
SENSITIVITY CURVE FOR
3 MeV PROTON-INDUCED
X-RAY EMISSION
COUNTS / μg / μC
(136)
ATOMIC NUMBER
MYLAR ABSORBER
POLY ABSORBER
Ca
K
Cl
S
Mn
Co
Cu
Zn
Sn
Ba
Sr
Mo
Cd
Pb
Kα
Lα
10⁴
10³
10²
10
20
40
60
80

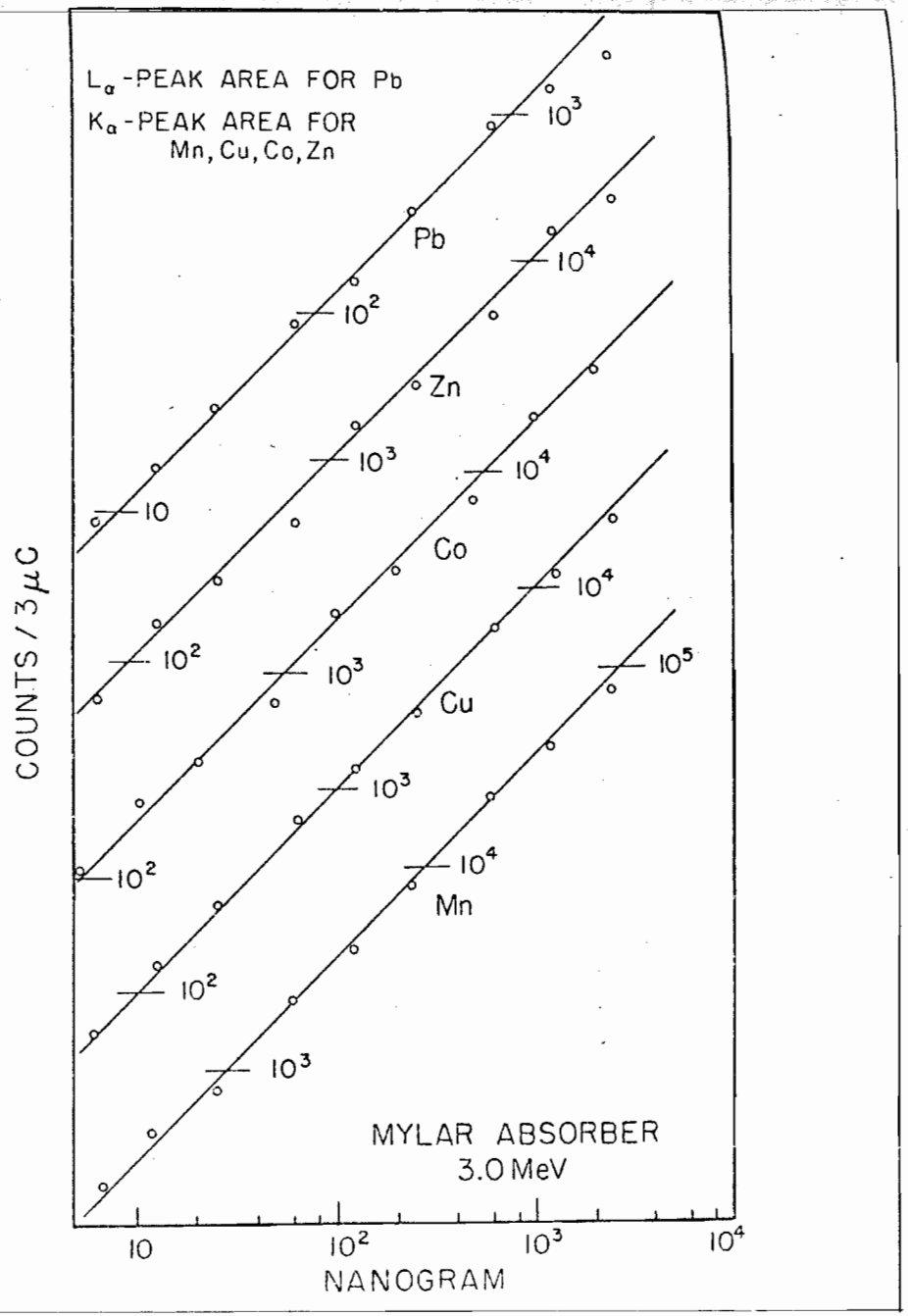
Lα-PEAK AREA FOR Pb
Kα-PEAK AREA FOR
Mn, Cu, Co, Zn
COUNTS / 3μC
NANOGRAM
MYLAR ABSORBER
3.0 MeV
Pb
Zn
Co
Cu
Mn
10
10²
10³
10⁴
10⁵

system is the linearity of the measured signal response over a mass range of several orders of magnitude. Standard point deposits ranging from 5 ng to 2 μg were prepared for selected elements and analyzed with the PIXE system. The results are displayed in Figure 3.13. Based on these results and results obtained later using higher concentrations, the system response was determined to be linear over a mass range of 5 ng to 40 μg for elements heavier than Ca.

The validity of the calibration (Figure 3.12) obtained from point-deposit standards depends in part on the homogeneity of the proton beam: a point deposit must give rise to the same number of detected X-rays (within statistical fluctuations) regardless of where in the beam the target is positioned as long as the deposit is fully enclosed by the proton beam. Beam uniformity is also required if the point-deposit calibration is to be valid for thin targets of the same size or larger than the beam spot. The use of a diffuser foil in combination with a series of collimators provides a beam spot which is sufficiently uniform in intensity for quantitative PIXE analysis (Figure 3.2 and Section IIIB.1).

The thin-target calibration in Figure 3.12 determines the absolute response of the system--i.e., the physical quantity which is immediately determined is the absolute mass of an element Z contained within the irradiated region of the sample. For certain types of analyses (analysis of

aerosol samples, for example), it is more convenient to calibrate the system in terms of the areal density (g/cm^2) of an element Z present in the sample. If the beam is homogeneous over its entire area, the point-deposit response curves (Figure 3.12) can be divided by the irradiated target area to yield the areal density calibration. Alternatively, one can calibrate the system directly in terms of areal densities by measuring elemental standards with known areal densities (Section IIIC.3).

Quantitative analysis of thin targets is carried out using Equation 3.1 with the appropriate values for f(Z) and Q inserted. Samples are routinely analyzed with the semi-automatic-computer code TRACE (Section IIID) which extracts X-ray peak areas N_Z (after subtracting the background level and correcting for interferences) and calculates elemental abundances using Equation 3.1.

IIIC.3 Uniform areal density standards

The fabrication of standards of uniform areal densities suitable for PIXE (and XRF) analysis has proven to be a difficult task (Stiles et al., 1976). Commercial efforts to produce such standards have until recently relied on two techniques--vacuum deposition on thin films (Micromatter Corporation, Seattle, Washington) and solution deposition on membrane filters (Columbia Scientific Industries, Austin,

Texas).

The cost of commercially available standards and their failure in some cases to provide sufficient reliability, led us to develop a simple and inexpensive technique for producing precision solution deposits. The technique is described in detail in articles by Baum et al. (1975, 1977). Briefly, the method consists of depositing a calibrated solution onto a membrane filter using the device shown in Figure 3.14a consisting of a matrix of precision capillaries. When dipped in a standard solution, the capillaries fill by capillary action. The device is then placed on the membrane filter (Type AAWP, Millipore Corporation, Bedford, Massachusetts) and the capillaries drain simultaneously. By design and by proper membrane choice, the volume deposited by each capillary and the spacing of the capillaries is such that the individual deposits barely overlap (Figure 3.14b)--nearly, but not quite saturating the membrane filter. It was found that by freeze-drying the wetted filters immediately after deposition, migration of the solution to the outer periphery during the drying process was eliminated, thus preventing the usual concentration build-up at the outer edges of the filters.

The uniformity of standards prepared in this way was determined by making a scan across the diameter of the filter with the proton beam and measuring the X-ray yield at each position. The results of such a scan for a strontium

Figure 3.14a Side view of the capillary depositer showing the 37 precision capillaries, the aluminum disc and silicone adhesive.

Figure 3.14b Illustration of the deposition pattern produced by the depositor. The volume deposited by each capillary and the spacing of the capillaries are such that, for the proper membrane, the individual deposits barely overlap.

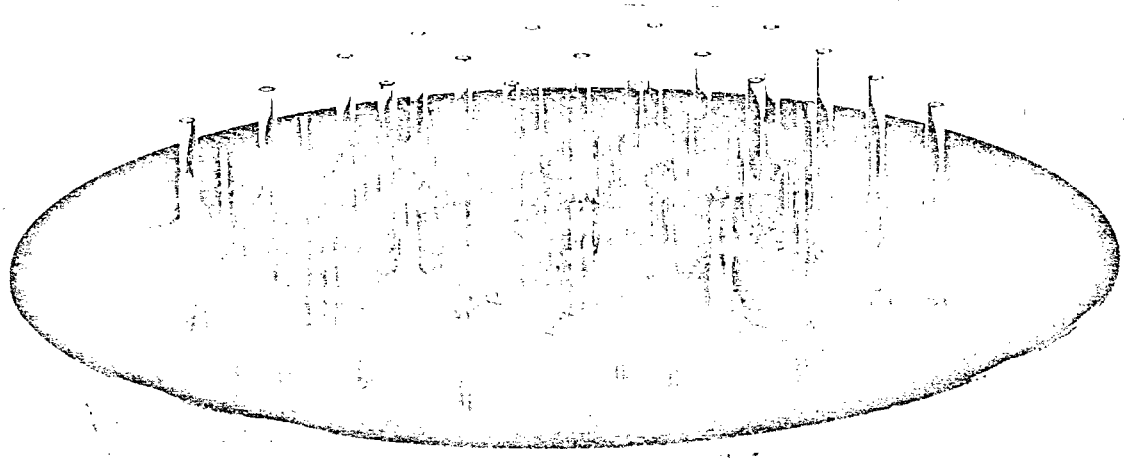

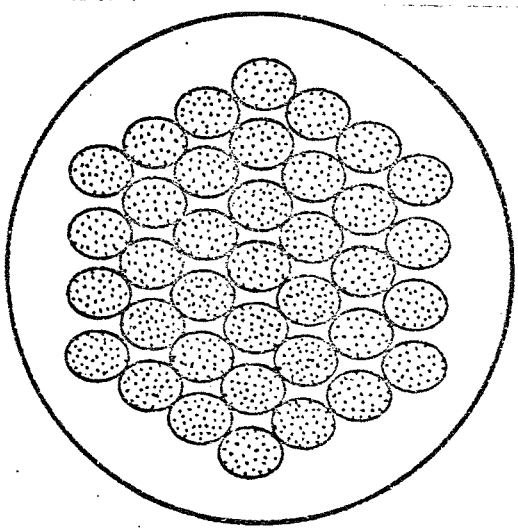

standard are shown in Figure 3.15, illustrating the high degree of uniformity ($\sim \pm$ 2%) achieved with this technique. The low values at the extreme positions of the scan indicate that the proton beam is partially off the edge of the standard.

The reproducibility of the standards was determined by measuring replicate filters with an independently calibrated XRF system. These results are shown in Table 3.1 under the heading "Liquid Deposits". The values labeled "Ratio I" represent the ratio of the areal density measured by XRF to the amount deposited. The various replicates shown no more than $\pm$1% deviation from the mean value of any of the metals.

An attempt was made to determine the accuracy the standards by comparing the XRF measurements on our deposits to XRF measurements made on vacuum-deposited standards (Micromatter). The Micromatter foils used for the comparison were previously scanned at our laboratory using PIXE and found to be quite uniform. The resulting XRF measurements are reported under the heading "Ratio II" in Table 3.1. The last column represents the ratio between Ratio's I and II and is therefore independent of the calibration of the XRF system. The results indicate agreement within 5% between the Duke standards and the Micromatter foils for the elements Ni, Cu, and Zn. The relatively large disparity found for Pb and Mn is not understood; however, the agreement between the expected concentrations of these elements and

Figure 3.15 Concentration profile of a solution-deposited standard exhibiting uniformity of ± 2% across the central region of the target. Low values at the extreme positions are due to partial irradiation with the proton beam.

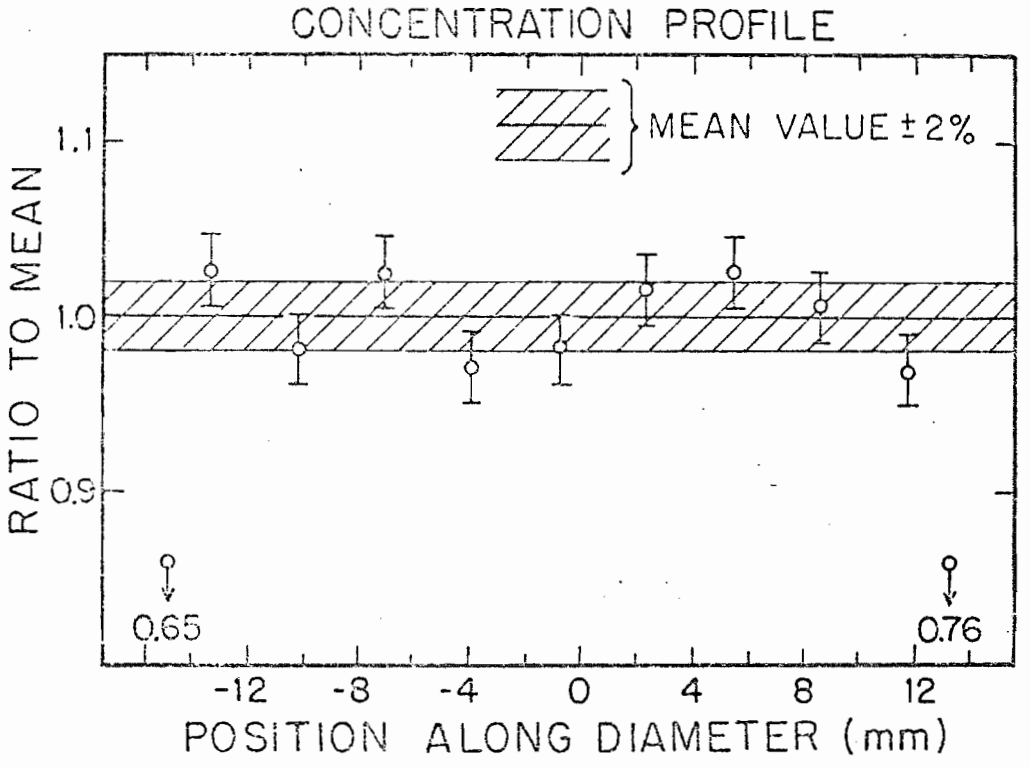
CONCENTRATION PROFILE
MEAN VALUE ± 2%
RATIO TO MEAN
1.1
1.0
0.9
0.65
0.76
-12
-8
-4
0
4
8
12
POSITION ALONG DIAMETER (mm)

Table 3.1

Results of Measurements of Replicates and Comparisons to Thin Film Standards

	Liquid Deposits		Micromatter Foils		
Element	Amount Deposited ($\mu g/cm^2$)	Ratio I	Amount by Weighing ($\mu g/cm^2$)	Ratio II	Ratio I Divided by Ratio II
Cu	11.15	1.05	85	1.03	
	11.15	1.07	104	1.02	
	11.15	1.08	128	1.00	
		<1.067>		<1.016>	1.050
Zn	11.33	1.10	125	1.14	
	11.33	1.11			
	11.33	1.11			
		<1.106>		<1.14 >	0.968
Ni	11.34	1.09	88	1.09	
	11.34	1.07			
	11.34	1.07			
		<1.076>		<1.09 >	0.986
Pb	11.33	1.01	133	0.839	
	11.33	0.99	126	0.838	
	11.33	0.98			
		<0.993>		<0.838>	1.184
Mn	11.27	1.01	66	1.146	
	11.27	1.03			
	11.27	1.01			
		<1.017>		<1.146>	0.888

Note: The symbol < > signifies the average ratio.

Reference: Baum et al. (1977).

the measured values for the Duke standards suggests that the problem lies in the vacuum-deposited standards.

The solution-deposition technique described above is a simple and inexpensive method for fabricating uniform, reproducible, calibrated standards which are suitable for both PIXE and XRF analysis. One disadvantage of these standards, particularly for use in PIXE systems, is that the thickness of the Millipore membrane filters ($\sim$ 4 mg/cm^2) requires that correction factors be applied to account for X-ray attenuation and proton energy loss effects. These effects are about 20% (assuming a carbon matrix) for elements heavier than Ti and significantly more for lighter elements (Figure 3.18).

Dzubay et al., (1977) have described a new type of uniform areal density standard which appears to be very promising for calibration of XRF and PIXE systems. The standard consists of a polymer film cast from a homogeneous solution containing known amounts of an organometallic compound and the polymer. This process permits a large quantity of the polymer film to be manufactured at one time. The accuracy of these standards is dependent on knowing (1) the fractional weight of the calibration element in the polymer film, and (2) the mass per unit area of the polymer standard. The latter quantity is easily determined by weighing a standard of known size on a microbalance; and the fractional weight

can be determined at the time of fabrication of the film (if organometallic compounds of known purity are used) or by an independent analytical procedure. The usefulness of this approach requires that the organometallic compound be distributed homogeneously through the polymer. A number of these polymer standards were scanned with the Duke PIXE system and the majority were found to be uniform to better than 2%. The polymer standards were also found to be stable in beam currents less than approximately 30 na for 3 MeV protons. The thickness of the polymer films ranged from 2-4 mg/cm^2 requiring that target-thickness corrections be applied (Section IIIC.4).

IIIC.4 Thick-target calibration

The PIXE system at Duke has been applied to a wide variety of sample types requiring the analysis of both thick and thin targets. While it is more difficult in general to obtain quantitative results on thick targets, the use of thick targets is advantageous for certain types of samples (Section IIIE.5). It is desirable therefore to calibrate the PIXE system for thick-target analyses as well as thin-target analyses.

If the target thickness is greater than approximately 1 mg/cm^2 then the effects of proton energy loss and X-ray absorption in the sample cannot be dismissed, and the correction factor $C(Z)$ in Equation 3.1 is greater than 1.

Figure 3.16 Schematic of a thick-target analysis illustrating the processes of proton energy loss and X-ray absorption which contribute to a reduced X-ray yield at the detector.

Schematic of Thick-Sample Irradiation

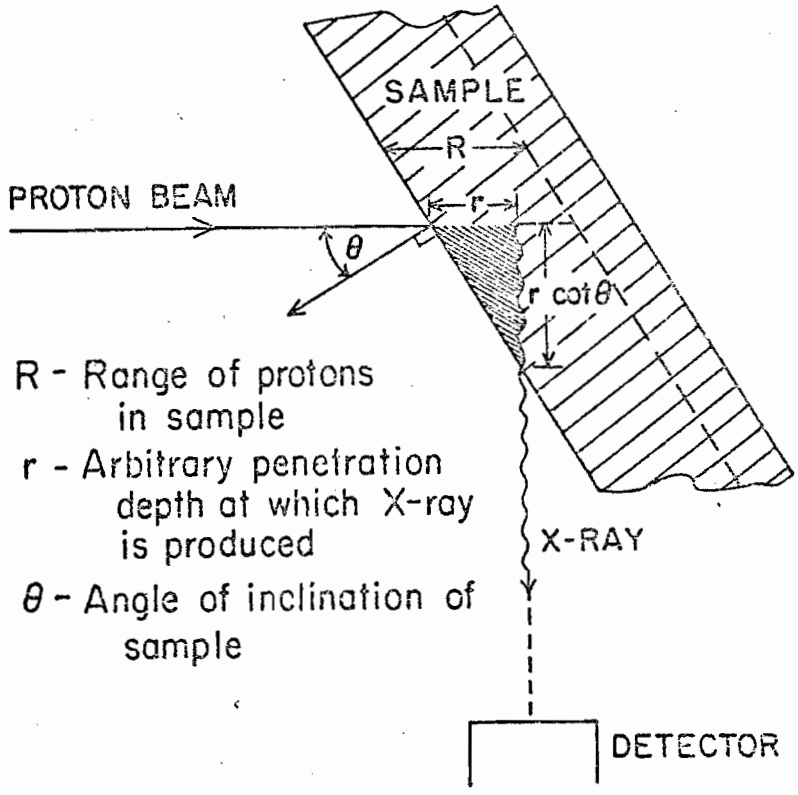

R - Range of protons in sample

r - Arbitrary penetration depth at which X-ray is produced

θ - Angle of inclination of sample

Figure 3.16 shows a schematic of a thick-target analysis indicating the two processes--proton energy loss and X-ray absorption--which contribute to a reduced X-ray yield. As the incident proton beam penetrates a thick target, it loses energy via collisions with atoms of the target matrix. This degradation in energy results in a decreasing probability for X-ray production as the penetration depth r increases. As an example, the stopping power for 3-MeV protons in a carbon matrix is about 110 keV/(mg/cm^2). In penetrating a depth of 2 mg/cm^2 in carbon, the proton beam loses approximately 10% of its original energy.

The resulting decrease in the detected X-ray yield is compounded by the attenuation of X-rays passing through the target in the direction of the detector. For samples in which the proton beam loses a significant fraction of its incident energy, the total expected X-ray yield must be obtained by integrating the product of the X-ray production and X-ray absorption over the penetration depth of the proton beam in the sample. The ratio of the X-ray yield N_o, calculated by assuming no proton energy loss or X-ray absorption effects (i.e., the thick target is treated as a thin target throughout), to the measured X-ray yield N is the correction factor C(Z) used in Equation 3.1. It is shown in Appendix A that

$$C(Z) = \sigma_Z(E_0) \cdot R \left[\int_{E_0}^{E_f} \frac{\sigma_Z(E) \cdot T_Z(E)}{S(E)} dE \right]^{-1} \qquad (3.2)$$

where: E_0 = incident proton energy (keV)

E_f = final proton energy (keV)

= 0 for infinitely thick samples

$\sigma_Z(E)$ = X-ray production cross section for element Z at proton energy E (cm^2/atom)

R = penetration depth of the proton beam in the sample (= T/cos θ for moderately thin samples, where T = target thickness and θ = angle between proton beam axis and the normal to the plane of the target).

= "Range" of protons for an infinitely thick sample (mg/cm^2)

$T_Z(E)$ = transmission factor for characteristic X-ray of element Z at depth r(E)

$$= \exp\left[-\int_{E_0}^{E} U_Z \frac{\cot \theta}{S(E)} dE \right]$$

U_Z = composite attenuation coefficient (cm^2/g) for characteristic X-rays of element Z in the target matrix:

$$= \sum_j \frac{\mu_{Zj} \, n_j}{M} A_j$$

where $\sum_j$ represents the sum over all major elements in the matrix, and

μ_{Zj} = attenuation coefficient (cm^2/g) for X-rays of element Z in matrix element j

n_j = number of atoms of element j per molecule of matrix

A_j = atom weight (amu) of element j

M = formula weight (amu) of the matrix

S(E) = composite stopping power of the matrix (keV cm^2/g)

$$= \sum_j \frac{n_j A_j S_j(E)}{M}$$

$S_j(E)$ = stopping power of matrix element j for protons of energy E (keV cm^2/g)

The thick-target calibration is obtained from Equation 3.1 with the calculated value of C(Z) inserted.

It is apparent from Equation 3.2 that the value of C(Z) depends upon the bulk chemical composition of the target being analyzed; each different sample type requires a different set of values for C(Z), and in order to determine the minor and trace constituents in a given specimen, the major composition of the sample must be known or estimated. Alternatively, the method of internal standards can be used in which known concentrations of selected elements are added to the sample thus providing an internal calibration which automatically provides correction for matrix effects. This technique is not however without problems as discussed in

section IIIC.5.

Program FUDGE, described in Appendix A, was written at this laboratory for calculating thick-target correction factors $C(Z)$ for 28 elements (22 K-line emitters and 6 L-line emitters) given the following input: (1) the bulk composition of the sample, (2) the incident proton energy, (3) the target angle, and (4) the target thickness (if not infinite).

Figures 3.17 and 3.18 show calculations of $C(Z)$ for carbon matrices of several different thickness. In Figure 3.17, the individual contributions to $C(Z)$ due to proton energy loss and X-ray absorption are shown for an infinitely thick carbon target. The curves for $C(Z)$ are observed to reach a minimum near $Z = 26$. The X-ray absorption effect dominates the total correction factor for very light elements ($Z \lesssim 20$), while for medium and heavy elements ($Z \gtrsim 30$), the proton energy loss term is most important. For a 1 mg/cm^2 carbon target rotated to an angle of 30°, the total correction factor is less than 10% for all $Z \geq 19$. Hence, 1 mg/cm^2 is considered to be approximately the upper limit for a thin target.

A useful quantity in thick-target analysis is the "effective mass" $\bar{M}(Z)$ of the target. The effective mass represents the amount of sample which would yield the observed number of X-rays if X-ray absorption and proton energy loss in the sample were negligible. With this approach one

Figure 3.17 Thick-target yield correction factors (solid curve) versus atomic number for an infinitely thick carbon matrix. Individual contributions due to proton energy loss (dashed curve) and X-ray absorption (dotted curve) are also indicated.

Figure 3.18 Thick-target yield correction factors versus atomic number for carbon matrices of varying thicknesses.

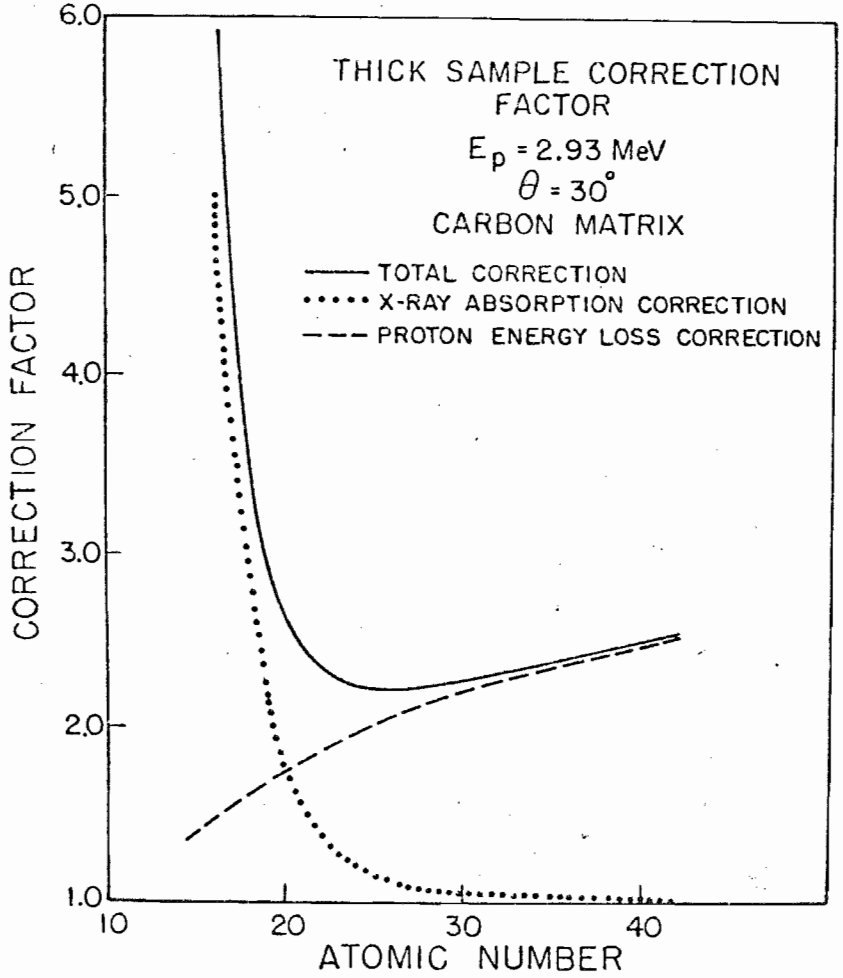
THICK SAMPLE CORRECTION FACTOR
E_p = 2.93 MeV
θ = 30°
CARBON MATRIX
TOTAL CORRECTION
X-RAY ABSORPTION CORRECTION
PROTON ENERGY LOSS CORRECTION
CORRECTION FACTOR
ATOMIC NUMBER
6.0
5.0
4.0
3.0
2.0
1.0
10
20
30
40

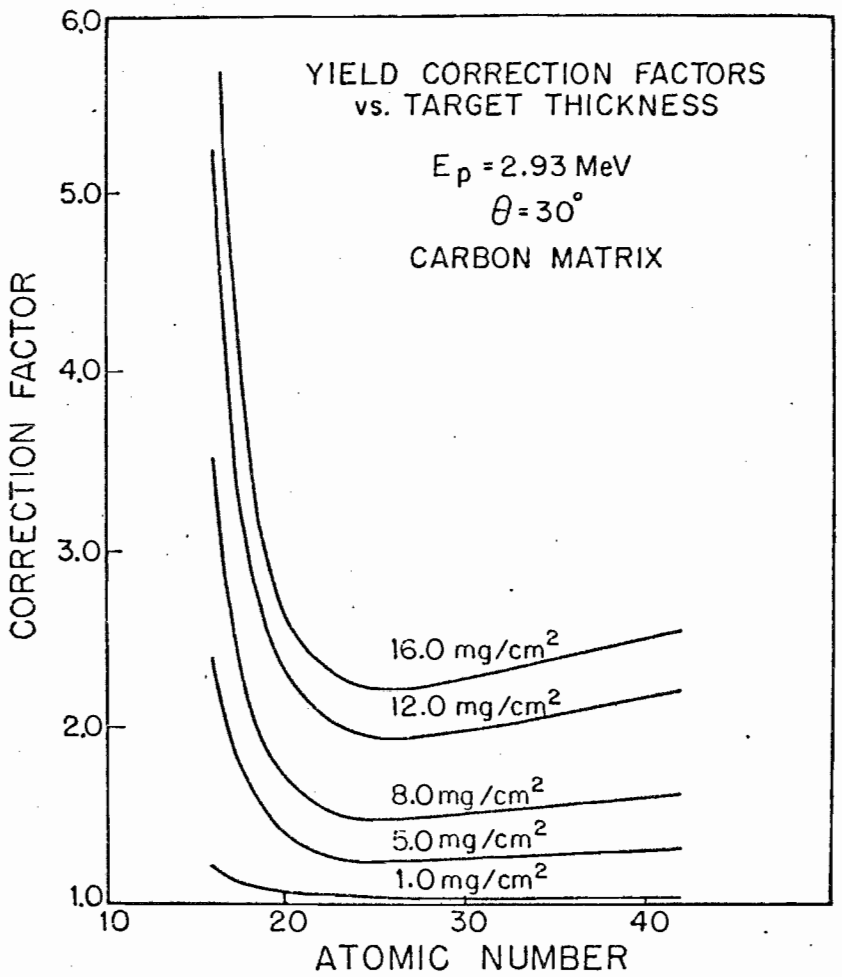
YIELD CORRECTION FACTORS vs. TARGET THICKNESS
E_p = 2.93 MeV
θ = 30°
CARBON MATRIX
16.0 mg/cm^2
12.0 mg/cm^2
8.0 mg/cm^2
5.0 mg/cm^2
1.0 mg/cm^2
CORRECTION FACTOR
ATOMIC NUMBER
6.0
5.0
4.0
3.0
2.0
1.0
10
20
30
40

Table 3.2

Thick target correction factors and effective masses for several common matrix compositions.[a)]

Element	Carbon		Polyethylene $(CH_2)_n$		Cellulose $(C_6H_{10}O_5)_n$		Dried Tissue	
	Correction Factor	Effective Mass	Correction Factor	Effective Mass	Correction Factor	Effective Mass	Correction Factor	Effec. Mass
S	5.94	1.03	4.26	1.13	8.66	0.66	7.86	0.80
Cl	4.42	1.39	3.35	1.44	6.23	0.91	7.24	0.87
K	3.01	2.04	2.53	1.91	3.83	1.48	4.34	1.46
Ca	2.69	2.28	2.36	2.05	3.26	1.74	4.10	1.54
Ti	2.38	2.58	2.20	2.19	2.68	2.12	3.14	2.01
V	2.32	2.65	2.17	2.22	2.54	2.24	2.89	2.18
Cr	2.28	2.69	2.17	2,23	2.45	2.32	2.72	2.32
Mn	2.27	2.71	2.17	2.22	2.39	2.38	2.61	2.42
Fe	2.27	2.71	2.19	2.21	2.36	2.41	2.54	2.49
Co	2.28	2.70	2.21	2.19	2.35	2.42	2.49	2.53
Ni	2.29	2.68	2.23	2.17	2.35	2.42	2.46	2.56
Cu	2.31	2.66	2.25	2.14	2.35	2.42	2.45	2.58
Zn	2.33	2.64	2.28	2.12	2.36	2.40	2.45	2.58
Ga	2.35	2.61	2.31	2.09	2.38	2.39	2.45	2.57
As	2.40	2.56	2.36	2.05	2.42	2.35	2.47	2.55
Se	2.43	2.53	2.39	2.02	2.44	2.33	2.49	2.54
Br	2.46	2.50	2.42	2.00	2.46	2.31	2.51	2.52
Rb	2.51	2.45	2.47	1.95	2.51	2.26	2.55	2.48
Sr	2.53	2.43	2.50	1.93	2.54	2.24	2.57	2.46
Y	2.56	2.40	2.52	1.91	2.56	2.22	2.59	2.43
Zr	2.59	2.38	2.55	1.89	2.59	2.20	2.61	2.41
Mo	2.64	2.33	2.60	1.86	2.64	2.16	2.66	2.37

Table 3.2 (continued)

Thick target correction factors and effective masses for several common matrix compositions.[a)]

Element	Carbon		Polyethylene $(CH_2)_n$		Cellulose $(C_6H_{10}O_5)_n$		Dried Tissue	
	Correction Factor	Effective Mass	Correction Factor	Effective Mass	Correction Factor	Effective Mass	Correction Factor	Effec. Mass
Ba	2.39	2.57	2.20	2.19	2.69	2.11	3.17	1.99
W	2.27	2.70	2.22	2.17	2.31	2.46	2.40	2.63
Au	2.33	2.64	2.29	2.11	2.35	2.42	2.41	2.61
Hg	2.34	2.62	2.30	2.10	2.36	2.41	2.42	2.61
Pb	2.37	2.60	2.33	2.08	2.38	2.38	2.44	2.59
Pb	2.35	2.61	2.32	2.08	2.36	2.41	2.40	2.63
Th	2.48	2.48	2.44	1.98	2.49	2.29	2.52	2.50

a) Incident proton energy = 3 MeV; target angle = 30°; cross-sectional area of proton beam = 0.4 cm^2.

can use the thin-target response curve to determine the concentration. That is, the concentration (ppm) of an element Z in the target is given by

$$PPM_Z = G_Z/\bar{M}(Z)$$

where G_Z is the abundance of element Z(g) determined from Equation 3.1 using the thin-target calibration (C(Z)=1). Values for $\bar{M}(Z)$ are calculated by program FUDGE according to the formula

$$\bar{M}(Z) = \frac{\text{irradiated sample mass}}{C(Z)} .$$

Values for C(Z) and $\bar{M}(Z)$ for our typical target angle of $\theta = 30°$ are listed in Table 3.2 for several common matrix compositions. For a given matrix, the effective mass shows a rather weak dependence on atomic number for $Z \gtrsim 20$. As indicated in Table 3.2, neglecting this Z dependence and using an average value of $\bar{M}(Z)$ for the elements from V to M_o will result in errors of no more than 7%. It is our common practice therefore to apply individual corrections to elements lighter than V and to apply a single, average correction factor to V and all heavier elements.

Numerous analyses have been conducted on calibrated thick targets in order to determine empirical values for the effective mass in a number of different biological specimens.

Pellets of Bovine Liver, Orchard Leaf and Coal, all Standard Reference Materials available from the National Bureau of Standards, have been analyzed, and the effective mass determined for each material knowing the expected concentrations for several elements. In addition, the effective mass was determined for pellets made from lyophilized placenta tissue which was doped with calibrated amounts of V, Ni, and Pb. The resulting values of the effective mass ranged between 2.2 and 2.8 mg (for a moderately heavy element such as Ni or Fe). Based on this range of values observed for the effective mass of biological samples, an average value of 2.5 mg for elements heavier than Ca has been adopted as being representative of most biological (carbon-based) samples. For Ca and lighter elements, the effective mass values should be determined for each value of Z and for the appropriate matrix. If a biological specimen can be approximated by either a carbon matrix or a cellulose matrix, then the use of 2.5 mg for the effective mass will approximate both the empirical and the calculated (Table 3.2) values to 15% or better.

The discussion to this point has emphasized targets which are infinitely thick. Target thicknesses greater than 1 mg/cm^2 and less than about 12 mg/cm^2 are not sufficient to completely stop a 3 MeV proton beam, but do require correction factors for proton energy loss and X-ray absorption. These correction factors can be calculated using program FUDGE

if the target thickness is known (or can be determined) and if the bulk composition of the sample can be reasonably approximated. Alternatively, one can use the technique of doping the sample with an internal reference standard as discussed in the next section.

IIIC.5 Additional calibration procedures

In order to provide independent checks on the system calibration described in the previous sections, it has been found useful to employ several additional calibration procedures. These are: (1) the addition of an internal reference standard to the sample, (2) the use of NBS Standard Reference Materials, and (3) interlaboratory comparisons.

1. Internal calibration

The addition of an internal reference standard to the sample is useful for thin targets in which the sample is spread over an area larger than the beam area, and for thick targets of unknown thickness or composition for which the matrix effects cannot be adequately determined by FUDGE. The technique calls for adding a known concentration of the dopant element (C_D) to the sample being analyzed. The unknown concentration of an element of interest (C_U) is then simply determined by

$$\frac{C_U}{C_D} = \frac{N_U}{N_D}\frac{f_D}{f_U} \quad \text{(thin targets)}$$

$$\frac{C_U}{C_D} = \frac{N_U}{N_D}\frac{f_D}{f_U}\frac{\bar{M}_D}{\bar{M}_U} \quad \text{(thick targets)} \qquad (3.3)$$

where: N_U = measured X-ray yield of the element of interests (counts)

N_D = measured X-ray yield of the dopant (counts)

f_D, f_U = thin-target response factor for the dopant and element of interest respectively (counts/$\mu g \cdot \mu C$)

$\bar{M}_D, \bar{M}_U$ = effective target mass for the dopant and for the element of interest respectively (g).

An approximate determination of C_U for thick samples is possible only if the ratio $\bar{M}_D/\bar{M}_U \simeq 1$, i.e.--if matrix effects are the same for the dopant element and the element of interest. This approximation will be satisfied if the dopant element and the element of interest are close neighbors on the periodic table.

The internal doping procedure has the virtue that any systematic errors in the calibration or in the data collection process which affect the dopant and the element of interest by the same amount (e.g., improper determination of integrated beam charge) are effectively cancelled out in Equation 3.3. The doping procedure is not without serious drawbacks however: the dopant must be accurately calibrated by an independent method and free of contaminants; it must

not cause precipitation of any elements in the sample nor be subject to loss by adsorption on the walls of the vessel; the dopant must be distributed uniformly throughout the sample; the X-ray spectrum of the dopant element must not interfere with X-ray lines from the sample--this is made difficult by the fact that possible interelement interferences between a dopant element and elements present in an unknown sample cannot be anticipated; finally, the validity of the internal standard technique for thick samples require that the dopant and the element of interest have similar atomic numbers--i.e., if a broad range of elements are of interest, several dopants should ideally be added to the sample.

In our laboratory, we have employed the doping procedure for wet-ashed samples of bovine liver and for thick pellets pressed from lyophilized placenta tissue. The latter specimen was doped in two different experiments with (1) 40 ppm V, 40 ppm Ni, and 200 ppm Pb, and (2) 30 ppm V, and 28 ppm Ni. The internal standards used for the doping were nickel cyclohexane butyrate and bis (1-phenyl-1,3,butanedions) oxovanadium (IV). These organometallics were dissolved in chloroform and approximately 1 ml of the dopant solution was added to 500 mg of lyophilized placenta tissue. This slurry is well mixed and the chloroform solvent is then removed by evaporation. Figure 3.19 is the resulting PIXE spectrum obtained from a placenta pellet doped with V, Ni, and Pb.

Figure 3.19 PIXE spectrum from analysis of a placenta pellet. The lyophilized placenta was doped with 40 ppm V, 40 ppm Ni, and 200 ppm Pb prior to pelletizing.

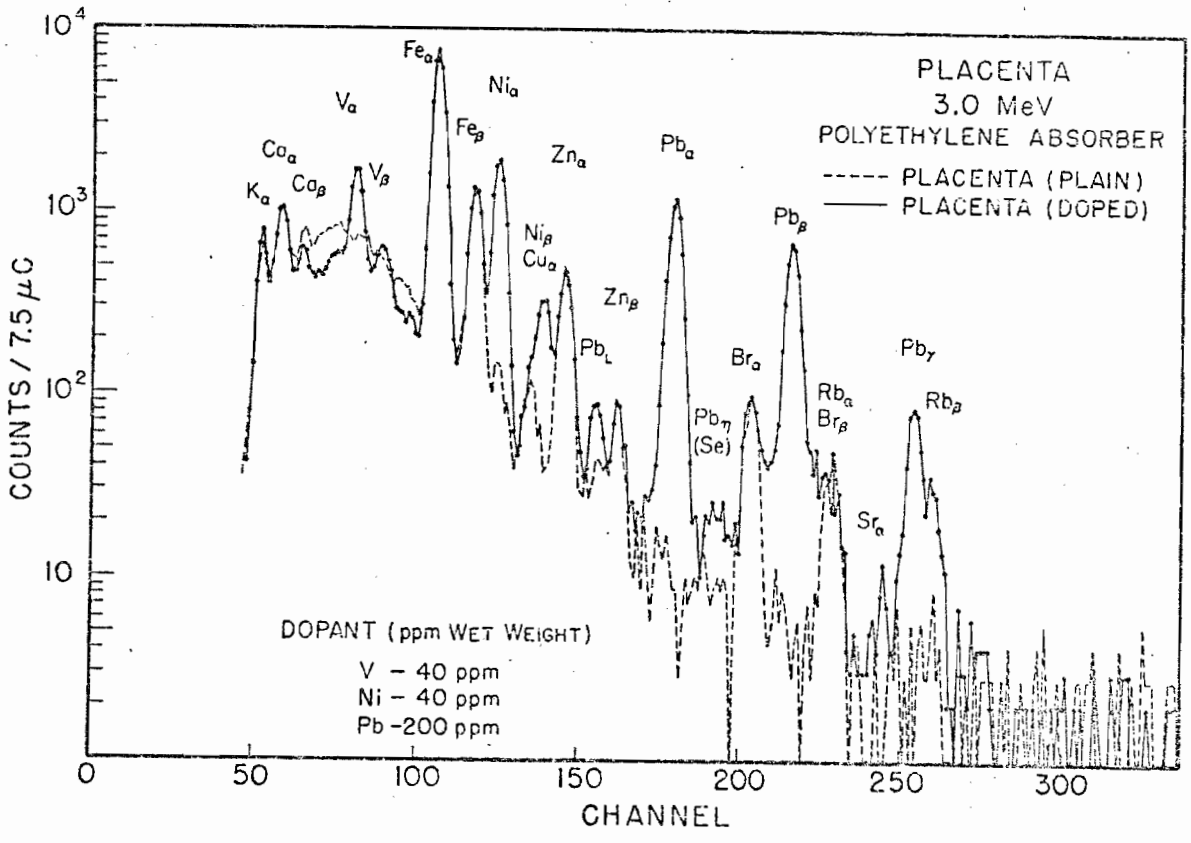
PLACENTA
3.0 MeV
POLYETHYLENE ABSORBER
----- PLACENTA (PLAIN)
—— PLACENTA (DOPED)
DOPANT (ppm WET WEIGHT)
V – 40 ppm
Ni – 40 ppm
Pb –200 ppm
COUNTS / 7.5 μC
CHANNEL
Ka
Caα
Caβ
Vα
Vβ
Feα
Feβ
Niα
Niβ
Cuα
Znα
Znβ
PbL
Pbη (Se)
Pbα
Brα
Pbβ
Rbα
Brβ
Srα
Pbγ
Rbβ

Table 3.3

Elemental Abundances in Placenta Tissue

ELEMENT	PPM(dry weight)[a]	DETECTION LIMIT(ppm)	STD. DEV.[b]
K	11,930	190	390
Ca	640	30	52
Ti	13.7	6.5	5.0
V	5.1	4.5	2.0[c]
Cr	ND[d]	2.9	
Mn	ND	1.8	
Fe	690	1.3	7.6
Ni	ND	1.0	
Cu	8.3	0.9	0.9
Zn	58	0.8	1.5
Ga	ND	0.8	
As	ND	0.8	
Se	1.6	0.8	0.35
Br	39	0.9	3.7
Rb	17	1.2	3.4
Sr	ND	1.4	
Zr	ND	1.8	
Pb	ND	2.9	

a) Based on effective mass values calculated for thick C matrix.

b) Based on 6 measurements unless otherwise noted

c) Based on 3 measurements

d) Not detected.

Concentrations on upper limits for 18 elements in placenta tissue are tabulated in Table 3.3, based on internal calibration with V and Ni dopants. The average effective masses determined from measurements on 3 doped pellets were 2.83 mg and 2.67 mg for V and Ni respectively, in good agreement with the average value of 2.5 mg assumed for biological samples.

2. Standard Reference Materials

The National Bureau of Standards makes available a number of Standard Reference Materials (SRM's) suitable for providing calibrations for analytical systems. The concentrations of the major and minor elemental constituents of these reference materials are certified by the NBS based on determinations by at least two independent analytical methods. Reference materials which are particularly useful in calibrating systems applied to the analysis of environmental and biological samples include rock, orchard leaf (SRM 1571), and bovine liver (SRM 1577). The NBS also provides SRM's related to pollution monitoring: fuel oil, fly ash (SRM 1633), and coal (SRM 1632).

The SRM's which we have found most useful for providing a check on the system's calibration are the coal, orchard leaf, and bovine liver samples. PIXE analyses of these standards will be compared in the following tables to certified

values provided by the NBS. The fuel oil and fly ash and also a gasoline sample obtained from the NBS all presented problems in terms of preparing suitable targets for PIXE analysis. This limited the usefulness of these materials as standards; for completeness, our analyses of these SRM's are included in Section IVA.

NBS coal, orchard leaf, and bovine liver are available in the form of finely ground, homogeneous powders which are particularly suitable for making thick pellets. (Section IIIE.2). In addition, we have had some success in preparing thin targets of these SRM's using low temperature wet-ashing techniques. For each of the three SRM's, the NBS specifies a minimum sample size of 250 mg as constituting a representative sample (due to granularities and inhomogeneities in the sample material). Since the 3 MeV proton beam at Duke effectively samples only about 3 mg of a thick pellet, some variability due to unrepresentative sampling is anticipated in results obtained from pellets. Targets prepared from ashed residues on the other hand generally constitute more representative samples. A more detailed discussion of the various sample preparation techniques which have been used at Duke and their relative merits is provided in Section IIIE.

Table 3.4 shows results obtained on pelletized and ashed samples of coal. The PIXE values have been normalized to the Fe concentration (8700 ppm) reported by the NBS. The

Table 3.4

EPA-NBS COAL ANALYSES

Element	Pellet ppm (d.l.)	Ashed ppm (d.l.)	NBS ppm ± Δppm	Other labs avg. ppm
K	4500 (60)	2100 (60)		2800 ± 300
Ca	3900 (40)	3000 (40)		4300 ± 500
Ti	1250 (15)	640 (12)		1100 ± 100
V	(35) (10)	(43) (7)	35 ± 3	
Cr	18 (5)	12 (5)	20 ± 0.5	
Mn	56 (4)	52 (4)	40 ± 3	
Fe	(8700) (3)	(8700) (3)	(8700) ± 300	
Ni	21 (2)	13 (2)	15 ± 1	
Cu	19 (2)	18 (1.4)	18 ± 2	
Zn	43 (2)		37 ± 4	
Ga	8 (1.5)	6 (1.3)		
As	3.3 (1.2)	6 (1.1)	5.9 ± 0.6	
Se	4 (1.2)	2.2 (1.0)	2.9 ± 0.3	
Br	26 (1.4)	0.2 (1.0)		19 ± 2
Rb	31 (1.2)	18 (1.2)		21 ± 2
Sr	175 (3)	135 (1.5)		161 ± 16
Y		7 (2)		
Zr	22 (4)	24 (2)		
Mo	9 (6)	1.2 (3)		
Hg	2 (5)		0.12 ± 0.02	
Pb	20 (5)	37 (4)	30 ± 9	

numbers in parentheses following the Duke measured values represent the detection limits determined according to the three sigma (3σ) criterion. The agreement between the Duke PIXE values and the values reported by the NBS and other labs is reasonable for most elements considering the inhomogeneities of the sample. Based on the normalization to the Fe concentration, the effective irradiated mass for the thick coal pellets was approximately 2.2-2.3 mg. The ashed samples were prepared from an original sample mass of 12.5 mg by digesting the sample in an acid solution, taking the mixture to dryness over low temperatures and dissolving the ashed residue in 1 mℓ of an acid solution. Aliquots of 20-60 μℓ of this resulting solution were deposited onto thin mylar or nuclepore substrates in an area smaller than the beam spot. No corrections for target thickness effects were applied to the ppm values reported for the ashed samples, but the low values observed for K and Ca suggest that X-ray absorption and proton energy loss effects in the ashed samples may be significant. The low values for Ti, Cr, and Br in the ashed samples may indicate the loss of these metals during the ashing process (this was expected for the Br value). The high values for Mn reproduced in both the pellets and ashed samples is due to the low energy tail on the large Fe K_α signal (6.4 keV) which contributes counts in the region of Mn K_α (5.9 keV). No correction has been made for this effect

which enhances the Mn signal by approximately 0.3% of the Fe K_α signal.

Data was recently collected on five NBS orchard leaf pellets and the results are tabulated in Table 3.5. Each pellet was irradiated in two positions and the results in Table 3.5 represent the mean values of the ten analyses with the standard deviations given in parentheses. The measured abundances were converted to the corresponding ppm concentrations by assuming the effective mass values for an infinitely thick carbon matrix calculated by FUDGE (Table 3.2). The agreement between our measurements and the NBS certified values is excellent with the exception of Ca which indicates that our calibration curve may not be correct for this element.

Similar data has been obtained on five bovine liver pellets. The data was part of a study comparing thick-target analyses and thin-target analyses in terms of sensitivity, accuracy and precision, and ease of sample preparation (Willis et al., 1977a). Thin targets of bovine liver were prepared by ashing a representative sample of bovine liver (> 250 mg) and depositing approximately 40 μℓ of the ashed solution onto nuclepore substrates. Elemental abundances for the ashed samples were determined by normalizing the data to a known amount of Sr dopant added to the ashing solution. The elemental concentrations for the pellets were determined using the effective mass values calculated by FUDGE for an

Table 3.5

Elemental Abundances in NBS Orchard Leaf (SRM 1571)

Element	DUKE[a] ppm(± std. dev.)	NBS[b] ppm ± Δppm
K	16,800(1700)	14,700 ± 300
Ca	15,000(1200)	20,900 ± 300
Cr	<5	(2.3)
Mn	91(4)	91 ± 4
Fe	301(22)	300 ± 20
Ni	1.3(0.4)	1.3 ± 0.2
Cu	14(2)	12 ± 1
Zn	25(1.2)	25 ± 3
As	14.6(3)	10 ± 2
Se	<1	0.08 ± .01
Br	11.6(1.6)	(10)
Rb	11.1(1.4)	12 ± 1
Sr	34(4)	(37)
Pb	42(6)	45 ± 3

a) Duke values are based on measurements of 10 pellets. Effective mass values for an infinitely thick carbon matrix are assumed.

b) NBS values in parentheses are not certified.

Table 3.6

Elemental Abundances in NBS Bovine Liver (SRM 1577)

Element	DUKE Pellets[a] ppm(± std. dev.)	DUKE Ashed[b] ppm(± std. dev.)	NBS ppm ± Δppm
K	9400(800)	---	9700 ± 600
Mn	9.2(1.8)	9.0(2.2)	10.3 ± 1
Fe	273(8.5	293(21)	270 ± 20
Cu	186(5.5)	194(13)	193 ± 10
Zn	132(3.3)	144(12)	130 ± 10
As	0.6(0.5)	0.2(0.3)	(0.055)
Se	1.4(0.5)	0	1.1 ± 0.1
Br	9.5(1.0)	0	---
Rb	16.8(1.9)	20.9(2.5)	18.3 ± 1.0

a) Based on 9 measurements.

b) Based on 8 measurements.

infinitely thick carbon matrix. Vaporization of the pellet matrix due to beam heating resulted in significantly higher effective mass values than calculated by FUDGE. The data for the pellets was corrected for vaporization of organic matter due to beam heating by scaling all effective mass values upwards by the same factor that was needed to provide agreement between the Duke measurements for the Fe concentration and the NBS value.

The results of our analyses are shown in Table 3.6 for nine elements between K and Rb. The agreement of both sets of data with NBS values for elements present in abundances greater than 10 ppm is within 14% or better. Note that the elements Se and Br are not present in the ashed samples; these are presumably volatilized during the wet ashing process.

In summary, NBS Standard Reference Materials provide a convenient check on the calibration of the PIXE system. In working with well-characterized sample materials, much valuable information has been learned about the benefits and handicaps of various target preparation techniques; the analysis of SRM's has helped locate some of the difficulties associated with the computer analysis of complex spectra and has led to a more careful treatment of the fitting procedure and the assignment of detection limits; finally, SRM's serve as an accurate check on proton energy loss and X-ray absorp-

tion calculations provided by FUDGE.

3. Interlaboratory comparisons

During the early stages of PIXE development at Duke, two interlaboratory comparisons took place sponsored jointly by Lawrence Livermore Laboratories and Columbia Scientific Industries. The second camparison, completed in 1974 (Camp et. al., 1975), involved the participation of 22 laboratories representing six different analytic techniques. The primary objective of the sponsors of the intercomparison was to evaluate the precision and accuracy of X-ray spectrometric techniques and to offer some comparison to other accepted methods. Each participating laboratory benefited from the intercomparison by learning how its results compared on an absolute basis with the known values, and how the laboratory fared in the intercomparison relative to other laboratories using the same or different analytical techniques.

Three types of samples were sent to each laboratory for analysis. Sample A was a dried solution deposit on a 47 mm diameter Millipore filter. The solution contained 10 elements (Al, S, K, V, Cr, Mn, Fe, Zn, Cd, Au) in concentrations ranging from 1 to 100 $\mu g/cm^2$. (The information provided to the participating laboratories included the elements present in each sample but not the concentrations.) Sample B was a standard rock specimen, ground to a fine powder to

simulate naturally occurring particulates, and deposited homogeneously on a Millipore filter using the puff technique. In order to prevent sample losses during shipping and handling, the filter was coated with a thin layer of paraffin in benzene. The average particle size was less than 5 microns and the loading was about 300 $\mu g/cm^2$. Sample C was a natural aerosol sample collected by the EPA from the stack of a fossil-fueled power plant. The filter media was Millipore reenforced with a nylon mesh which unfortunately contained considerable amounts of Ti.

Each sample was scanned with our proton beam in three to six positions across the diameter and the average values were reported. Table 3.7 presents the results obtained from a six-position scan of sample A which was prepared using a multi-drop technique and which was supposedly uniform. Variations of 5-10% about the mean were observed for most of the elements measured indicating that some non-uniformities did exist. Variations of similar size could therefore be expected in results obtained from those methods which utilized only a small sample area for the measurements.

Six analytical techniques were represented among the 22 participating laboratories. These were: energy dispersive X-ray fluorescence (XRF-ENERGY), wavelength dispersive X-ray fluorescence (XRF-λ), PIXE, atomic absorption (AA), emission spectroscopy (ES) and neutron activation analysis (NAA). The measurements reported by each laboratory for sample A were

Table 3.7

Rapid scan of "uniformly deposited" interlaboratory comparison specimen. Values are in $\mu g/cm^2$.

	Position					
Element	A	B	C	D	E	F
V	4.95	5.84	5.43	5.5	5.17	4.80
Cr	7.05	8.23	7.76	7.44	7.20	6.73
Mn	3.88	4.62	4.34	4.17	4.33	4.15
Fe	19.3	22.0	21.2	20.6	19.5	18.4
Zn	1.51	1.63	1.66	1.65	1.55	1.71
Au	3.46	3.32	3.26	3.38	4.18	3.12
Cd	35.5	39.3	39.2	38.8	39.1	38.9

divided by the overall average and these normalized results are summarized in Figure 3.20. Each laboratory is represented by a clusterof data points grouped between the short vertical bars located along the horizontal axis. Elemental concentrations reported by each laboratory are shown by the data points within each cluster in order of increasing atomic number. Each data point represents the average of measurements carried out on two replicate samples. Gaps within a cluster correspond to elements which were not measured because of inadequate calibration, absorption problems, etc. The error bars attached to the data represent the root mean square value of the difference between the pair of replicate results and the investigator's quoted error on that pair.

The results of the analysis of sample A (Figure 3.20) are in general quite good in view of the target non-uniformities previously discussed. The dopant elements spanned most of the periodic table and were selected in part to evaluate the abilities of the X-ray techniques to make accurate absorption corrections and to unfold interelement interferences. The Duke measurements in Figure 3.20 are shown in the sixth cluster from the left in the PIXE category. We did not report measurements for Al (too low in energy to be detected) or S (uncertain calibration), but the remaining measurements with the exception of K were within 12% of the expected values. The high K value apparently reflects the fact that one of the two replicates we analyzed contained an abnormally

Figure 3.20 Results from interlaboratory comparison of a multielement standard. Duke measurements for eight elements are shown in the sixth cluster of points in the PIXE category. See text for discussion of the results.

Figure 3.21 PIXE spectrum from analysis of micronized rock sample.

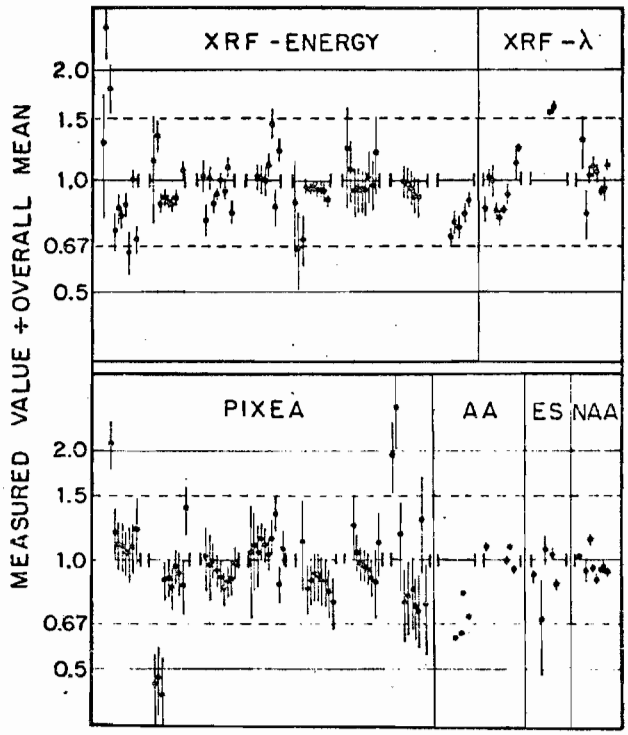
XRF - ENERGY
XRF - λ
PIXEA
AA
ES
NAA
MEASURED VALUE + OVERALL MEAN
2.0
1.5
1.0
0.67
0.5

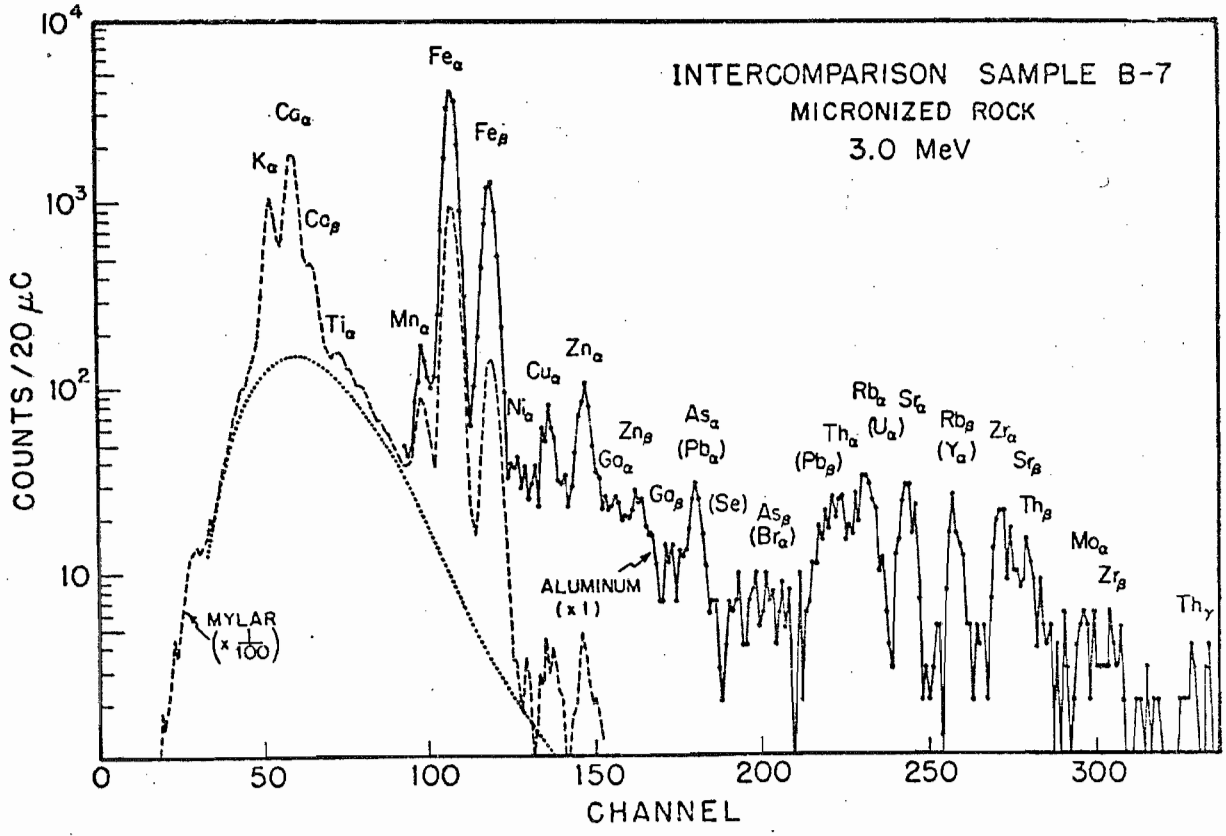
INTERCOMPARISON SAMPLE B-7
MICRONIZED ROCK
3.0 MeV
COUNTS / 20 μC
CHANNEL
Ca_α
K_α
Ca_β
Ti_α
Fe_α
Fe_β
Mn_α
Cu_α
Ni_α
Zn_α
Zn_β
Ga_α
Ga_β
As_α (Pb_α)
(Se)
As_β (Br_α)
(Pb_β)
Th_α
Rb_α (U_α)
Sr_α
Rb_β (Y_α)
Zr_α
Sr_β
Th_β
Mo_α
Zr_β
Th_γ
ALUMINUM (x 1)
MYLAR (x 1/100)

Table 3.8

Results of interlaboratory comparison for micronized rock.
Values are reported in per cent by weight.

Element	Duke	Mean	Element	Duke	Mean
K	4.0 ± 0.6	3.5	V	<0.013	0.003
Ca	4.4 ± 0.6	6.9	Cr	<0.010	0.002
Ti	0.06 ± 0.01	0.06	Ba	<0.040	0.043
Mn	0.18 ± 0.02	0.17	Br	<0.001	NA
Fe	3.3 ± 0.5	3.4	Mo	<0.001	NA
Ni	0.003 ± 0.001	0.002	Hg	<0.004	NA
Zn	0.022 ± 0.006	0.020	Cu	0.012 ± 0.003	NA
Ga	0.002 ± 0.001	0.003	As	0.002 ± 0.002	NA
Sr	0.020 ± 0.003	0.027	Se	0.001 ± 0.001	NA
Y	0.006 ± 0.002	0.016	Rb	0.025 ± 0.003	NA
Zr	0.017 ± 0.003	0.028			
Pb	0.015 ± 0.003	0.006			
Th	0.021 ± 0.002	0.026			

(1SO)

NA = Not available because too few laboratories reporting data

high concentration relative to the other filter. A measure of the consistency obtained by the Duke PIXE system is given by the relative standard deviation of the normalized data. This is 9% excluding the K data.

The micronized rock sample--sample B--yielded a very complex spectrum as shown in Figure 3.21. Twenty-eight elements are listed as present in this standard material, and we were able to determine abundances or upper limits for 23 of the elements. These are reported in Table 3.8 and compared to the mean values as determined from all laboratories. The agreement with the available mean values is quite good considering again the sample inhomogeneities.

Sample C proved difficult to analyze because of gross non-uniformities in the sample and because of an enormous Ti background. Our results averaged about 60% below the mean values reported by other laboratories. Possible explanations for this discrepancy are that the filter was improperly loaded or that the particulate matter was so deeply embedded in the 5 mg/cm^2 membrane that the target-thickness correction factors which we took to be negligible were in fact abnormally large. The standard deviation of the normalized data for all labs was in general considerably greater than that observed for either samples A or B suggesting that considerable differences in elemental concentrations may have existed among the type C samples analyzed by the different laboratories.

In conclusion, with the exception of sample C, the intercomparison provided gratifying confirmation of our ability to analyze complex samples with good accuracy and precision for $Z > 20$. Agreement was to within 12% of the expected values for nearly all of the elements analyzed in samples A and B, despite significant sample non-uniformities.

IIID. Data Analysis: Program TRACE

The PIXE system at Duke is capable of collecting data at an average rate of approximately one spectrum every five minutes. During one eight hour run, nearly 100 spectra can be collected. If each spectrum is to be analyzed for 15 elemental abundances, then a single day of analysis easily generates 1500 abundances which must be accurately determined. In order to take full advantage of the rapid, multielemental capabilities of PIXE, one must have access to a computer code capable of analyzing X-ray spectra rapidly and accurately, with a minimum amount of operator input.

The following paragraphs describe the spectrum-analysis program TRACE (Willis et al., 1976, 1977b) designed several years ago specifically for off-line analysis of data generated with the PIXE system at Duke. TRACE is a versatile, least-squares fitting program which features Gaussian line shape fits to spectral peaks, background fitting by means of an exponential function, and a routine for minimization

of χ^2 which combines a gradient search method with linearization of the fitting function. TRACE is currently capable of providing fits for 10-20 elements in one to two minutes.

IIID.1 Data collection, PIXE spectra, and system calibration

Data is stored as described in Section IIIB.3 into 384 discrete-energy channels of an analog-to-digital converter (ADC). An on-line program permits individual peak areas to be determined after subtracting a linear background. At the completion of a PIXE analysis, the spectrum is transferred to magnetic tape for off-line analysis with TRACE at a later time.

The crab muscle spectrum of Figure 2.1 is reproduced in Figure 3.22 illustrating the dominant features of PIXE spectra. These include: (1) a broad and smoothly varying background caused primarily from bremsstrahlung and Compton scattering processes (Section IIE); (2) multiple characteristic X-ray lines identifying elements present in the sample, and (3) interferences between X-ray lines of different elements.

Samples of interest to the PIXE analyst frequently generate X-ray line spectra for twenty or more elements simultaneously, giving rise to complex spectra containing more than thirty X-ray lines and complicated by multiple interferences. Interelement interferences can occur either as an interference

Figure 3.22 Typical PIXE spectrum for 3.0 MeV protons obtained on a biological sample with a Si(Li) detector. Items 1-3 represent features of interest described in text. Note the vertical scale is a log scale.

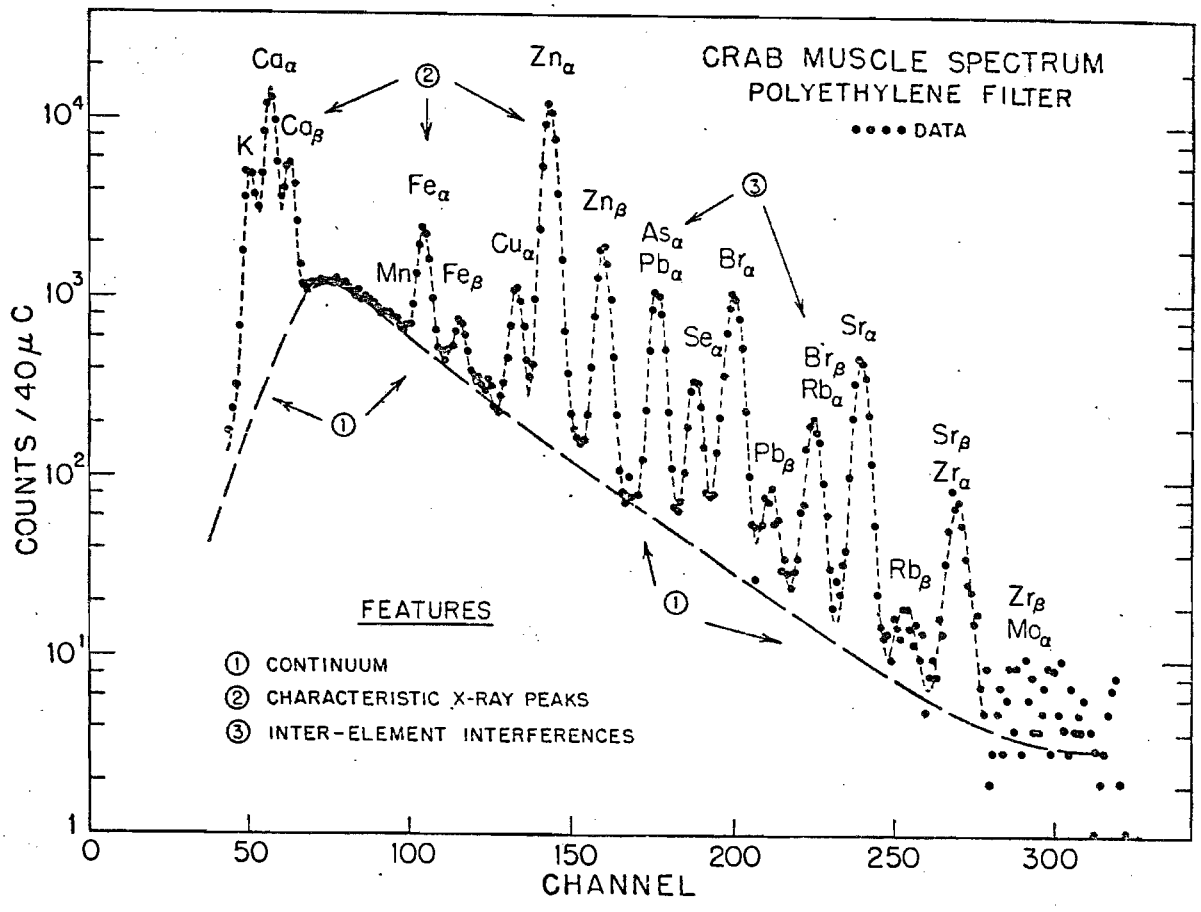
CRAB MUSCLE SPECTRUM
POLYETHYLENE FILTER
DATA
COUNTS / 40 μC
CHANNEL
FEATURES
① CONTINUUM
② CHARACTERISTIC X-RAY PEAKS
③ INTER-ELEMENT INTERFERENCES
Ca$_\alpha$
Ca$_\beta$
K
Fe$_\alpha$
Zn$_\alpha$
Zn$_\beta$
Mn
Fe$_\beta$
Cu$_\alpha$
As$_\alpha$
Pb$_\alpha$
Br$_\alpha$
Se$_\alpha$
Sr$_\alpha$
Br$_\beta$
Rb$_\alpha$
Pb$_\beta$
Sr$_\beta$
Zr$_\alpha$
Rb$_\beta$
Zr$_\beta$
Mo$_\alpha$

between the K_β signal from element Z and the K_α signal from element (Z+1) or (Z+2), or as an interference between a particular K-line of a low or medium Z element with an L-line of a high Z element. Commonly encountered interference include the Pb L_α - As K_α interference and the Br K_β - Rb K_α interference (see Figure 3.22). Fortunately, only a few of the combinations of elements which have potential interferences are found naturally in sufficient concentrations to be of concern. Accurate unfolding of these interelement interferences is a required feature in any spectrum analysis program and demands that the K-line and L-line intensity ratios be well determined.

Calibration of the Duke PIXE system (in terms of X-ray counts of a given element per mass of element present and for a specified amount of proton charge) is accomplished by means of carefully prepared chemical standards deposited on thin Nuclepore membranes and analyzed with the PIXE system maintaining fixed target-detector geometry and a beam energy of 3.0 MeV (Section IIIC).

Experimental detection efficiencies for each absorbing filter were obtained in this way for approximately 17 elements spanning the elemental region of good sensitivity. The efficiency tables used in TRACE to convert X-ray counts into elemental abundances were generated from a least-squares fit to the experimental values. The X-ray efficiency for

each element (and a given absorber) was extracted from the peak area of the reference line for that element. For all elements of interest, with the exception of Pb, the dominant X-ray line (K_α or L_α) is chosen as the reference line. The Pb L_β line was selected as the reference line for Pb because it is free of interference from other X-ray lines. In addition the spectral lines from these calibrated standards were fitted with single Gaussian line shapes in order to obtain the K_α: K_β and L_α: L_β: L_γ intensity ratios yielding the best fits. The resulting table of ratios for each absorber are supplied to the fitting program.

The efficiency tables supplied to TRACE are based on thin-target measurements. Therefore the elemental abundances determined by TRACE for thick targets currently must be corrected for proton energy loss and X-ray absorption. Program FUDGE described in Appendix A calculates these thick-target correction factors which are then applied to the TRACE determinations.

IIID.2 Off-line data reduction: program TRACE

1. Introduction

Program TRACE was designed for use on a DDP-224 computer (Minneapolis Honeywell Corporation) which is interfaced to a CRT display and light pen unit. This computer has 24 bit words and 1.9 μs cycle time. The code is presently semi-

automatic in operation, initially requiring some operator interaction with the CRT system in selecting backgrounds. TRACE features include single Gaussian fits to spectral peaks using the gradient-expansion algorithm of Marquardt as given in Bevington (1969) to minimize χ^2. Backgrounds are fitted with a function of the form $\exp[P_y]$ where P_y is a polynomial whose degree y is selected by the operator, and whose coefficients are determined from a least-squares fit to the log of the background points selected by the operator or by the computer. The code requires approximately 14K of memory words and is capable of processing a 10-20 element spectrum in one to two minutes.

The sequence of steps used by TRACE to fit a spectrum is indicated below:

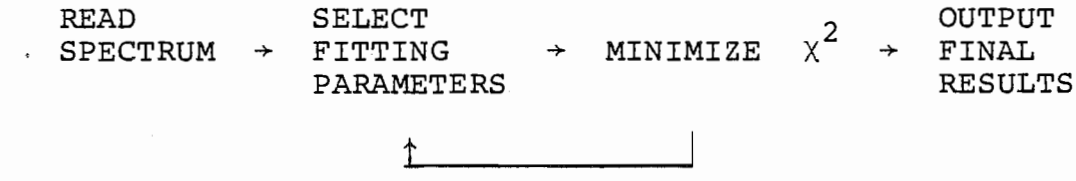

A flow chart is presented in Figures 3.23a and 3.23b to provide a more detailed description of the program design and for reference during the following sections.

2. Fitting parameters

The fitting procedure used in TRACE consists of computing a fitting function FIT(x,P) which approximates the original data at each channel x of the spectrum. Here P is

Figure 3.23 Flow diagram for program TRACE

3.23a Initial peak and background fit calculation.

3.23b Minimization of χ^2 and numerical results.

FLOW CHART - PROGRAM "TRACE"

A. INITIAL PEAK AND BACKGROUND FIT CALCULATION

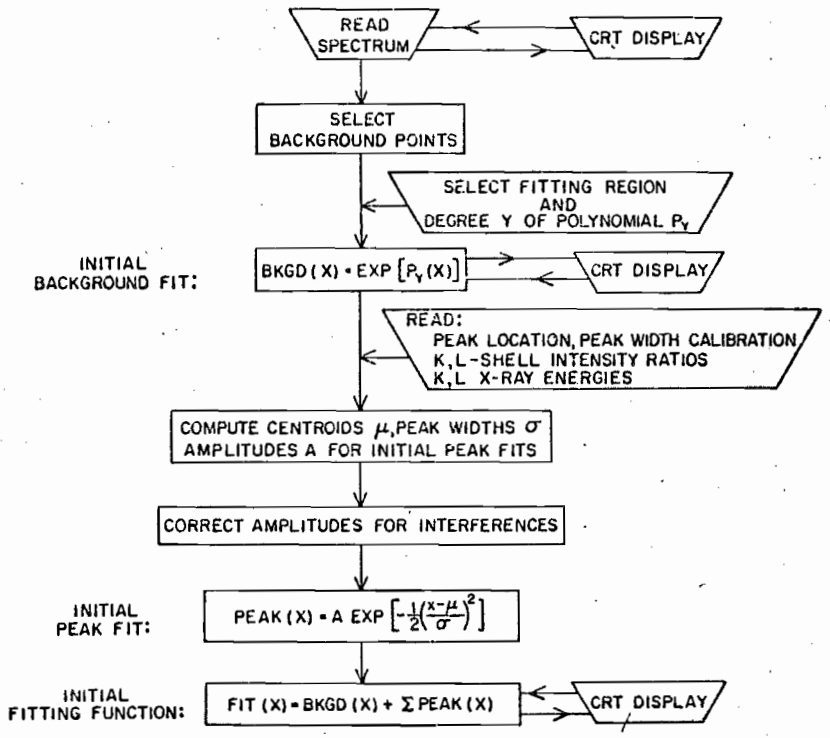

FLOW CHART - PROGRAM "TRACE"

B. MINIMIZATION OF χ^2, NUMERICAL RESULTS

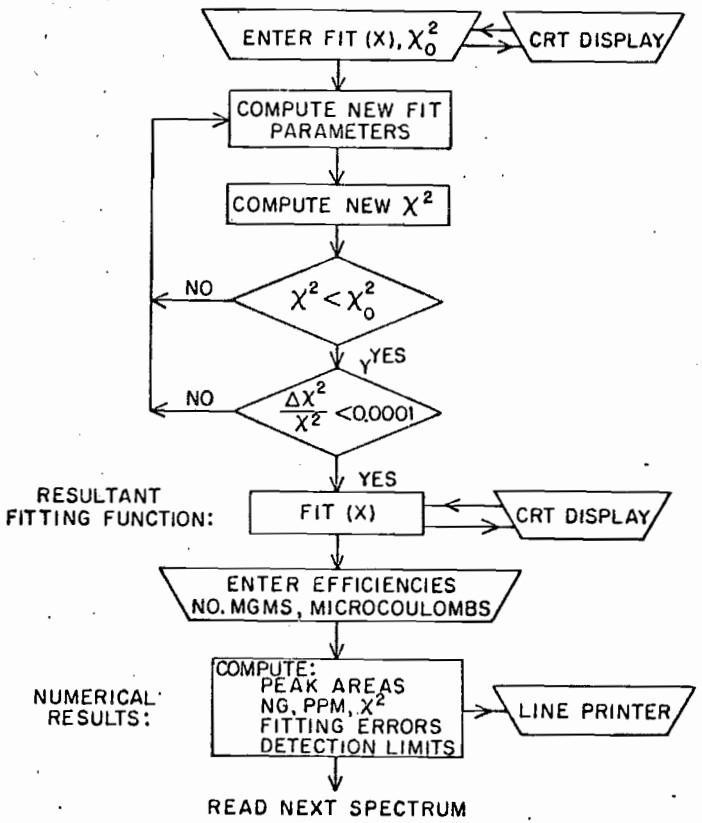

a set of fitting parameters which can be varied during the iterative fitting routine to improve the goodness of the fit. The array P includes the amplitudes of the Gaussian line shapes used to fit the reference lines in the spectrum. The other quantities which determine the Gaussian peak fit in addition to the amplitude are the peak width σ and the peak centroid μ. Peak widths and centroids are determined for each element from (two parameter) linear calibrations which relate σ and μ to X-ray energy. The slope and intercept values determining these calibrations are included as elements in the array P. Finally, the coefficients to the polynomial function $P_y(x)$ which determines the fitted background shape according to $BKGD(x) = EXP[P_y(x)]$ are also contained in P. .

The fitting algorithm used in TRACE seeks to minimize χ^2 with respect to small changes in each parameter of a subset of P. The present operation of the code calls for the operator to select the parameters which are allowed to vary with the restriction that the number of variable parameters does not exceed 13--the current size allocated in TRACE for the matrix containing the fitting parameters.

The ability to choose the fitting parameters adds a degree of versatility to the program although it has been our experience that excellent results can be obtained by fixing the background parameters and permitting only the amplitude,

centroid calibrations are carefully selected, one need only iterate on the peak amplitudes for a satisfactory fit. The calculation time for a fit is approximately linearly related to the number of variable parameters. It is desirable therefore to minimize the number of fitting parameters whenever possible.

3. Background fitting

Since TRACE as it is currently written can fit a maximum of nine to thirteen elements at one time, while many samples contain twenty or more observed elements, it is necessary to divide most PIXE spectra into sections (typically three or four) containing X-ray lines of no more than thirteen elements and to fit each section separately. At the start of a fitting session, the operator inputs up to ten "fitting lists" each of which specifies the following: the minimum and maximum channel limits defining the region to be fit; a flag selecting the proper absorber efficiencies and intensity ratios; a list of elements to be searched for in the defined region of interest; and the number of fitting parameters to be varied during the iterative fitting routine. The fitting regions are selected by the operator with consideration given to convenience in fitting the background shape and secondly to the potential for interelement interferences. Erroneous results can be obtained if the reference line of a

fitted peak overlies an X-ray signal from a second element which is not included in the fitting list. An example of four typical regions selected for a TRACE fit is shown in Figure 3.24.

The procedure used in obtaining the initial background fit is outlined in Figure 3.23a of the flow chart. By means of a light pen interactive scope display, the operator selects from the spectrum a number of points which describe the background shape. For routine analyses of a series of spectra having similar background shapes, the background point selection can be made automatically by the computer. In this case, background points are chosen in selected channel regions by determining the local minimum (or average thereof in regions of poor statistics) for each region. The logarithms of the X-ray counts corresponding to the selected background channels are least squares fitted to a polynomial $P_y(x)$ where the degree y of the polynomial ($y \leq 4$) is selected by the operator by means of a four-way switch interfaced with the computer. The initial background fit at channel x is calculated as:

$$BKGD(x,P_y) = EXP\ [P_0 + P_1\ x + P_2\ x^2 + P_3\ x^3 + P_4\ x^4].$$

As mentioned in the previous section, the operator may choose to hold fixed any combination of the five background para-

Figure 3.24 PIXE data and computer fit to typical biological spectrum obtained with polyethylene absorber. The four regions along the abscissa represent successive regions included in the TRACE fit.

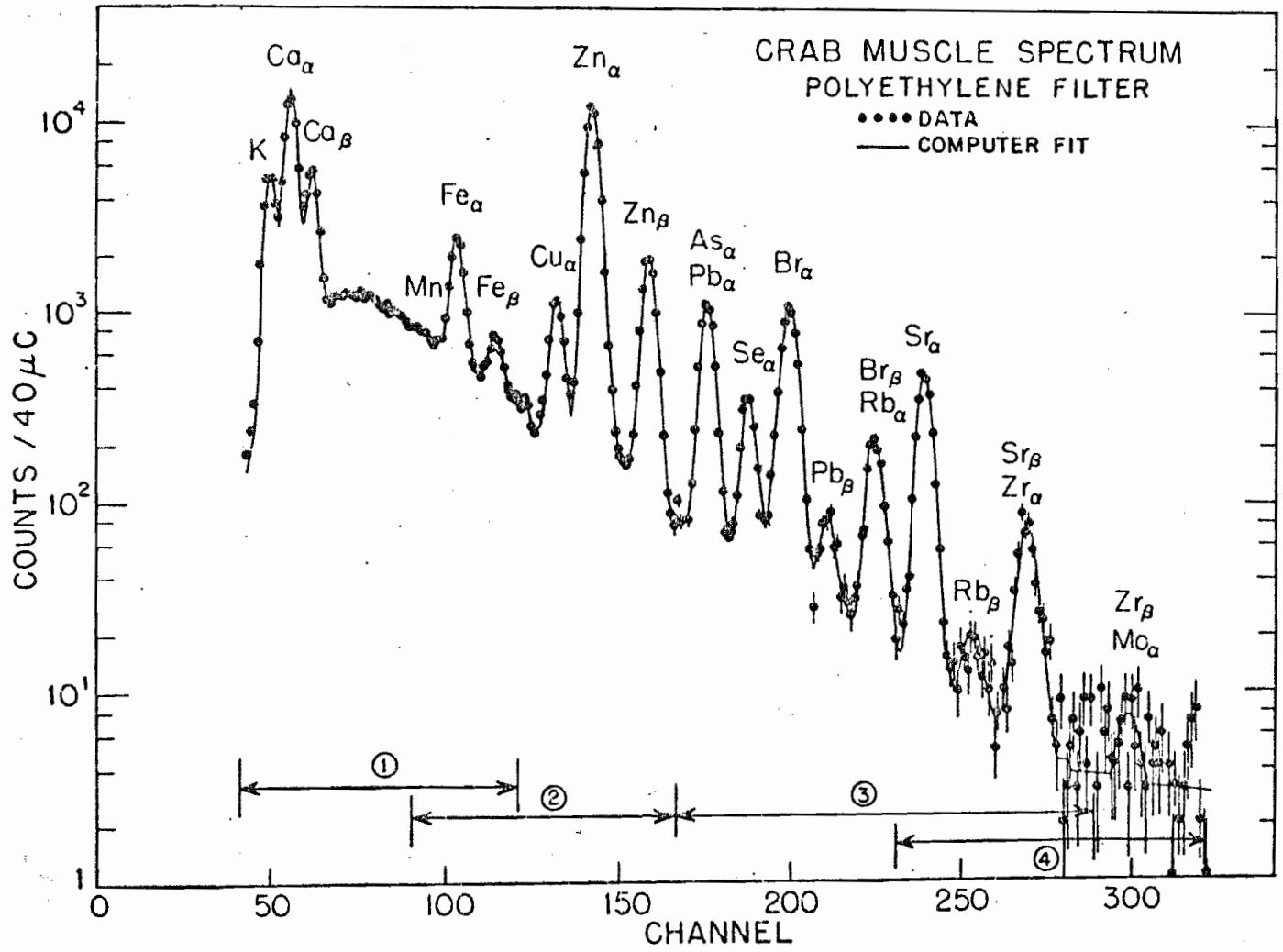
CRAB MUSCLE SPECTRUM
POLYETHYLENE FILTER
•••• DATA
—— COMPUTER FIT
Ca$_\alpha$
Ca$_\beta$
K
Zn$_\alpha$
Zn$_\beta$
Fe$_\alpha$
Fe$_\beta$
Mn
Cu$_\alpha$
As$_\alpha$
Pb$_\alpha$
Br$_\alpha$
Se$_\alpha$
Br$_\beta$
Rb$_\alpha$
Sr$_\alpha$
Pb$_\beta$
Sr$_\beta$
Zr$_\alpha$
Rb$_\beta$
Zr$_\beta$
Mo$_\alpha$
①
②
③
④
COUNTS / 40 μC
CHANNEL
10^4
10^3
10^2
10^1
1
0
50
100
150
200
250
300

(195)

Figure 3.25a Typical TRACE fit for a spectrum obtained with a mylar absorber. The dashed curve represents the background employed in the fit. Here the sample was a nuclepore membrane used in an air sampling device.

3.25b Typical TRACE fit for a spectrum obtained with an aluminum absorber. The dashed curve represents the background used in the fit. The air filter is a nuclepore membrane.

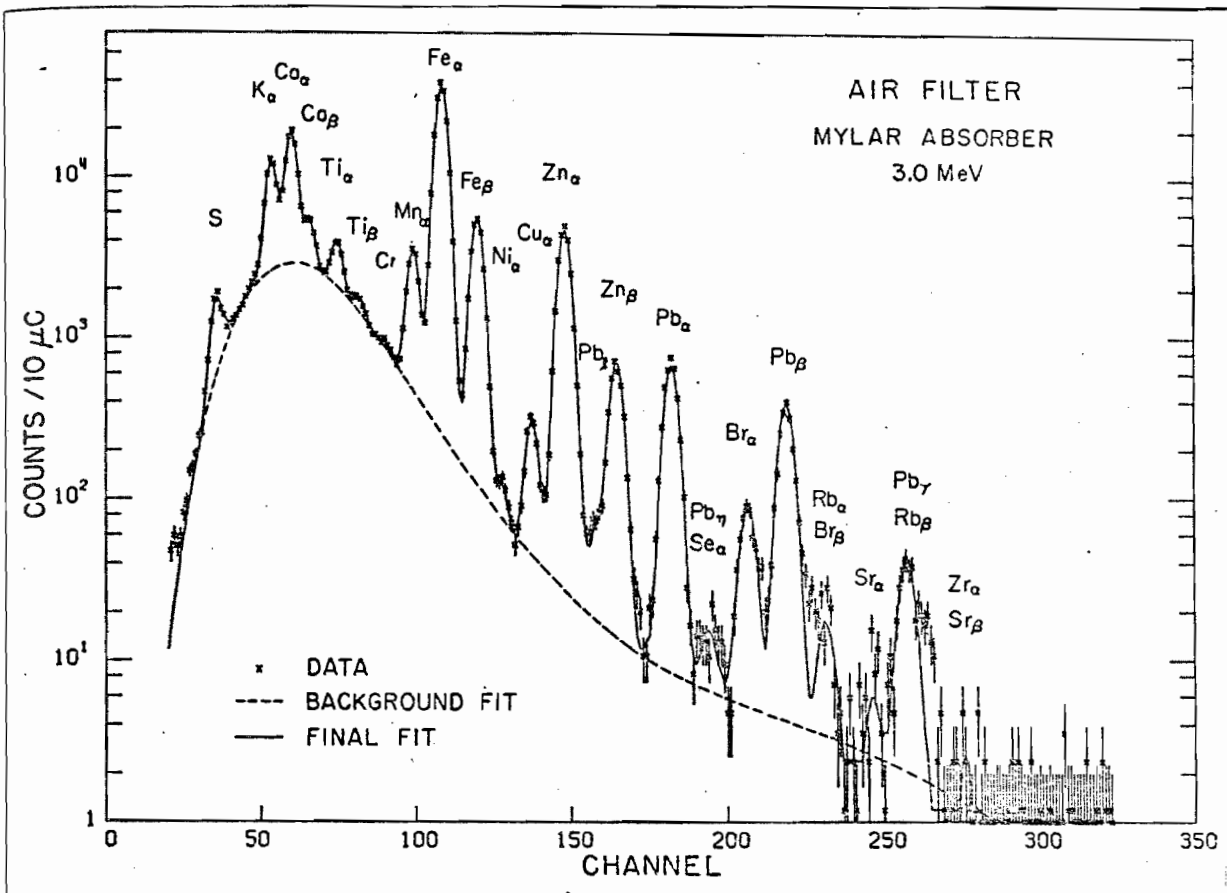
AIR FILTER
MYLAR ABSORBER
3.0 MeV
COUNTS / 10 μC
CHANNEL
DATA
BACKGROUND FIT
FINAL FIT
S
K$_\alpha$
Ca$_\alpha$
Ca$_\beta$
Ti$_\alpha$
Ti$_\beta$
Cr
Mn$_\alpha$
Fe$_\alpha$
Fe$_\beta$
Ni$_\alpha$
Cu$_\alpha$
Zn$_\alpha$
Zn$_\beta$
Pb$_\alpha$
Pb$_\beta$
Br$_\alpha$
Pb$_\eta$
Se$_\alpha$
Rb$_\alpha$
Br$_\beta$
Pb$_\gamma$
Rb$_\beta$
Sr$_\alpha$
Zr$_\alpha$
Sr$_\beta$

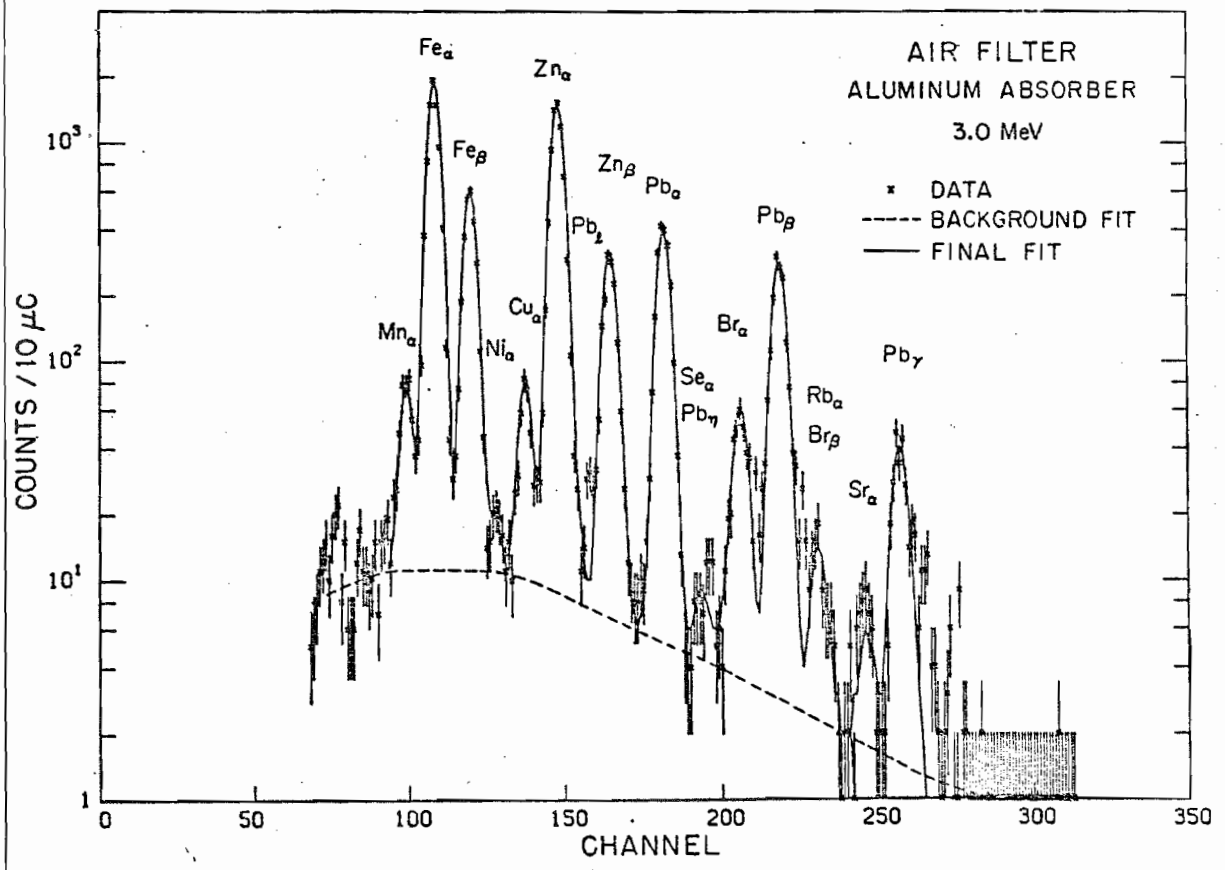
AIR FILTER
ALUMINUM ABSORBER
3.0 MeV
DATA
BACKGROUND FIT
FINAL FIT
COUNTS / 10 μC
CHANNEL
Fe$_\alpha$
Fe$_\beta$
Zn$_\alpha$
Zn$_\beta$
Pb$_\alpha$
Pb$_\beta$
Pb$_\gamma$
Mn$_\alpha$
Ni$_\alpha$
Cu$_\alpha$
Br$_\alpha$
Se$_\alpha$
Pb$_\eta$
Rb$_\alpha$
Br$_\beta$
Sr$_\alpha$

meters P_0 - P_4. Most commonly, all five are fixed so that the background shape remains constant during the iterative fitting routine. Examples of background fits obtained in this way are shown in Figures 3.25a and 3.25b for spectra obtained with the mylar and aluminum absorbers respectively.

4. Peak fitting

After subtraction of the fitted background in a selected region, the remaining spectrum of X-ray peaks is fitted with a set of single Guassian line shapes with the peak fit to an element j given by:

$$PEAK_j(x,A_j,\sigma,\mu) = A_j \cdot RATIO_j \cdot EXP\left[-\tfrac{1}{2}\left(\frac{x-\mu}{\sigma}\right)^2\right].$$

Here, x is the channel location at which the function is evaluated, A_j is the amplitude computed for the reference line of the element j, $RATIO_j$ represents the intensity ratio of the line being fit with respect to the reference line ($RATIO_j = 1.0$ when fitting the reference line), and μ and σ represent the current best estimates for the centroid and width, calculated at the X-ray energy of the line being fitted.

The peak centroid μ and peak width σ are calculated according to the following linear calibration:

$$\text{peak centroid } \mu = P_5 + P_6 \cdot E$$

$$\text{peak width } \sigma = P_7 + P_8 \cdot E.$$

Here E represents the appropriate energy and $P_5 - P_8$ are fitting parameters included in the array P. The initial values for σ and μ used to obtain the starting guesses for the functions $PEAK_j$ are computed from the above calibrations based on values of the parameters P_5 to P_8 which are read into the program at the start of a fitting session. The usual fitting procedure is to obtain best values for P_5 to P_8 by allowing these parameters to converge to final values during the first fit of a fitting session. These values are read in as the new initial guess parameters for subsequent fits. The values of these peak centroid and width parameters change very little for different spectra obtained during the same experimental period, being determined primarily by the detector resolution function and amplifier gain which are not expected to change during the course of a run. Our experience in fact has been that with a good set of starting values for the peak location and peak widths, excellent fits are commonly obtained after one or two iterations in the fitting loop.

The initial guess amplitude A_j for a K-line element Z is roughly corrected for $K_\alpha - K_\beta$ interferences by simply subtracting the initial guess amplitude of the K_β line for element $(Z - 1)$ from A_j for all elements between $Z = 17(Cl)$ and $Z = 33(As)$. For this range of Z, the K_β line of an

element (Z - 1) roughly overlaps with the K_α line of element Z. If Pb and As are both included in the fitting list, a similar correction is made for the Pb(L_α) - As(K_α) interference. These simple corrections serve to improve the starting guess parameters which are then used in the χ^2 fit calculations.

The quality of fits which can be obtained by approximating X-ray lines with single Guassian line shapes are indicated in Figures 3.26a and 3.26b. Vertical error bars attached to the data points represent the statistical errors assigned to the data. The two-Gaussian fit to the Ni K_α, K_β doublet is generally quite good although the computed fit does extend too low in the region between the K_α and K_β peaks. The counts in this region may be distortion associated with detector effects. The upper spectrum in Figure 3.26b shows the normal four-Gaussian fit to the dominant Pb lines--L_α, L_β, L_γ, and L_ℓ. The broadened shoulders of the L_β and L_γ peaks are due to additional Pb lines including the L_{β_5}, L_{β_6}, L_{γ_3} and L_{γ_5} lines as indicated in the figure. For rare spectra such as this Pb standard which contain unusually intense Pb lines, it is easy to add four additional Gaussians, for example, to the TRACE Pb fit in order to fit the L_η, L_{β_6}, L_{β_5}, and L_{γ_3} lines. Such a fit is shown in the lower half of Figure 3.26b for the same Pb spectrum. We would like to emphasize that, excluding air filter analyses, most of the biological and environmental samples which we have analyzed

Figure 3.26a PIXE data represented by crosses with error bars for a Ni monoelemental standard. Solid curve shows a two-Gaussian computer fit with some background continuum included. The higher background on left hand side indicates low-energy tailing.

3.26b PIXE data represented by crosses with error bars for a Pb monoelemental standard. Top half: Computer fit with a four-Gaussian function plus a continuous background. Bottom half: Computer fit with an eight-Gaussian function plus a continuous background.

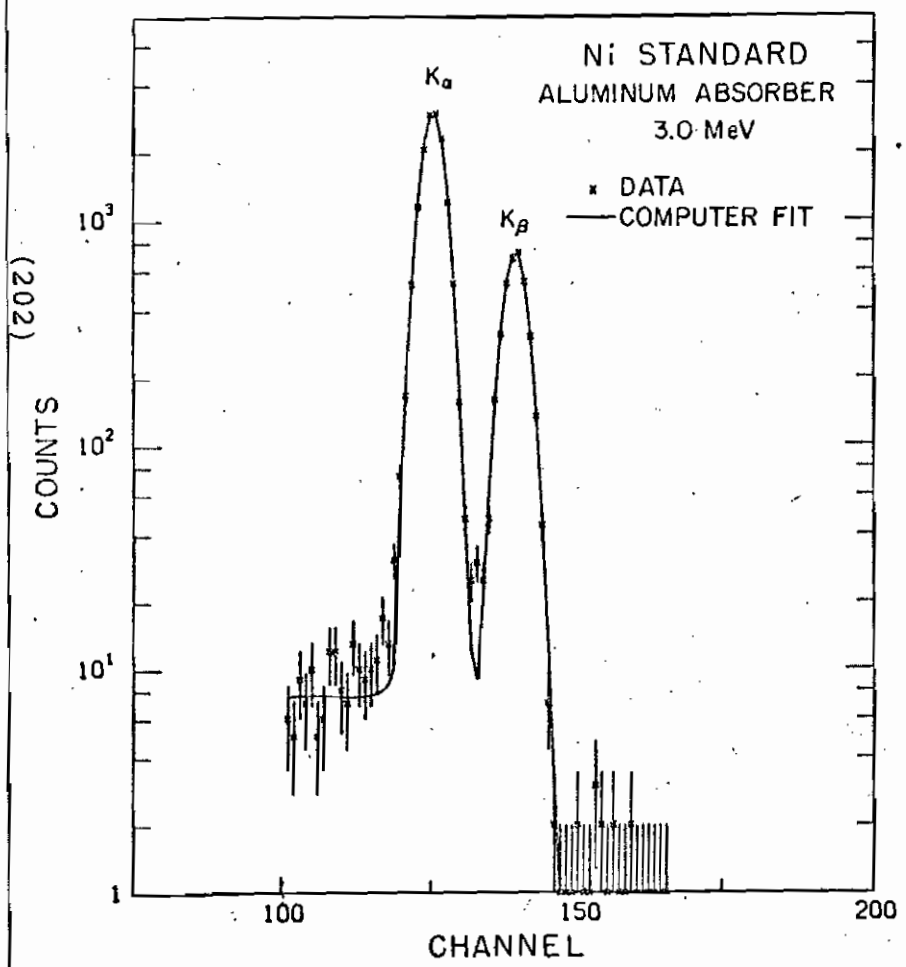
Ni STANDARD
ALUMINUM ABSORBER
3.0 MeV
x DATA
—COMPUTER FIT
K_α
K_β
COUNTS (202)
CHANNEL
1
10^1
10^2
10^3
100
150
200

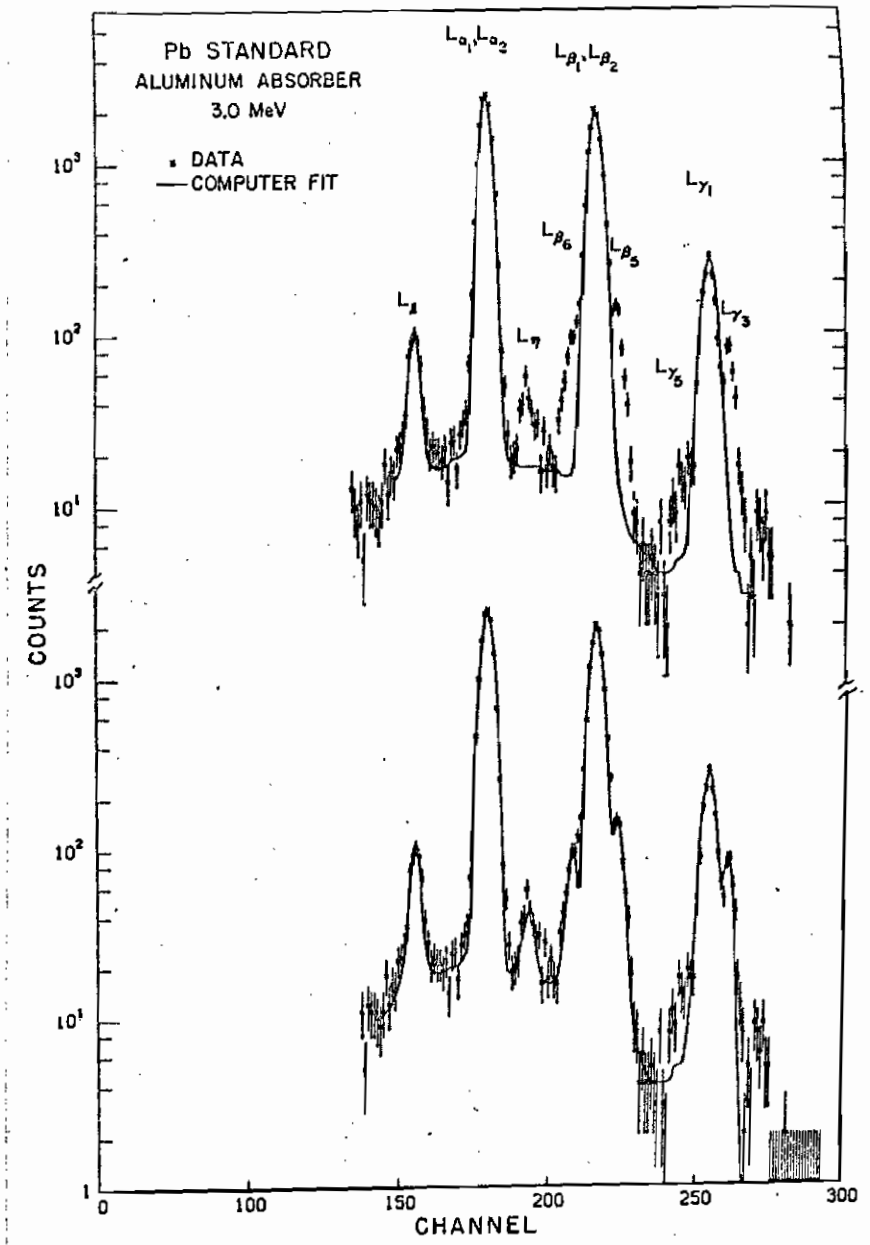
Pb STANDARD
ALUMINUM ABSORBER
3.0 MeV
x DATA
—COMPUTER FIT
$L_{\alpha_1}, L_{\alpha_2}$
L_{β_1}, L_{β_2}
L_{β_6}
L_{β_5}
L_{γ_1}
L_{γ_3}
L_{γ_5}
L_η
L_1
COUNTS
CHANNEL
1
10^1
10^2
10^3
0
100
150
200
250
300

have levels of Pb which are so low that in routine analyses it is sufficiently accurate to only fit the four dominant Pb lines. Because both the detection efficiencies and the L-line intensity ratios are taken from similar single Gaussian line fits, failure to fit the L_β and L_γ shoulders does not introduce errors in the determination of Pb in a sample. However, caution must be observed in determining Se and Rb in the presence of large amounts of Pb because the Se K_α peak falls in the region of the Pb L_η peak and the Rb K_α peak appears in the region partly filled in by the Pb L_{β_5} peak. An estimate of the maximum errors introduced in the determination of Se and Rb in the presence of intense Pb signals was obtained by fitting the Pb spectrum of Figure 3.26b with Se and Rb included in the fitting list. The results indicate that failure to fit the Pb L_η and L_{β_5} lines can lead to a maximum error in the determination of Se of 0.4% of the Pb abundance and a maximum error in Rb determinations of 0.07% of the Pb abundance. The greatest uncertainty seems to be associated with the background level assignments in these two regions.

The present version of TRACE is capable of calculating fits to twenty-two K-line elements ($16 < Z < 42$) and five L-line elements (Pb, Hg, Th, Au, Ba). Elements which are not included in the present list can be easily added by card input.

In addition to the complexities introduced by interelement interferences, a number of other phenomena which are as-

sociated with the presence of unusually large concentrations of one or more elements in the sample can complicate the analysis of PIXE spectra. These include Si escape peaks, pile-up peaks, and low-energy tailing. Escape peaks or pile-up peaks can interfere with or be interpreted as elemental X-ray lines. Low-energy tailing is a detector effect resulting in a tail extending from the low-energy side of an X-ray line making background determinations difficult, and possibly obscuring low intensity peaks. Pile-up, escape peaks, and low-energy tailing are not of concern for the majority of sample types analyzed at this laboratory, and no corrections for these effects are normally included explicitly in TRACE. However, escape peaks are treated by adding additional lines of the appropriate escape peak energies and intensities relative to the parent X-ray lines when the accuracy to be reported supercedes that obtained in normal cases.

5. Minimization of χ^2

The background fit $BKGD(x,P_y)$ and the collection of peak fits $\sum_j PEAK_j(x,A_j,\mu,\sigma)$ are summed at each channel x to yield the total fitting function $FIT(x,P,A_j)$ where:

$$FIT(x,P,A_j) = BKGD(x,P_y) + \sum_j PEAK_j(x,A_j,\mu,\sigma).$$

The fitting function is parameterized by the background coefficients P_0 - P_4, the peak amplitudes A_j, and the peak loca-

tion and peak width parameters P_5 - P_8.

The fitting function and current best estimates of the fitting parameters are entered into the curve-fitting subroutine "CURFIT" (taken from Bevington, 1969). This routine calculates a least-squares fit to the fitting function by the method of Marquardt which combines a gradient-type search for minimum χ^2 with linearization of the fitting function. The algorithm to minimize χ^2 is shown in Figure 3.23b. The program is designed to exit from the iterative fitting loop either automatically (at the end of three iterations, or if the relative improvement in χ^2 is less than 0.0001) or manually by means of a sense switch interfaced to the computer. Normally, convergence toward the final parameter values is sufficiently rapid that acceptable fits are obtained after one or two iterations. Table 3.9 lists the calculated abundances and minimum detection limits of three TRACE fits for the initial guesses and the first four iterations. A column showing the elapsed fitting time is included for each list. The fit for the low Z elements of list 1 was obtained from the air filter spectrum (Figure 3.25a) taken with a mylar filter. Abundances for the remaining elements were obtained from fits for a successive spectrum obtained with a polyethylene absorber and the same air filter. The results of Table 3.9 indicate that the TRACE fits for this sample generally converged after one or two iterations to within a few per cent of the probable final

Table 3.9

Calculation Times and Convergence Tests for TRACE Fits

LIST 1. MYLAR ABSORBER

NUMBER OF ITERATIONS	ELEMENTAL ABUNDANCES IN NANOGRAMS								TIME (sec.)
	S	Cl	K	Ca	Ti	Cr	Mn	Fe	
0	2572	44	1514	1244	0	9.4	278	3910	1
1	2352	0.8	1529	1357	121	6.1	270	3704	18
2	2440	0	1544	1366	139	5.8	270	3704	35
3	2426	0	1544	1367	141	5.8	269	3690	52
4	2455	0	1558	1360	136	5.8	268	3690	69
MDL	70	29	12	7.6	6.3	4.1	2.9	2.4	

LIST 2. POLYETHYLENE ABSORBER

NUMBER OF ITERATIONS	ELEMENTAL ABUNDANCES IN NANOGRAMS					TIME (sec.)
	Mn	Fe	Ni	Cu	Zn	
0	288	3730	12.0	53.2	1000	1
1	290	3590	10.4	45.6	936	13
2	287	3570	10.3	45.0	927	25
3	285	3570	10.4	45.1	927	37
4	283	3570	10.7	45.3	928	49
MDL	3.6	2.5	1.6	1.4	1.3	

LIST 3. POLYETHYLENE ABSORBER

NUMBER OF ITERATIONS	ELEMENTAL ABUNDANCES IN NANOGRAMS							TIME
	As	Se	Br	Rb	Sr	Zr	Pb	(sec.)
0	37.9	5.5	61.8	17.8	17.6	15.4	1130	1
1	21.2	4.3	61.6	9.5	10.7	8.6	1130	23
2	16.5	4.1	62.5	7.4	9.2	7.3	1140	46
3	16.6	4.1	63.0	7.3	9.1	7.2	1150	72
4	16.3	4.1	63.5	7.1	9.0	7.2	1150	94
MDL	2.0	2.1	2.2	2.3	2.4	2.7	6.8	

values (indicated in the fourth iteration). The total computation time for the 18 elements reported is less than two minutes for two iterations for each list and less than one minute for one iteration.

6. Numerical results

Using the current best estimates for the amplitude A_j and widths σ of the fitted reference peaks, TRACE computes the fitted peak areas according to:

$$AREA_j = \sqrt{2\pi} \cdot \sigma \cdot A_j .$$

These are converted to elemental abundances using the appropriate detection efficiencies and the number of microcoulombs of proton charge.

The uncertainties associated with a particular fitting parameter can be estimated by the change in χ^2 observed when the parameter is changed while keeping all other parameters fixed at optimum values. TRACE calculates estimates of the error in each peak area calculation based on uncertainties in the amplitude parameters A_j and width parameters σ. These error estimates improve as the fit improves and χ^2 approaches 1. For the complex, multi-line spectra of interest here, χ^2 per point is frequently greater than unity. One measure of the maximum uncertainties associated with the sample preparation, data collection, and TRACE analysis can be obtained by performing multiple analyses on a known stan-

dard and determining the variance of the distribution of the observed results. One such series of measurements was performed on four identically prepared samples of NBS Bovine Liver (Standard Reference Material 1577). Table 3.10 summarizes the results obtained from these measurements. The uncertainties quoted for the average PIXE values represent the variances calculated for the four measurements. The agreement between the PIXE results and the NBS values is excellent with the exception of Ca and PB. (The high Pb value observed with PIXE is due in part to contaminants in the acid used in the ashing preparation of the samples. The low Ca value may indicate a need to recalibrate the Ca efficiency used by TRACE. Some Se and Br may have been lost in the ashing process.) The quality of the TRACE fit to the summed spectrum of the four measurements is displayed in Figure 3.27.

In our data analyses thus far, we have required as a detectability criterion that the peak in question contain a number of counts greater than three times the standard deviation of the underlying background counts. TRACE currently calculates these interference-free Minimum Detection Limits (MDL) for each fitted element. A more meaningful quantity, as pointed out by Currie (1968) and discussed in Section IIF.2, is the determination level L_Q representing the minimum detected signal which can be measured quantitatively to a specified precision. Secondly, the minimum detection limits currently

Table 3.10 NBS Bovine Liver Analyses

Element	Sample[a]					PIXE[b]	NBS[c]
	A	B	C	D	SUM[d]	Avg. Values	
K	0.90%	0.93%	0.89%	1.01%	0.90%	0.93(.05)%	0.97(.06)%
Ca	---	---	---	---	100	100	123
Cr	1.3	2.6	2.7	0	1.6	2.4(0.7)	
Mn	10.9	10.5	8.5	8.0	8.6	9.5(1.4)	10.3(1.0)
Fe	270	282	287	310	272	287(17)	270(20)
Ni	0.8	0.8	0.1	1.2	0.4	0.7(0.5)	
Cu	186	196	193	207	183	196(8)	193(10)
Zn	140	142	146	152	138	145(5)	130(10)
Ga	1.0	1.0	0.3	1.9	0.8	1.1(0.7)	
As	<0.6	<0.7	<0.7	1.0	<0.3	<0.7	.055
Se	1.2	1.3	1.2	1.1	1.2	1.2(0.1)	1.1(0.1)
Br	5.6	7.1	5.1	6.6	5.9	6.1(0.8)	
Rb	20	18	17	17	18	18(1.0)	18.3(1.0)
Sr	(54)	(54)	(46)	(49)	(49)[f]	---	0.14
Mo	2.3	5.2	1.9	4.9	3.4	3.5(1.5)	3.2
Pb	3.5	1.8	3.5	3.5	2.7	3.0(0.8)[e]	0.34(.08)

a) Samples are acid ashed and represent 0.13-0.15g of Bovine Liver
b) PIXE values are based on internal Sr standard
c) NBS results quoted with uncertainties are certified values
d) SUM represents the composite spectrum obtained by adding the spectra from samples A, B, C, and D
e) See text
f) Dopant

Figure 3.27 TRACE fit to spectrum for ashed Bovine Liver SRM 1577. The substrate for the ashing deposit is nuclepore. Vertical bars through the data represent the statistical uncertainties in the data.

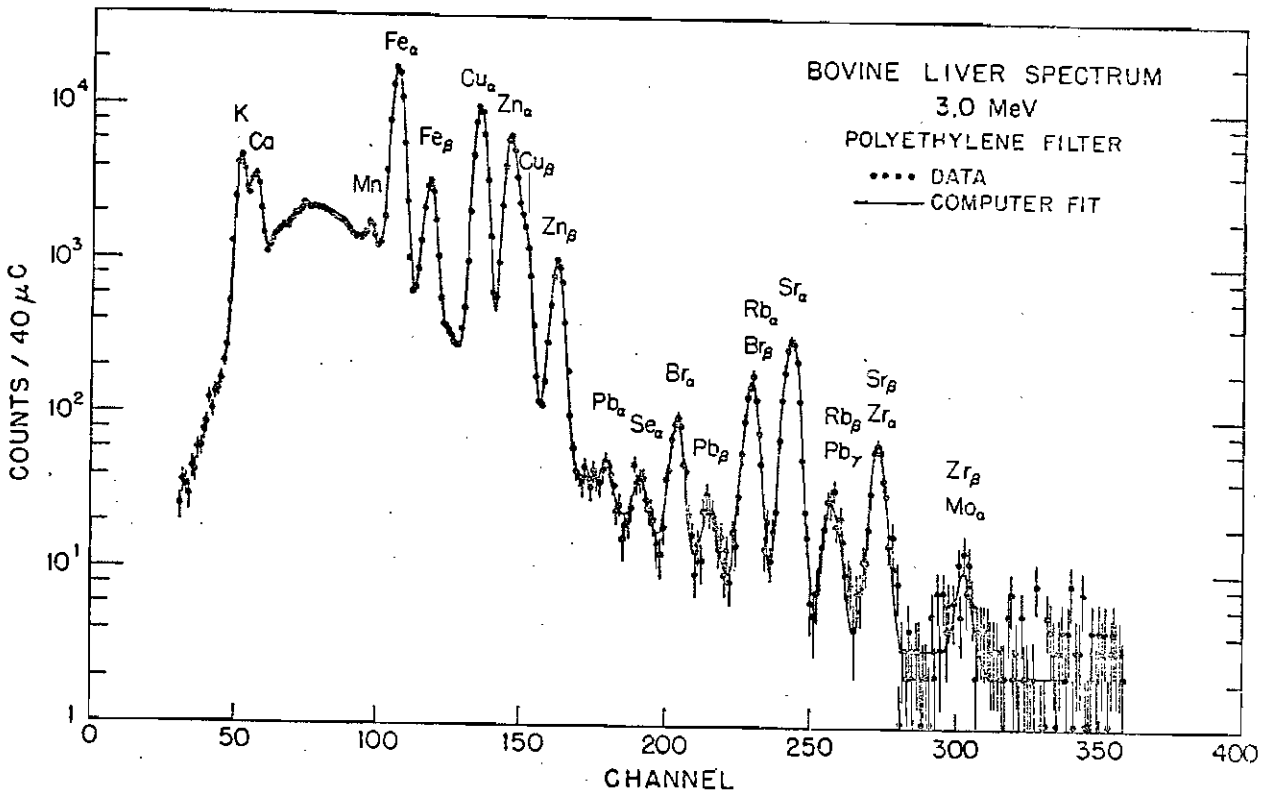
BOVINE LIVER SPECTRUM
3.0 MeV
POLYETHYLENE FILTER
•••• DATA
—— COMPUTER FIT
COUNTS / 40 μC
CHANNEL
K
Ca
Mn
Fe$_\alpha$
Fe$_\beta$
Cu$_\alpha$
Zn$_\alpha$
Cu$_\beta$
Zn$_\beta$
Pb$_\alpha$
Se$_\alpha$
Br$_\alpha$
Pb$_\beta$
Rb$_\alpha$
Br$_\beta$
Sr$_\alpha$
Rb$_\beta$
Pb$_\gamma$
Sr$_\beta$
Zr$_\alpha$
Zr$_\beta$
Mo$_\alpha$

calculated by TRACE do not account for the additional uncertainty in peak detection or calculated abundances due to interelement interferences. We are in the process now of revising the treatment of minimum detection limits along the lines of Currie and including interference effects.

IIID.3 Conclusion

Program TRACE was developed in the modest time of about six weeks. With only minor changes, it has provided us with all of our data analyses during the last couple of years. Improvements continue to be made in the program and in particular, we are exploring ways to safely minimize the operator-interactive aspects of the present code, although this has provided the code with an added versatility. The present background fitting procedure is somewhat cumbersome and we feel that this is an area which can be improved. Finally, changes are being made in the code to provide a more careful analysis of errors including Poisson statistics, interelement interferences, and fitting errors in addition to the adoption of more meaningful quantities to replace the currently used detectability criterion.

A number of different approaches to automatic data analysis have been employed and are described in the literature (Harrison and Eldred, 1974; Arinc et. al., 1977; Kaufmann and Akselsson, 1975; Hasselmann et. al., 1977). Most of these codes have in common the feature of generating

Gaussian line shapes to fit the characteristic X-ray peaks, but codes differ in the treatment of the background. Harrison and Eldred subtract a stored blank spectrum (scaled to the spectrum being analyzed) and fit only the residual X-ray peak spectrum. Hasselmann et al. uses scaled background functions which have been fitted to typical target matrices. Only the height of the background function is varied during the fitting procedure. Kaufmann and Akselsson use parameterized functions which describe the essential physical processes influencing the X-ray spectrum: detector resolution, bremsstrahlung continuum, Compton tail, and absorption of X-rays in the sample and the filters. The method of least-squares is then applied to a generalized fitting function which includes Gaussian peak fits and the parameterized background function both multiplied by the absorption function.

Rather than generating Gaussian fits to the spectral lines, one can also use pure elemental line shapes which have been experimentally measured and stored in the computer. This approach which is taken by Arinc et al. provides its own intrinsic energy and width calibration, and eliminates the need for tables of intensity ratios. The use of stored line standards has the advantage of minimizing fitting errors. In particular, the phenomenon of low-energy tailing which can be a source of concern in Gaussian peak-fitting routines is included in the stored line shapes. Major disadvantages of

this approach include the need to measure pure element line shapes for all elements of interest, and the relatively large demand for computer space to store the library of line standards.

IIIE. Sample Preparation Techniques

IIIE.1 Introduction

Our experience at Duke in analyzing a wide range of sample types (including leaves, grass, pine needles, butterfly wings, soil and rock samples, gasoline and fuel oil, air filters, whole blood, serum, and urine, and tissues and organs of humans and other animals) indicate the need for a correspondingly wide range of target preparation techniques. The choice of a particular technique will be governed by considerations of the required accuracy, precision, and sensitivity of the analysis, as well as the time and cost limitations of the various preparation methods.

The ideal target for PIXE analyses would have the following properties: (1) Thinness to avoid beam energy loss and X-ray absorption and to minimize self-fluorescence effects; (2) homogeneity; (3) high electrical and heat conductivity; (4) stability in vacuum; (5) stability to beam damage; (6) sufficient concentration so that elements of interest can be detected; and (7) minimal sample preparation. In practice, the ideal target is probably never encountered. In general,

compromises must be made among the various desirable properties listed above and the manner of preparing a sample for PIXE irradiation.

IIIE.2 Solid specimens

A variety of techniques have been employed for the preparation of solid specimens. Many solid samples are self-supporting, requiring no preparation other than attaching the specimen to the target rod for irradiation. Self-supporting targets minimize handling of the samples and therefore reduce the potential for contamination. Some of the self-supporting specimens which have been analyzed at our laboratory are leaf and grass samples, air filters, thick sections of fish tissue, hair and pine needles, cloth, and ion exchange membranes.

Specimens which can be dried or lyophilized and ground to a fine powder are often suitable for making pellets which we have found in most cases to be excellent targets for PIXE analysis. The procedure calls for grinding approximately 100 mg of the sample to a fine powder using a mortar and pestle. This powder is then compacted in a hydraulic press using a case-hardened stainless steel die at 1300 atm for 1 minute. Pellets 13 mm in diameter and 29 mm in diameter have been used successfully. The smaller pellets are typically glued (using a small amount of clean adhesive on the back surface) to a strip of aluminized mylar attached to the target

frame . The larger pellets are self-supporting and can be mounted directly onto the target frame for irradiation. Certain sample materials such as ground soil and fly ash produced very brittle pellets. It was found that these materials could be made into more durable pellets by the addition of a few percent of purified ceresin (a paraffin-like substance) to the ground sample to act as a binding agent. In addition, one can add one or more internal calibration standards to the ground sample prior to pelletizing, taking care that the dopant(s) is distributed uniformly throughout the sample. Specimens which have been analyzed in pellet form include the NBS standard reference materials of orchard leaf, coal, and bovine liver, lyophilized blood and placenta, human lung samples, and clay and soil samples.

A technique which has had limited success for granular or powdered materials is to make a thin packet by enclosing a small amount of the sample between two layers of thin mylar or commercial plastic wrap. The sample is spread out uniformly over an area roughly the size of the beam spot, and the two layers of mylar or plastic wrap are glued or heat sealed around the periphery of the deposit to prevent the escape of the sandwiched material. This technique is used when the amount of sample material available is small, or if other preparation techniques fail.

From the viewpoint of quantitative analysis, it is

often desirable to use targets which are thin to the proton beam ($\leq$ 1 mg/cm^2). In this case, the sample is deposited in liquid form (either in its natural state or in solution) or as a solid (microtomed tissue slices, for example) onto a thin supporting substrate. The desired properties of the substrate material include resistance to beam heating, receptivity to the deposited sample, mechanical strength, and low areal density ($\lesssim$ 1 mg/cm^2). In addition, the substrate should produce a clean background spectrum, free of X-ray peaks due to trace impurities in the material. A variety of materials have been evaluated at Duke in terms of the above properties. These include commercially available and self-made carbon foil, mylar (DuPont), Millipore (Millipore Corp.), nuclepore (General Electric) and Formvar (Shawinigan Products Corp.). Properties of the most commonly used materials are summarized in the review by Johansson et al. (1976).

Of the materials tested, we have found 3-micron thick mylar (0.4 mg/cm^2) and 8-micron porosity nuclepore (1.1 mg/cm^2) to be most suitable for PIXE analysis. Both materials are extremely durable and resistive to beam heating. Nuclepore is perforated with microscopic pores which enables this material to bond better to liquid deposits. Mylar however is very suitable as a support for solid samples. Aluminized mylar is frequently used in order to improve the heat and charge conduction properties. Both mylar and nuclepore are

relatively free of contaminants as shown in the spectra of Figure 3.28a which include a spectrum of Formvar. Formvar generated the least background of all materials tested, but lacked sufficient mechanical strength for widespread usage. Figure 3.28b shows a spectrum of a "point" solution deposit containing approximately 6 ng of Mn, Cu, and Pb, which was deposited on nuclepore. The spectrum is superimposed on a spectrum obtained from irradiating a blank nuclepore membrane. The cross-hatched areas and the amounts listed underneath the curves indicate the approximate levels of contaminants observed in the blank membrane.

Thin targets have been made from frozen tissue samples by slicing the tissue with a precision microtome and depositing the section on a Formvar or nuclepore substrate. Thicknesses as low as 10-30 microns have been analyzed in this way. The specimen plus substrate is mounted on a 2.54 cm diameter fiber or graphite washer ring for ease in mounting on the target frame. We have also had good success in mounting moderately thick tissue slices onto nuclepore backings. It was found that as the hydrated tissue slices dried, they formed a sufficiently strong bond with the nuclepore backing that no additional adhesive was required.

Considerable experience has been gained in the preparation of sample materials by the technique of multiple low temperature wet-ashing (Middleton and Stuckey, 1954; Gorsuch,

Figure 3.28a Comparison of PIXE spectra obtained from mylar, nuclepore, and formvar substrates.

Figure 3.28b Comparison of PIXE spectra obtained from: (1) a blank nuclepore substrate, and (2) the same substrate onto which a doped solution containing approximately 6 ng of Mn, Cu, and Pb was deposited. The approximate levels of contaminants in the nuclepore substrate are indicated in the shaded regions.

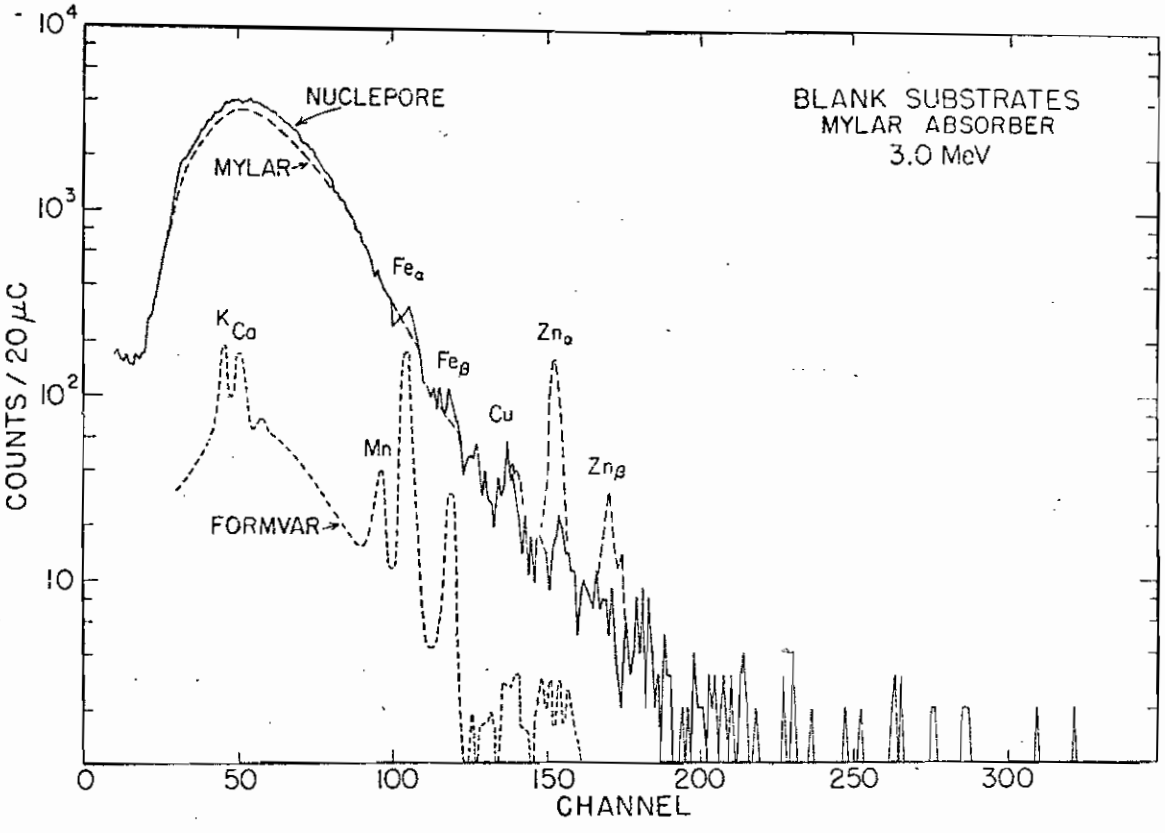
NUCLEPORE
MYLAR
FORMVAR
BLANK SUBSTRATES
MYLAR ABSORBER
3.0 MeV
Fe_α
K_{Co}
Fe_β
Mn
Cu
Zn_α
Zn_β
COUNTS / 20 μC
CHANNEL

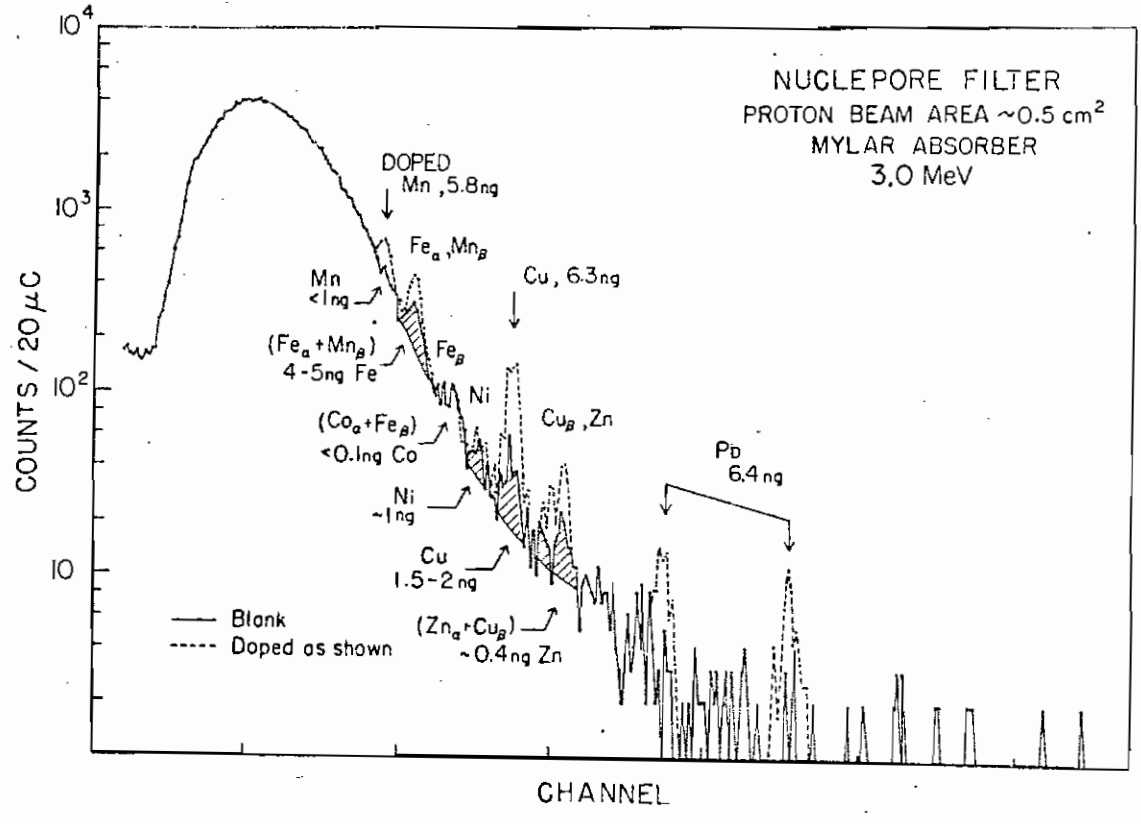
NUCLEPORE FILTER
PROTON BEAM AREA ~0.5 cm²
MYLAR ABSORBER
3.0 MeV
DOPED
Mn, 5.8ng
Fe_α, Mn_β
Cu, 6.3ng
Mn
<1ng
$(Fe_\alpha + Mn_\beta)$
4-5ng Fe
Fe_β
Ni
$(Co_\alpha + Fe_\beta)$
<0.1ng Co
Cu_β, Zn
Pb
6.4 ng
Ni
~1ng
Cu
1.5-2 ng
$(Zn_\alpha + Cu_\beta)$
~0.4ng Zn
Blank
Doped as shown
COUNTS / 20 μC
CHANNEL

1970). Ashing provides a means of concentrating non-volatile metals in the sample by removing most of the organic compounds. By using low temperatures (300° C or less) the loss of volatile elements of interest is minimized.

Our experience indicates that different sample materials may require different ashing conditions. The general procedure calls for treating the sample (usually between 0.1 g and 1 g) with high purity nitric acid and heating gently at 300° C until a black residue remains. This process is repeated several times until a white residue is left indicating the removal of the organic content. The ashed residue is then dissolved in distilled, deionized water or a weak acidic solution and deposited in 20 μℓ aliquots on a mylar or nuclepore backing. This procedure proved unsatisfactory for a number of samples--coal and certain marine specimens were particularly difficult to ash. A more rigorous digestion procedure was employed for bovine liver and human lung samples which also resisted the more gentle techniques. This method required heating the sample in a mixture of concentrated HNO_3 and H_2SO_4 (2:1) overnight or until a clear solution was obtained. Unfortunately, this acid mixture has a very low vapor pressure and requires an intolerably long time to dry, even under vacuum. By evaporating the digested sample to dryness and redissolving in dilute HNO_3 before making deposits, this problem was avoided.

Wet ashing offers a number of potential advantages

over other preparation techniques: (1) it is possible to concentrate the sample, thereby improving the sensitivity--targets prepared from ashed deposits may represent 10-100 times more sample mass than is analyzed for unconcentrated targets; (2) targets can be kept thin for best quantitative results and to minimize beam heating and charge accumulation problems; (3) the addition of an internal calibration standard is made easier for samples prepared in solution; (4) targets prepared from solutions are homogeneous.

It is our feeling however that the problems associated with ashing generally outweigh the benefits to be gained. Ashing requires the most preparation time and the most expense of all techniques, and also has the greatest potential for introducing contaminants into the sample. The loss of volatile elements such as Se, Br, and Hg can be expected as a result of the ashing procedure. Furthermore, we have observed the formation of crystalline residues in the dried deposits of all biological specimens which we have ashed. These residues may be the result of insoluble materials formed during the ashing process (e.g., $CaSO_4$), or they may be inorganic compounds (e.g., silicates) present in significant amounts in the original specimen. Such residues make quantitative evaluation difficult. In addition, chunks of these materials ranging in size up to 100 μm contribute to an increased background spectrum, and may also result in reduced

X-ray yields due to absorption effects. Losses in the expected X-ray signals have in fact been observed for highly concentrated samples, i.e. samples which contain large amounts of inorganic materials. Thus it appears that a natural limit exists in the wet ashing procedure for concentration and subsequent quantitative determination of trace elements in biological and environmental samples.

IIIE.3 Liquid specimens

The current design of the Duke PIXE system requires that liquid specimens be dried prior to irradiation in vacuum. The usual procedure is to deposit a calibrated amount of the sample (typically 10-80 μℓ) using a precision micropipette (Eppendorf) onto a nuclepore or mylar backing. The deposit is then allowed to dry prior to irradiation. Quantitation of the resulting target is obtained directly from the thin-target response (Figure 3.12) if the target thickness is less than approximately 1 mg/cm^2 and if the deposit is fully enclosed by the proton beam during analysis. Otherwise, calibration can be achieved by the addition of internal standards. In many cases, liquid specimens can be preconcentrated in order to improve sensitivity (Section IIIE.4). An added advantage of liquid specimens is that the resulting targets are usually very homogeneous.

Some difficulties have been experienced with liquid specimens. Certain samples including whole blood, serum,

and urine dried to form brittle deposits which flaked easily; the dried deposits of certain ashed samples and of sea water contained crystalline residues which complicated the analysis of these samples and resulted in reduced sensitivity. To prevent the loss of sample material from the target face, brittle or crystalline samples were covered with a thin layer of mylar or plastic wrap.

Liquid specimens which have been analyzed at Duke include blood, urine, serum; tap, sea, and deionized water; gasoline, fuel oil, and acidic soil extracts. The water and gasoline samples were preconcentrated for improved sensitivity. The blood, urine, and serum analyses were made on deposits of the original untreated sample and on deposits of ashed samples. Results of these analyses are presented in Section IVA.

IIIE.4 Preconcentration procedures; benefits and handicaps

Sensitivity for a given specimen can be appreciably improved by using preconcentration techniques which include wet and dry ashing, use of ion exchange membranes, and condensing of liquid samples. The primary benefits to be gained by such methods are improved signal-to-noise ratios and higher counting rates yielding lower detection limits.

The effectiveness of preconcentration in the analysis of tap water is demonstrated in Figure 4.1a. Here we compare spectra obtained from 80 μℓ deposits on nuclepore of condensed

(100: 1 concentration) and unconcentrated tap water samples. The condensed sample was prepared by evaporating 100 mℓ of tap water to dryness and dissolving the residue in a solution containing 1 mℓ distilled deionized water and 0.1 mℓ of clean nitric acid. Compared to the untreated tap water spectrum, the concentrated sample yields improved counting statistics and better signal-to-noise ratios. The determination levels (at 10% precision) for the concentrated tap water sample were shown earlier in Figure 2.16 and indicate sensitivities between 1 and 10 ppb for $22 \leq Z \leq 40$. Corresponding determination levels for the unconcentrated sample ranged from 10-50 times higher when the sample was deposited on the same substrate.

It can be easily shown that if the concentration factor is F_C, and if we assume that the preconcentration techniques enhance only the characteristic X-ray yields and not the background, then the 3σ detection limit (d. l.) for the preconcentrated sample should scale according to the following: (1) for equal accumulated charge, d. l. scales as $(F_C)^{-1}$; (2) for equal peak areas or counting statistics, d.l. scales as $(F_C)^{-1/2}$. As an example, we would expect approximately 100-fold improvement in sensitivity for the concentrated water sample discussed above, whereas factors of only 10 to 50 improvement were actually observed. The factors which limit the improvements to be gained by preconcentration

are target thickness effects and enhanced background levels. Because of target thickness effects (proton energy loss and X-ray absorption), the effective irradiated mass increases more slowly than the concentration factor F_C. Our experience with preconcentration techniques suggests that it is very difficult to produce thin preconcentrated samples unless we are dealing with an ultra pure liquid such as deionized water. Secondly, the bremsstrahlung levels for preconcentrated samples do not remain the same as for the unconcentrated samples but are increased due to appreciable bremsstrahlung generated by the enhanced heavier elements themselves. The intensity of the bremsstrahlung produced by the interaction of protons or secondary electrons with target atoms of charge Z scales as Z^2. Therefore, techniques such as ashing which increase the effective Z of the target by removing the low Z organics, provide limited gains in terms of sensitivity.

Efforts to analyze gasoline using preconcentration methods have had limited success. Figure 4.4a (Section IVA.2), shows a spectrum obtained from the residue of 2.5 ml of gasoline. Sample preparation involved evaporating an initial volume of 5 ml of gasoline to dryness and dissolving the residue in 20 µl of distilled deionized water. Ten µl of the final solution was deposited on a nuclepore backing and dried in a dessicator. The resulting spectrum yields detectability limits of approximately 1 ppb for the elements Fe,

Cu, Zn, and Pb. Further improvement is possible by depositing on thinner substrates. Unfortunately, the evaporation process as well as placing of the sample in vacuum may result in significant losses of volatile elements, particularly the bromine which occurs in the additive $Pb(CH_3)_4Br$.

The use of ion-exchange membranes as preconcentrating sampling matrices shows promise particularly for the study of trace metals in various liquids (Lochmüller et al., 1974b). Ion-exchange membranes are impregnated with a cation exchange resin and when placed in a solution or stream containing metal ions, will absorb the ions until a point of equilibrium is reached, thus acting as preconcentration devices. The membranes have several attractive features: they are self-supporting and relatively impervious to beam heating; equilibration times are long and therefore the membranes tend to average out short-term perturbations in the environment being studied; very low levels of metal concentrations are obtained with minimal target preparation. Other preconcentration techniques would require impractical preparation and expense of time and effort to achieve similar detectability limits.

In Section IVA.1 measurements obtained with ion-exchange membranes which have been equilibrated in 1-liter solutions of deionized water containing varying concentrations of Pb are discussed. Clean signals have been observed with PIXE for concentrations as low as 0.002 ppm Pb representing 10^{-8} molar Pb concentration. It appears that detect-

ability limits in the ppb range are possible for certain metals, but further studies are necessary to determine the effects of selective uptake of metals in the membranes, as well as to establish quantitatively the relationship between solution concentrations and membrane concentrations for metals of interest.

Ashing as a method for sample preconcentration was discussed in detail in Section IIIE.2. Some results obtained with the method of wet ashing are presented in the following figures and tables. Figure 3.29 shows spectra obtained from ashed and pelletized samples of NBS orchard leaf. The spectra have been normalized to the same background levels in order to illustrate the improved sensitivity and signal-to-noise obtained with ashing. In this case, the minimum detectable concentrations for the ashed sample are a factor of 3-5 times lower than for the pellet. Table 3.11 presents a comparison between analyses of pelletized and ashed blood samples provided by the Environmental Protection Agency. The 3σ detection limits in parentheses indicate a factor of nearly 2 improvement in detection limits for the ashed sample over much of the elemental region. Note however the loss of K and Br in the ashed sample and the enhanced Zn signal which suggests possible contamination of the ashing solution. A similar comparison for coal is provided in Table 3.4. The gains in sensitivity afforded by ashing techniques are limited because of thick-target effects, and because of bremsstra-

Figure 3.29 Comparison of PIXE spectra obtained from analysis of ashed and pelletized samples of NBS orchard leaf. The spectra are normalized to the same background levels demonstrating the improved signal-to-noise obtained with the ashing procedure.

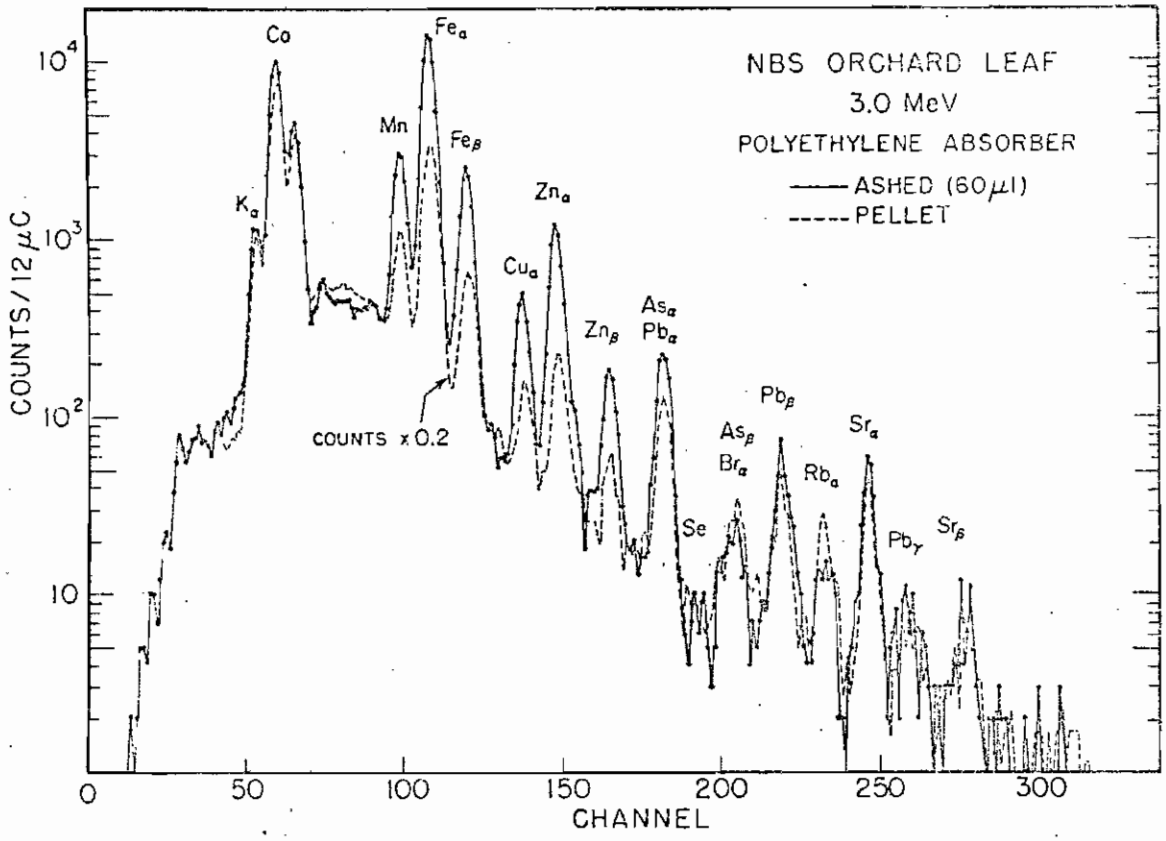
NBS ORCHARD LEAF
3.0 MeV
POLYETHYLENE ABSORBER
ASHED (60μl)
PELLET
COUNTS/12 μC
CHANNEL
COUNTS x 0.2
Co
Fe$_\alpha$
Mn
Fe$_\beta$
K$_\alpha$
Zn$_\alpha$
Cu$_\alpha$
Zn$_\beta$
As$_\alpha$
Pb$_\alpha$
Se
As$_\beta$
Br$_\alpha$
Pb$_\beta$
Rb$_\alpha$
Sr$_\alpha$
Pb$_\gamma$
Sr$_\beta$
10^4
10^3
10^2
10
0
50
100
150
200
250
300

Table 3.11

EPA Blood on ppm (wet weight) basis.

Element	Pellet	Ashed	Com. Lab
K	1650(3)	470(8)	
Ca	32(1.5)	60(3)	
Ti	(1.0)	(1.0)	
V	0.3(0.7)	0.0(0.7)	<0.5
Cr	0.0(0.6)	0.3(0.4)	0.02 → 0.2
Mn	0.7(0.5)	1.3(0.3)	0.1 → 0.4
Fe	550(0.4)	550(0.2)	433 → 550
Ni	0.0(0.3)	0.1(0.2)	0.01 → 0.3
Cu	2.0(0.2)	2.6(0.1)	0.4 → 0.8
Zn	9.6(0.2)	14.3(0.1)	2.2 → 10
As	0.1(0.2)	0.1(0.1)	0.0002 → 0.001
Se	0.1(0.2)	0.0(0.1)	0.09 → 0.15
Br	3.1(0.2)	0.2(0.1)	
Rb	2.0(0.2)	2.7(0.1)	
Sr	0.3(0.2)	0.1(0.2)	
Hg	0.0(0.7)	0.3(0.4)	0.001 → 0.002
Pb	0.4(0.5)	0.4(0.5)	0.10 → 0.15

Note: 3σ detection limits are indicated in parentheses.

hlung generated by the concentrated elements themselves and by insoluble or inorganic residues remaining in the ashed deposit.

In summary, preconcentration techniques offer the following advantages and disadvantages:

Advantages

1. Improved signal-to-noise (implying shorter counting times and/or lower detection limits).
2. Impurities in target backings assume less importance.
3. More representative results through sampling of a larger volume.

Disadvantages

1. Greatly increased preparation time.
2. Increased probability for introduction of impurities.
3. Loss of volatiles through evaporation or ashing.
4. Necessity for relatively large quantity of sample material.
5. Matrix effects must be considered (thick target X-ray absorption and proton energy considerations).

IIIE.5 Thin-target versus thick-target analysis

A topic which continues to be debated among PIXE analysts concerns the relative merits of thin-target and thick-target analyses. The question is discussed in detail by Willis et al. (1977a) and some of the conclusions will be presented here.

First let us summarize the strengths and weaknesses of the two approaches. From the standpoint of quantitative measurements it is in general preferable to use thin targets which require minimal or no corrections for matrix-dependent effects (X-ray absorption and proton energy loss). Additional advantages of solution-deposited thin targets are target homogeneity, ability to concentrate the sample, and the fact that thin targets are not subject to problems of charge accumulation and beam heating. The primary difficulty with thin targets is in their preparation; solution deposits of ashed residues is the technique most commonly used, and the numerous difficulties of this procedure have been discussed (Section IIIE.2).

Thick targets on the other hand offer advantages in terms of minimal sample preparation, high counting rates, and no unwanted background contributions from supporting substrates since these are not irradiated by the beam. Thick-target analyses have been criticized on the grounds that (1) correction factors for matrix-dependent effects are difficult to determine, (2) inhomogeneities within the target, surface irregularities, and loss of volatile elements due to beam heating may preclude quantitative measurements, and (3) the amount of sample irradiated is too small to be representative of the bulk sample.

In an attempt to investigate the relative accuracy, precision, and sensitivity of thick-target versus preconcen-

trated thin-targets, thin and thick targets prepared from NBS bovine liver (SRM 1577) were analyzed with the Duke PIXE system. Five thick pellets were prepared as described in Section IIIE.2 and irradiated on both sides. For thin targets, ashed solutions were prepared by a standard acid digestion procedure using a mixture of concentrated nitric and sulfuric acid. A sufficient amount of material (> 250 mg) was used to ensure a representative sample. Eight samples were carried individually through the same ashing procedure, and 20 µl deposits of each solution were made on nuclepore backings. Calibration of the ashed samples was accomplished by the addition of a known amount of Sr to the ashing solution. Concentrations reported for the pellets were determined using effective mass values calculated for a carbon matrix and adjusted for sample losses due to beam heating. All targets were irradiated with 10 µC of charge (approximately 10 minutes).

Results of the analyses were reported earlier in Table 3.6. Agreement between the NBS and PIXE values is good for both the ashed and pelletized samples with the exception of Se and Br in the ashed samples. These elements are volatilized during the ashing procedure.

The scatter in the PIXE measurements is indicated in Table 3.6 by the standard deviation of the measured values (in parentheses). Comparison of the standard deviation in the ashed and pellet samples indicates consistently less scatter in the pellet data even though the ashed targets

Table 3.12

Detection Limits for Pellets and Ashed Deposits of NBS Bovine Liver

	Nuclepore membrane		Bovine Liver ashed deposits		Bovine Liver pellets		Zero blanks	
	Fe	Sr	Fe	Sr	Fe	Sr	Fe	Sr
Blank (counts)	307	1.2	927	13.3	838	7.6	0	0
L_Q (ng)	2.8	14	4.4	17	4.2	16	L_Q^0=0.9	14
L_D (ng)	0.8	1.1	1.3	2.7	1.2	2.1	L_D^0=.02	0.4

were prepared from a representative sample and were presumably more homogeneous than the pellets.

Detection limits for the two types of targets are compared in Table 3.12 for the elements Fe and Sr. Following the usage of Currie (1968) and Section IIF.2, L_D (ng) is defined as the minimum abundance which will be detected by the analytical procedure at a specified level of confidence. The quantity L_Q (ng) is defined as the minimum abundance which can be determined quantitatively to a specified level of precision (here we use 10%). The results in Table 3.12 indicate that the detection limits for the thick pellets are as good as, or slightly better than those for the thin ashed samples.

These results suggest that under suitable conditions, thick-target analyses can provide comparable sensitivity and accuracy to thin-target analyses, and improved precision. Experimental results obtained for a number of biological samples give confidence in our ability to calculate appropriate target thickness correction factors (Section IIIC). Additional considerations relating to the precision and accuracy of thick-target measurements have been experimentally investigated and are discussed in Section IIIG. These considerations include: estimated uncertainties in the FUDGE calculations; sample losses due to beam heating; charging of insulating targets; X-ray absorption effects versus target angle; self-fluorescence; and surface irregularities. The

levels of uncertainty associated with these potential problems do not, in our opinion, rule out the use of thick targets for biological and environmental analyses.

The question of the relative sensitivity of thick-target versus thin-target analysis is considered in Section IIIF. Our own experimental results are in basic agreement with calculations by Folkmann (1976b) which predict that thick targets offer somewhat better sensitivity than thin targets in the region $Z < 30$, while this trend is reversed for heavier elements. Our experience with preconcentration techniques such as wet ashing indicates that while factors of 3 to 5 times can typically be gained in the sensitivity of biological analyses, it is very difficult to accurately maintain the thinness of such targets.

IIIF. PIXE Sensitivity

A major attraction of PIXE is the method's high sensitivity over a broad elemental range (e.g., Figure 2.14). By sensitivity we mean the detection limits L_D and L_Q (counts) and the corresponding minimum detectable concentrations T_D and T_Q (ppm) as defined in Section IIF.2. The discussion of PIXE sensitivity in Section IIF.2 focused on the optimization of the system's sensitivity via the choices of bombarding particle and energy. The following paragraphs discuss the manipulation of certain experimental parameters in order to obtain further improvement in sensitivity.

In order to determine how sensitivity scales as a function of various experimental parameters, it is convenient to employ the minimum detection limit L_D' given by the three sigma criterion:

$$L_D'(\text{counts}) = 3\sqrt{N_B}$$

where N_B is the number of background counts within an energy interval ΔE corresponding to the FWHM of the overlying X-ray signal. The minimum detectable concentration T_D' corresponding to L_D' counts is:

$$T_D'(\text{ppm}) = 3\sqrt{N_B}/(\varepsilon\ Q\ \bar{M})$$

where ε = thin-target response factor for the element of interest (counts/μg · μC)

Q = total integrated charge incident on the target (μC)

$\bar{M}$ = effective irradiated mass (g).

It is easily shown that for a <u>thin</u> uniform target,

$$T_D'(\text{ppm}) \propto (\Omega\ \Sigma_d\ N_p\ t_M)^{-1/2}\ (\Delta E)^{1/2}.$$

Here, Ω = detector solid angle (steradians)

Σ_d = detector efficiency for the element of interest (including absorption losses in window, filters, and air space)

N_p = number of protons incident on the sample

t_M = thickness of the target (g/cm^2) after rotation to angle θ.

ΔE = detector resolution (eV).

The scaling properties of the minimum detected concentration T_D'(ppm) are summarized in Table 3.13. Suggestions for optimizing the sensitivity are offered based on these scaling properties. In practice, the improvements in sensitivity are limited by practical considerations and/or conflicting constraints. For example, sensitivities can be improved by accumulating more charge on the sample (or equivalently, counting for a longer period of time), but limits are imposed by target damage due to excessive beam heating and the financial costs of longer runs. Likewise, increasing the area of the detector to improve sensitivity will likely be accompanied by a corresponding loss in detector resolution; moving the detector closer to the target may not be feasible because of counting rate limitations.

Some gains in sensitivity are possible by manipulating the counting rate R. For a typical sample, the majority of X-rays entering the detector are low-energy X-rays. The use of low-Z filters to reduce this often excessive counting rate, effectively improves sensitivity for more energetic X-rays. Counting rate performance can be further improved by pulse pile-up rejection as is done at Duke. Optimal performance at high counting rates is obtained by employing triggered beam pulsing (Cahill, 1975; Koenig et al., 1977). It appears

Table 3.13

Scaling Properties of Minimum Detectable Concentration T_D'(ppm)

Experimental Parameter:	T_D' scales as:	Comments:
1. Detector solid angle: (Ω)	$(\Omega)^{-1/2}$	1) Decrease detector-target distance 2) Increase detector area Limitations: counting rate R, resolution ΔE
2. Detector resolution: (ΔE)	$(\Delta E)^{1/2}$	1) Avoid excessive counting rates
3. Integrated charge: (Q)	$(Q)^{-1/2}$	1) Use higher currents for same analysis time or 2) Longer analysis time at same current Limitations: counting rate R, target damage, economic costs
4. Counting rate: (R)	$(R)^{-1/2}$	Limitations: electronic pulse-processing time requirements 1) Use low-energy filtration 2) Use pulse pile-up rejection or pulsed beam for optimum high countrate performance
5. Analysis time: (t)	$(t)^{-1/2}$	For same beam current Limitations: cost of accelerator use
6. Target thickness: (t_M)	$(t_M)^{-1/2}$	For <u>thin</u> targets--e.g., $t_M \lesssim 1$ mg/cm^2 See <u>text</u> for thick targets

possible using a pulsed beam to increase the output counting rate by factors of 1 to 5 times the output rate provided by conventional electronic pile-up rejection. Such increases would improve sensitivity by as much as a factor of 2.

Sensitivity for thin targets is improved by increasing the target thickness t_M within the constraint that $t_M \lesssim 1$ mg/cm^2. For greater target thicknesses, X-ray absorption and proton energy loss affect the sensitivity in a complex way. The question of the relative sensitivity of thick-target vs. thin-target analysis has been investigated by Folkmann (1976b) who calculated the minimum concentration giving a peak to background ratio of 1. The results of these calculations for 3-MeV protons on thick and thin carbon matrices are shown in Figure 3.30. These results indicate that in favorable circumstances, thick targets provide better sensitivities for light elements ($17 \lesssim Z \lesssim 30$) while thin targets yield better sensitivities for heavier elements. Thick and thin-target sensitivities merge for extremely low-energy X-rays ($Z \lesssim 17$) since the majority of these X-rays are produced only in the outermost (thin) layer of the target.

Experimental data obtained in our work is in essential agreement with Folkmann's calculations. Figure 3.31 compares PIXE spectra obtained from pelletized placenta and a thin layer of the same sample. The effective irradiated mass for the thin layer was determined to be approximately

Figure 3.30 Calculated concentrations yielding a peak to background ratio of 1 for 3-MeV protons on thick and thin carbon matrices. Calculation assumes a target rotation angle of 45°. Note the convergence of the two curves at low atomic number. (Adapted from Folkmann, 1976b).

Figure 3.31 PIXE spectra obtained from analysis of a thin layer and a thick pellet of lyophilized placenta tissue. Note the improved sensitivity for the pellet for elements lighter than Zn.

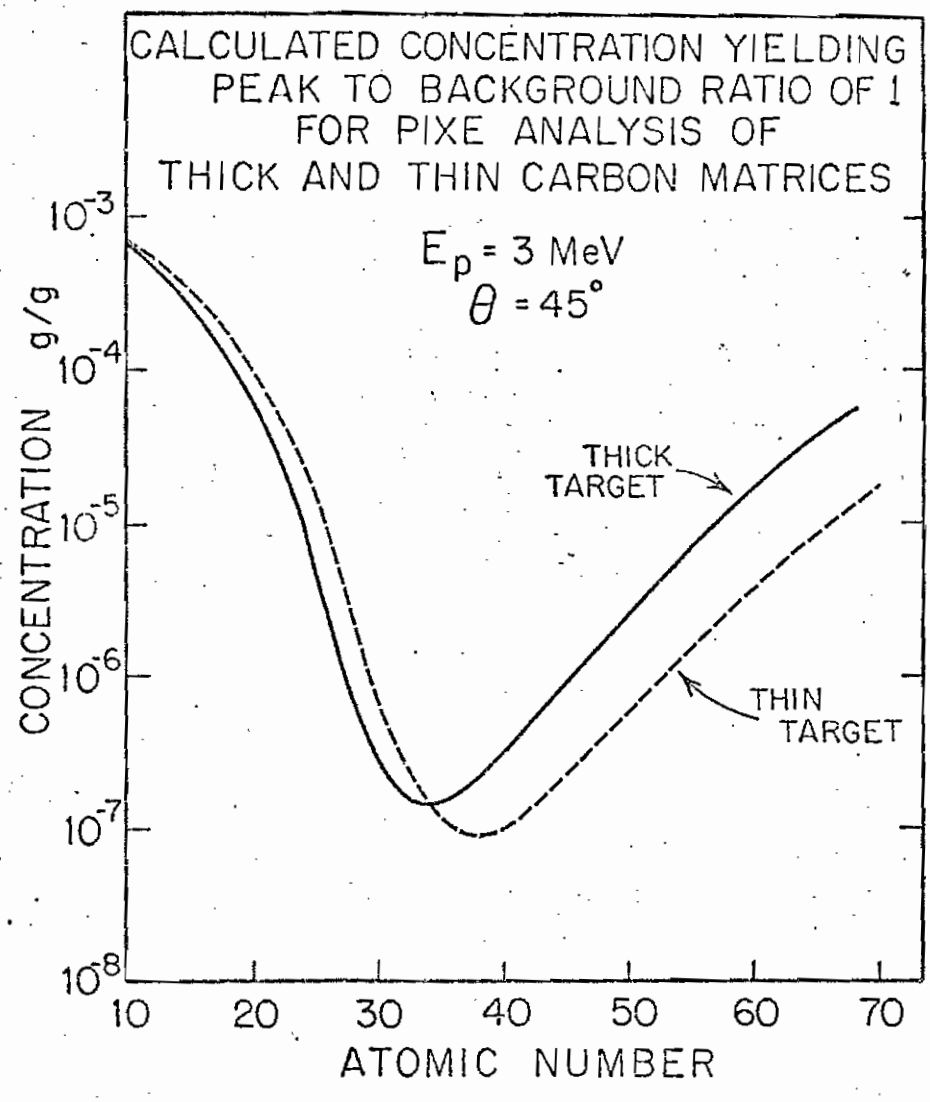
CALCULATED CONCENTRATION YIELDING
PEAK TO BACKGROUND RATIO OF 1
FOR PIXE ANALYSIS OF
THICK AND THIN CARBON MATRICES
E_p = 3 MeV
θ = 45°
THICK TARGET
THIN TARGET
CONCENTRATION g/g
10^{-3}
10^{-4}
10^{-5}
10^{-6}
10^{-7}
10^{-8}
10
20
30
40
50
60
70
ATOMIC NUMBER

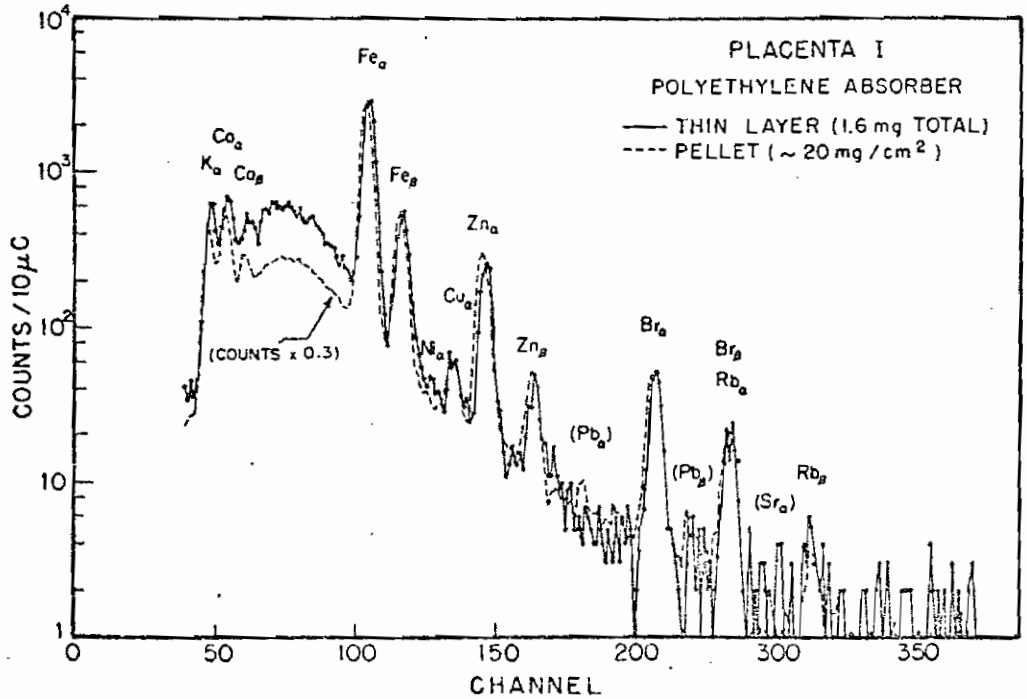
PLACENTA I
POLYETHYLENE ABSORBER
THIN LAYER (1.6 mg TOTAL)
PELLET (~ 20 mg/cm²)
COUNTS / 10 μC
10^4
10^3
10^2
10
1
Co_α
K_α Co_β
Fe_α
Fe_β
Zn_α
Cu_α
Ni_α
Zn_β
(Pb_α)
Br_α
Br_β
Rb_α
(Pb_β)
(Sr_α)
Rb_β
(COUNTS x 0.3)
0
50
100
150
200
300
350
CHANNEL

Table 3.14

NBS ORCHARD LEAVES (SRM 1571)

Element	Thin Layer ppm(d.l.)	Pellet ppm(d.l.)	Ashed ppm(d.l.)	NBS ppm ± Δppm
K	21,000(40)	22,000(30)	16,000(10)	14,700 ± 300
Ca	15,700(20)	18,000(20)	13,000(5)	20,900 ± 300
Ti	15(12)	6(7)	1.9(2)	
V	0.0(8)	0.0(6)	2.2(2)	
Cr	1.0(5)	0.0(5)	0.5(2)	2.6 ± 0.3
Mn	89(4)	93(3)	56(0.7)	91 ± 4
Fe	(300)(3)	(300)(2)	(300)(0.6)	300 ± 20
Ni	2.4(1.5)	1.1(1.4)	1.5(0.5)	1.3 ± 0.2
Cu	15(1)	12(1.3)	9(0.5)	12 ± 1
Zn	30(1)	26(1.3)		25 ± 3
As	14(1)	12(2)	12(0.4)	10 ± 2
Se	1.5(1)	1.2(2)	0.0(0.4)	0.08 ± 0.01
Br	13(1)	22(2)	0.6(0.4)	(10)
Rb	12(1)	13(2)	10(0.6)	12 ± 1
Sr	33(1)	34(3)	35(0.5)	(37)
Zr	(151)(1)	3(4)	0.6(0.6)	
Ba	33(45)	30(40)	20(14)	
Hg	4(4)	6(8)	0.0(3)	0.155 ± 0.015
Pb	51(3)	40(6)	31(2)	45 ± 3

0.8 mg compared to an effective mass of 2.7 mg for the pellet. Analysis of these spectra indicates that ppm detection limits for the pellet are from 1 to 2 times lower than the corresponding thin-target detection limits for elements lighter than Zn (Z = 30). For Z > 30 pellet sensitivities begin to deteriorate as the background rises relative to the thin sample. In this region, detection limits for the thin layer are 1 to 3 times lower than those for the pellet. Similar results are reported in Table 3.14 comparing pelletized, ashed, and thin layer targets of NBS orchard leaf. Here the pellet shows perhaps slightly better sensitivity for the lighter elements and steadily deteriorating sensitivity relative to the thin layer for the heavier elements.

One can calculate approximate detection limits by assuming reasonable values for the determining experimental parameters. Such calculations were shown earlier in Figure 2.18 (from Folkmann, 1974b) for 3-MeV proton bombardment of a thin carbon matrix. These calculations indicate that concentrations as low as 0.1 ppm might be detected for selected elements. In Table 3.15 we have summarized experimental PIXE detection limits (using the 3σ criterion) for six elements and a variety of specimens and sample types. The six elements listed cover most of the detectable range of elements. The detection limits are based on an accumulated charge of 10 μC which is typical for a PIXE run. This is equivalent to a 250 sec irradiation period with 40 nA of

Table 3.15

PIXE detectability limits for 10 μc of charge and for 0.4 cm^2 of irradiated area

Sample (type)	Coal (pellet)	Fuel Oil (on Nuclepore)	Orchard Leaf (pellet)	Placenta (pellet)	Blood (pellet)	Hair (6 cm-whole)
Element	ppm	ppm	ppm	ppm	Wet wt.ppm	ppm
K	60	11	30	100	3	10
Mn	4	2.5	3	0.7	0.5	2
Cu	2	0.6	1.3	0.4	0.2	1.0
As	1.2	0.6	2	0.5	0.2	0.8
Sr	3	1.0	3	0.5	0.2	0.6
Pb	5	1.8	6	0.8	0.5	1.2

Sample (type)	Human Tissue (30 μm section)	Fish Muscle (Whole)	Leaves (Whole)	Tap Water (condensed 100:1)	Mylar Blank (4 μm)	Nuclepore Air Filter (1 mg/cm^2)
Element	dry wt. ppm	wet wt. ppm	ppm	wet wt.ppm	ng/0.4 cm^2	ng/0.4 cm^2
K	250	40	60	0.016	5.1	10
Mn	2.3	0.6	2.4	0.0007	1.8	1.5
Cu	0.8	0.1	1.3	0.0004	0.4	0.5
As	0.6	0.1	2.4	0.0004	0.3	0.6
Sr	0.5	0.3	3.5	0.0008	0.4	1.0
Pb	1.4	0.8	12.6	0.0016	0.8	2.0

beam. In general, the type of sample (pellet, deposit, etc.) was the one which proved most satisfactory for that particular specimen. Detection limits for K have been extracted from spectra taken with the mylar absorber, while the remaining values apply to data taken with the polyethylene absorber.

Several features are to be observed in Table 3.15. Dry weight detection limits typically range between 0.5 and 5 ppm for the elements between Cu and Sr. The values quoted in Table 3.15 are the interference-free detection limits and are therefore somewhat better than can be expected for samples which present serious interference problems, as is the case for example in the determination of Co in an iron-rich specimen such as blood. The deterioration of the detection limits for elements lighter than Fe reflects the increased bremsstrahlung background in this region.

Certain specimens exhibit atypical detection limits due to their particular elemental compositions. The relatively high detection limits in the roadside leaf specimens for the As to Pb region result from this specimen's unusually large Br concentration. The low energy tail of the Br peak raises the background levels (hence detection limits) for elements whose X-ray lines appear on the low energy side of Br. Also shown in Table 3.15 are the detection limits in ng/0.4 cm^2 for aerosol deposits on nuclepore filters indicating detection limits near the 1 ng/0.4 cm^2 level for most elements of interest.

It is possible as discussed in Section IIIE.4 to obtain substantial improvements in sensitivity by preconcentrating certain samples--typically by ashing or condensing the sample material. The benefits of preconcentrating techniques are evident in the extremely low detection limits observed for the condensed tap water sample.

The results of Table 3.15 are in good agreement with the expected detection limits calculated by Folkmann et al. (1974b), and also agree well with the 1-5 ppm detection limits reported by Cooper (1973) for elements between V and Mo. Further experimental results from Duke will be presented in Chapters IV and V.

One can also consider the sensitivity of PIXE in terms of the minimum detectable mass. For most of the samples of interest at Duke, a minimum detectable concentration of 1 ppm represents a detected mass of $\gtrsim 10^{-9}$ g. By using a focused beam, much smaller quantities can be detected. If ppm sensitivity can be maintained down to microbeam dimensions (e.g., 10 μm beam diameters) then it might be possible to detect abundances as low as 10^{-15} g.

IIIG. Accuracy and Precision Considerations

Tables 3.16 and 3.17 to be described below summarize the factors which determine the accuracy and precision of PIXE analyses. When possible, reasonable estimates of the corresponding uncertainties are included. These apply to

the system presently operating at Duke and should not be viewed as optimum values.

IIIG.1 Accuracy

The accuracy of PIXE analyses for both thick and thin targets is determined primarily by the system calibration. For thin targets, our calibration is based on measurements of solution deposited standards (Section IIIC.2). This calibration has been checked on numerous occasions with freshly prepared calibrated standards. Independent checks on the system calibration have been provided by analyses of NBS SRM's and the results of interlaboratory comparisons (Section IIIC.5). Based on these results, we estimate the uncertainty in our thin-target calibration to be 10% or less for elements between K and Mo (excluding Ca which requires recalibration). For heavier elements, the calibration uncertainty is somewhat higher. The calibration uncertainty includes contributions arising from target preparation, peak fitting errors, and changes in target-detector geometry which may have occurred since the initial system calibration.

The calibration for thick targets is determined by correction factors calculated by the program FUDGE and applied to the thin-target calibration. For an ideal, homogeneous thick target, the bulk composition of which is known, we estimate the uncertainties in the FUDGE calculations to be approximately 15% (Appendix A). The total uncertainty in

Table 3.16

Factors Determining Accuracy of PIXE

	Factor	% Uncertainty	Remarks
1.	System calibration		
	Thin targets:	10% for $19 \leq Z \leq 42$ (except Ca) 10-20% for $Z > 42$	Uncertainties include: target preparation, peak fitting errors, changes in detection geometry.
	Thick targets:	20-25%	
2.	Peak statistics:	$100 \cdot (N_x)^{-1/2}$ %	
3.	Charge integration		
	Instrumental:	< 1%	
	Leakage current:	< 2% for $I \geq 10$ nA	For I<10 nA, leakage current must be considered.
4.	Deadtime correction:	negligible	
5.	Beam energy:	2%	
6.	Beam intensity profile:	few percent	Uncertainties due to beam non-uniformities and non-rectangularity of beam profile.
7.	Irradiated sample area: Area = $\pi r^2/\cos\theta$	6%	Uncertainty applies to mass per unit area determinations.
8.	TRACE fitting errors:	variable	Uncertainties include: background determination, peak area calculation, and interelement interference corrections.

the thick-target calibration is estimated to be roughly 20%.

Uncertainties in the total accumulated charge can arise due to instrumental error (< 1%) or "leakage current" problems. Leakage current is the current which is measured by the current integrator when there is no proton beam in the irradiation chamber. During the course of a run the leakage current is periodically monitored for fluctuations. The leakage current on the Duke PIXE system is typically 0.6 nA ± 0.2 nA. The amount of uncertainty introduced into the accumulated proton charge by this much leakage current depends on how much proton current is run on the sample. Failure to correct for current leakage fluctuations can result in errors of 2% or less in the integrated proton charge for beam currents greater than 10 nA.

Uncertainties in the proton beam energy also contribute to uncertainties in elemental abundances. Energy calibration tests made during the past three years indicate that the uncertainty in the beam energy is usually less than 20 keV out of 3 MeV (< 1%). This results in an uncertainty in the proton-induced X-ray yield of approximately 2% or less.

The non-rectangularity of the beam profile (Figure 3.2) as well as the ±10% fluctuations observed in the beam intensity across the central region of the beam contribute small uncertainties in analyses for target diameters > 3 mm. Uncertainties of approximately 6% or less in the determination of the irradiated sample area for large-area samples

contribute to the total uncertainty in mass per unit area determinations.

Finally, data analysis with TRACE introduces uncertainties through the background determination, peak area calculation, and interelement interference corrections. These uncertainties cannot be estimated for the general case however.

In Section IIIE.5 we reported the results from PIXE analyses of ashed and pelletized NBS bovine liver (SRM 1577). The agreement of both sets of samples with the NBS values was found to be 14% or better for elements present in concentrations greater than 10 ppm. We consider this to be a reasonable measure of the overall accuracy of the present PIXE system at Duke.

IIIG.2 Precision

Table 3.17 summarizes the factors affecting the precision of PIXE measurements. A number of these factors were previously discussed as they affect PIXE accuracy. Additional factors affecting system reproducibility during and between experimental runs include the target rotation angle (reproducible to ±1°) and the target-detector geometry (solid angle reproducible to ±2%). In the following paragraphs, some precision considerations for thick-target analyses will be discussed.

Table 3.17

Factors Determining Precision of PIXE

	Factor	% Uncertainty	Remarks
1.	Peak statistics	$100 \cdot (N_x)^{-1/2}$ %	
2.	Charge integration	< 2% for I > 10 nA	Uncertainty primarily due to fluctuations in leakage current.
3.	Beam intensity profile	few percent	Affects reproducibility of spot deposits and non-uniform targets larger than the beam.
4.	Target angle	1% (for thin targets)	
5.	Target-detector geometry	2%	
6.	Beam energy	< 2%	
7.	TRACE fitting errors	variable	
8.	Volatilization	variable	Due to vacuum volatilization and beam heating effects.
	THICK-TARGET ANALYSIS		
9.	Volatization	variable	Particularly severe for K, Br, As, Se, Cd, Hg and organic compounds.
10.	Target non-uniformities	variable	Surface and depth non-uniformities
11.	Target angle	< 3% for soft X-rays	Corrections calculated by FUDGE
12.	Enhancement effects	< 2-3%	For typical biological specimens
13.	Target charging	negligible	Eliminated by heated filament
14.	Fitting errors (K_β: K_α intensity ratios)	∿ 1% for soft X-rays	
15.	Surface irregularities	variable	

A source of concern in PIXE analysis is the possible loss of volatile elements, particularly K, Br, Hg, As, Se, and Cd. Such losses may occur because of excessive sample heating or because of the requirement that the sample be placed in vacuum. Volatilization due to beam heating is of particular concern for thick samples in which some or all of the energy of the proton beam is absorbed by the sample in the form of heat. The problem of volatilization losses and sample deterioration for different modes of sample excitation (X-ray, protons, and electrons) is examined in some detail in the article by Shaw and Willis (1977).

Several researchers have reported results of beam heating volatility tests in the literature. Johansson et al. (1975) observed no significant losses of any elements present in aerosol samples. Campbell et al. (1974, 1975) investigated volatility losses in wet-digested samples of liver and kidney deposited on thin carbon backings. These targets were irradiated for 1 hour at 0.5 μA of current and no sample losses were observed. Valkovic et al. (1975) detected losses of K and Br from samples of blood serum deposited on aluminized formvar backings and irradiated with 150 nA of beam; no other elements were volatilized for currents below a few hundred nanoamperes. These results suggest that volatilization losses for thin targets on heat-conductive backings are insignificant with the possible exceptions of K and Br.

Less information is available concerning volatili-

zation losses in thick samples. Willis et al. (1977a) reported some results of beam heating tests conducted on thick biological samples. These tests consisted of making a number of successive runs on the same sample, often at increasing beam currents, and allowing the beam to remain on target in between periods of data accumulation. Table 3.18 summarizes the results for 3-MeV protons for four successive analyses of a thick section of crab muscle using a beam current of 80 nA--nearly twice the current typically used on this type of sample. Of the elements listed, only As shows evidence of evaporation. Similar tests have been conducted on thick leaf specimens and fish muscle with no losses observed. On the other hand, thick slices of rat liver containing large concentrations of Hg and irradiated at 60 nA show rapid Hg losses (Figure 3.32). Since beam-heating losses are matrix dependent, and tests such as those of Table 3.18 are easily conducted, we recommend that similar tests be conducted on specimens of interest in order to evaluate the likelihood of volatilization losses.

The effects of beam heating are not restricted to the volatilization of trace elements in the sample. Perhaps the greatest single contribution to imprecision in thick-target analyses is sample deterioration and the volatilization of organic compounds in the target matrix. The selective vaporization of the organic matrix of thick biological samples effectively enhances the concentration levels of the inorganic

Table 3.18

Evaporation test with 80 nA of 3-MeV protons incident on a thick section of crab muscle. Values given in ppm (dry weight).

Element	Run 1 (ppm)	Run 2 (ppm)	Run 3 (ppm)	Run 4 (ppm)	mdl (ppm)
K	9200	9900	10600	10200	70
Ca	1000	1070	1090	1050	20
Ti	3	5	0.0	2	5
V	0.6	4.7	0.0	2.8	4
Mn	3	2	2	1	1.5
Fe	34	31	31	31	1.2
Ni	0.1	1.8	1.3	1.2	1.0
Cu	22	23	24	23	1.0
Zn	333	352	358	357	0.8
As	24.8	19.9	16.6	16.0	0.8
Se	4.7	2.8	1.9	2.2	0.8
Br	37.3	40.1	29.6	41.4	1.0
Rb	5.3	4.3	5.4	5.2	1.0
Sr	24.6	27.0	22.4	23.2	1.0
Pb	0.0	0.5	0.3	0.0	3.0
Acc. μC[a]	0	50	100	150	
Time elapsed[b]	0	10	20	30	

a Total accumulated charge in μC at the beginning of run.

b Total time in min that beam was on target before beginning run.

Figure 3.32 PIXE spectrum of rat liver indicating the loss of Hg due to beam heating. Beam current was 60 nA.

Figure 3.33 Measurements of beam heating effects on bovine liver pellets. The percent increase in effective mass for Fe, Zn, and Cu is shown as a function of the amount of charge accumulated on target. See text for discussion.

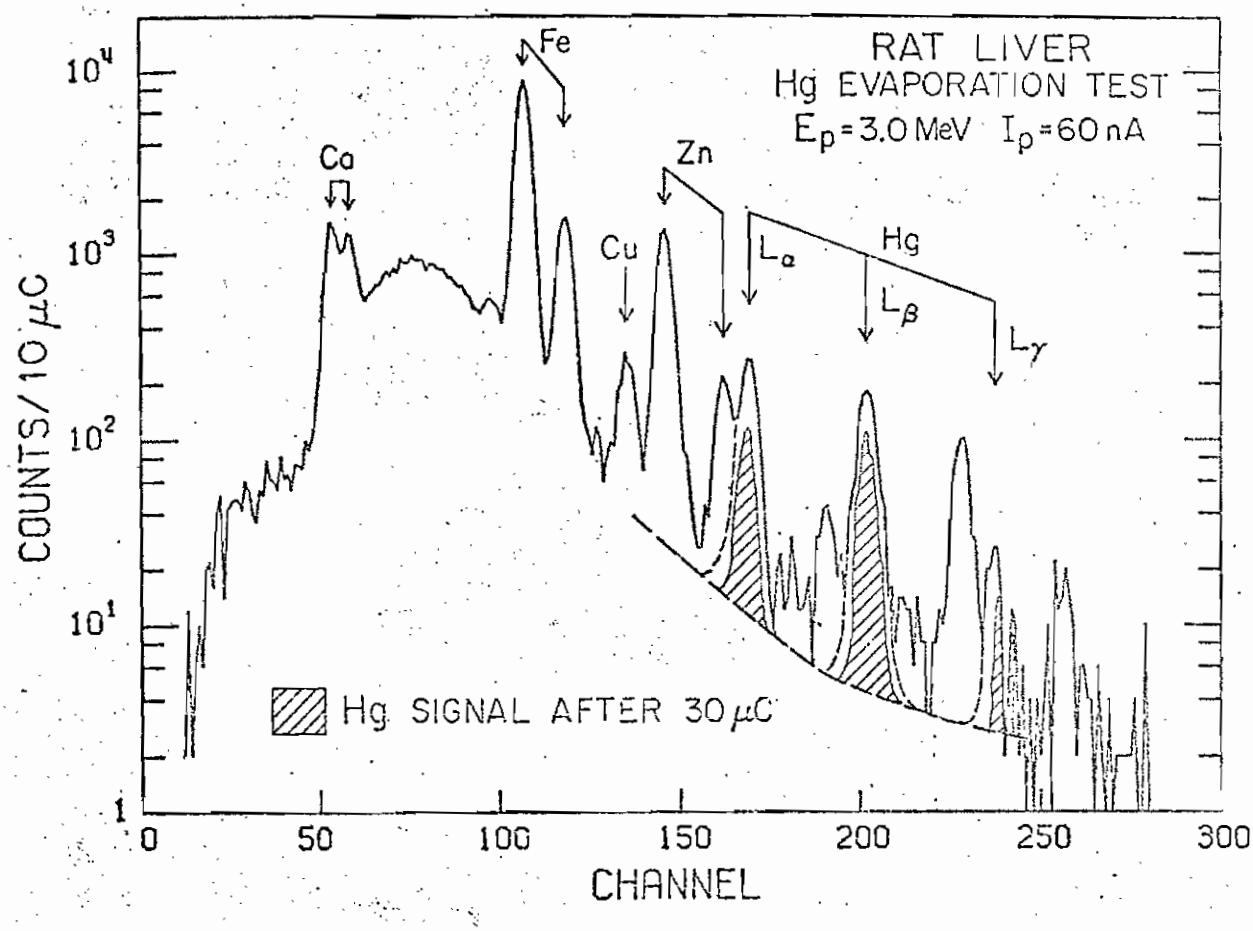
RAT LIVER
Hg EVAPORATION TEST
E_p=3.0 MeV I_p=60 nA
Ca
Fe
Cu
Zn
Hg
L_α
L_β
L_γ
Hg SIGNAL AFTER 30 μC
COUNTS/10 μC
CHANNEL

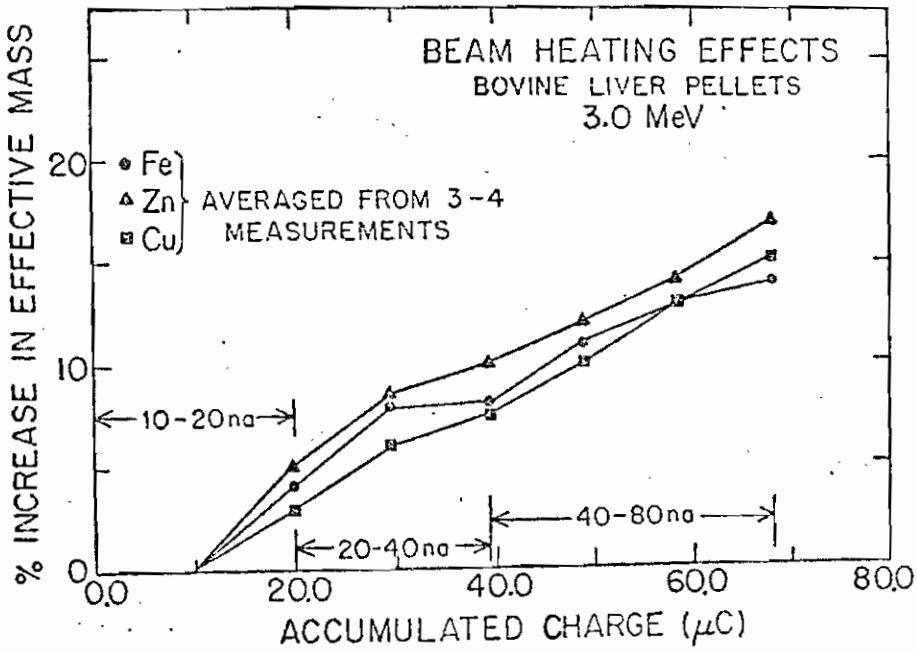
BEAM HEATING EFFECTS
BOVINE LIVER PELLETS
3.0 MeV
Fe
Zn
Cu
AVERAGED FROM 3-4 MEASUREMENTS
10-20na
20-40na
40-80na
% INCREASE IN EFFECTIVE MASS
ACCUMULATED CHARGE (μC)

constituents thus jeopardizing quantitative analysis. This effect has been observed most dramatically in thick pellets of bovine liver. Figure 3.33 shows the percent increase in the effective irradiated mass of bovine liver as a function of accumulated charge on the target. The effective mass values for Figure 3.33 are based on the measured X-ray yields for the elements Fe, Cu, and Zn.

Several features are of note in Figure 3.33. After approximately 70 μC of accumulated charge, with beam currents as shown in the figure, the effective mass values are increased by nearly 15% relative to the corresponding values determined for 10 μC. For lighter elements, the effective mass is more sensitive to X-ray absorption losses in the sample matrix; hence, vaporization of the matrix should result in even greater increases in the effective mass values for low Z elements. Evidence for this was observed for K, but the results were not conclusive--possibly because of the simultaneous volatilization of the K. It is interesting to note in Figure 3.33 that the rate at which the organic matrix is vaporized does not appear to be a function of the beam current. Rather, the vaporization occurs most rapidly during the initial irradiation period. Extrapolation of the beam heating curves back to zero μC would suggest an additional 5% increase in the effective mass during the first 10 μC of irradiation. The effects shown in Figure 3.33 can only be

predicted by conducting similar tests on each type of specimen. Failure to account for these sample losses may result in errors approaching 10-15%.

Another potential problem with thick-target analysis is charge accumulation in the target resulting in excessive bremsstrahlung background due to voltage breakdown. This problem can be very satisfactorily eliminated by the introduction in the target chamber of a heated filament which neutralizes the target (Section IIIB.2). The effect of the filament on the quality of PIXE spectra was shown earlier in Figure 3.5.

Quantitative analyses for low Z elements (X-ray energies < 4 keV) in thick samples are extremely difficult for a number of reasons. Although the irradiated mass of an infinitely thick sample is independent of the target angle θ, the detected X-ray yields show a θ-dependence due to X-ray absorption effects. These effects are particularly severe for X-ray energies < 4 keV. Several angle rotation tests have been conducted on infinitely thick targets in an effort to quantify this θ-dependence. The results from such a test on two infinitely thick placenta pellets are presented in Table 3.19 for target angles of 25°, 35°, and 45°. As expected, the absorption effects are most noticeable for K and Ca. The observed changes in the X-ray yields are approximately 30% for K and 27% for Ca for $\Delta\theta = \pm 10°$ about a target angle of 35°. The same change in θ produces less than a 5% change in the X-ray yields for Zn. For normal

Table 3.19

Placenta: tests of absorption as function of specimen inclination angle[a].

Element	10.8 mg pellet (ng/0.4cm^2)			22.4 mg pellet (ng/0.4 cm^2)		
	25°	35°	45°	25°	35°	45°
K	19000	26000	31000	19000	27000	36000
Ca	1200	1600	2000	1100	1600	1900
Fe	1440	1690	1790	1990	2250	2480
Zn	210	230	200	210	220	230

[a] No absorption correction applied.

operation, we set $\theta = 30°$ or $35°$, and we estimate our error in measuring this angle to be $\pm 1°$. According to Table 3.19 such an error leads to uncertainties in the K and Ca abundances of approximately $\pm 3\%$ and $\pm 2.5\%$ respectively. Recall that correction factors which take into account absorption losses for specific target angles are calculated with program FUDGE.

In thick targets, the possibility of enhanced X-ray yields due to secondary excitation cannot be ignored. The only source of importance according to Ahlberg (1977) for secondary excitation is primary induced X-rays. Maximum enhancement occurs for elements whose K- or L-shell absorption edge lies immediately below the energy of the primary radiation. Examples which are of particular concern for biological specimens are the enhancement of Cr by an abundant Fe concentration, and the enhancement of K by a strong Ca signal. Calculations by Ahlberg (1976, 1977) of enhancement effects in tooth enamel (40% Ca) and pure Fe give enhancements of approximately 15% for K and 45% for Cr respectively, when using 2.5 MeV protons. Such concentrations however are very atypical of most biological samples. The dry weight concentration of Fe in blood for example is approximately 0.3%. To a first order approximation, the enhancement effect scales linearly with the concentration of the abundant element (Ahlberg, 1977) so that for Fe and Ca concentrations below 5%, the expected enhancements of Cr and K respectively are

on the order of 2-3% or less.

Another problem adding to the difficulties of obtaining quantitative results for light elements in thick samples is the increased K_β/K_α intensity ratios in thick targets relative to the ratios for thin targets (used for calibration) due to the greater transmission of the more energetic K_β X-rays through the sample en route to the detector. For an infinitely thick sample of $(CH_2)_n$ (polyethylene) oriented at 30°, this effect produces an increase of 8% in the β/α intensity ratio for K (and somewhat less for Ca). The potassium K_β/K_α ratio is required in extracting the Ca peak area since the potassium K_β X-ray underlies the Ca K_α peak. Our spectrum analysis program which extracts X-ray peak areas and calculates elemental abundances uses intensity ratios which are based on thin-target spectra. In using the thin-target ratio to extract the Ca K_α peak area for a thick sample, the Ca abundance will be overestimated by a factor estimated to be between 0.6% and 1.1% of the K abundance unless suitable corrections are applied.

Some additional sources of uncertainty in thick-target analysis which can only be evaluated on an individual basis are target inhomogeneities, both on the surface and as a function of depth, and surface irregularities. These are part of the price one pays in return for the positive benefit of minimal sample preparation. Target inhomogeneities combined with non-uniformities in the beam intensity profile can

result in appreciable uncertainties in the measured elemental abundances. Irregular surfaces can significantly alter the absorption of soft X-rays as calculated by FUDGE for a smooth surface. A detailed discussion of these effects is given by Ahlberg (1975).

The analysis of replicate ashed and pelletized bovine liver samples discussed in Section IIIE.5 provides a measure of the overall precision of the Duke PIXE system including target inhomogeneities and errors introduced by the ashing procedure. The mean elemental concentrations and the standard deviations for both preparation techniques were shown earlier in Table 3.6. These results indicate a precision of 12% or better for elements which are present in concentrations of 10 ppm or greater. For thin samples which do not require ashing, the precision should be somewhat better.

CHAPTER IV

APPLICATIONS: GENERAL SURVEY

During the past four years the Duke PIXE system has made a major contribution to the stature of PIXE by demonstrating the applicability of the technique to a broad range of analytical problems. The major thrust of the efforts at Duke has been the analysis of biological and environmental samples. Several major in-depth studies have been conducted related to these areas and are described in Chapter V. In addition, we have conducted analyses of a great variety of sample materials in the course of investigating new areas of PIXE applicability. A brief survey of many of these applications is presented in this chapter. It is our hope that the following two chapters will serve to demonstrate the powerful capabilities of the PIXE technique for multielemental analysis. Additional applications by other researchers to the analysis of biological samples, aerosols, and miscellaneous samples are presented in the proceedings of the recent conference on PIXE held in Lund, Sweden (Nucl. Instrum. Methods, 142 (1977)). For convenience, the areas of application to be reviewed are grouped into three arbitrary and

overlapping categories: environmental, soil and botanical, and biomedical studies.

IVA Environmental Applications

IVA.1 Water Analysis

PIXE has been applied to the analysis of fresh water samples collected from the tap, from wells, and from fresh-water streams. Several preparation procedures were investigated including spot deposits of the original sample onto a thin backing, preconcentration of the sample followed by spot deposits, and the use of ion-exchange membranes for sample collection.

The maximum permissible levels established by the EPA for selected inorganic contaminants (Cr, As, Se, Pb, Hg, Cd, Ba, Ag) in drinking water are 50 ppb or less. In order to attain such levels of sensitivity using PIXE, the inorganic constituents in the water sample must be concentrated. Figure 4.1a shows the spectra obtained from analyses of plain and condensed (100:1) tap water. The preparation procedure for the condensed sample was described earlier in Section IIIE.4. The plain tap water sample was prepared simply by depositing 80 μl of the sample onto a nuclepore backing. Comparison of the background levels in Figure 4.1a indicates a factor of 10-50 gain in sensitivity using preconcentration. Abundances or upper limits for 12 elements in tap water are

Figure 4.1a PIXE spectra from the analysis of plain and condensed (100:1) tap water. The substrate is a nuclepore membrane.

Figure 4.1b PIXE spectra of condensed tap water using 2.5-MeV (solid curve) and 3.0-MeV (dashed curve) protons. The spectra have been normalized to the same characteristic X-ray yields in order to demonstrate the improvement in signal-to-noise by using 2.5-MeV excitation. Elemental abundances (ppb) or upper limits are listed for 12 elements.

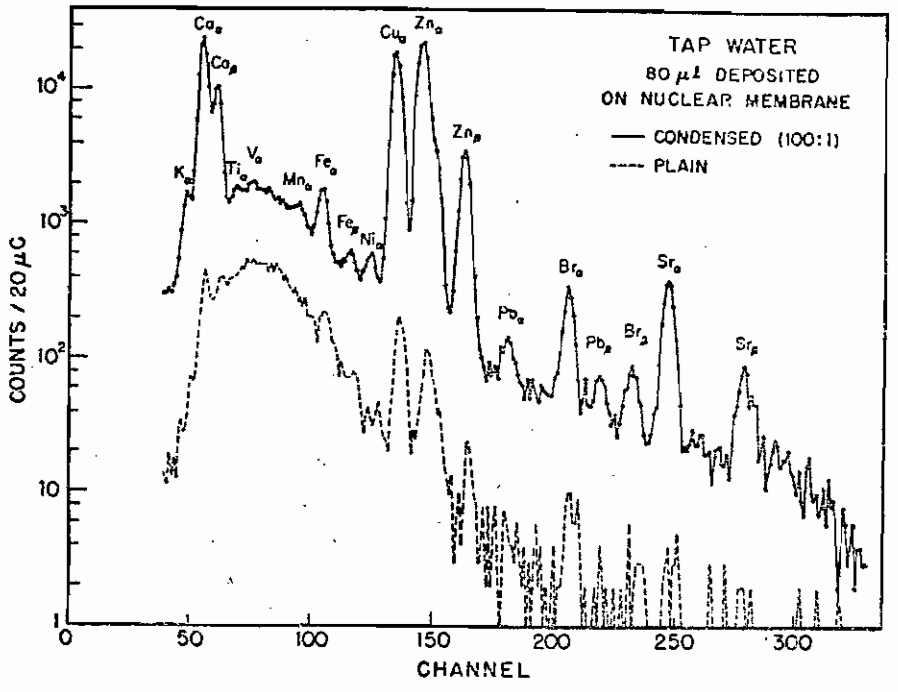
TAP WATER
80 μl DEPOSITED
ON NUCLEAR MEMBRANE
CONDENSED (100:1)
PLAIN
COUNTS / 20 μC
CHANNEL
Ca$_\alpha$
Ca$_\beta$
K$_\alpha$
Ti$_\alpha$
V$_\alpha$
Mn$_\alpha$
Fe$_\alpha$
Fe$_\beta$
Ni$_\alpha$
Cu$_\alpha$
Zn$_\alpha$
Zn$_\beta$
Pb$_\alpha$
Br$_\alpha$
Pb$_\beta$
Br$_\beta$
Sr$_\alpha$
Sr$_\beta$

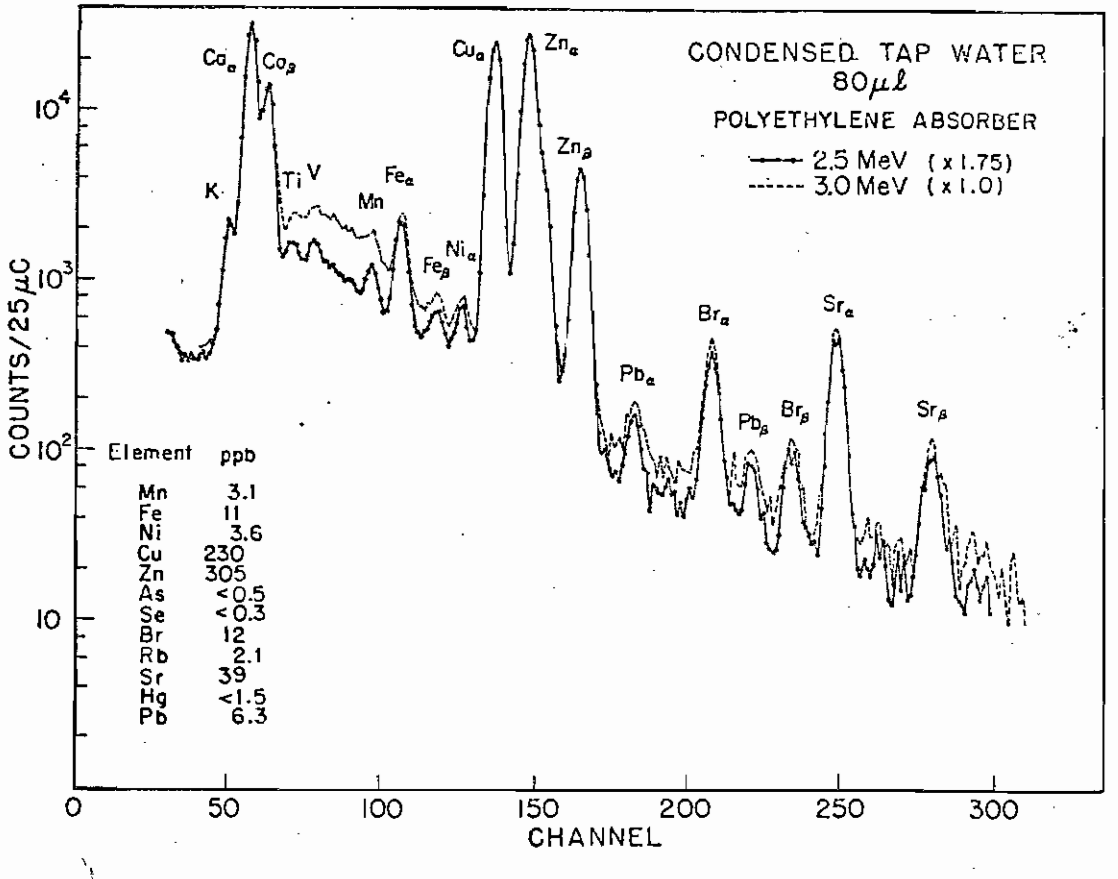
CONDENSED TAP WATER
80μl
POLYETHYLENE ABSORBER
2.5 MeV (x 1.75)
3.0 MeV (x 1.0)
COUNTS/25μC
CHANNEL
Element ppb
Mn 3.1
Fe 11
Ni 3.6
Cu 230
Zn 305
As <0.5
Se <0.3
Br 12
Rb 2.1
Sr 39
Hg <1.5
Pb 6.3

given in Figure (4.1b) which compares spectra from the same condensed tap water sample obtained at two different bombarding energies. The comparison shows that the lower excitation energy (2.5 MeV) yields better peak to background ratios for low-Z elements ($Z \lesssim 30$). Quantitative determination levels (at 10% precision level) for the spectra in Figure 4.1b indicate sensitivities between 1 and 10 ppb for $22 \leq Z \leq 40$. (See Figure 2.16). It should be mentioned that the nuclepore backings, at 1.1 mg/cm^2, are much thicker than necessary for this type of analysis. By using thinner substrates, the sensitivity can be improved even more, although eventually the concentration of inorganics such as Ca in the sample itself will limit the improvement.

The use of ion-exchange membranes as preconcentrating sampling matrices was tested at our laboratory as described by Lochmüller et al. (1974a). Some of the results are presented here. Ion-exchange membranes can be impregnated with a cation exchange resin which will attract metal ions from the solution or stream in which the membranes are placed. Such membranes are sturdy and self-supporting and are ideal in several ways as sampling devices for monitoring metal levels in streams, and as targets for PIXE analysis. Quantitative analysis requires that the membranes be calibrated as a function of solution concentration for each particular cation of interest. Such calibrations furthermore are complicated by the presence of competing ions; hence, precise

Figure 4.2 PIXE spectra from the analysis of ion exchange membranes equilibrated with lead solutions of varying concentration.

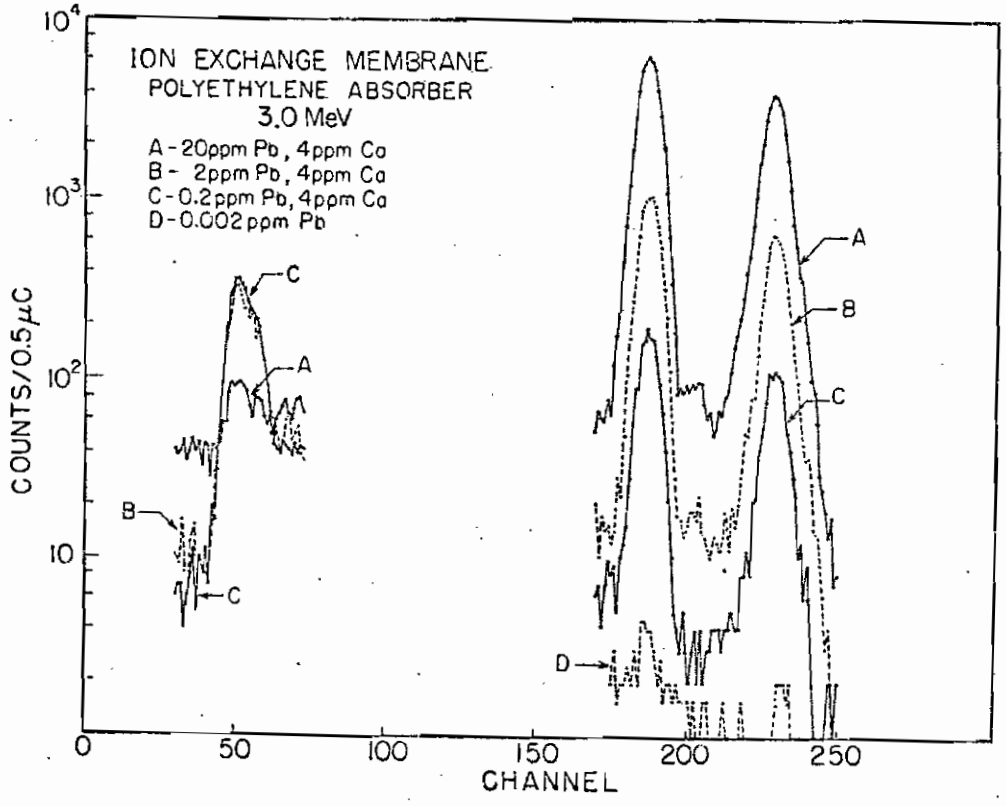
ION EXCHANGE MEMBRANE
POLYETHYLENE ABSORBER
3.0 MeV
A - 20ppm Pb, 4ppm Ca
B - 2ppm Pb, 4ppm Ca
C - 0.2ppm Pb, 4ppm Ca
D - 0.002ppm Pb
COUNTS/0.5μC
CHANNEL
A
B
C
D

quantitative determination of many elements simultaneously would be enormously complicated. Nevertheless such membranes can be very useful for monitoring changes in the metal levels of streams and public water supplies.

An indication of the sensitivity of ion-exchange membranes is provided in Figure 4.2. Shown here are PIXE analyses of ion-exchange membranes which were equilibrated in solution containing a fixed Ca concentration and varying Pb concentrations. A significant Pb peak can be detected at concentrations as low as 1 ppb. In addition to water, a number of other liquid specimens, including beer, milk, urine, and stream water (in situ) have been analyzed using ion-exchange membranes. The membranes selected for this work were Type MC-3142, obtained from Ionac Chemical, Birmingham, New Jersey.

IVA.2 Energy-related samples

In 1972, the National Bureau of Standards in cooperation with the Environmental Protection Agency sponsored an interlaboratory comparison of 4 energy-related materials considered to be important sources of trace elements emitted into the atmosphere. These materials were gasoline, residual fuel oil, coal, and coal fly ash. In 1974, Standard Reference Materials became available from the NBS for this coal (SRM 1632) and this fly ash (SRM 1633); and the fuel oil also has since become available as a Standard Reference Material.

Gasoline was found to be too volatile to be a meaningful calibration standard and was dropped from the NBS-EPA standards program. These materials have been analyzed at Duke and some of the results are presented here for comparison to the NBS values.

a). Residual Fuel Oil

Some difficulties were experienced in preparing suitable targets from residual fuel oil because of the sample's extreme viscosity (akin to thick molasses) at room temperature and its propensity to flow easily when heated by the proton beam. The initial method of target preparation was to deposit a small amount ($\sim$ 25 µl) of the fuel oil onto a nuclepore backing over an area smaller than the beam size (0.4 cm^2) to ensure irradiation of the entire deposit. It was found that beam currents $\gtrsim$ 15 nA were sufficient to cause the deposit to flow in a very short time beyond the region of the proton beam spot. Efforts to contain the deposit in the center of the nuclepore substrate by sealing a thin mylar film over the deposit were unsuccessful. The best results eventually were obtained by depositing a very small quantity ($\sim$ 1 mg) of the fuel oil on nuclepore and irradiating the sample initially with a very low intensity beam ($\sim$ 3 nA). As the beam current was gradually raised, the oil sample became more resistant to flow perhaps because of radiation damage to the oil molecules.

Figure 4.3a PIXE spectrum from the analysis of residual fuel oil deposited on nuclepore.

Figure 4.3b PIXE spectra from the analysis of an NBS coal pellet using the mylar and aluminum absorbers.

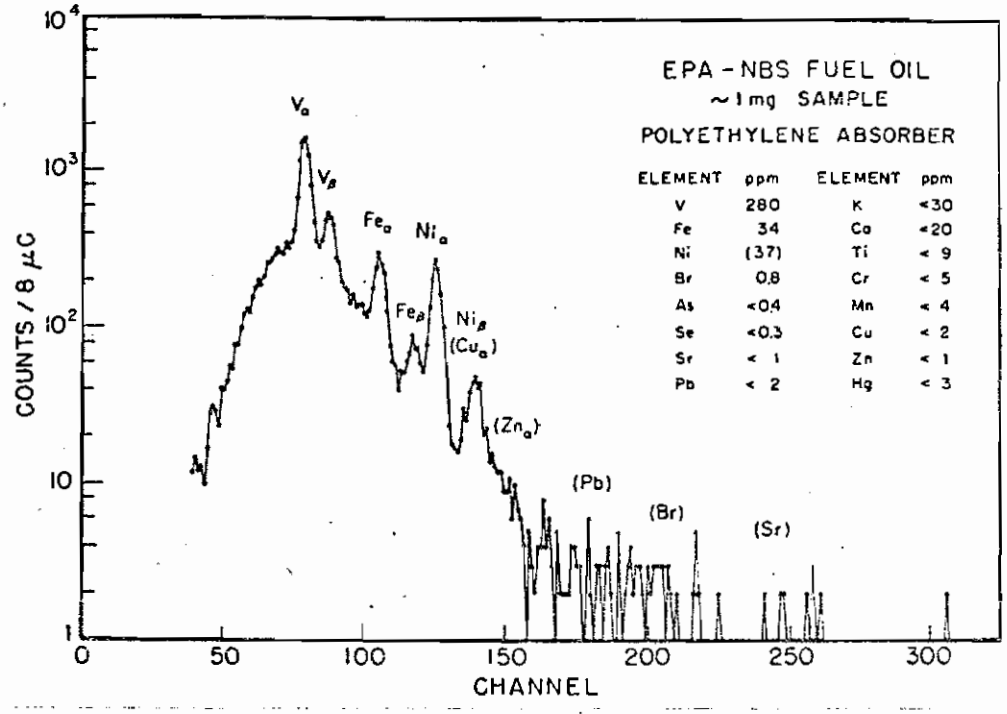
EPA - NBS FUEL OIL
~1 mg SAMPLE
POLYETHYLENE ABSORBER
ELEMENT ppm ELEMENT ppm
V 280 K <30
Fe 34 Ca <20
Ni (37) Ti < 9
Br 0.8 Cr < 5
As <0.4 Mn < 4
Se <0.3 Cu < 2
Sr < 1 Zn < 1
Pb < 2 Hg < 3
COUNTS / 8 μC
CHANNEL

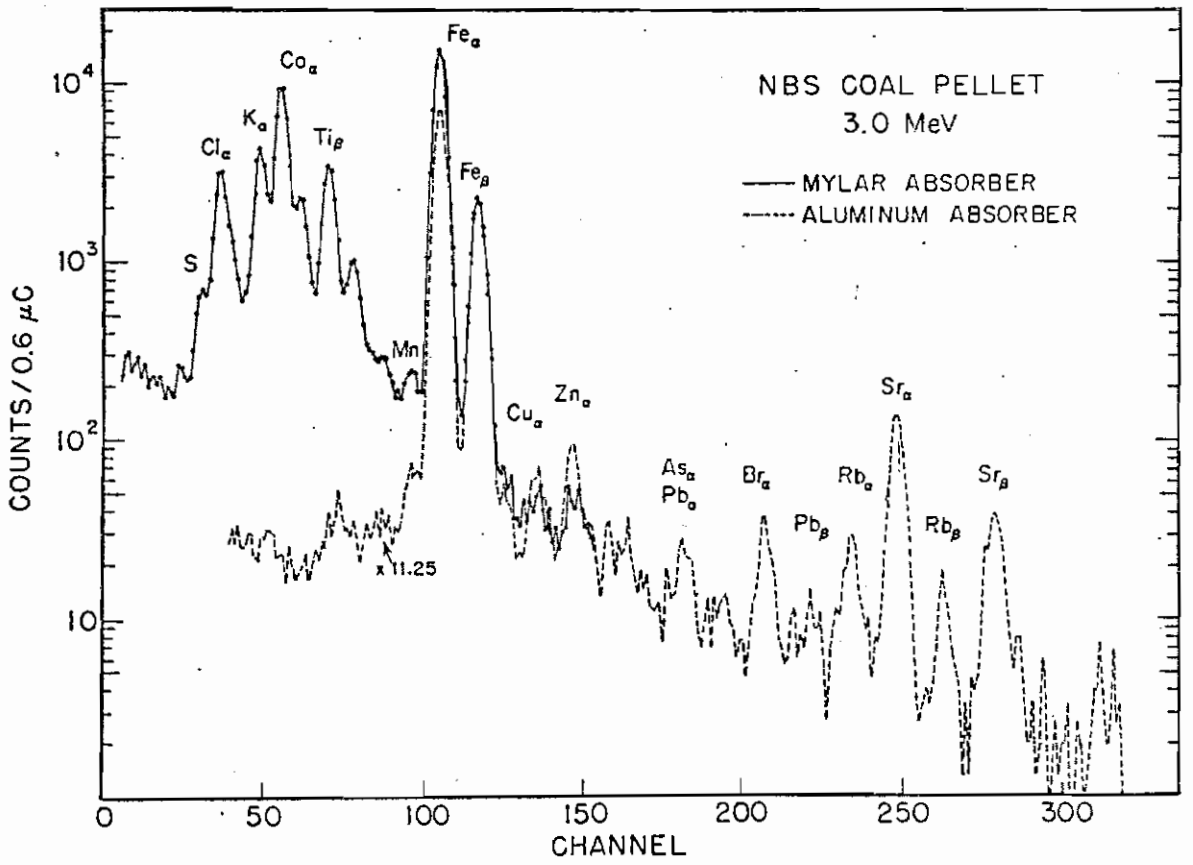
NBS COAL PELLET
3.0 MeV
MYLAR ABSORBER
ALUMINUM ABSORBER
COUNTS / 0.6 μC
CHANNEL
x 11.25

The resulting PIXE spectrum is displayed in Figure 4.3a along with the extracted concentrations normalized to the NBS value for Ni. The background generated by the moderately thick nuclepore backing plus the oil sample itself clearly limit the detection sensitivity for such a small amount of sample. Even so the 3σ detection limits obtained on this sample for a relatively short run were below 10 ppm for $Z \geq 22$ (Ti).

b). Coal (SRM 1632)

The coal and coal fly ash samples prepared by the NBS were collected from five coal-fired power plants geographically distributed in the U.S., in order that the trace metal levels would approximate the average values to be expected from domestic coal and coal fly ash produced in the U.S. The coal sample consisted of particles in sizes ranging from 44-125 μm. For both coal and fly ash, 250 mg of sample were recommended by the NBS to ensure a representative sample. Our sample preparation of NBS coal was described earlier in Section IIIC.5 and consisted of low temperature wet ashing and pelletizing.

The PIXE spectra obtained from a coal pellet using the mylar and aluminum absorbers are shown in Figure 4.3b, and the elemental abundances observed in both the ashed and pelletized samples are tabulated in Table 3.4 (Section IIIC.5). Detection limits were in the 1-10 ppm range for $Z \geq 23$ (V).

The agreement of our values with NBS and other laboratories is reasonably good in view of the small (and therefore not truly representative) sample quantities analyzed.

c). Gasoline

Efforts to obtain quantitative results on gasoline were complicated because of the extreme volatility of gasoline, and also because the deposited sample could not be confined to an area smaller than the beam. Limited success was obtained as described in Section IIIC.5 by condensing 5 ml of gasoline at low temperatures and depositing an amount of the residue representing approximately 2.5 ml onto a nuclepore backing. The resulting spectrum is shown in Figure 4.4a. The concentration of Pb in the original sample was determined to be approximately 150 ppm or greater, depending on the losses of Pb which occurred during the condensation process. Leaded gasoline typically contains about 600 ppm of lead on a wet weight basis.

d). Coal Fly Ash (SRM 1633)

Coal fly ash constitutes the particulate matter which is carried up the stacks of coal-fired power plants. It can be collected by means of mechanical collectors or electrostatic precipitators to prevent its emission into the atmosphere. The NBS fly ash samples were collected from the same power plants which provided the coal samples used in making the NBS

Figure 4.4a PIXE spectrum from the analysis of condensed gasoline.

Figure 4.4b PIXE spectrum from the analysis of a pellet of NBS fly ash.

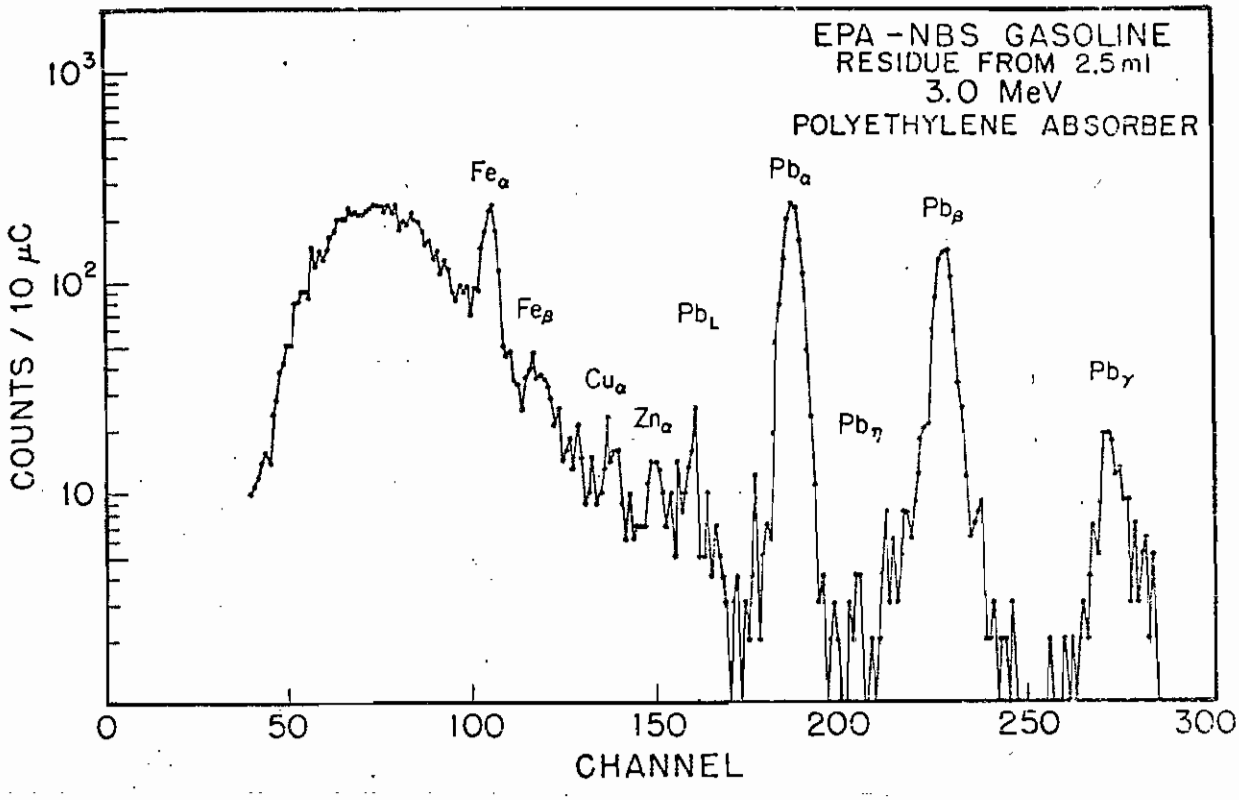
EPA-NBS GASOLINE
RESIDUE FROM 2.5 ml
3.0 MeV
POLYETHYLENE ABSORBER
COUNTS / 10 μC
CHANNEL
Fe$_\alpha$
Fe$_\beta$
Cu$_\alpha$
Zn$_\alpha$
Pb$_L$
Pb$_\alpha$
Pb$_\eta$
Pb$_\beta$
Pb$_\gamma$

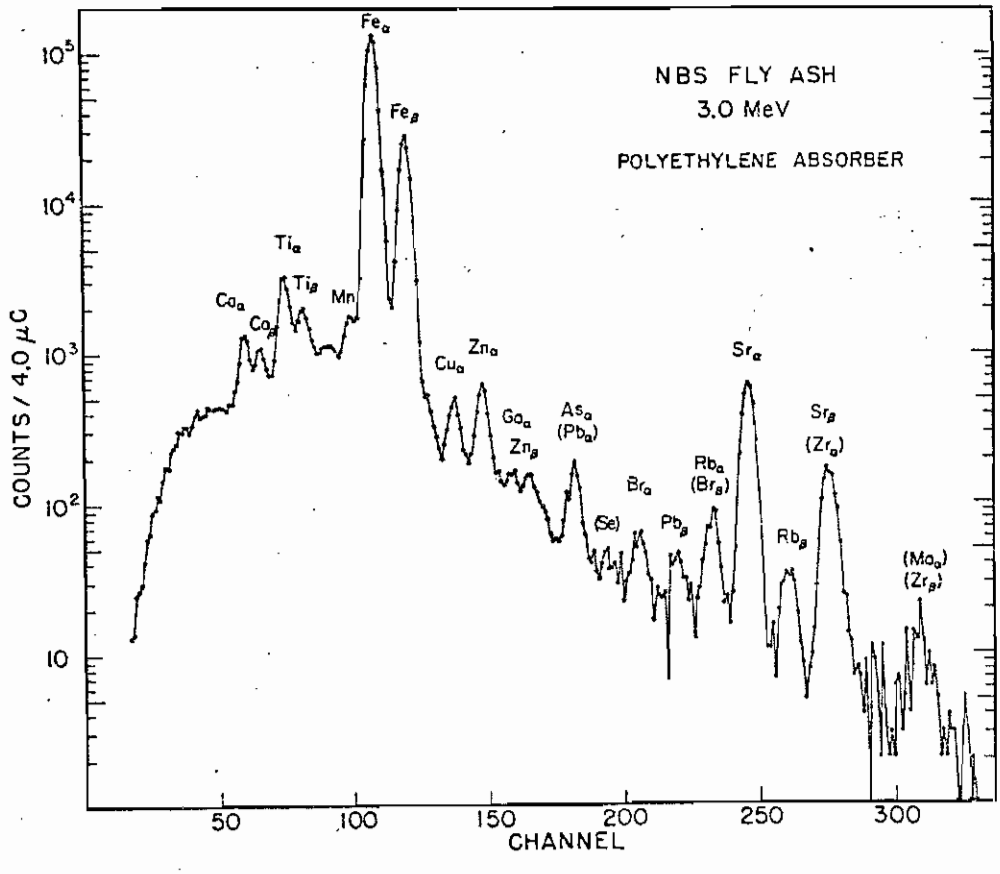
NBS FLY ASH
3.0 MeV
POLYETHYLENE ABSORBER
COUNTS / 4.0 μC
CHANNEL
Fe$_\alpha$
Fe$_\beta$
Ca$_\alpha$
Ca$_\beta$
Ti$_\alpha$
Ti$_\beta$
Mn
Cu$_\alpha$
Zn$_\alpha$
Ga$_\alpha$
Zn$_\beta$
As$_\alpha$ (Pb$_\alpha$)
(Se)
Br$_\alpha$
Pb$_\beta$
Rb$_\alpha$ (Br$_\beta$)
Sr$_\alpha$
Rb$_\beta$
Sr$_\beta$ (Zr$_\alpha$)
(Mo$_\alpha$) (Zr$_\beta$)

Table 4.1

EPA-NBS fly ash analyses

Element	Thin layer ppm[a] (d.l.)	Thick layer ppm[b] (d.l.)	NBS ppm ± Δppm	Other labs avg. ppm
K	11,500(300)	6,200(1,980)	17,200	
Ca	31,400(170)	20,650(280)		37,000
Ti	3,140(100)	5,400(50)		6,600
V	200(63)	480(30)	214 ± 8	
Cr	136(42)	290(19)	131 ± 5	
Mn	500(30)	740(20)	493 ± 7	
Fe	45,000(20)	60,000(14)		60,000
Ni	94(14)	133(12)	98 ± 3	
Cu	115(10)	115(10)	128 ± 5	
Zn	200(18)	195(8)	210 ± 20	
Ga	42(6)	33(10)		
As	52(6)	40(9)	61 ± 6	
Se	10(7)	9(10)	9.4 ± 0.5	
Br	42(7)	18(12)		8.5
Rb	150(4)	176(14)	112	
Sr	1,470(10)	1,430(14)	1,380	
Zr	190(13)	240(14)		450
Mo	35(19)	13(19)		< 500
Pb	64(21)	156(38)	70 ± 4	

a) Normalized to 45,000 ppm Fe. No absorption corrections applied.

b) Normalized to 60,000 ppm Fe. No absorption corrections applied.

coal standard. The particle size was limited to 88 μm or less.

Sample preparation was very difficult because the fly ash was intractable to chemical ashing and lacked sufficient binding for making pellets. Attempts to sandwich the granular material between thin mylar films were not very successful. The technique which yielded the best results was to press pellets from a mixture containing fly ash and a small fraction (approximately 5% or less) of clean ceresin to act as a binding agent.

The results of fly ash analyses obtained from a thin sandwiched layer and the average of six thick pellets are summarized in Table 4.1. Normalization of the thin layer values to 4.5% Fe appeared to give the best overall agreement with the NBS values. The data for the pellets were normalized to the expected Fe concentration of approximately 6%. Fly ash contains large concentrations of Al, S, and Si which cause severe X-ray absorption effects for low energy X-rays, particularly in the thick targets. The values in Table 4.1 purposely have not been corrected for X-ray absorption effects; this is especially reflected in the low concentrations measured for K, Ca, and Ti. The high values for Mn are due to a contribution of X-ray counts in the region of the Mn K_α line arising from the low energy tail on the immense Fe K_α peak as discussed earlier in the section on X-ray background problems. A spectrum of a thick fly ash pellet is displayed in Figure 4.4b.

IVA.3 Aerosol Analysis

The study of airborne particulate matter is of increasing concern to environmental scientists. Major efforts are being directed toward quantifying the sources of particulate matter in the atmosphere, including natural processes and man's contribution, and in determining the associated environmental and biological health effects. Both PIXE and XRF are ideally suited to meet the analytical requirements for this important area of research. These requirements include:

1. the ability to perform quantitative and accurate analyses at a low cost per sample
2. the ability to work with small amounts of sample--i.e., high sensitivity
3. multielement capability
4. the ability to provide particle size information which is essential in identifying the sources of generation and in determining biological consequences
5. capability of processing large sample sets in order to provide statistically significant results--hence, the technique must be fast and economical.

A number of applications of PIXE to aerosol analysis are reviewed in Johansson et al. (1976) and in the proceedings of the Lund conference of PIXE and its applications (in Nucl. Instrum. Methods, 142 (1977)). The work of Cahill and coworkers at the University of California at Davis (Cahill, 1975) in particular demonstrates the powerful capabilities

of PIXE in aerosol analysis. Cahill's system is fully automated and can analyze as many as 700 samples a day at a cost between $5 and $10 per sample. Using ion scattering analysis in conjunction with alpha induced X-ray analysis, Cahill is able to provide concentrations or upper limits for virtually the entire periodic table.

At Duke University we have participated in a number of aerosol studies in conjunction with the National Environmental Research Center at Research Triangle Park, N. C. One major study involved the analysis of aerosol samples collected by the EPA at 34 monitoring stations across the country during one 24 hour period. Sample collection was accomplished by means of the simple filter cassette shown in Figure 4.5a which contained a nuclepore filter 37 mm in diameter. The filter cassette was preceded by a cyclone separator which removed the larger particulates and allowed the finer respirable suspended particulates (RSP) to be collected on the nuclepore filter.

Because of the turbulence introduced by the cyclone separator into the air stream passing through the filter cassette, there was an interest in determining the distribution of particulates over the filter. The relatively small beam area employed in PIXE analysis was ideally suited for this type of investigation. Several filters were rapidly scanned in five positions across the diameter and the abundances for the dominant elements were determined at each position. The

Figure 4.5a Cassette device used for collection of aerosol samples.

Figure 4.5b Results of a PIXE scan of a nuclepore air filter. The filter was analyzed in the five positions as shown and the dominant elemental abundances for each position are indicated in the bar graph.

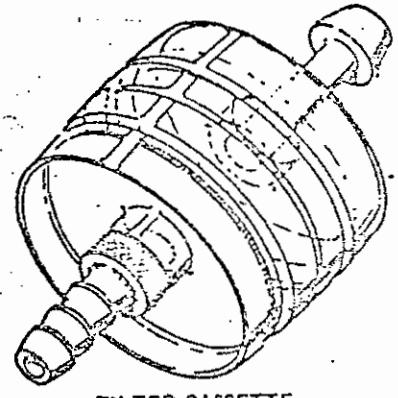

FILTER CASSETTE

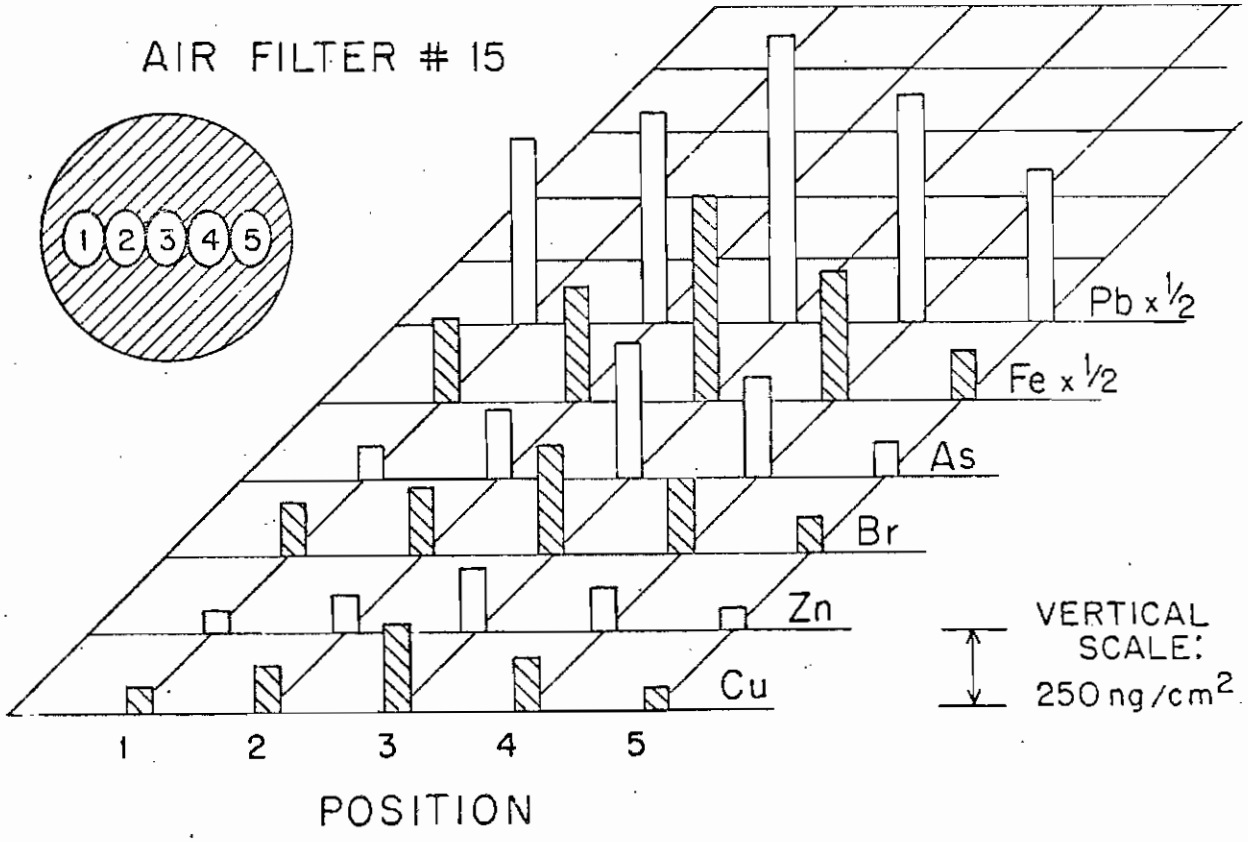

results for one of these scans are shown in Figure 4.5b. The concentrations for all six elements are greatest near the filter's center and fall off by factors of 2-3 at the edges of the filter. This type of information is difficult to obtain with a conventional broad-beam XRF system and illustrates one application of PIXE's scanning capabilities.

Average areal concentrations (ng/0.4 cm^2) were obtained for the 34 EPA samples by analyzing each filter in the center position with the mylar, polyethylene, and aluminum absorbers, and at the two edges using the polyethylene absorber. Appropriate factors to account for the non-uniform concentration profiles were determined from the polyethylene runs and applied to the measurements taken at the center position.

Three X-ray absorbers were used in order to maximize the PIXE detection sensitivity and the system efficiency in different elemental regions. The use of the three absorbers is illustrated in Figure 3.8 (Section IIIB.3) showing spectra of an air sample collected in Kearns, Utah. The thin mylar absorber provides maximum sensitivity for light elements, but the beam current must be kept low in order to avoid excessive counting rates. The aluminum absorber results in maximum absorption of low energy X-rays and allows higher beam currents to be used in order to maximize the efficiency for the heavier elements.

Results of the PIXE analysis of the 34 air filters are tabulated in Tables 4.2a, b, and c. Abundances for 22

elements are listed in units of ng/0.4 cm^2 (representing the abundances collected from about 2 m^3 of air). Collection sites are identified by the letter code beneath each table. Some of the more noteworthy features include: (1) the unusually high levels observed in the sample from Kearns, Utah--particularly S, Cl, Ca, As, and Mo, as well as the high As and Mo abundances from Magna, Utah; (2) the extremely low levels observed for sample R44 collected on Long Island; (3) variations of more than an order of magnitude for some elements at different sites in the same city; (4) the nearly constant ratio of Pb to Br ranging from 6:1 to 10:1 for all sites.

Typical interference-free detection limits for these air filter analyses are listed in the last column of Table 4.2c. These numbers are for an exposed membrane and therefore include background contributions arising from the deposited particulates as well as the nuclepore membrane. The adjacent column lists the abundances and corresponding detection limits observed in a clean nuclepore membrane. In the absence of interferences, the detection sensitivity is less than 2.5 ng/cm^2 for a number of elements. It is interesting to compare these typical PIXE detection limits to the corresponding elemental abundances observed in a representative air sample. Figure 4.6 displays such a comparison, using abundance data collected by Cooper et al. (1973) for a variety of cities. The range of values observed for each elemental abundance (ng/m^3) is indicated by the vertical bar

Table 4.2a

Elemental Abundance on Air Filters in Units of ng/0.4 cm^2 or about ng/2m^3 of Air.

Element \ Station	B3	B5	B6	B8	B9	B12	B18	B19	S14	K23	M22	M25	M26
S	2,400	3,300	3,380	2,200	2,700	2,400	3,000	6,000	1,500	11,500	1,700	1,900	6,100
Cl	5	30	35	120	16	180	70	90	1.0	2800	54	30	40
K	360	720	580	460	280	420	120	150	170	620	110	200	240
Ca	180	580	305	320	230	605	135	210	130	2000	180	350	340
Ti	36	40	23	30	42	42	12	18	13	10	7	14	14
V	2	0.0	3	5	5	3	5	6	2	2	4	1.0	0.5
Cr	1	2	1.5	2.5	0.0	3	1.0	2.5	0.5	1.5	1.7	1.5	1.0
Mn	100	180	16	40	6	83	1.5	6	14	1.2	2.8	5	3
Fe	1,200	1,960	380	575	440	860	147	242	200	350	204	620	560
Ni	11	5	6	7	8	8	8	12	6	2.6	4	2.8	1.6
Cu	15	24	10	17	10	15	8	23	6	295	105	65	238
Zn	340	670	150	200	80	370	8	57	120	178	36	38	101
As	10	15	3	11	12	14	0.0	15	5	786	72	102	450
Se	4	3	1.8	1.9	2.3	2	0.7	2.6	1.8	28	3	1.8	15
Br	18	43	24	35	23	63	37	87	17	26	50	45	24
Rb	1.4	4	4	2.5	1.2	2	0.9	0.0	1.4	4	1.0	2.3	0.0
Sr	4	6	3	5	3	5	3	6	1.4	43	0.5	5	4
Zr	1.4	8	0.5	2.5	3	4	0.2	2.8	(0.6)	3	1.8	2.2	0.0
Mo	2.1	0.9	1.0	0.0	0.0	0.4	1.4	0.0	(0.6)	211	12	20	148
Ba	17	17	0.0	20	35	32	3	20	3	10	20	18	0.0
Hg	1.2	1.0	0.0	0.6	2.6	0.7	1.4	0.9	0.5	0.1	0.1	0.0	1.2
Pb	272	670	247	419	337	545	290	730	328	322	336	296	247

Code: B = Birmingham, Alabama; S = Salt Lake City, Utah; M = Magna, Utah; K = Kearns, Utah

Table 4.2b

Elemental Abundance on Air Filters in Units of ng/0.4 cm^2 or about ng/2m^3 of Air.

Element \ Station	L15	L33	L35	L36	L40	L42	L51	Q28	C30	C32	C54	C58
S	2,000	4,400	1,440	4,800	2,100	4,800		1,800	1,050	2,900	4,400	3,010
Cl	50	105	1100	10	120	10	20	170	60	50	120	20
K	160	120	160	190	170	190	90	170	81	90	240	210
Ca	650	180	190	240	180	270	150	170	32	90	1,100	310
Ti	17	14	9	5	4	18	10	30	8	20	19	52
V	1.0	7	8	10	7	3	5	15	3	7	4	8
Cr	0.0	2	3	1.2	1.5	6	1.0	0.3	1.5	0.3	3	3
Mn	6	7	4	3	4	5	4	4	1.2	4	22	16
Fe	400	220	110	99	146	225	110	340	80	185	280	690
Ni	5	12	14	15	11	13	10	11	8	15	5	5
Cu	68	11	14	5	6	17	5	32	7	18	32	20
Zn	54	64	36	25	17	36	19	187	11	26	35	41
As	115	13	10	5	11	4	2.0	14	0.8	4	4	5
Se	2	5	3	2.5	3	2.3	1.2	8	0.6	3	1.9	2.7
Br	106	85	101	47	70	46	33	131	12	16	66	46
Rb	0.0	0.7	0.0	0.0	1.5	3	0.0	3	0.0	0.3	0.9	0.5
Sr	5	4	1.8	1.1	4	5	2.0	4	0.1	0.0	2.3	5
Zr	5	2.1	1.4	0.6	0.1	1.2	0.1	3	0.5	2.4	1.4	4
Mo	13	0.0	0.0	0.0	0.0	0.0	0.0	0.0	0.0	0.0	0.0	0.0
Ba	12	6	25	18	20	20	4	0.0	4	25	27	60
Hg	2.0	0.0	1.5	1.4	1.5	0.7	1.2	0.0	0.0	1.2	0.1	1.9
Pb	670	860	610	374	620	512	350	826	95	153	420	455

Code: L = Los Angeles, California; Q = Queens, New York; C = Charlotte, North Carolina

Table 4.2c

Elemental Abundance on Air Filters in Units of ng/0.4 cm^2 or about ng/2m^3 of Air.

Element \ Station	R44	C60	C61	C62	C64	C66	C68	C69	C71	BLANK	d.l.
S	0.0	1,800	2,600	3,050	3,060	4,600	2400	1300	1450	0.0 ± 150	150
Cl	0.0	100	10	40	50	2	50	40	0.0	0.0 ± 80	50
K	0.0	270	170	180	230	180	150	230	385	9 ± 7	10
Ca	0.0	720	530	360	330	240	325	1600	390	0.0 ± 5	6
Ti	1.5	35	24	24	20	16	14	17	18	0.0 ± 3	4
V	3.5	7	3	5	6	3	2	2	3	0.0 ± 2.5	3
Cr	2	13	2	3	2	0.0	0.0	2	2	0.8 ± 2.0	2.5
Mn	1.2	8	9	10	8	9	7	28	6	0.9 ± 1.8	1.5
Fe	11	450	278	270	290	175	156	274	206	7.5 ± 1.1	1.1
Ni	5	13	5	5	6	5	4	5	4	5.5 ± 0.6	0.8
Cu	1.7	150	43	70	13	9	30	16	14	1.0 ± 0.5	0.5
Zn	6	120	25	32	32	20	15	54	45	0.0 ± 0.4	0.4
As	0.0	16	1.0	5	8	5	8	6	8	0.0 ± 0.5	0.6
Se	0.0	2	1.5	0.9	1.6	1.0	1.6	1.0	1.2	0.0 ± 0.6	0.6
Br	3	130	41	40	43	22	43	22	65	0.4 ± 0.6	0.7
Rb	0.0	4	0.2	1.7	0.0	0.5	0.0	0.5	2.0	0.0 ± 0.5	0.8
Sr	0.0	5	0.8	1.8	1.4	1.7	1.4	1.7	1.1	0.0 ± 0.5	1.0
Zr		5	0.0	2.6	1.3	1.3	1.3	1.3	1.1	0.0 ± 0.5	1.5
Mo		0.0	0.0	1.7	0.6	2.3	0.6	2.3	2.3	0.0 ± 0.5	2.5
Ba	6	0.0	40	0.0	10	15	15	17	18	0.0 ± 35	35
Hg	0.4	2.1	0.4	0.0	0.1	0.3	1.5	0.7	0.0	0.0 ± 1.3	2.0
Pb	14	980	325	390	312	167	560	440	280	0.0 ± 1.7	2.0

Code: R = River Head, New York; C = Chattanooga, Tennessee; Blank = Blank nuclepore membrane; d.l. = typical detectibility limits

Figure 4.6 Typical values and ranges of trace element concentrations found in urban aerosols. (Data taken from Cooper et al., 1973). Also shown are the PIXE detection limits from Table 4.2c.

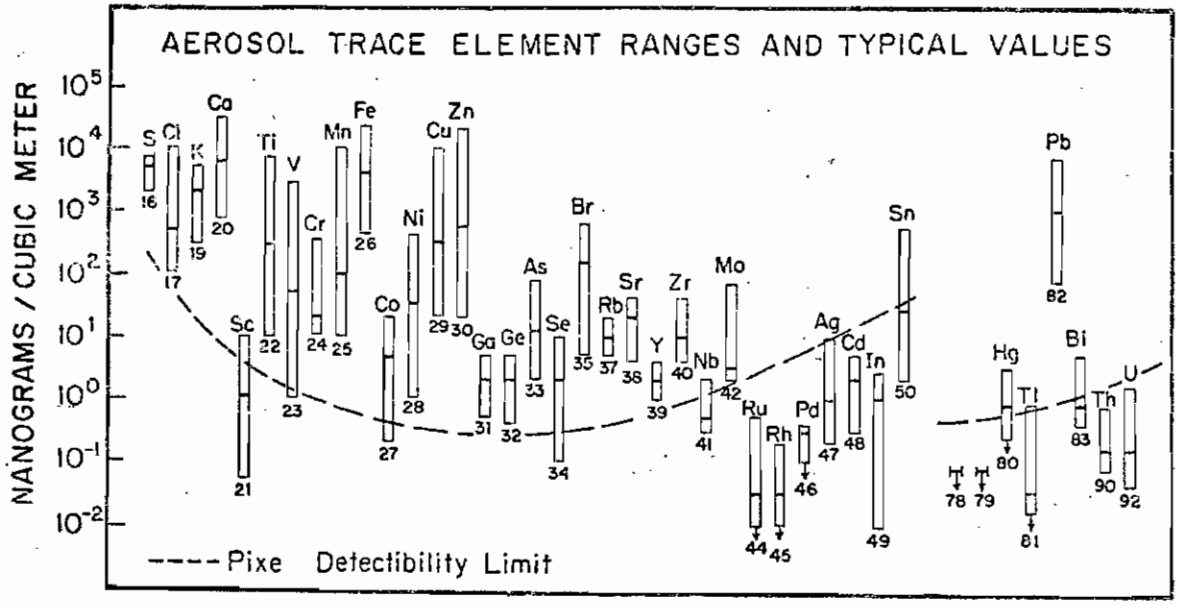
AEROSOL TRACE ELEMENT RANGES AND TYPICAL VALUES
NANOGRAMS / CUBIC METER
10^5
10^4
10^3
10^2
10^1
10^0
10^{-1}
10^{-2}
S 16
Cl 17
K 19
Ca 20
Sc 21
Ti 22
V 23
Cr 24
Mn 25
Fe 26
Co 27
Ni 28
Cu 29
Zn 30
Ga 31
Ge 32
As 33
Se 34
Br 35
Rb 37
Sr 38
Y 39
Zr 40
Nb 41
Mo 42
Ru 44
Rh 45
Pd 46
Ag 47
Cd 48
In 49
Sn 50
H 78
H 79
Hg 80
Tl 81
Pb 82
Bi 83
Th 90
U 92
Pixe Detectibility Limit

while the mean value is represented by the horizontal cross bar. The dashed curves are the typical interference-free detection limits taken from Table 4.2c and normalized to the correct units. Figure 4.6 suggests that it should be possible to detect nearly all elements in the range $16 \leq Z \leq 42$ plus Pb in most aerosol samples given the same experimental conditions and operating parameters that were used to generate Tables 4.2a, b, c. These conditions include: (1) a small area of irradiation; (2) relatively large target-detector distance ($\sim$ 10 cm); (3) relatively low counting rate ($\lesssim$ 1000 cps); (4) 6 minute analysis time. Significant improvements can be made in these detection limits by optimization of these parameters.

In addition to analyzing aerosol samples collected on nuclepore membranes, we have made measurements of particulates deposited on fiber glass filter media. These filters are not well suited for X-ray analysis because of their thickness which makes quantitative analyses difficult, and because of the presence of large concentrations of impurities in the filter--particularly SiO_2, Ti, Zn, as well as other elements. On the other hand, this type of filter has been the standard type used by the EPA for several years and many such exposed filters from numerous sites have been kept in storage because until now, the only information that has been obtained from them is the total mass accumulated during the 24 hour monitoring period. Certainly much more infor-

mation exists on each one, if methods can be devised to decipher it. To test the power of PIXE for analyzing fiber-glass filters, a Durham, N. C. air sample was collected over a 24 hour period. The PIXE spectra that were obtained are shown in Figure 4.7 and 4.8 using the mylar absorber and aluminum absorber respectively. Because these filters are so thick, very little of the particulates are deposited on the back surface of the filter which may therefore serve as the "blank". The spectra in Figures 4.7 and 4.8 were obtained by irradiating the front surface of the filter and then rotating the target 180° to measure the blank spectrum on the reverse side. Although the background intensity severely limits the sensitivity, the signals from Fe, Br, and Pb clearly stand out above the background.

Another study conducted for the EPA utilized the scanning capabilities of PIXE to map the concentrations for several elements deposited on the front surface of a large, rectangular fiber glass filter. The filter, measuring 20 cm × 25 cm, was employed in a type of air sampler known as a "high-vol" sampler. The scan was conducted as shown in Figure 4.9 along two orthogonal axes and along one diagonal. Abundances for Fe, Pb, and Br were determined at each position of the scan, and the results obtained along the horizontal scan are plotted in Figure 4.10 relative to the average concentration. Except for the corners and the extreme edges of the exposed filter, the Pb and Br concen-

Figure 4.7 PIXE spectra from the analyses of the front and back of a fiber glass air filter exposed for 24 hours in Durham, N.C. Mylar absorber is employed. The reverse side approximates a "clean" blank, since very little of the air particulate matter is deposited on this surface.

Figure 4.8 PIXE spectra from the analyses of the same filter as in Figure 4.7. The aluminum absorber is employed to improve sensitivity for the heavier elements.

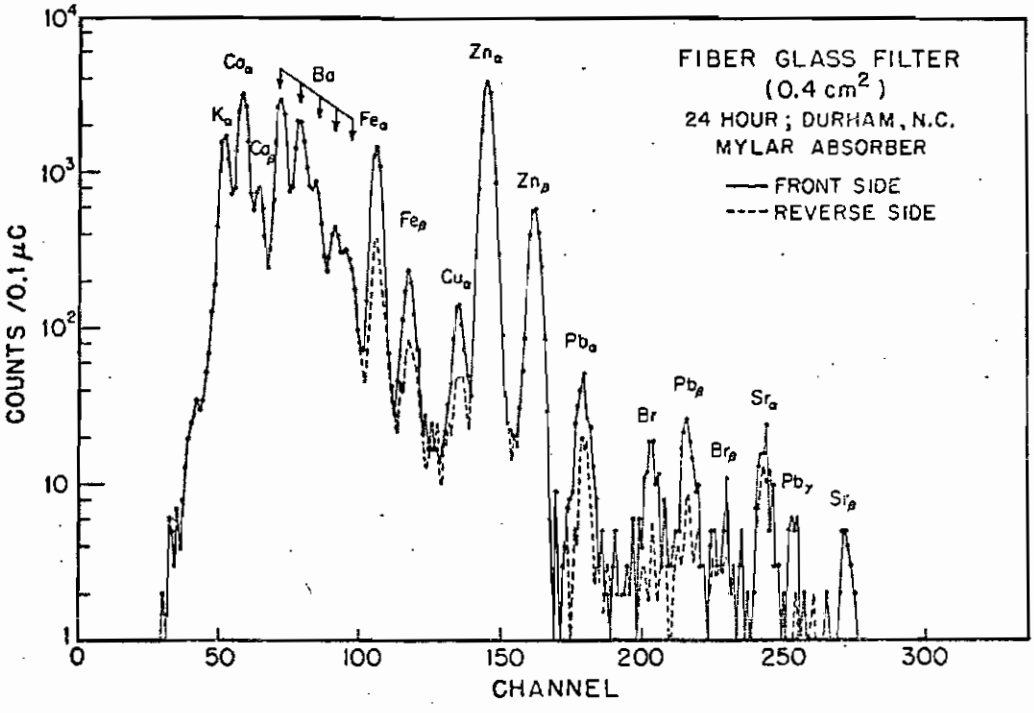
FIBER GLASS FILTER
(0.4 cm²)
24 HOUR; DURHAM, N.C.
MYLAR ABSORBER
FRONT SIDE
REVERSE SIDE
COUNTS /0.1 μC
CHANNEL
Co_α
K_α
Ba
Co_β
Fe_α
Zn_α
Zn_β
Fe_β
Cu_α
Pb_α
Br
Pb_β
Br_β
Sr_α
Pb_γ
Sr_β

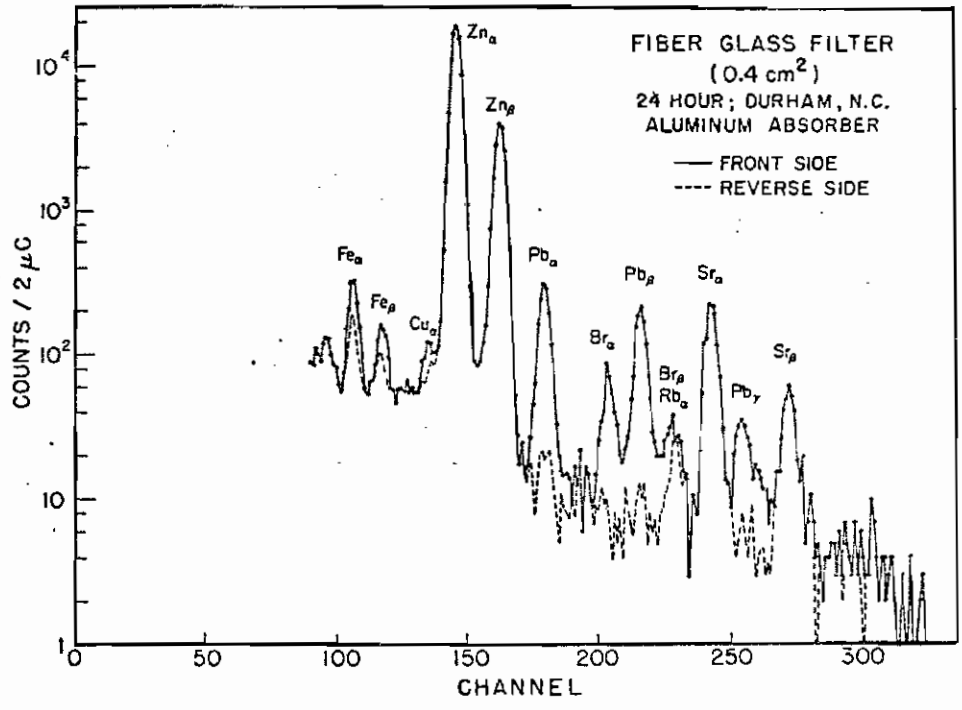
FIBER GLASS FILTER
(0.4 cm²)
24 HOUR; DURHAM, N.C.
ALUMINUM ABSORBER
FRONT SIDE
REVERSE SIDE
COUNTS / 2 μC
CHANNEL
Zn_α
Zn_β
Fe_α
Fe_β
Cu_α
Pb_α
Br_α
Pb_β
Sr_α
Br_β
Rb_α
Pb_γ
Sr_β

Figure 4.9 Positions at which PIXE analyses were performed for the scan of an environmental air filter.

Figure 4.10 Results of the PIXE scan for Fe, Pb, and Br along the horizontal direction as shown in Figure 4.9.

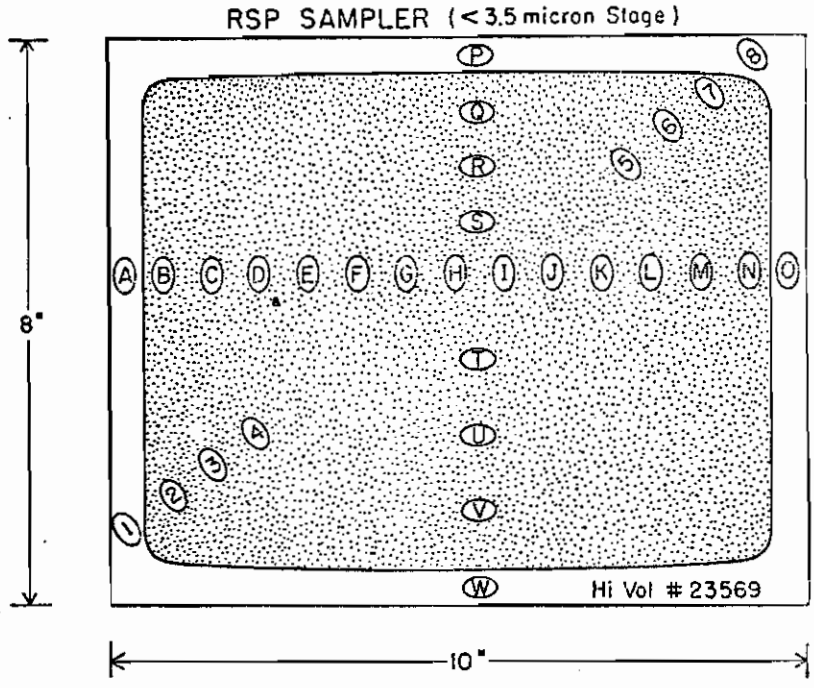
RSP SAMPLER (< 3.5 micron Stage)
8"
10"
Hi Vol # 23569

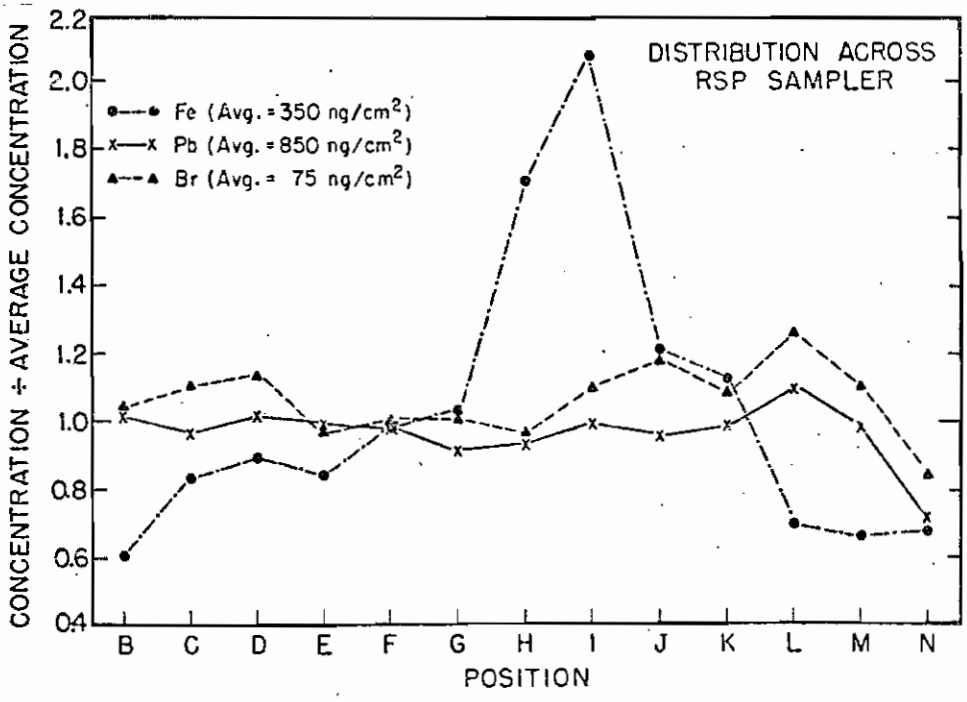
DISTRIBUTION ACROSS RSP SAMPLER
Fe (Avg. = 350 ng/cm²)
Pb (Avg. = 850 ng/cm²)
Br (Avg. = 75 ng/cm²)
CONCENTRATION ÷ AVERAGE CONCENTRATION
POSITION

trations were within ±15% of the mean concentration. The distribution of Fe particulates, which are generally larger than Br or Pb particulates, showed a factor of 2 deviation from the mean concentration near the center of the filter.

The analysis of air quality in industrial factories is another important area in which PIXE is being applied. One brief study was carried out at Duke in cooperation with the School of Public Health at the University of North Carolina. The purpose of the study was to investigate the air quality inside a number of rubber manufacturing plants. Air samples collected on nuclepore membranes were analyzed at Duke and the results indicated that the air inside such plants was relatively free of heavy metals.

IVA.4 Miscellaneous Applications

The ease and rapidity with which PIXE data is generated for many samples makes PIXE a very suitable technique for rapid screening of samples when quantitative accuracy may not be required--e.g., one may simply be interested in knowing whether or not a selected element or elements are present in the sample.

The spectra displayed in Figures 4.11 and 4.12 serve to demonstrate this application of PIXE. Figure 4.11 shows a spectrum of a chip of interior wall paint taken from the author's kitchen. The presence of Pb in the paint had been suspected and is clearly confirmed in Figure 4.11.

Figure 4.11 PIXE spectrum from analysis of a chip of interior wall paint. The aluminum absorber is employed. Note the strong Pb signal.

Figure 4.12 PIXE spectrum from analysis of a commercial spray adhesive. Note the presence of Pb.

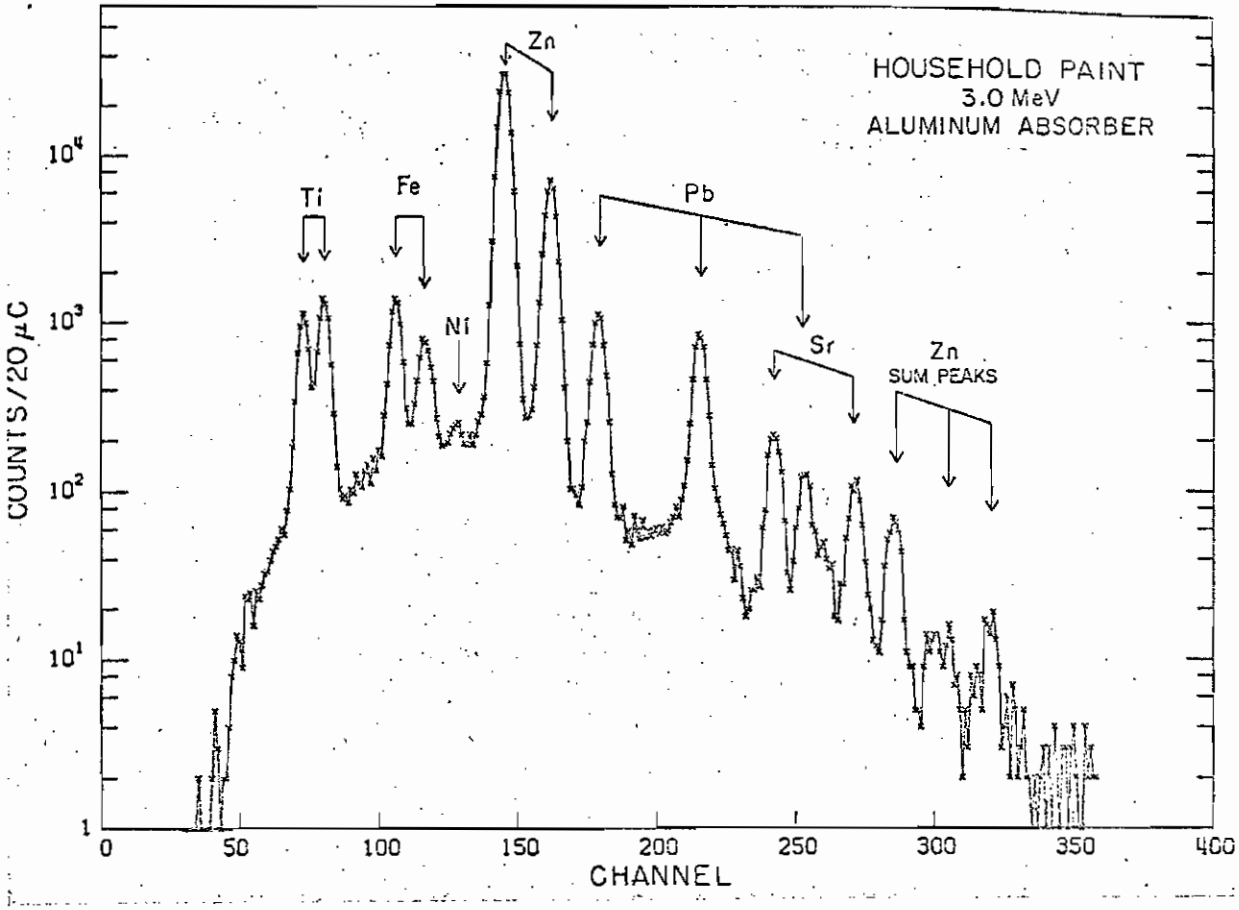
HOUSEHOLD PAINT
3.0 MeV
ALUMINUM ABSORBER
Zn
Ti
Fe
Ni
Pb
Sr
Zn
SUM PEAKS
COUNTS/20 μC
CHANNEL

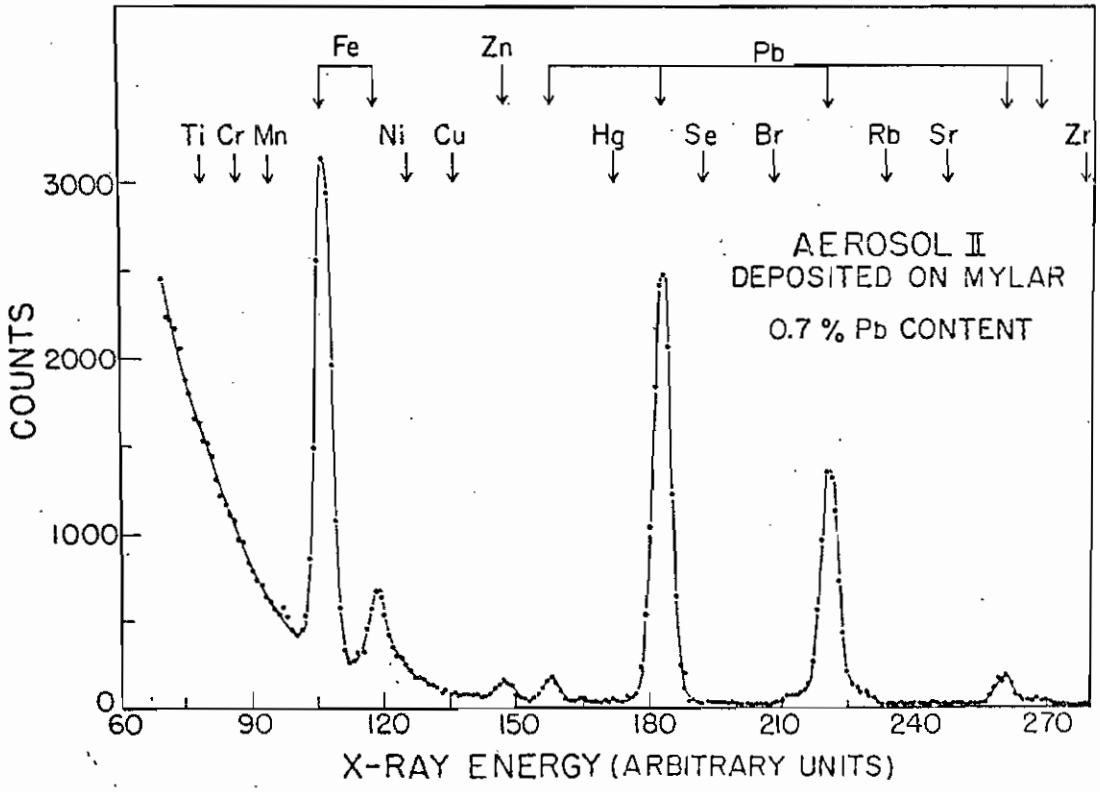
Fe
Zn
Pb
Ti Cr Mn
Ni Cu
Hg
Se
Br
Rb Sr
Zr
AEROSOL II
DEPOSITED ON MYLAR
0.7 % Pb CONTENT
COUNTS
X-RAY ENERGY (ARBITRARY UNITS)

Figure 4.12 was obtained from a commercial spray adhesive (no longer available) which we were investigating for use in mounting samples. The adhesive was simply sprayed onto a mylar film for analysis. Our initial interest was to determine qualitatively the levels of contaminants present in the adhesive. The large Pb concentration observed in the spectrum was unexpected. Analysis of the sample indicated a Pb concentration of 0.7% which for instance, exceeds the level permitted by Federal law in paints. Subsequent analyis by XRF and atomic absorption analysis verified our findings and the Consumer Product Safety Commission as well as the product's manufacturer were notified of these results.

IVB. Biological and Medical Analyses

PIXE has been found to be a very useful tool for the analysis of biological and medical specimens (Walter et al., 1977 and accompanying articles in Section V of the same reference). In particular, the ability to detect many elements simultaneously in small amounts of sample and with good sensitivity makes PIXE valuable in several types of investigations: (1) studies in which the sample quantity may be limited, as for example the analysis of certain enzymes; (2) studies requiring multielement information, as for example the trace metal metabolism of hospital patients on controlled diets; (3) large-scale baseline studies in which the objective is to determine normal metal levels in

particular type of biological or environmental specimen, and which often involves the analysis of a large number of samples. One example of this third application is the study conducted on human lung samples described later in this section.

A major effort at Duke has been devoted to the application of PIXE to biological and medical samples. The variety of samples investigated has necessitated a number of different approaches to target preparation many of which have been described in Section IIIE. One important consideration in conducting biological or environmental analyses is the natural variation in trace element levels observed in different samples of the same species and even in adjacent regions within the same specimen. This natural variance can mask systematic effects (due to environmental factors for example) which one may be trying to investigate, and raises the question of what constitutes a representative sample. In general, one requires a large, statistically meaningful sample set in order to investigate systematic variations in bioenvironmental samples.

IVB.1 Human tissue analysis

Numerous tissue samples, prepared by several different methods, have been analyzed at Duke. These specimens include: microtomed sections of tissue from 7 organs of a deceased male, lyophilized placenta tissue, human lung samples,

and tissue specimens from a Cr suicide case.

Initial studies of human tissue were carried out on 10-30 μm thick tissue sections sliced in a frozen state with a microtome. The sections were laid across a thin supporting film of formvar attached to graphite or fiber washers for mounting on the target rod. A spectrum obtained from a microtomed kidney section is shown in Figure 4.13. It is estimated that the amount of tissue analyzed by a beam of 0.5 cm^2 area on a 30-μm thick slice is only about 0.4 mg. This emphasizes the need for clean, ultra-thin backings for such samples. One must also be concerned about obtaining representative results from such small samples quantities. More representative samples can be obtained by layering several thin slices on a single backing. The primary advantage of using thin tissue sections is that proton energy loss and X-ray absorption effects are negligible. One must however be concerned about the possibility of sample contamination during the freezing process or from the microtome blade as well as trace impurities in the target backing. In addition to kidney, thin sections of heart, lung, spleen, liver, brain, and testes were analyzed. The results shown earlier in Table 3.15 for a thin section of human tissue indicate that dry weight detection limits below 1 ppm are possible for several elements.

A second study concerned the analysis of tissue and blood samples of a person suspected of committing suicide by

Figure 4.13 PIXE spectra from analysis of a microtomed section of human kidney using mylar and polyethylene absorbers.

Figure 4.14 PIXE spectra from analyses of thick sections of stomach and kidney from a subject poisoned by a chromium solution. Note the high levels of Cr, As, and Hg.

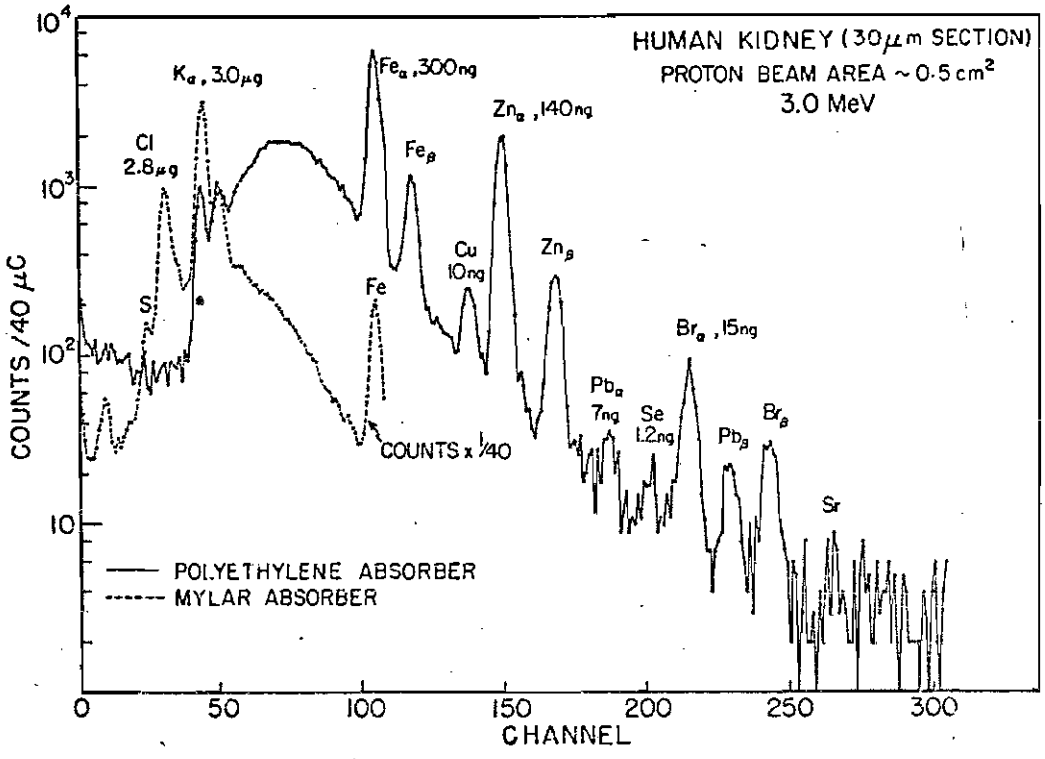
HUMAN KIDNEY (30μm SECTION)
PROTON BEAM AREA ~0.5 cm²
3.0 MeV
Kα, 3.0μg
Cl 2.8μg
S
Feα, 300ng
Feβ
Fe
Cu 10ng
Znα, 140ng
Znβ
Pbα 7ng
Se 1.2ng
Brα, 15ng
Pbβ
Brβ
Sr
COUNTS x 1/40
POLYETHYLENE ABSORBER
MYLAR ABSORBER
COUNTS / 40 μC
CHANNEL

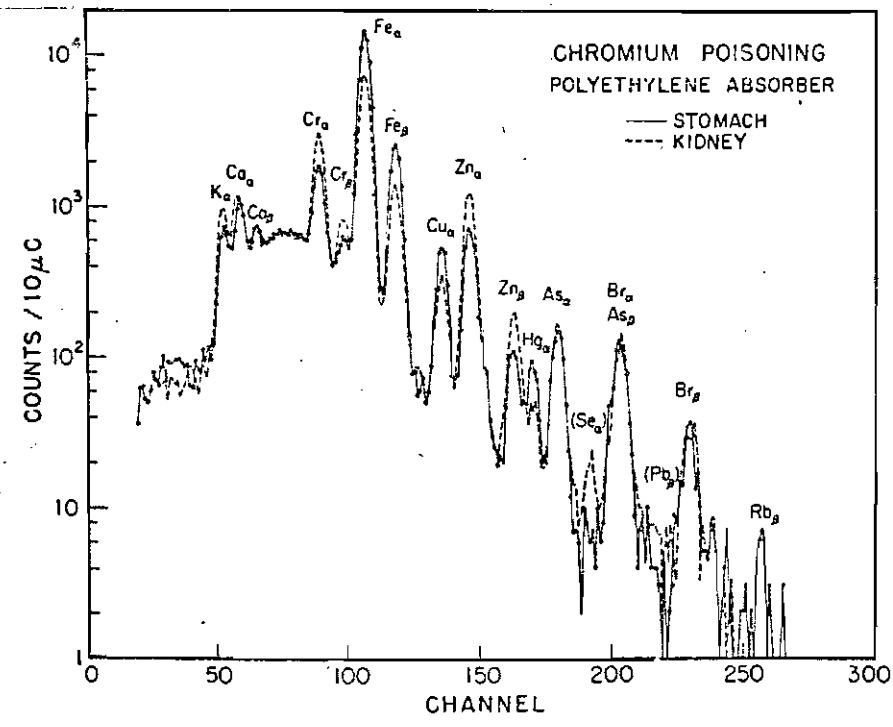
CHROMIUM POISONING
POLYETHYLENE ABSORBER
STOMACH
KIDNEY
Kα
Caα
Caβ
Crα
Crβ
Feα
Feβ
Cuα
Znα
Znβ
Asα
Hgα
Brα
Asβ
(Seα)
Brβ
(Pbβ)
Rbβ
COUNTS / 10 μC
CHANNEL

Table 4.3

Elemental Abundance in ppm (Dry Weight) for Human Tissue Sections from Chromium Poisoning Subject

ELEMENT	STOMACH	HEART	KIDNEY	SPLEEN	LUNG	LIVER	BRAIN	WHOLE BLOOD	DETEC. LIMIT
K	5600	7900	6600	15,000	14,000	10,500	33,000	7,800	250
Ca	450	100	730	(100)	(300)	(250)	(250)	50	40[a]
Cr	79	9.9	170	40	64	170	3.7	18	2.7
Mn	2.4	1.1	0.0	4	0.8	0.0	2.2	4.3	2.3[b]
Fe	710	190	430	1,900	1,400	820	460	2,100	1.8
Ni	1.0	1.2	0.2	0.1	0.8	0.2	0.8	1.5	1.1
Cu	25	14	21	4.6	20	74	32	3.0	0.8
Zn	58	58	110	65	75	112	68	27	0.7
As	20	3.7	21	6.1	10.1	16	3.6	0.7	0.6
Se	0.3	0.5	2.0	0.3	0.6	1.4	1.1	0.1	0.5
Br	27	9.5	24	18	40	11.5	13	10.3	0.5
Rb	9.7	8.8	8.4	14	16	19	27	6.2	0.5
Sr	0.8	1.0	0.8	0.1	1.3	0.8	1.4	0.3	0.5
Hg	20	5.2	9.7	9.5	14	2.5	3.0	10.8	2.1
Pb	1.1	2.8	1.9	0.6	1.3	2.8	3.6	0.7	1.4

a) 40 or 3% of Potassium, whichever is greater.

b) 2.3 or 2% of Cr, whichever is greater.

ingesting a Cr-Cu solution. Thick sections of 7 organs and dried blood samples were analyzed directly with PIXE using no preparation other than mounting the samples for irradiation. Resulting spectra for stomach and kidney samples are superimposed in Figure 4.14. Although the Cr concentrations in both organs are indeed high (Table 4.3), the high levels of As and Hg were not expected, and suggest that additional factors may have contributed to the subject's death. These results emphasize the value of a multielement technique such as PIXE. Table 4.3 presents the results of our analysis for 20 elements and 8 samples. An independent analytical laboratory checked our results for Cr and Cu for other portions of the same sample, and they found good agreement for 13 of the 16 values. The last column of Table 4.3 shows the average detection limits for these samples to be at the ppm (dry weight) level.

Placenta tissue has been analyzed as part of a study by the EPA into the possible adverse effects of polluted environments on unborn children. The tissue had been lyophilized and homogenized producing a dry powder which was conveniently pressed into 13 mm diameter pellets. Spectra are shown in Figure 4.15 of two placenta pellets, one of which had been doped with the listed concentrations of V, Ni, and Pb prior to pelletizing. The internal calibration provided a check on thick-target correction factors calculated by FUDGE. A second set of 6 placenta pellets, includ-

ing 3 plain pellets and 3 pellets doped with approximately 30 ppm (dry weight) of V and Ni, were analyzed and the results were presented earlier in Table 3.3. The doped pellets yielded effective mass values for placenta of 2.83 mg and 2.67 mg for the V and Ni respectively. These values agree fairly well with the corresponding values of 2.68 mg (V) and 2.73 mg (Ni) calculated by FUDGE for an infinitely thick C matrix. (The experimental effective mass observed for V is somewhat difficult to ascertain because of uncertainties in the background assignment in this region.) This agreement is encouraging evidence that quantitative, accurate analyses can be carried out on some thick biological or dominantly organic samples. The abundances listed in Table 3.3 are based on the effective mass values for a thick carbon matrix (Table 3.2). Actually, only a few elements in placenta are detected in a typical 5 min analysis even though the detection limits are near the ppm level (dry weight basis).

A number of analyses of hair samples using PIXE have been reported (Horowitz and Grodzins, 1976; Cookson and Pilling, 1975; and Valkovic et al., 1973). In particular, the use of a highly focused beam to scan the length of a strand of hair can provide a time record of the body's ingestion or exposure to heavy metals. An indication of the elements which can be observed in human hair samples is given in Figure 4.16 which shows one of our PIXE spectra

Figure 4.15 PIXE spectra from analyses of plain and doped placenta pellets. The dopant solution contained 40 ppm Ni, 40 ppm V, and 200 ppm Pb.

Figure 4.16 PIXE spectrum from analysis of human hair.

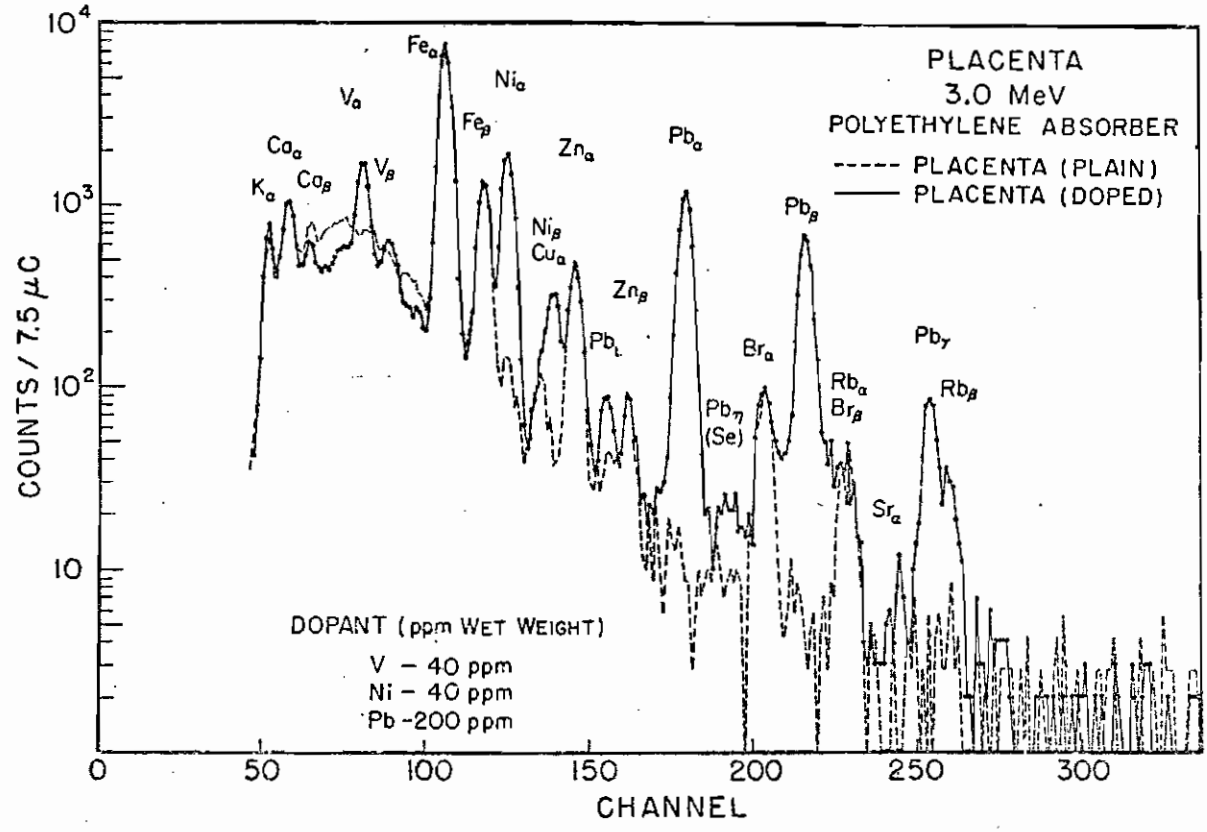
PLACENTA
3.0 MeV
POLYETHYLENE ABSORBER
----- PLACENTA (PLAIN)
—— PLACENTA (DOPED)
DOPANT (ppm WET WEIGHT)
V – 40 ppm
Ni – 40 ppm
Pb –200 ppm
COUNTS / 7.5 μC
CHANNEL
Ka
Caa
Caβ
Va
Vβ
Fea
Feβ
Nia
Niβ
Cua
Zna
Znβ
Pba
Pbβ
Pbγ
PbL
Pbη (Se)
Bra
Rba Brβ
Rbβ
Sra

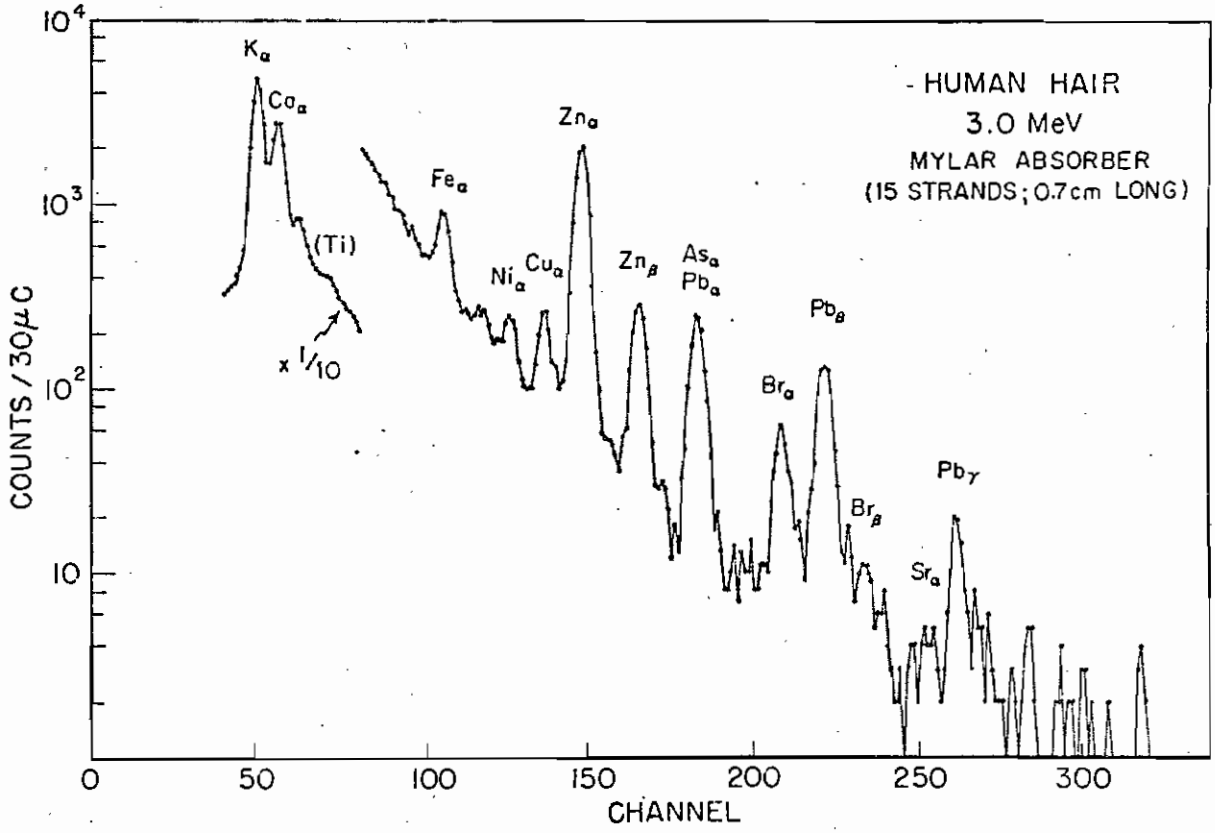
HUMAN HAIR
3.0 MeV
MYLAR ABSORBER
(15 STRANDS; 0.7cm LONG)
COUNTS / 30μC
CHANNEL
Ka
Caa
(Ti)
x 1/10
Fea
Nia
Cua
Zna
Znβ
As a Pba
Pbβ
Bra
Brβ
Pbγ
Sra

Table 4.4

EPA Hair

Element	Specimen A ppm (d.l.)	Specimen B ppm (d.l.)	Commercial Lab ppm
S	(20,000)		
Cl	400(50)		
K	870(10)		
Ca	150(6)		
Ti	18(3)		
V	0.7(3)	2.5(3)	0.9
Cr	0.0(3)	0.0(2)	0.9
Mn	1.8(2)	0.5(1.4)	1.0
Fe	38 (1.4)	19(1.0)	17
Ni	3.3(1.1)	2.6(0.8)	3.7
Cu	8.6(1.0)	6.7(0.8)	9.8
Zn	107 (0.9)	104 (0.7)	110
Ga	1.9(0.8)		
As	1.6(0.8)	0.0(0.8)	0.06
Se	0.1(0.8)	0.3(0.7)	0.35
Br	5.9(0.6)	9.3(0.8)	
Rb	0.8(0.5)	0.0(0.8)	
Sr	0.7(0.6)	0.5(0.1)	
Hg	3.5(1.4)	1.6(2.5)	2.2
Pb	23 (1.2)	97 (2.1)	15.6

for hair samples. This particular specimen was provided by the EPA. In order to obtain good sensitivity in a reasonable time, 15 strands of hair were aligned in a single layer and stretched across a 2.54 cm diameter fiber washer ring. Results of the analysis of this sample and a second sample from the same specimen are tabulated in Table 4.4, and compared to a chemical analysis conducted by a commercial laboratory. Because of the uncertainty in the amount of hair irradiated by the beam, the PIXE values in Table 4.4 are normalized to the Zn abundance (110 ppm) determined from the chemical analysis. The gross variations observed between the two specimens for a number of elements is surprising since the two specimens were each composed of approximately 10 strands selected randomly from the original sample. For comparison, analyses of hair samples from several healthy residents of Durham showed much lower Pb concentrations.

During the past year, the Duke PIXE system has been used as part of an interdisciplinary study of pulmonary disease (Gutknecht et al., to be published). One major aspect of this project involved characterizing the trace element concentrations in pigmented and non-pigmented lung tissue collected from individuals with known medical, occupational, and smoking histories. The presence of black pigmented tissue in the excised lung has been associated with the gradual accumulation over many years of respirated particulate matter which collects especially around terminal bronchioles.

Some questions which prompted the present investigation were: (1) Can the presence of certain metals in the pigmented areas be correlated to certain pulmonary diseases? and (2) Do these pigmented areas provide the best and most meaningful indication of an individual's exposure to gaseous and particulate pollutants?

The lungs used in this study were obtained intact from autopsies and were formalin-fumed and lyophilized. Initial sample preparation consisted of simply slicing a 1 cm-thick section of the dried lung and attaching the sample using a clean adhesive to a strip of aluminized mylar. Unfortunately, this simple procedure had to be abandoned for quantitative analyses because of the extreme porosity of the lung which made it virtually impossible to obtain reasonable estimates of the effective irradiated mass. Subsequent samples were prepared by ashing the lung in a mixture of concentrated HNO_3 and H_2SO_4 (2:1). This was taken to dryness and the residue dissolved in dilute HNO_3 prior to deposition onto nuclepore membranes. Volatilization losses incurred during the above procedures were investigated by analyzing bovine liver samples prepared in identical fashion. Losses of Se and Br were observed as expected but the other detected elements between K and Mo appeared unaffected.

The results of our analyses are still being interpreted. Some preliminary results are displayed in the bar graphs of Figures 4.17 and 4.18 for the elements Zn and Pb

respectively. Each pair of bars represents one individual. The shaded bar indicates the abundance observed in the pigmented area and the non-shaded bar represents the concentration observed in the non-pigment area. Individuals are grouped according to their histories as emphysemic or normal, and the latter group is further differentiated into smokers and non-smokers. All of the emphysemic subjects were smokers. The vertical scale represents the ppm concentration (on log scale for Zn).

Several features are noteworthy in Figures 4.17 and 4.18. First, there are gross variations observed between individuals. Some intra-sample variance contributes to there variations. Secondly, there appears to be no clear correlation between the measured levels of Zn and Pb, and an individual's history as emphysemic or normal, smokers or non-smoker. The most striking feature to be noted is that when an unusually large concentration is observed in the samples of an individual, the greater concentration is found in the pigmented area. This feature is brought out more clearly for Pb in the presentation shown in Figure 4.19. The ratio of (P-N)/(P+N) is plotted versus (P+N) for each individual, where P is the concentration of Pb in the pigmented region and N is the concentration in the non-pigmented region. In this way, the inter-sample variation is suppressed. As Figure 4.19 shows, when the total concentration (P+N) is small, the ratio (P-N)/(P+N) is close to zero indicating

Figure 4.17 Results from PIXE analyses of Zn in pigmented (cross-hatched bars) and non-pigmented (clear bars) regions of lung samples from 24 individuals. Results are presented in ppm dry weight and are categorized according to the individual's history as emphysemic, normal (smoker), or normal (non-smoker).

Figure 4.18 Results from PIXE analyses of Pb in pigmented and non-pigmented regions of lung samples from 22 individuals. See caption above.

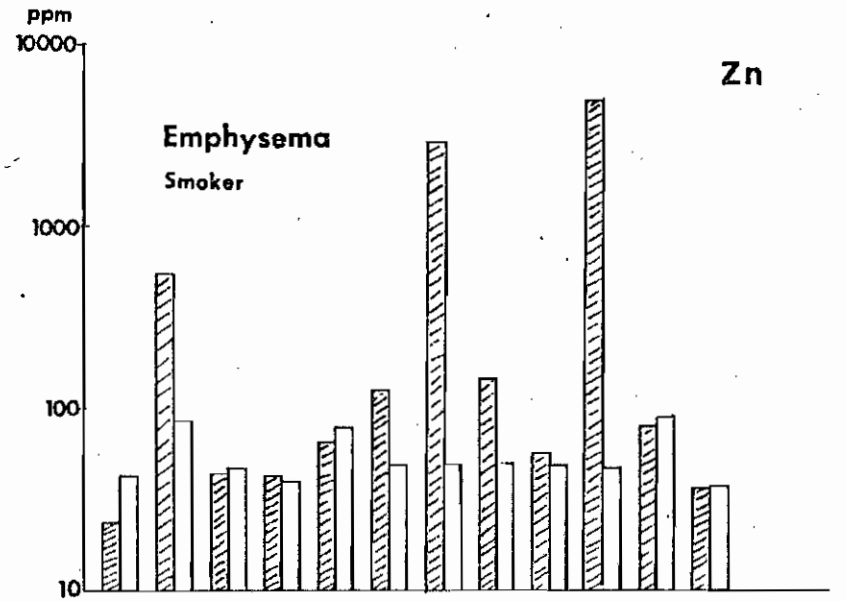
ppm
10000
1000
100
10
Zn
Emphysema
Smoker


EMPHYSEMA
Smoker
Pb
ppm
50
0

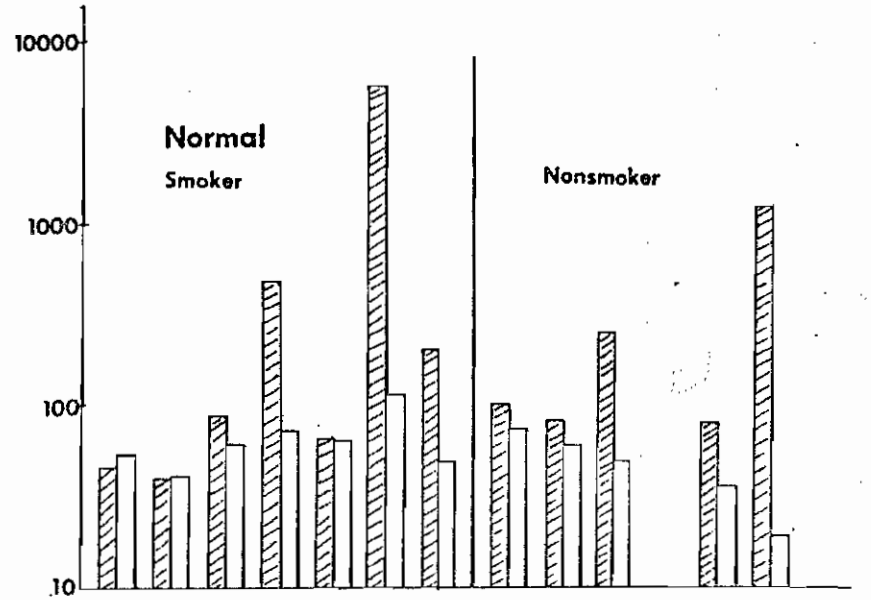
10000
1000
100
10
Normal
Smoker
Nonsmoker

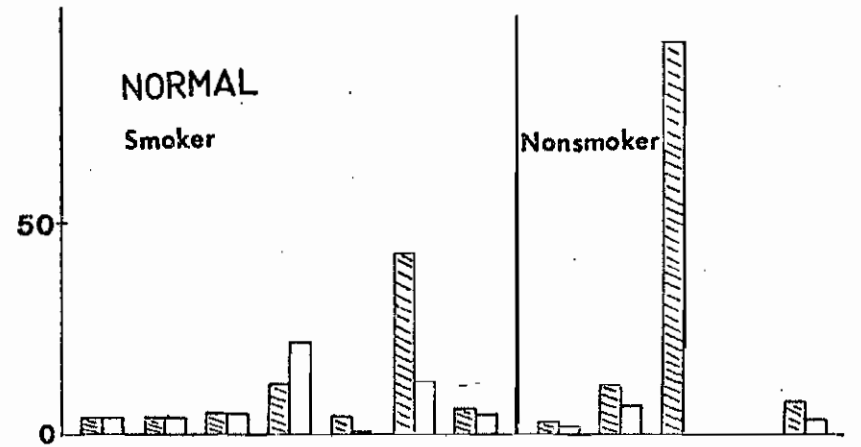
NORMAL
Smoker
Nonsmoker
50
0

Figure 4.19 Parts per million Pb in pigmented region minus ppm in non-pigmented region divided by the sum as a function of the total Pb concentration in both regions. See text for discussion.

Figure 4.20 PIXE spectra from analyses of two urine samples. Sample V came from a subject involved in a study of Hg pollution. Sample VI is from a subject with cancer of the prostrate.

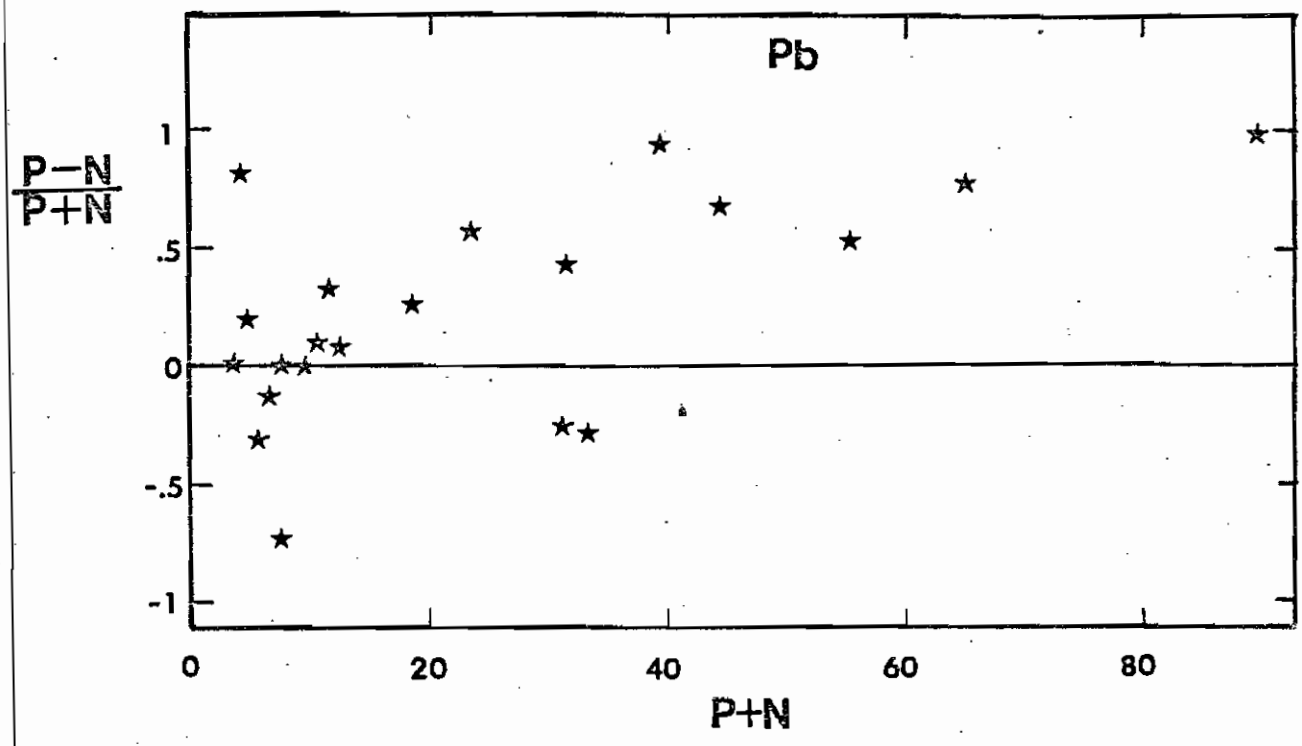
Pb
P−N / P+N
1
.5
0
-.5
-1
0
20
40
60
80
P+N

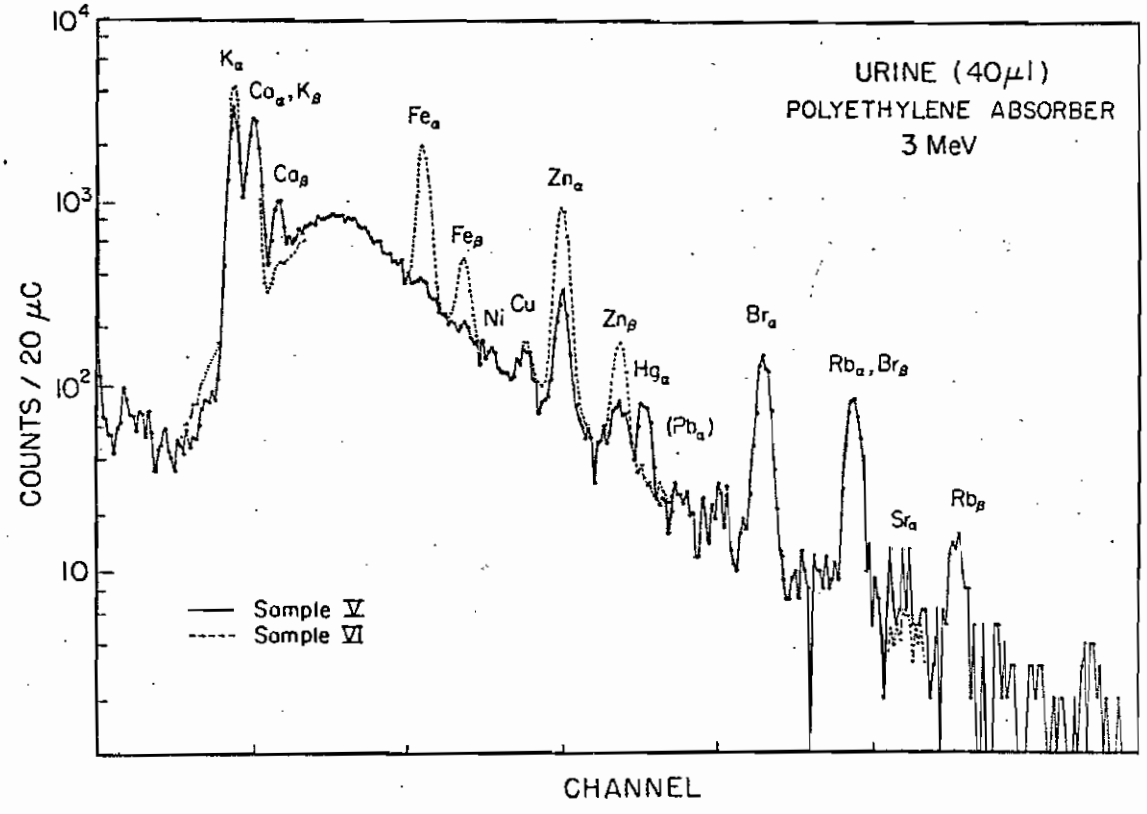
URINE (40μl)
POLYETHYLENE ABSORBER
3 MeV
Kα
Coα, Kβ
Coβ
Feα
Feβ
Ni
Cu
Znα
Znβ
Hgα
(Pbα)
Brα
Rbα, Brβ
Srα
Rbβ
Sample V
Sample VI
COUNTS / 20 μC
CHANNEL

that the Pb is distributed nearly equally between the pigmented and non-pigmented areas ($P \approx N$). The positive and negative fluctuations observed can probably be attributed to intra-sample variations and experimental uncertainties. As (P+N) gets larger, the ratio (P-N)/(P+N) clearly increases towards the value of 1 indicating that the Pb burden is increasingly concentrated in the pigmented area.

Work is continuing on this project in the search for more correlations between metal burdens and the subject's medical, occupational, and smoking history.

IVB.2 Bodily fluids

Samples of whole blood, blood serum, and urine have been studied at Duke. Several preparation techniques were tried including drop deposits of whole and ashed samples, and pellets (of lyophilized blood).

Figure 4.20 shows spectra of two urine samples prepared by depositing 40 µl of each specimen onto nuclepore membranes. Sample V was collected from a subject involved in a study of Hg pollution in the Cape Fear River Basin area of North Carolina. Sample VI was collected from a patient with cancer of the prostate. Both spectra show surprisingly similar levels of K, Cu, Br, and Rb. The latter sample however had appreciably higher levels of Fe and Zn, while sample V produced a clear Hg signal. In order to check the Hg concentration in this sample, and to check the

Figure 4.21 PIXE spectra from analyses of two urine samples doped with 1 ppm Pb (solid line) and 1 ppm Hg (dashed line), respectively.

Figure 4.22 PIXE spectrum from analysis of lyophilized blood pellet.

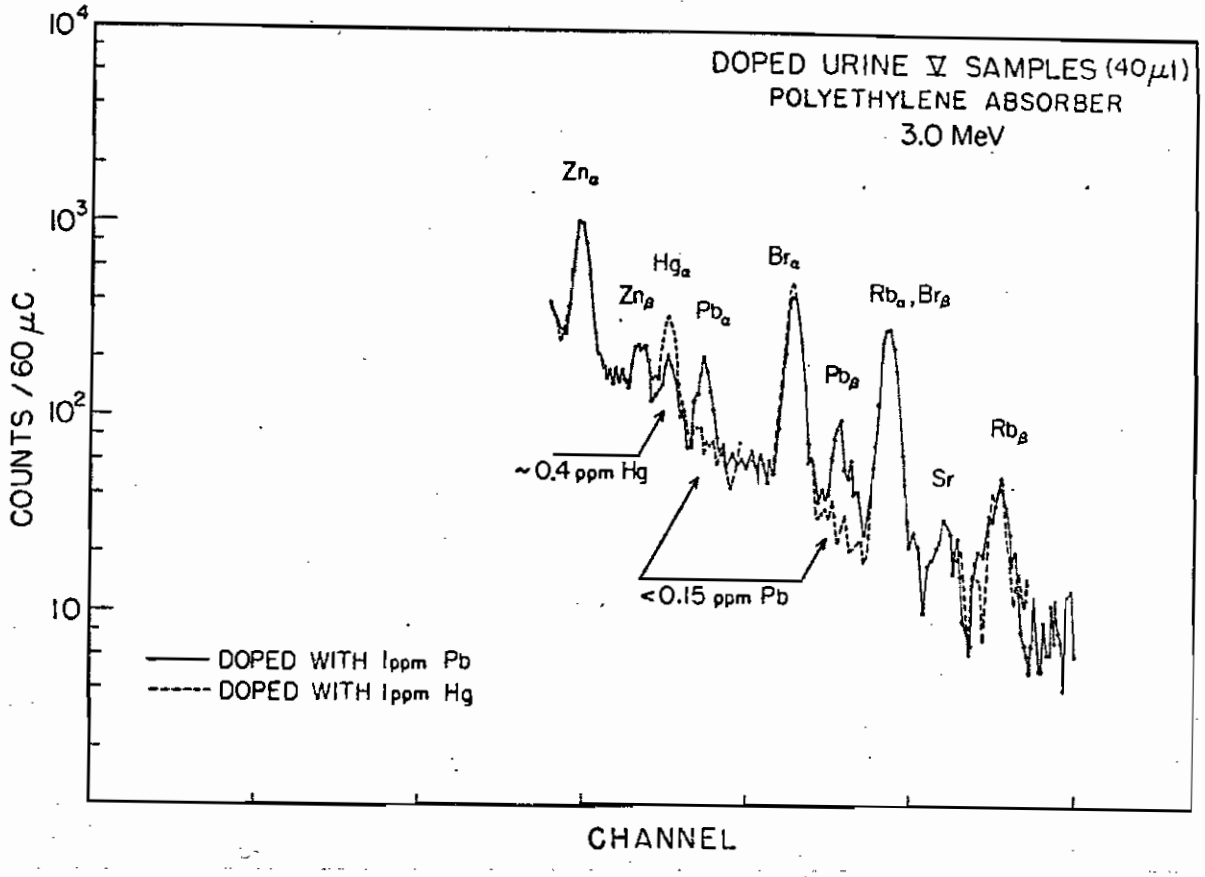
DOPED URINE V SAMPLES (40μl)
POLYETHYLENE ABSORBER
3.0 MeV
Zn$_\alpha$
Hg$_\alpha$
Zn$_\beta$
Pb$_\alpha$
Br$_\alpha$
Rb$_\alpha$, Br$_\beta$
Pb$_\beta$
Rb$_\beta$
Sr
~0.4 ppm Hg
<0.15 ppm Pb
DOPED WITH 1ppm Pb
DOPED WITH 1ppm Hg
COUNTS / 60 μC
CHANNEL

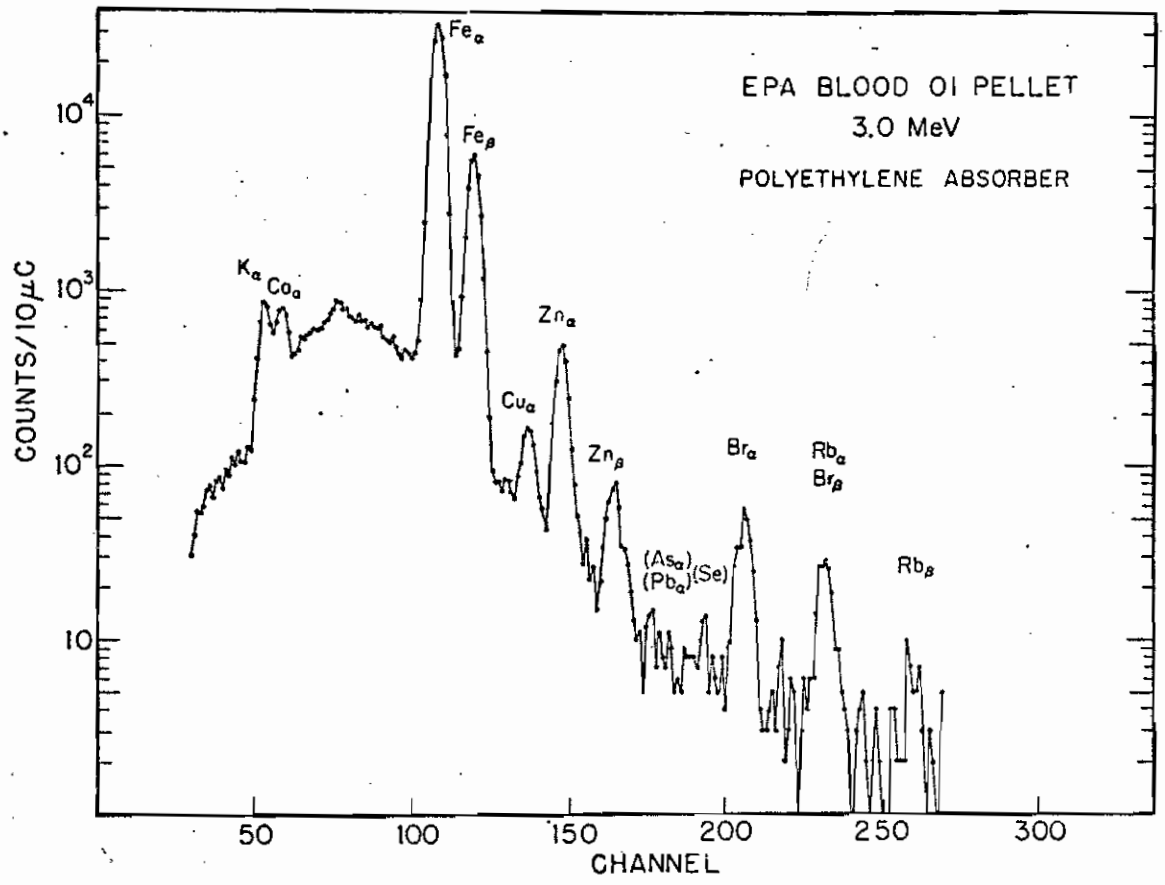
EPA BLOOD 01 PELLET
3.0 MeV
POLYETHYLENE ABSORBER
Fe$_\alpha$
Fe$_\beta$
K$_\alpha$ Co$_\alpha$
Zn$_\alpha$
Cu$_\alpha$
Zn$_\beta$
Br$_\alpha$
Rb$_\alpha$ Br$_\beta$
(As$_\alpha$) (Pb$_\alpha$) (Se)
Rb$_\beta$
COUNTS/10μC
CHANNEL

sensitivity for Hg and Pb analysis in urine, targets were prepared from 2 doped urine samples--one containing 1 ppm Hg, and the other doped with 1 ppm Pb. The spectra are shown in Figure 4.21. Comparison of the two spectra yields an estimated Hg concentration of 0.4 ppm in sample V, and a detection limit for Pb of approximately 0.15 ppm. These and other urine analyses conducted at Duke suggest that urine analysis may be a simple and sensitive indicator of metal imbalances in the body.

The analysis of blood samples was made difficult by problems in preparing suitable targets. Whole blood coagulates as it dries, causing the deposit to pull away from the substrate. The addition of distilled deionized water to the blood in order to weaken the coagulation process was helpful but did not eliminate the problem. In order to prevent the loss of sample material via cracking and flaking, mylar-mylar and mylar-nuclepore sandwiches were employed with moderate success. A more convenient preparation method which yields good results, but unfortunately requires relatively large quantities of freeze-dried blood, is to press pellets from the lyophilized blood. Figure 4.22 shows a spectrum obtained in approximately 6 min for a pellet made from lyophilized blood provided by the EPA. Few elements are observed in the spectrum even though the detection limits are as low as 0.2 ppm (wet weight) for many elements. The use of low temperature wet ashing in order to improve

sensitivity for blood analyses was discussed earlier in Section IIIE.4. Table 3.11 from that section compares the elemental abundances (ppm wet weight) for pelletized blood and ashed blood samples, and demonstrates that ashing can improve sensitivity by nearly a factor of two for many elements. Table 3.11 suggests however that K and Br have been volatilized in the ashing process, and that the Zn concentration in the ashed sample may have been enhanced due to trace impurities in the ashing solution. Also listed in Table 3.11 are the abundances determined by a commercial laboratory. These values suggest that PIXE detection sensitivities must be improved in order to provide analyses for several of the most interesting elements associated with pollution, but that the sensitivities are sufficient for some baseline nutrition studies. We have also investigated deposits of serum and, like whole blood, the levels of heavy metals is quite low, but differences in elemental abundances for nutritional studies can be looked at.

IVB.3 Animal studies

PIXE is a convenient method for monitoring elemental abundances and interelement relationships in laboratory animals used in controlled experiments. We participated in one study conducted by scientists at the National Institute of Environmental Health Sciences (NIEHS) who were investigating Cd toxicity in laboratory rats. One particular concern was whether the presence of Cd in the rat's

body would affect the levels of other trace metals. Thick sections of kidney and liver tissue were analyzed with PIXE for both control rats and rats fed on a diet spiked with Cd. A spectrum from a non-control rat kidney is shown in Figure 4.23 with selected elemental abundances listed. This spectrum is fairly significant in that Cd is the heaviest element for which we have obtained a usable peak from K X-ray emission. The value determined from the Cd peak in Figure 4.23 is 72 ppm (wet weight). This value was confirmed by atomic absorption analysis at a commercial laboratory.

The advantages of PIXE's multielement capability are illustrated in the analysis of lung macrophage taken from a laboratory rabbit. The spectrum is shown in Figure 4.24. Although our interest was simply to determine detection limits for this type of sample, the spectrum revealed information that came as a surprise to the researchers involved in the laboratory experiment. The large Hg peak observed in Figure 4.24 was not anticipated since the rabbit was presumably well cared for with no known history of exposure to Hg. Clearly such information can become significant when one is attempting to formulate valid scientific conclusions based on the health of the animals.

IVB.4 Fresh-water fish

In Section VB a major study investigating metal

Figure 4.23 PIXE spectrum from analysis of a thick section of rat kidney. Note the clear presence of Cd in channels 400 and 450.

Figure 4.24 PIXE spectrum from analysis of rabbit lung alveolar macrophage. Note the presence of Hg.

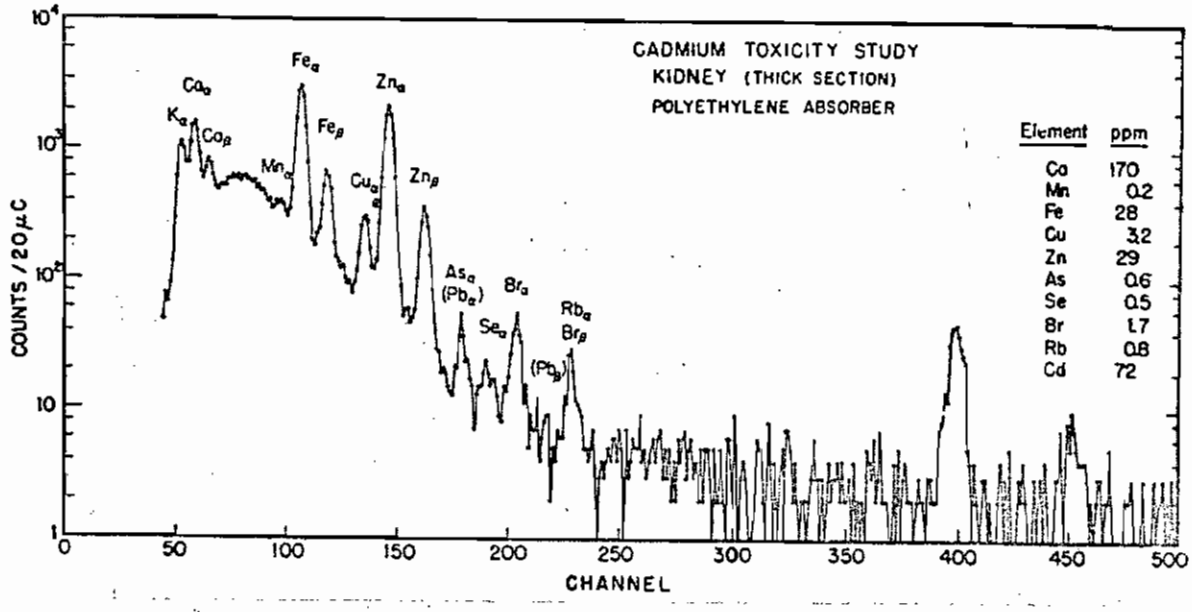
CADMIUM TOXICITY STUDY
KIDNEY (THICK SECTION)
POLYETHYLENE ABSORBER
Element ppm
Ca 170
Mn 0.2
Fe 28
Cu 3.2
Zn 29
As 0.6
Se 0.5
Br 1.7
Rb 0.8
Cd 72
COUNTS / 20 μC
CHANNEL

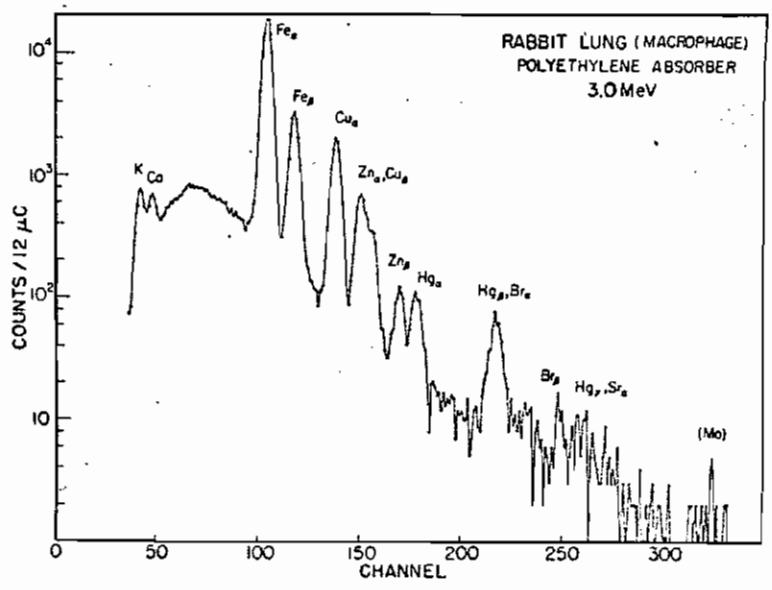
RABBIT LUNG (MACROPHAGE)
POLYETHYLENE ABSORBER
3.0 MeV
COUNTS / 12 μC
CHANNEL

toxicities in marine life is discussed. Our first application of PIXE to the analysis of fish tissue was a study of a fresh water fish taken from a "clean" stream near Durham. The particular section of the stream investigated was located near the sewage outfall from a moderately large city. Water samples collected upstream and downstream from this outfall using ion-exchange membranes showed very low levels of pollutant metals. Analyses of the fish tissue and several organs also gave low metal abundances. Figure 4.25 shows a spectrum from a thick section of muscle which was simply removed from the fish with a clean scalpel and attached to the target rod. For the relatively short analysis represented in Figure 4.25, only a few metals are observed above the detection limits which range in the tenths of ppm (wet weight). The abundances listed were obtained by normalizing the results to the Fe abundance of 6.2 ppm determined by atomic absorption analysis. The major benefit derived from this initial study was the demonstrated ability of the PIXE technique to obtain useful information from such analyses. There is some evidence that populations of fish can serve as very sensitive monitors of trace contaminant levels in bodies of water. Studies on the physiological response of fish to changes in their environment may be facilitated by the use of PIXE.

Figure 4.25 PIXE spectrum from analysis of a thick section of carp muscle. Elemental abundances or upper limits are in ppm wet weight.

Figure 4.26 PIXE spectra of four metalloproteins after subtraction of background due to nuclepore substrate. (a) Fe (II) cytochrome c (b) Cu (II) cytochrome c (c) Zn (II) carbonic anhydrase (d) Co (II) carbonic anhydrase. Trace impurities are indicated by arrows.

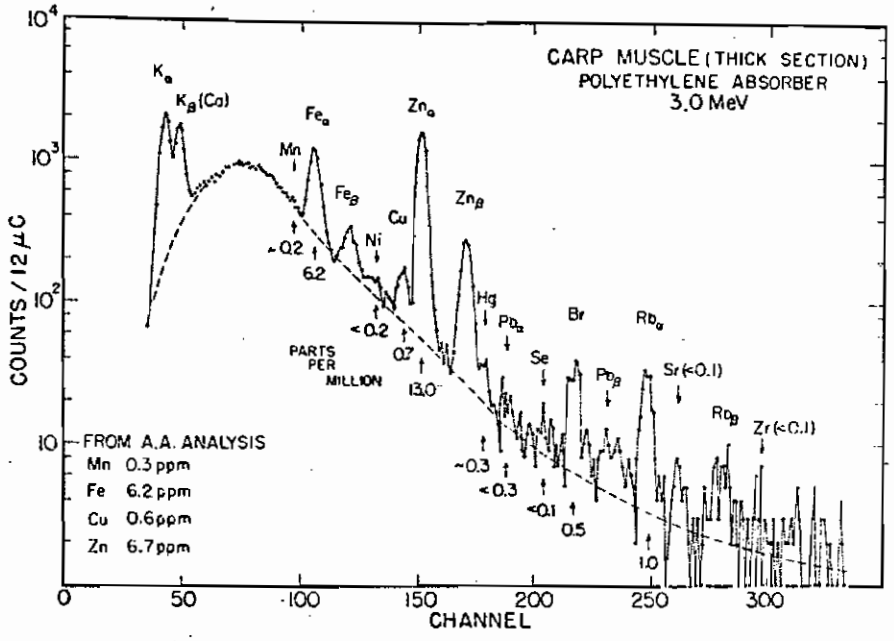
CARP MUSCLE (THICK SECTION)
POLYETHYLENE ABSORBER
3.0 MeV
COUNTS / 12 μC
CHANNEL
PARTS PER MILLION
FROM A.A. ANALYSIS
Mn 0.3 ppm
Fe 6.2 ppm
Cu 0.6 ppm
Zn 6.7 ppm

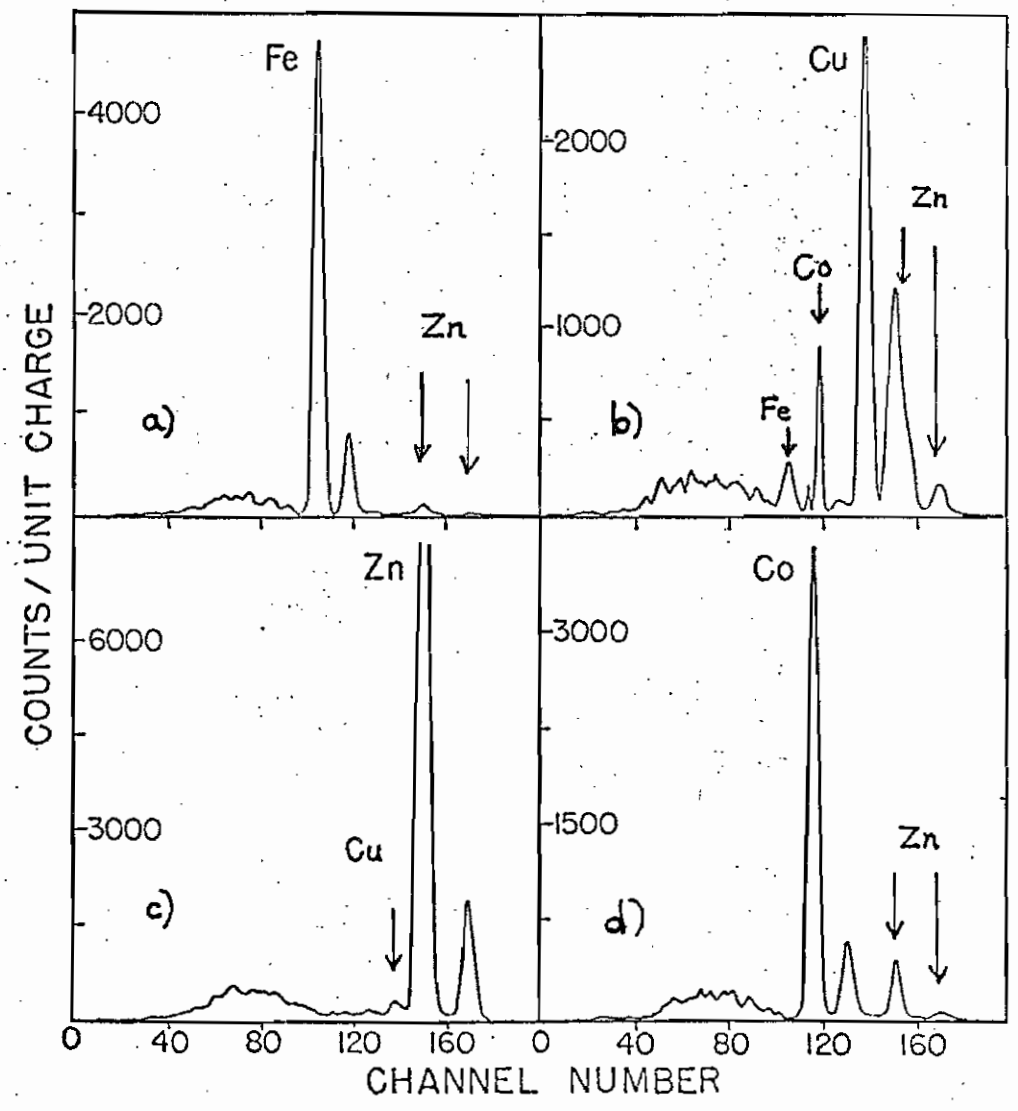
COUNTS / UNIT CHARGE
CHANNEL NUMBER
a)
b)
c)
d)
Fe
Zn
Cu
Co

IVB.5 Enzyme and protein analyses

A major attractive feature of PIXE is its ability to obtain good sensitivity on small quantities of sample. Two studies which utilized this feature at Duke involved the analysis of enzymes and metalloproteins. These substances are frequently difficult to obtain in sufficient quantities for conventional analytical techniques.

The first study involved the analysis of two enzymes--dismutase oxidase and sulphaoxidase. Detection limits for ashed dismutase deposited on formvar backings were found to be 0.1 to 0.5 ppm for the elemental range from Mn to Mo.

The analyses of metalloproteins was part of an investigation into the levels of metal-ion contaminants in commercially prepared metalloproteins (Lochmüller et al., 1974a). Results of the analyses of four metalloproteins are shown in Figure 4.26a, b, c, and d. The materials analyzed were Fe (II) cytochrome c, Cu (II) cytochrome c, Zn (II) carbonic anhydrase, and Co (II) carbonic anhydrase for parts a, b, c, and d respectively of Figure 4.26. The trace impurities are indicated by arrows in the figure. These spectra were obtained using sample amounts ranging from 0.04 mg to 0.4 ng deposited on nuclepore.

IVC. Plant and Soil Analyses

One of the first applications of the Duke PIXE system

was the analysis of leaf specimens. Acting as natural collection devices, leaves provide information about airborn particulate matter and also reflect the trace element chemistry of the soil which nourishes the plant. Furthermore, leaves are excellent targets for PIXE analysis, requiring little or no preparation. Several studies have been investigated at Duke in an effort to correlate the metal abundances observed in plants with those present in the plant's environment. These studies are described in Section VA. In addition, a number of isolated studies described below, have been conducted relating to trace elements in plant and soil specimens.

One unusual study brought to our attention by the EPA involved the case of the "Clay Eaters" of North Carolina. These are groups of people living in several regions of the state who habitually eat clay as part of their diet. The EPA, concerned about the health effects of this practice, provided us with a specimen of clay obtained from a river bank in Mecklenberg County, North Carolina. Pellets were pressed from this clay and analyzed and the results are presented in the Table 4.5. The high levels of Ti, Ba, Pb, and other metals must certainly be cause for concern although it is not clear how much of these elements would be retained in the body.

Specially designed, climate-controlled botanical laboratories provide ideal controlled environments for in-

Table 4.5

EPA Clay

Location: Mecklenberg Co., Catawba River Bank near end of Mathis Road.; Dixie Station. Verified as being eaten.

Element	Pellet[a] (approx. ppm)	
K	3,120	(40)
Ca	420	(28)
Ti	4,400	(18)
V	0.0	(18)
Cr	48	(18)
Ba	280	(100)
Mn	920	(40)
Fe	76,000	(16)
Ni	44	(6)
Cu	46	(5)
Zn	50	(4)
As	3	(3)
Se	2	(3)
Br	5	(3)
Rb	40	(3)
Sr	68	(4)
Hg	3	(8)
Pb	48	(7)

a) No absorption correction applied.

vestigating the response of plants to changes in the trace element chemistry of the soil. PIXE will be a useful technique to complement such studies. In one experiment, we analyzed leaves of two tomato plants, one of which was grown in a controlled botanical laboratory. The major difference observed in the two leaf specimens was the relatively large concentration of Rb in the leaf of the laboratory-grown plant. This was attributed to the Vermiculite base in which the laboratory plants were grown.

Figure 4.27 presents the results of another leaf study. In this case we utilized the small beam area to examine a brown blemish and an adjacent normal green area of a maple sugar leaf. The interpretation of these results would require many more analyses, but we wish to emphasize that multielemental information such as that shown in Figure 4.27 can be generated in typically 10 min or less.

As a final example, we present some results obtained from PIXE analyses of tree bore plugs. Our interest in this study was to determine if the growth rings of a tree exhibited evidence of increased metal buildup, thus providing a time record of environmental pollution. The tree selected for this study was a 50-year old willow oak growing adjacent to a main thoroughfare near downtown Durham. The device used for extracting the tree bore plug consisted of a 30 cm-long hollow cylindrical tube which inserts into a second tube that is threaded for boring. Using this device we ob-

Figure 4.27 Results of a PIXE study of elemental abundances in a green region and an adjacent brown spot on a sugar maple leaf.

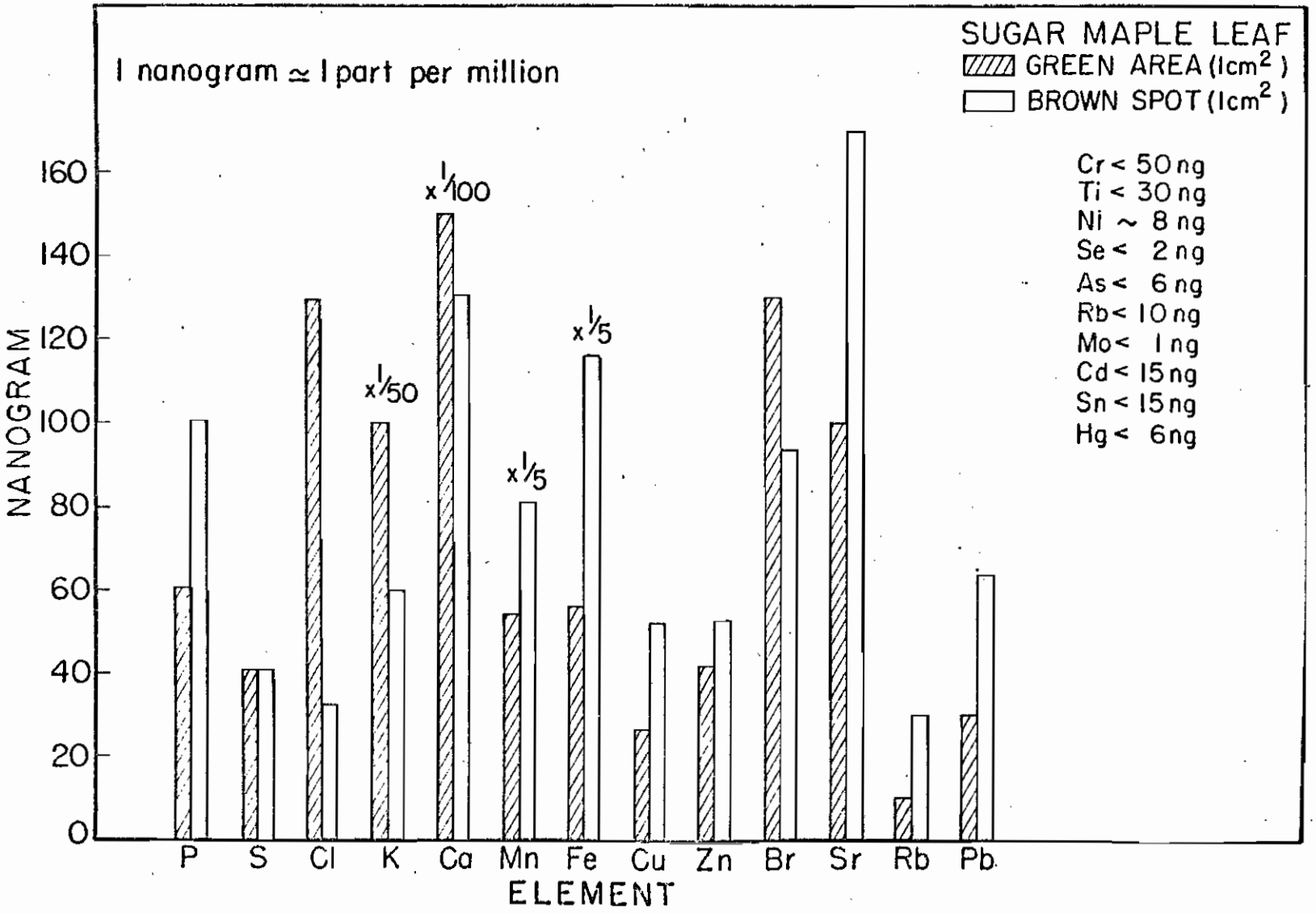
SUGAR MAPLE LEAF
GREEN AREA (1cm²)
BROWN SPOT (1cm²)
1 nanogram ≃ 1 part per million
Cr < 50 ng
Ti < 30 ng
Ni ~ 8 ng
Se < 2 ng
As < 6 ng
Rb < 10 ng
Mo < 1 ng
Cd < 15 ng
Sn < 15 ng
Hg < 6 ng
NANOGRAM
0
20
40
60
80
100
120
140
160
x 1/50
x 1/100
x 1/5
x 1/5
P
S
Cl
K
Ca
Mn
Fe
Cu
Zn
Br
Sr
Rb
Pb
ELEMENT

tained a plug from along a radial from the tree's center. This plug was approximately 25 cm long and 0.6 cm in diameter. Thin circular wafers were sliced from the plug approximately every 2.5 cm and attached to a long strip of mylar using a small amount of adhesive applied to the back of the wafer. The results of these analyses are shown in Table 4.6 where position A corresponds to the outermost ring and position I is slightly beyond the center. Typical detection limits are shown in the last column of Table 4.6. Gross variations were observed in the elemental abundances versus depth, but no systematic trends were observed.

In summary, the PIXE technique has proven its capabilities in diverse areas of investigation. As the value of multielement information becomes increasingly appreciated in medical, biological, botanical, and environmental sciences, the PIXE method clearly will be able to make significant contributions to these research areas.

Table 4.6 Elemental Composition in ppm as Function of Depth Into Tree.

Element	POSITION									Dectability Limit
	A	B	C	D	E	F	G	H	I	
K	3300	1800	4600	9400	10500	2700	5700	3600	4900	30
Ca	1700	900	1200	1500	6600	4600	5400	2300	3200	15
Cr	6	5	3	1.0	0.2	2.0	3	3	1.0	4
Mn	40	30	12	14	12	31	85	38	108	2
Fe	670	600	180	140	130	160	2400	360	1020	2
Ni	0.0	0.0	0.0	0.6	0.0	0.0	(5.6)	3	3	1.0
Cu	8	10	9	8	17	13	7	9	9	1.0
Zn	16	11	11	12	18	15	24	9	20	1.0
As	0.0	0.1	1.0	0.7	1.0	1.4	1.6	0.2	0.2	0.8
Br	1.0	0.0	1.2	5	.6	0.8	2	0.1	1.3	0.4
Rb	2	0.4	1.7	4	4	1.0	3	0.8	2	0.7
Sr	13	6	8	11	27	19	24	12	18	1.2
Pb	1.7	0.2	0.0	1.6	0.5	0.0	2	0.0	0.0	2

CHAPTER V

APPLICATIONS: MAJOR STUDIES

VA. Plant and Soil Analyses

In conjunction with the Botany Department at Duke University, we have conducted several related studies on trace element accumulation in plants and the surrounding soil. The objective of these studies and some of the results will be presented below. In addition, we describe sample collection and target preparation procedures. Leaf samples make excellent targets for PIXE analysis because sample collection is easy and target preparation is minimal. In most cases, the only preparation required was to gently rinse the leaf in a cleansing solution and allow it to dry in air. The dried leaves are self-supporting and moderately flat, and can be directly mounted on the target rod for analysis.

Two difficulties with large-scale environmental studies such as the plant and soil studies discussed here and the marine life studies presented in the following section are (1) the large sampling effort required, resulting in an enormous volume of data, and (2) the interpretation of the data. Both of these problems ultimately relate to the gross

variations in elemental composition which occur naturally between members of the same species and even between adjacent regions of a single specimen. Such variations constitute "background noise" which can mask systematic trends due to different environmental habitats for example. Large numbers of samples must therefore be analyzed if the results are to be statistically meaningful. The volume of data can easily reach enormous proportions. It is estimated for example that the plant and soil studies presented below generate some 17,000 elemental abundances to be processed.

VA.1 Introduction

The earliest study undertaken was an investigation of metal accumulation in certain species of plants found growing in the metal-rich environments adjacent to mining areas. Of particular interest to the botanist participating in this study was the development of metal tolerance in these species. This evolutionary response, observed in certain species of plants, is a well documented example of natural selection (Antonovics et al., 1971).

Plant and soil samples were collected from two abandoned mining sites in North Carolina (Gold Hill, N. C. and Silver Hill, N. C.). The only species found growing at the Gold Hill site were similax rotunda folia (green briar) and coreopsis major (yellow daisy). Acid extracts were prepared from the soils in which the collected plants were grow-

ing, by shaking 10 g of soil in 100 ml of an acetic acid solution for 12 hours. The resulting solution was filtered until clear and 50 µl of the filtrate was deposited on a nuclepore backing for analysis. Representative spectra for two soil extracts (one from each location) and one leaf sample (from Gold Hill) are displayed in Figures 5.1a and 5.1b respectively. Particularly noteworthy in Figure 5.1a are the high levels of Pb observed in both soil extracts, and the difference in the Cu:Zn ratios observed at the two locations. (Gold Hill was in fact a copper mine.) Not surprisingly, several of the metals which showed large concentrations in the soil extract--e.g. Mn, Zn, and Pb--also appeared in abundance in the leaf section shown in Figure 5.1b.

The above preliminary study led to a more intensive investigation (Stanford et al., 1975) of metal uptake in plants growing adjacent to a congested highway. Analyses of soil pellets and acetic extracts were also carried out in order to observe possible correlations between metal accumulation in the plants and the trace element chemistry of the soil which nourished the plants. The PIXE analyses supported a related study investigating the evolution of Pb tolerance in two common plant species: Plantago lanceolata (Ribwort Plantain) and Cynodon dactylon (Bermuda grass). The results provided evidence for evolution of Pb tolerance in plantain, while no such evidence was observed for Bermuda grass (Wu and Antonovics, 1976).

Figure 5.1a PIXE spectra from analyses of soil extracts from mining sites at Gold Hill (solid curve) and Silver Hill (dashed curve), N. C.

Figure 5.1b PIXE spectra from analysis of a leaf sample (coreopsis major) collected at Gold Hill, N. C. Spectra obtained with the mylar absorber (dashed curve) and polyethylene absorber (solid curve) are shown.

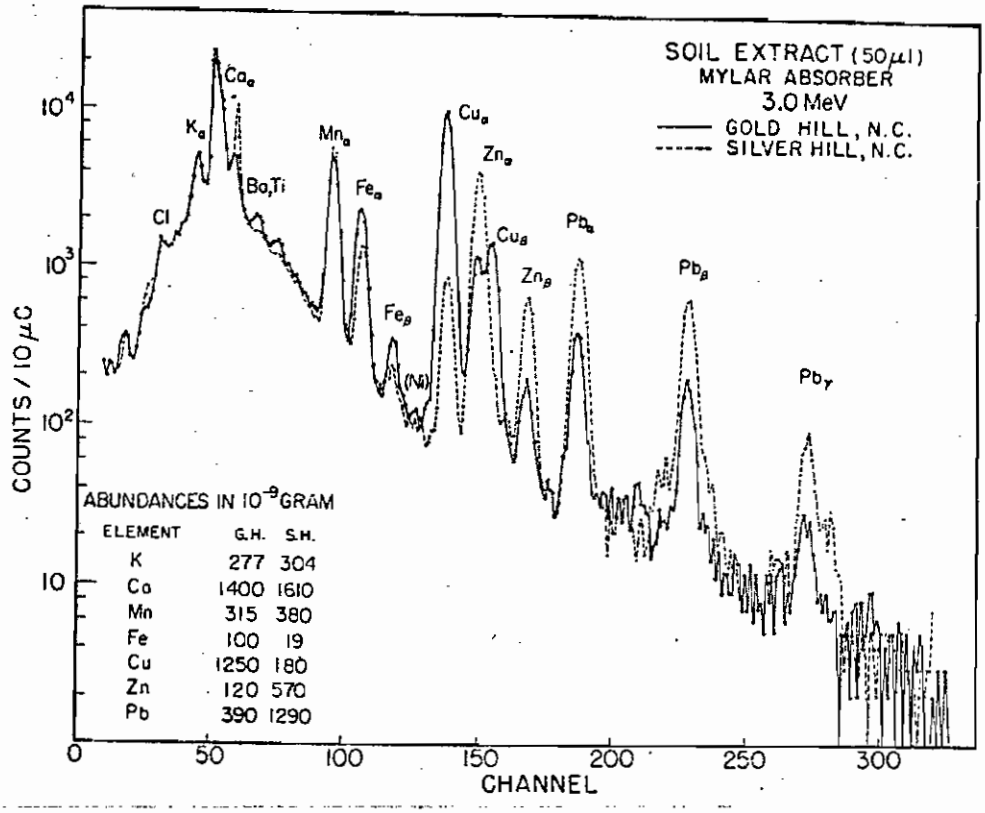
SOIL EXTRACT (50μl)
MYLAR ABSORBER
3.0 MeV
GOLD HILL, N.C.
SILVER HILL, N.C.
Cl
Ka
Caα
Ba,Ti
Mnα
Feα
Feβ
(Ni)
Cuα
Znα
Cuβ
Znβ
Pbα
Pbβ
Pbγ
COUNTS / 10μC
CHANNEL
ABUNDANCES IN 10⁻⁹ GRAM
ELEMENT G.H. S.H.
K 277 304
Ca 1400 1610
Mn 315 380
Fe 100 19
Cu 1250 180
Zn 120 570
Pb 390 1290

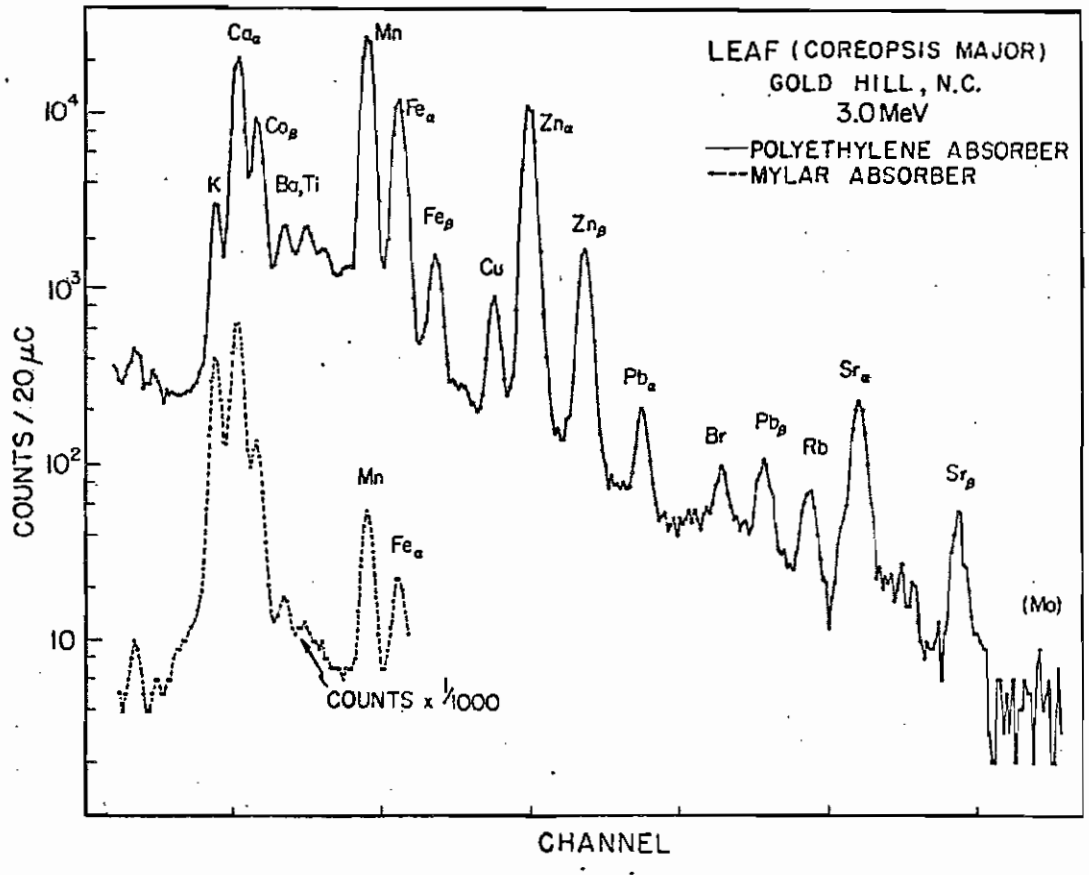
LEAF (COREOPSIS MAJOR)
GOLD HILL, N.C.
3.0 MeV
POLYETHYLENE ABSORBER
MYLAR ABSORBER
Caα
Mn
Feα
Coβ
K
Ba,Ti
Feβ
Cu
Znα
Znβ
Pbα
Br
Pbβ
Rb
Srα
Srβ
(Mo)
COUNTS x 1/1000
COUNTS / 20μC
CHANNEL

VA.2 Sample collection and preparation

The plant and soil studies were conducted over 3 seasons (March, August, and November). Five sites were chosen for the study, including three experimental sites and two control sites. The experimental sites, denoted as sites E1, E2, and E3, were located respectively 1 m, 5m, and 75 m from the intersection of two main thoroughfares near downtown Durham, N. C. The two control sites, C1 and C2, were located in an isolated forest area approximately two miles away.

Three entire ribwort plantain plants and the soil in which they were growing were collected from each site. In addition, samples of Bermuda grass were taken from each of the three experimental sites during the March collection. At least five leaves from each plant were selected for analysis in order of decreasing age. (The ribwort plantain sprouts leaves in a tight ascending helix around the central axis of the plant; by starting at the base of the plant, one can remove the leaves one by one in order of decreasing age.) The selected leaves were individually washed in a cleansing solution designed for plants, then rinsed several times in distilled deionized water, and dried flat.

Pellets and acetic extracts were prepared from each soil sample collected. For the first season of the study, each soil sample was dried, ground with a clean mortar and pestle, and strained twice through 0.99 mm mesh. One pellet was pressed from each soil sample. Acetic acid extracts were

prepared from each sample by shaking 10 g of soil in 10 ml of 0.5 molar acetic acid for 1 hour. These solutions were filtered until clear and approximately 40 µl of the filtrate were deposited on nuclepore membranes for irradiation. In a more detailed, nearly parallel study, the amounts of metals extracted from various soil samples were determined for four extraction solutions at pH values ranging from 1.5 to 9.2. The results of this study are presented in Baum et al., 1976.

For the third season of sample collection, cylindrical soil plugs extending to a depth of approximately 16-20 cm, were obtained at each collection site. The plugs were obtained by twisting an 8-cm diameter aluminum pipe into the ground. In order to investigate the metal concentrations in soil as a function of depth, individual samples were prepared from each 2.5-cm segment of the plug. The soil samples were ground and homogenized as described above, and one pellet was pressed from each sample.

VA.3 PIXE analysis

Most leaf specimens were irradiated in one position using two or all three X-ray filters in order to maximize sensitivity over the full elemental range of interest. The soil pellets were generally analyzed in 2 to 4 positions in order to average out any remaining inhomogeneities. The procedure was to irradiate each half of the front surface and then rotate the target rod through 180° in order to ir-

radiate the backside in two positions.

VA.4 Results

Representative spectra for the plant and soil analyses are shown in Figure 5.2, 5.3, and 5.4. Figure 5.2 shows spectra for single plantain leaves collected at two of the experimental sites. The enhanced levels of Br and Pb at the site closest to the road (site E1) are particularly noteworthy in this figure. Soil pellets and soil extracts were prepared from soil samples collected beneath these same plantain, and the resulting spectra shown in Figures 5.3 and 5.4 also exhibit the enormous Pb and Br levels at roadside. Figure 5.3 indicates that nearly all metal levels with the exception of Cu and Zr are higher at site E1.

The average elemental abundances for leaves, soil extracts, and soil pellets were determined at each of the five sites for the samples collected in March. Table 5.1 summarizes these results for sites E1 and E3, and the two control sites C1 and C2. In general, the average abundances observed for site E2 were intermediate between the E1 and E3 abundances. The results shown in Table 5.1 clearly confirm the expected presence of high metal content in roadside samples. The high levels of Pb and Br in all three sample types at roadside, and the very rapid fall-off in concentration of these elements with increasing distance from the highway, may be attributed to the additive $Pb(CH_3)_4Br$ in automo-

Figure 5.2 PIXE spectra from analyses of ribwort plantain leaves collected at roadside (solid line) and 75 m from roadside (dashed line). Note the enhanced Pb and Br signals in the roadside specimen.

Figure 5.3 PIXE spectra from analyses of soil pellets pressed from samples collected at roadside (solid line) and 75 m from roadside (dashed curve). Note the enhanced abundances in roadside soil.

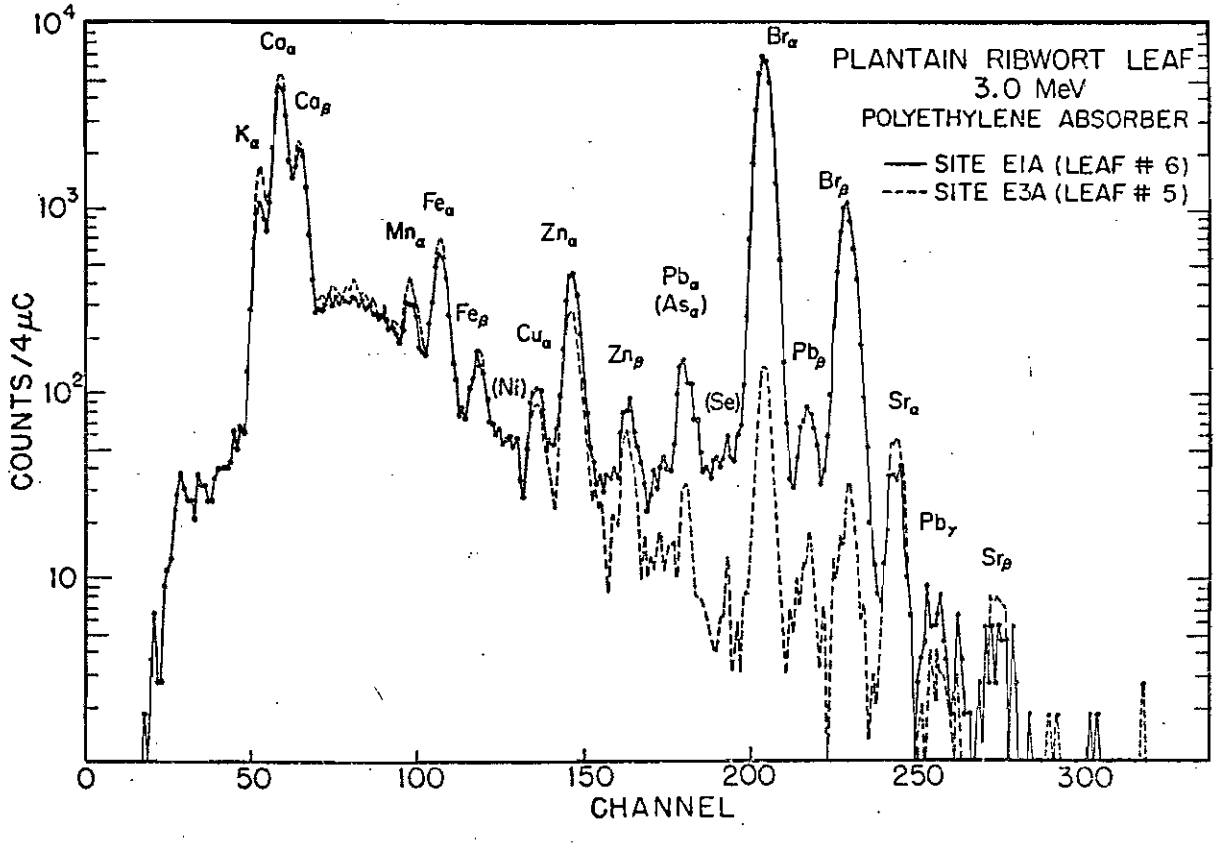
PLANTAIN RIBWORT LEAF
3.0 MeV
POLYETHYLENE ABSORBER
SITE E1A (LEAF # 6)
SITE E3A (LEAF # 5)
COUNTS/4 μC
CHANNEL
Ca_α
Ca_β
K_α
Mn_α
Fe_α
Fe_β
Cu_α
(Ni)
Zn_α
Zn_β
Pb_α (As_α)
(Se)
Br_α
Br_β
Pb_β
Sr_α
Pb_γ
Sr_β

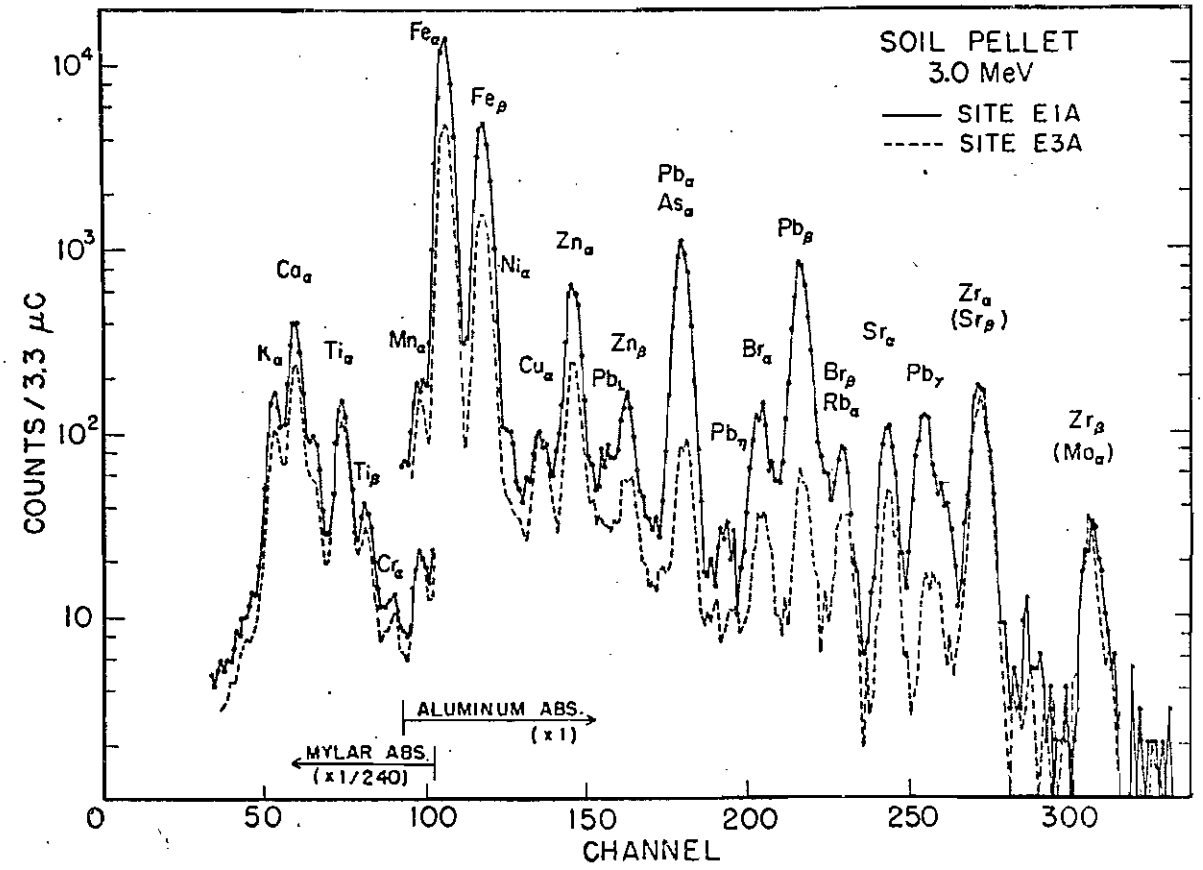
SOIL PELLET
3.0 MeV
SITE E1A
SITE E3A
COUNTS / 3.3 μC
CHANNEL
Fe_α
Fe_β
Ni_α
Zn_α
Pb_α As_α
Pb_β
Ca_α
K_α
Ti_α
Mn_α
Cu_α
Zn_β
Pb_L
Br_α
Pb_η
Br_β Rb_α
Sr_α
Pb_γ
Zr_α (Sr_β)
Ti_β
Cr_α
Zr_β (Mo_α)
ALUMINUM ABS. (x1)
MYLAR ABS. (x1/240)

Figure 5.4 PIXE spectra from analyses of soil extracts prepared from samples collected at roadside (solid line) and 75 m from roadside (dashed curve).

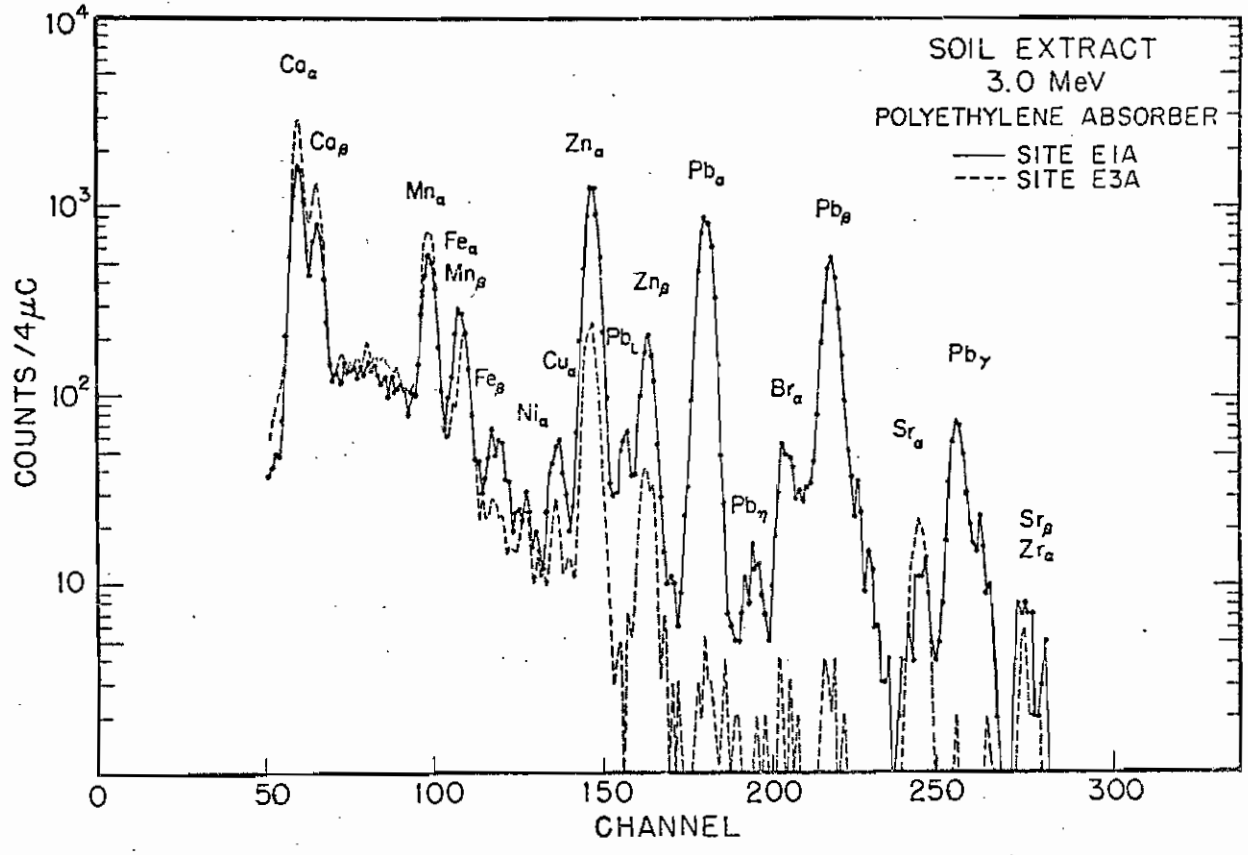
SOIL EXTRACT
3.0 MeV
POLYETHYLENE ABSORBER
SITE E1A
SITE E3A
COUNTS / 4μC
CHANNEL
Ca$_\alpha$
Ca$_\beta$
Mn$_\alpha$
Fe$_\alpha$
Mn$_\beta$
Fe$_\beta$
Ni$_\alpha$
Cu$_\alpha$
Zn$_\alpha$
Pb$_L$
Zn$_\beta$
Pb$_\alpha$
Pb$_\eta$
Br$_\alpha$
Pb$_\beta$
Sr$_\alpha$
Pb$_\gamma$
Sr$_\beta$
Zr$_\alpha$

tive gasoline. Several other elements (Ca, Fe, Cu, Zn) exhibit less dramatic, but systematic decreases as the distance from the highway increases.

The two control sites were located near each other in an area which was isolated from automotive traffic. Even though both sites were located in essentially the same environment, differences of a factor of two can be observed in some abundances listed in Table 5.1 for the two control sites (C1 and C2). The raw data showed similar gross variations in the elemental abundances of leaves gathered from the same plant, and soil samples (extracts and pellets) collected from the same site. For several elements (Cl, K, Ca, Mn, and Fe) differences in the average leaf abundances between sites C1 and C2 appear to correlate qualitatively with the differences observed in the soil extract values.

The data from the first season of collection demonstrated clearly that the metal content of a leaf may depend strongly on the age of the leaf. This dependence is shown in Table 5.2 which lists selected elemental concentration as a function of leaf age for one roadside plantain. Systematic increases in concentration were observed with increasing leaf age for the elements Ca, Mn, Fe, Zn, Br, Sr, and Pb. In this initial study, only the roadside plantain showed such metal accumulation with leaf age; however, only a few leaves were analyzed from the other plants.

During the last season of collection, the dependence of metal content on leaf age was investigated more thoroughly.

Table 5.1

Elemental abundances (ppm dry weight) for an average of at least nine leaves and six soil samples from each of two experimental and two control sites. Soil extract values represent the average of three specimens from each site.

Element	Leaves (ppm)				Soil Extracts (ppm)				Soil Pellets (ppm)			
	E1	E3	C1	C2	E1	E3	C1	C2	E1	E3	C1	C2
Cl	64,000	34,000	14,000	52,000	480	540	290	540	-	-	-	-
K	34,000	37,000	18,000	21,700	150	170	52	62	10,700	6,200	9,000	16,000
Ca	21,500	8,500	4,000	9,400	1,500	1,000	480	640	9,200	5,000	2,400	6,000
Ti	-	-	-	-	-	-	-	-	2,200	2,050	3,200	3,100
Cr	0.6	2.7	-	-	0.4	0.5	-	-	36	52	10	6
Mn	91	49	63	33	27	25	11	4.8	510	480	620	1,100
Fe	330	69	46	37	6.5	1.9	3.7	2.5	27,000	9,300	28,000	47,000
Ni	2.0	1.1	1.1	1.3	0.7	0.2	0.4	0.3	47	15	27	52
Cu	18	13	5.6	8.7	2.3	0.6	0.9	0.7	54	53	22	26
Zn	330	52	18	26	1.4	17	1.2	0.5	420	150	53	95
As	-	1.5	0.5	0.7	2.4	0.1	-	0.6	-	-	4	15
Br	7,900	105	44	6.2	14	0.3	0.2	0.2	160	28	4	7
Rb	32	7.3	3.5	5.7	0.2	0.2	0.1	0.1	42	49	100	175
Pb	440	8.7	3.9	4.0	370	0.9	0.3	0.2	2,900	210	52	46
Sr	110	46	46	79	4.5	6.5	6.2	6.9	180	72	120	250
Zr	-	-	-	-	-	-	-	-	310	560	340	225

Table 5.2

Metal Content of Plants and Soils

Variation of elemental composition in ppm dry weight as a function of age of plant leaves for site El[a].

Element	Leaf no.				
	6	10	13	15	19
Cl	34,000	41,000	67,000	67,000	109,000
K	32,000	41,000	59,000	57,000	59,000
Ca	11,000	13,000	21,000	24,000	36,000
Mn	28	53	80	88	150
Fe	94	120	270	210	320
Cu	22	20	21	17	15
Zn	130	170	460	480	640
Br	5,900	7,200	11,000	9,000	12,000
Sr	45	66	70	120	101
Pb	180	90	430	380	740

[a] The leaf numbers listed indicate the position along the steam with the lowest number corresponding to the youngest leaf.

All leaves large enough to be attached to the target rod were stripped from two roadside plantains, and single plantains from sites E2 and E3. Data for selected elements are presented in Figures 5.5 and 5.6 for sites E1 and E3 respectively. Increasing leaf number corresponds to increasing leaf age. In agreement with the earlier results given in Table 5.2, the roadside plant exhibited a clear "elemental build-up" with increasing leaf age for all elements shown except Cu. The element concentrations at site E3 showed little or no dependence on leaf age, although fewer leaves were available for analysis. Because all leaves were carefully washed, it would appear that the increased metal levels in the leaves are due to absorption through the root system rather than deposition of air particulates on the leaf surface.

A second study undertaken during the final collection phase was to determine the elemental abundances in soil as a function of depth for samples collected at the three experimental sites. The sample collection and preparation was described earlier. The results for sites E1 and E3 are shown in Figures 5.7 and 5.8 respectively. Abundances for several elements including Pb, Sr, Br, Zn, and Ca are seen to decrease systematically with depth as would be expected if the source of these elements was primarily airborne particulate matter. For the remaining elements--K, Mn, Fe, and Cu--no clear trends were observed. With the exception of K and Cu, the elemental concentrations were appreciably higher

Figure 5.5 Elemental abundances in plantain leaves versus leaf age for site 1 (roadside). Increasing leaf number corresponds to increasing leaf age.

Figure 5.6 Elemental abundances in plantain leaves versus leaf age for site 3 (75 m from roadside). Increasing leaf number corresponds to increasing leaf age.

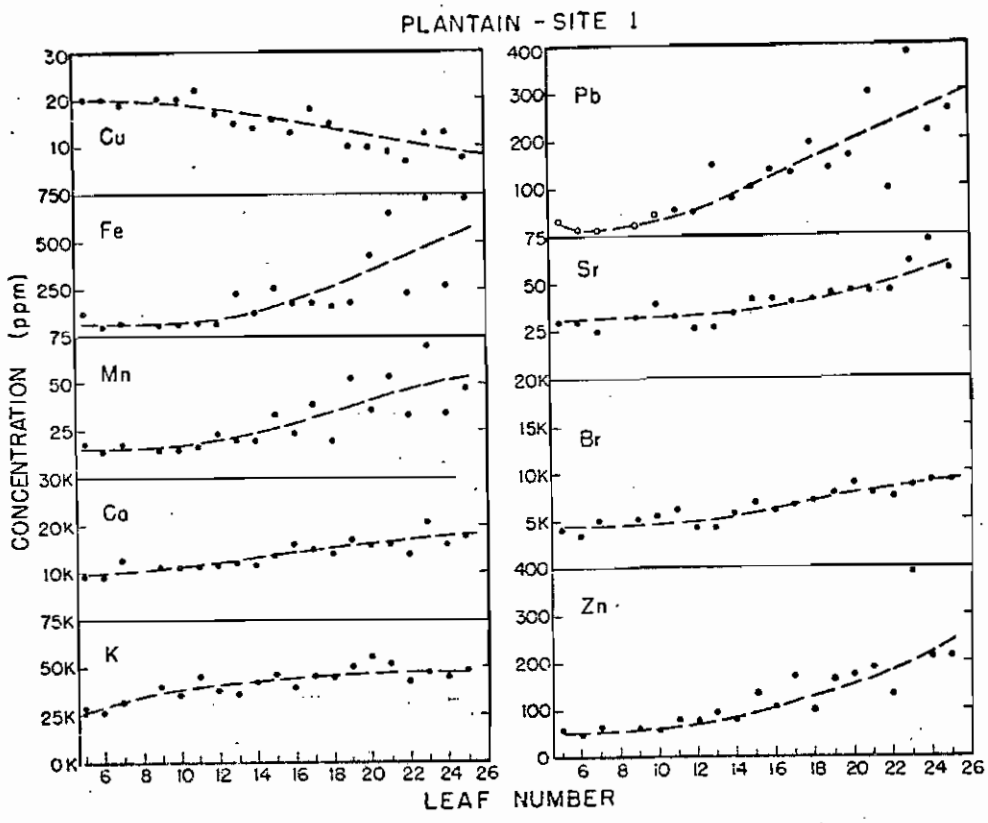
PLANTAIN - SITE 1
Cu
Fe
Mn
Ca
K
Pb
Sr
Br
Zn
CONCENTRATION (ppm)
LEAF NUMBER

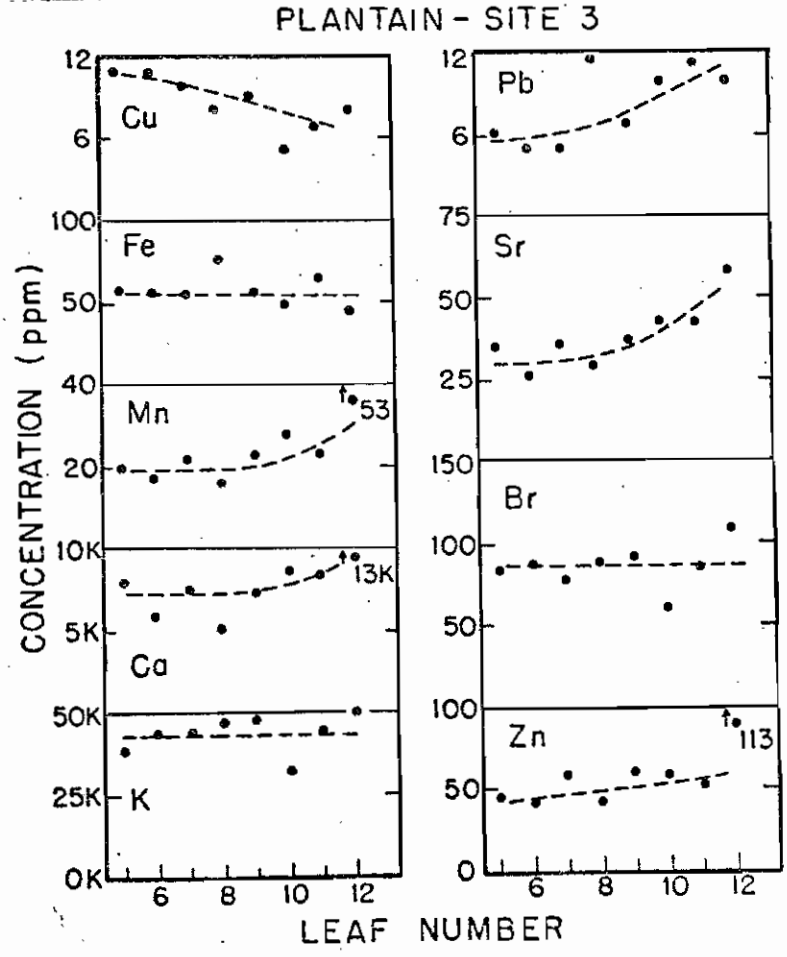
PLANTAIN - SITE 3
Cu
Fe
Mn
Ca
K
Pb
Sr
Br
Zn
53
13K
113
CONCENTRATION (ppm)
LEAF NUMBER

Figure 5.7 Elemental abundances in soil as function of sampling depth for site 1 (roadside). Note the behaviour of Pb, Sr, Br, and Zn.

Figure 5.8 Elemental abundances in soil as a function of sampling depth for site 3 (75 m from roadside).

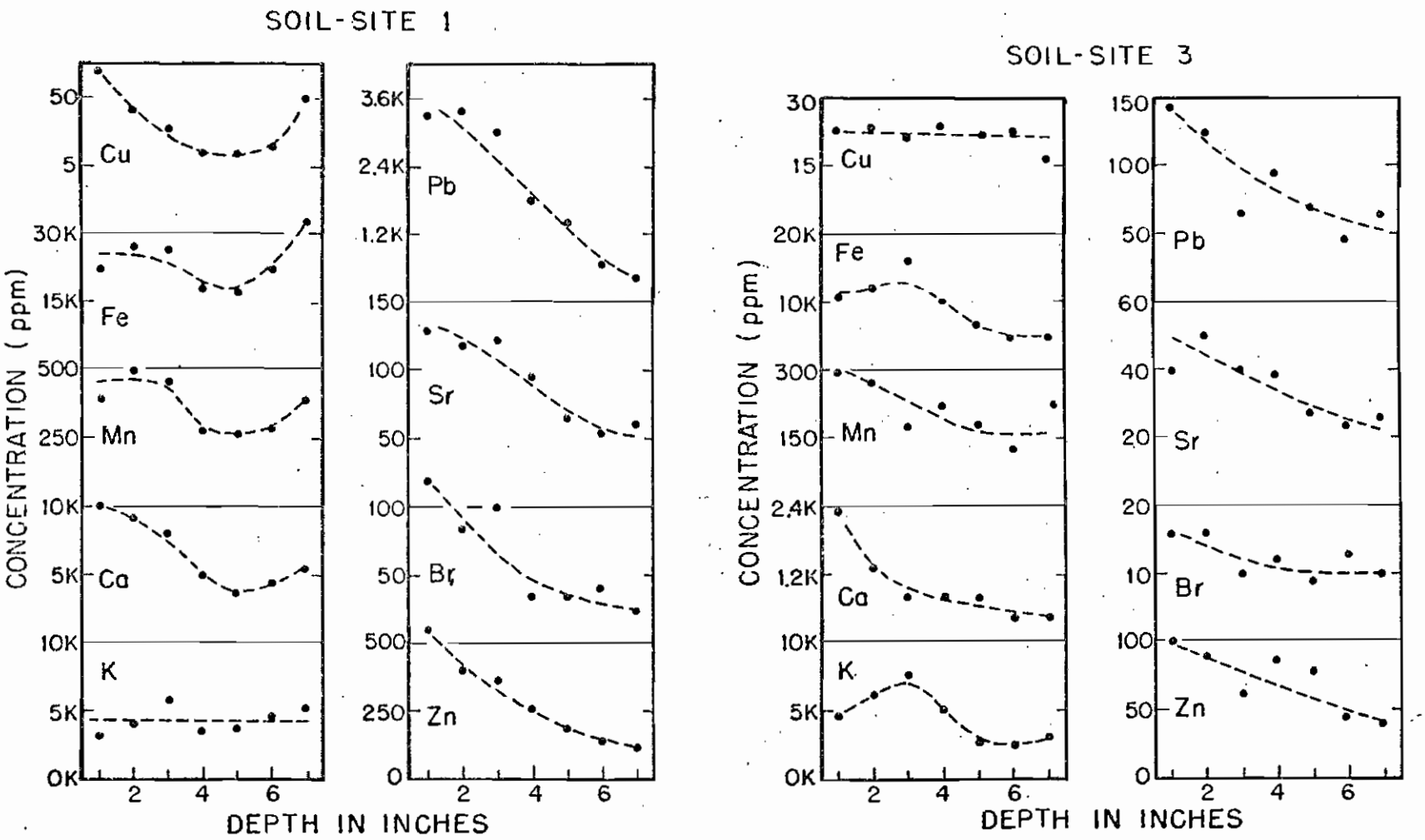
SOIL-SITE 1
SOIL-SITE 3
CONCENTRATION (ppm)
Cu
Fe
Mn
Ca
K
Pb
Sr
Br
Zn
DEPTH IN INCHES
DEPTH IN INCHES

at roadside.

The question of intra-sample variation in leaf specimens was investigated by using the relatively small area of the proton beam to analyze one half of a large oak leaf in 18 positions as shown schematically in Figure 5.9. The remaining half of the leaf was saved for analysis by atomic absorption spectroscopy. The results of the PIXE scan for nine elements are shown in Figure 5.10. Here, the elemental abundances normalized to the mean concentration are plotted as a function of the locations shown in Figure 5.9. For most elements, the intra-sample variation about the mean is 20% or less. The larger fluctuations observed in Fe may be due to difficulties in extracting the Fe abundance in the presence of Mn which was nearly 40 times more abundant.

VA.5 Conclusions

Plant and soil studies such as those reported here are made complicated by the natural variance inherent in environmental systems. Large-scale sampling is required, necessitating analytical techniques that are rapid, quantitative, and relatively inexpensive. PIXE is an excellent technique for such studies because it provides multielemental information with minimal sample preparation and analysis time. The future success of PIXE in this area of research will be determined primarily by the ability of the botanists to design meaningful research projects which can utilize

Figure 5.9 Schematic of oak leaf showing regions analyzed in leaf scan.

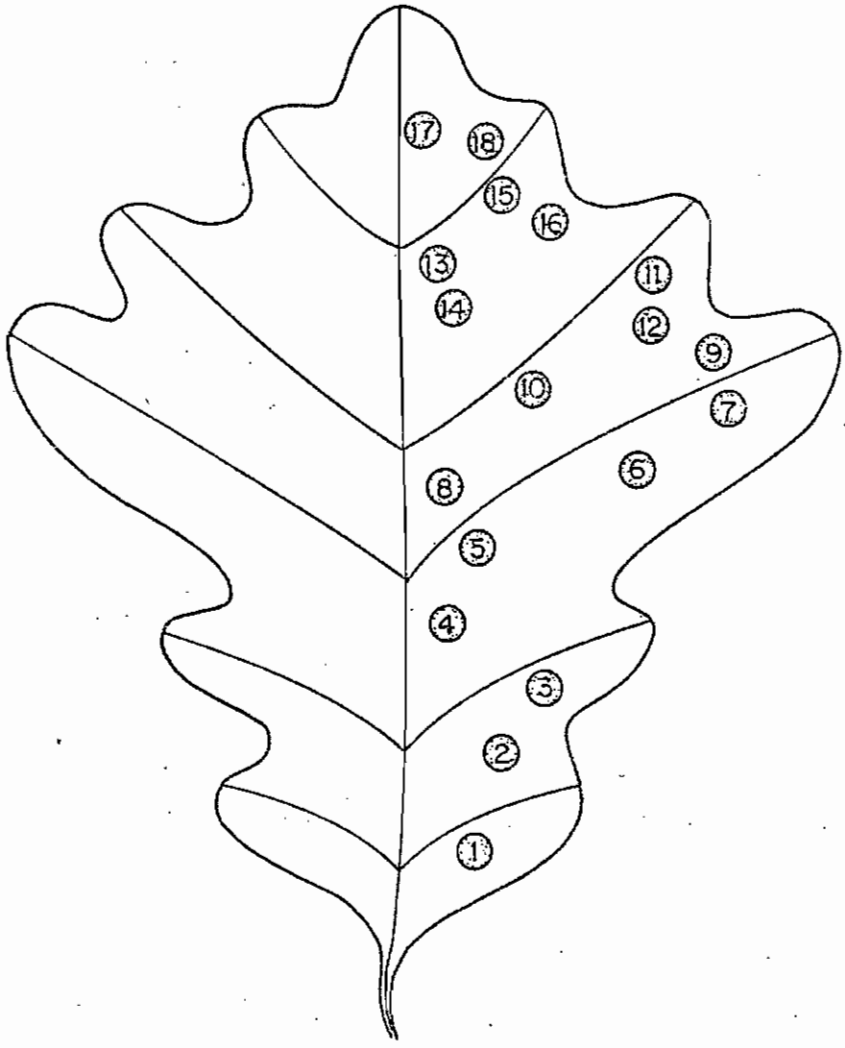

SCHEMATIC OF LEAF UNIFORMITY SCAN

REGIONS CHOSEN FOR IRRADIATION

Figure 5.10 Results of the PIXE scan of the oak leaf shown in Figure 5.9. Elemental abundances for nine dominant elements are normalized to the average abundance and plotted as a function of location analyzed (Figure 5.9).

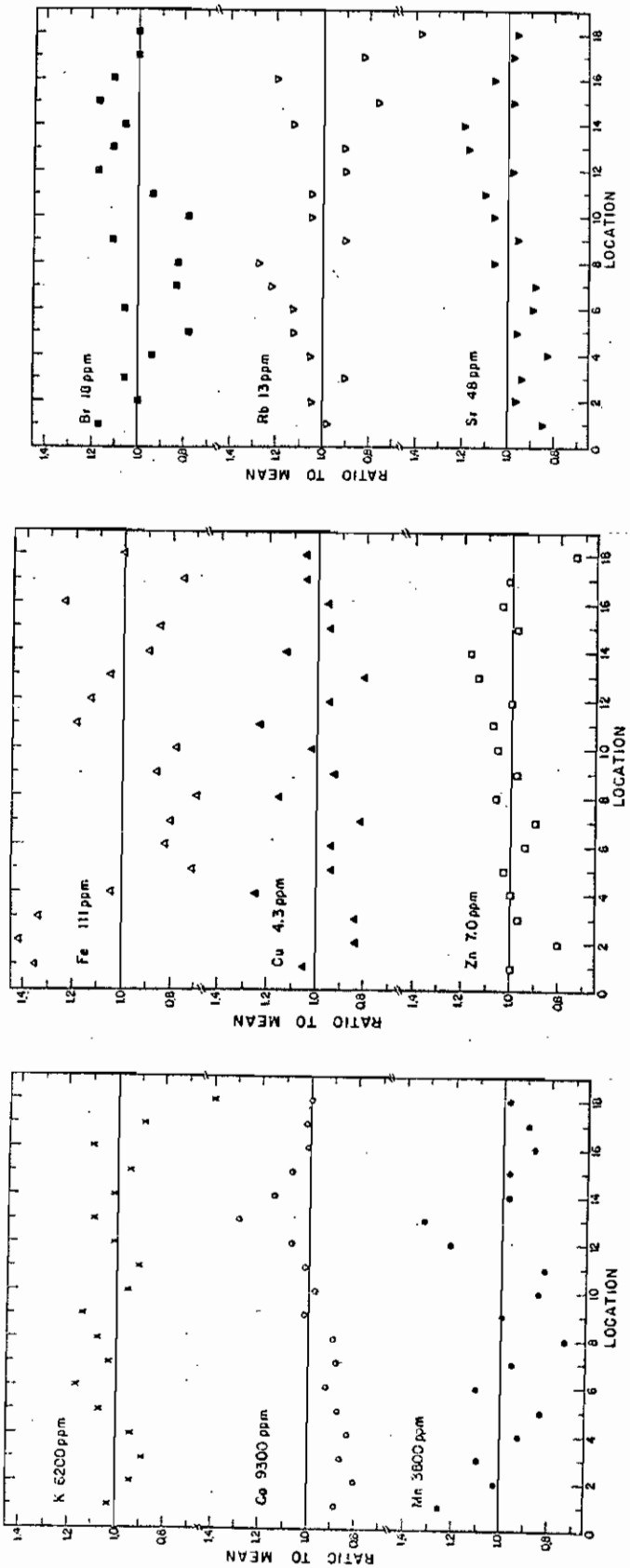
K 6200 ppm
Co 9300 ppm
Mn 3800 ppm
Fe 111 ppm
Cu 4.3 ppm
Zn 7.0 ppm
Br 10 ppm
Rb 13 ppm
Sr 48 ppm
RATIO TO MEAN
LOCATION

such kinds of multielemental information. Clearly the field of plant nutrition could be well served by the PIXE method.

VB. Marine Life Studies

VB.1 Introduction

In cooperation with the National Institute of Environmental Health Sciences, we have analyzed a large variety of marine specimens with a view toward (1) establishing PIXE detection limits and applicability of PIXE to the analysis of such samples, (2) determining the levels of observed trace elements in these samples, and (3) establishing possible correlations between the element levels found in marine life and the abundances of such elements in the marine environment. The primary study involved the analysis of three species of bottom-dwelling marine life collected from relatively clean and contaminated environments. PIXE analyses of these specimens were supplemented by atomic absorption analysis conducted at a commercial laboratory. Initial results of this study are reported in Fowler et al., 1975.

VB. Sample collection and preparation

The species collected for the study were Dover Sole (a fish which feeds off ocean-bottom sediments), and two species of crabs--Cancer Anthonyi and Mursia Gaudichaudii. The waters off Palos Verdes near Los Angeles were chosen as

the contaminated region due to the high concentrations of toxic metals known to exist in the bottom sediments. The control region was selected off Santa Barbara. Collection of the samples is described in Fowler et al. (1975).

Several types of samples were analyzed including the skin and muscle of the Dover Sole, and the digestive glands, gonads, and muscles of the crab specimens. Efforts to digest these samples by wet ashing generally proved unsuccessful; muscle tissue in particular contains large amounts of collagen which is not easily ashed. The digestive glands and the gonads therefore were simply spread over an area approximately equal to the beam area on a mylar film attached to the target rod. Muscle tissue was prepared for PIXE analysis by slicing thick sections approximately 1 cm^2 in area with a clean scalpel and attaching to a strip of aluminized mylar using a small amount of clean adhesive which was avoided during the irradiation.

VB.3 Results

During the initial phase of this study we performed a PIXE scan of one entire Dover Sole fish in order to obtain some measure of intra-sample variability. The analysis was primarily focused on muscle tissue, although some portions containing the skin were also analyzed. Results of the scan showed gross variations in a number of elemental abundances even between adjacent sections of tissue. We concluded that

Table 5.3

Elemental abundances (ppm wet weight) for gonad sections from Crab Mursia taken from contaminated area.

Element	Abundance (ppm)	Lowest Value (ppm)	Highest Value (ppm)	Detection Limit (ppm)
K	2320	750	3220	40
Ca	364	110	810	4
Ti	1.5	0.4	2.5	1.4
V	0.8	0.0	2.1	0.7
Cr	0.2	0.0	0.5	0.5
Mn	1.2	0.4	2.9	0.3
Fe	7.5	1.2	20	0.2
Co	0.2	0.0	0.3	0.2
Ni	0.6	0.1	3.0	0.2
Cu	6.3	3.0	12	0.1
Zn	20	8.8	41	0.1
As	4.3	0.9	6.9	0.1
Se	1.2	0.7	1.8	0.2
Br	23	9.4	34	0.2
Rb	1.6	0.8	2.3	0.2
Sr	8.6	2.2	19	0.2
Hg	0.5	0.1	0.7	0.5
Pb	0.1	0.0	0.9	0.7

Figure 5.11 Concentration ranges and mean values observed in PIXE analyses of gonad sections from Crab Mursia in contaminated region. Data represents analysis of approximately seven specimens. Mean values are indicated by the horizontal cross bars within each vertical bar. PIXE detection limits for the K and L X-rays are indicated by the dotted lines.

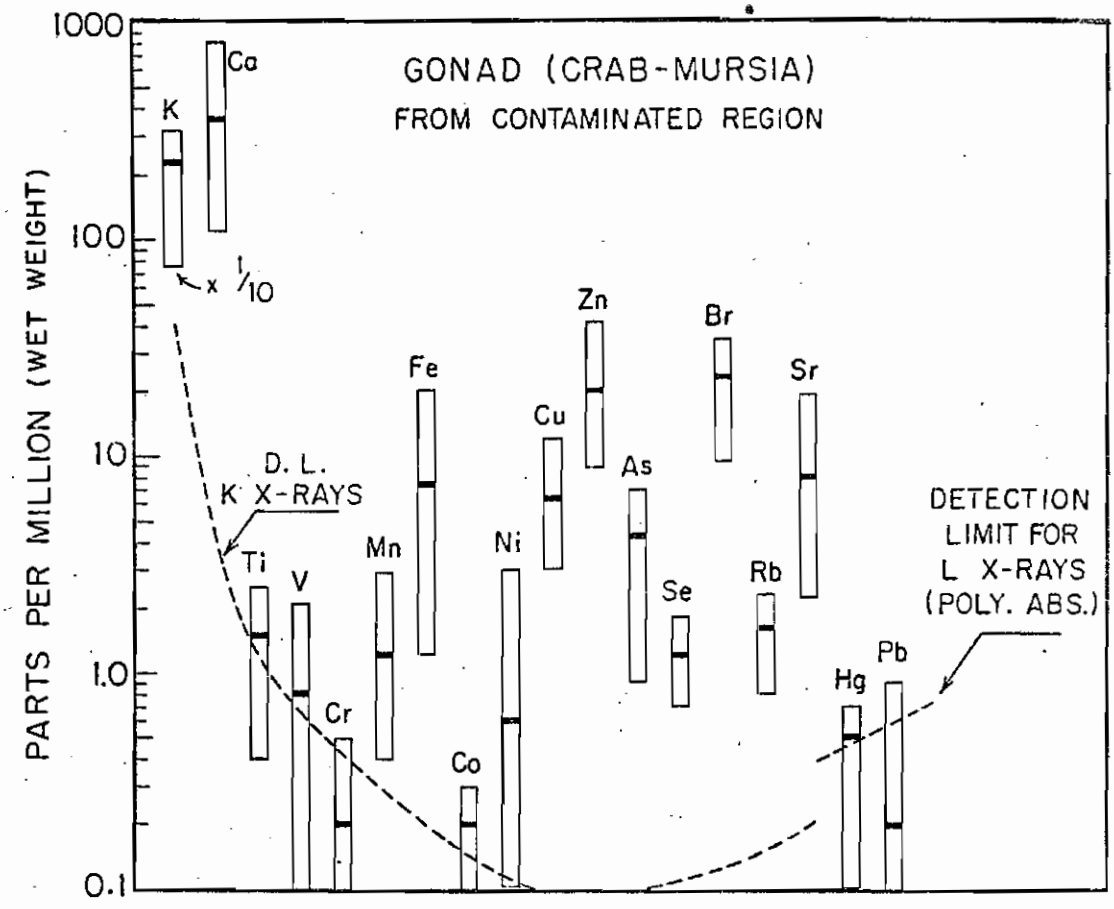
GONAD (CRAB-MURSIA)
FROM CONTAMINATED REGION
PARTS PER MILLION (WET WEIGHT)
1000
100
10
1.0
0.1
K
Ca
x 1/10
D. L.
K X-RAYS
Ti
V
Cr
Mn
Fe
Co
Ni
Cu
Zn
As
Se
Rb
Br
Sr
Hg
Pb
DETECTION
LIMIT FOR
L X-RAYS
(POLY. ABS.)

in view of such inhomogeneities, a single tissue analysis could not be considered representative of the entire specimen. Whenever possible therefore, several irradiations were conducted on samples cut from different sections of the same tissue or organ.

Large variability in elemental abundances was observed between different animals collected from the same environment. These variations frequently ranged over an order of magnitude. As an example, Table 5.3 summarizes the results obtained on gonad sections from approximately seven specimens of Crab Mursia collected from the contaminated region. These results are presented graphically in Figure 5.11 which shows the highest and lowest abundances observed, the mean value (indicated by the horizontal cross bar) and the 3σ detection limits.

Results of the PIXE analyses of crab muscle (Cancer Anthonyi) are summarized in a similar fashion in Figures 5.12 (control region) and 5.13 (contaminated region). Several features are noteworthy in these figures. Perhaps most striking is the overall similarity of the data obtained from the two regions. The toxic metals of primary interest to the researchers involved in this project were As, Se, and Pb. Surprisingly, the PIXE results showed larger concentrations of As and Se in the samples from the control region (50 ppm As, 16 ppm Se) than in samples from the contaminated region (17 ppm As, 5 ppm Se). Statistical analyses conducted on

Figure 5.12 Concentration ranges and mean values observed in PIXE analyses of muscle sections from Crab Anthonyi in control region.

Figure 5.13 Concentration ranges and mean values observed in PIXE analyses of muscle sections from Crab anthonyi in contaminated region.

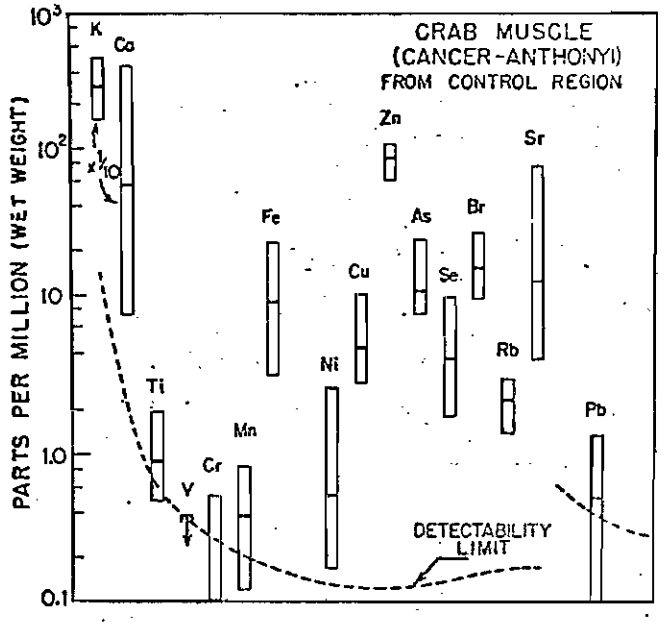
CRAB MUSCLE
(CANCER-ANTHONYI)
FROM CONTROL REGION
PARTS PER MILLION (WET WEIGHT)
10^3
10^2
10
1.0
0.1
K
Ca
x 1/10
Ti
V
Cr
Mn
Fe
Ni
Cu
Zn
As
Se
Br
Rb
Sr
Pb
DETECTABILITY LIMIT

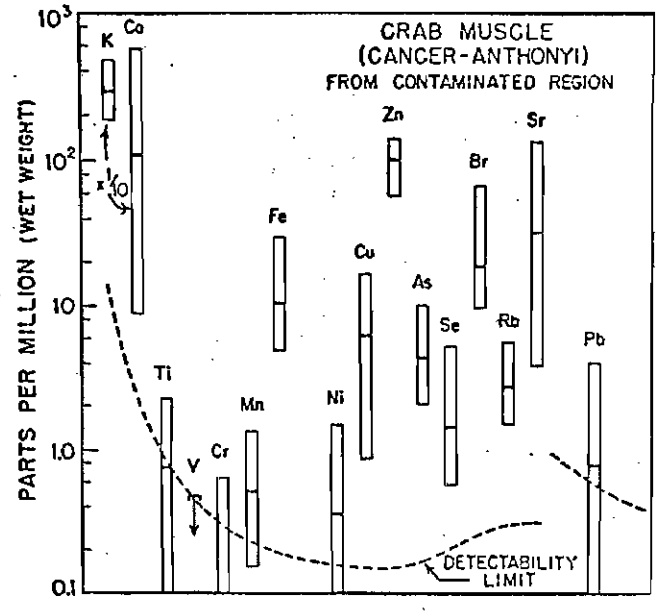
CRAB MUSCLE
(CANCER-ANTHONYI)
FROM CONTAMINATED REGION
PARTS PER MILLION (WET WEIGHT)
10^3
10^2
10
1.0
0.1
K
Ca
x 1/10
Ti
V
Cr
Mn
Fe
Ni
Cu
Zn
As
Se
Br
Rb
Sr
Pb
DETECTABILITY LIMIT

Figure 5.14 Concentration ranges and mean values observed in PIXE analyses of muscle sections from Dover Sole in control region.

Figure 5.15 Concentration ranges and mean values observed in PIXE analyses of muscle sections from Dover Sole in contaminated region.

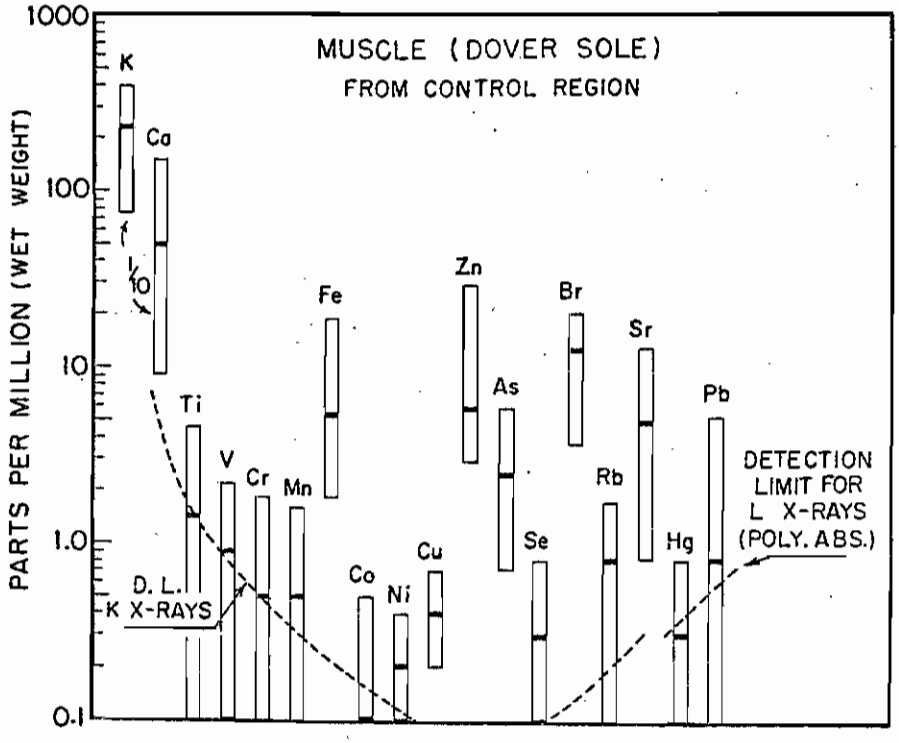
MUSCLE (DOVER SOLE)
FROM CONTROL REGION
PARTS PER MILLION (WET WEIGHT)
1000
100
10
1.0
0.1
K
Ca
x 1/10
Ti
V
Cr
Mn
Fe
Co
Ni
Cu
Zn
As
Se
Br
Rb
Sr
Hg
Pb
D. L.
K X-RAYS
DETECTION
LIMIT FOR
L X-RAYS
(POLY. ABS.)

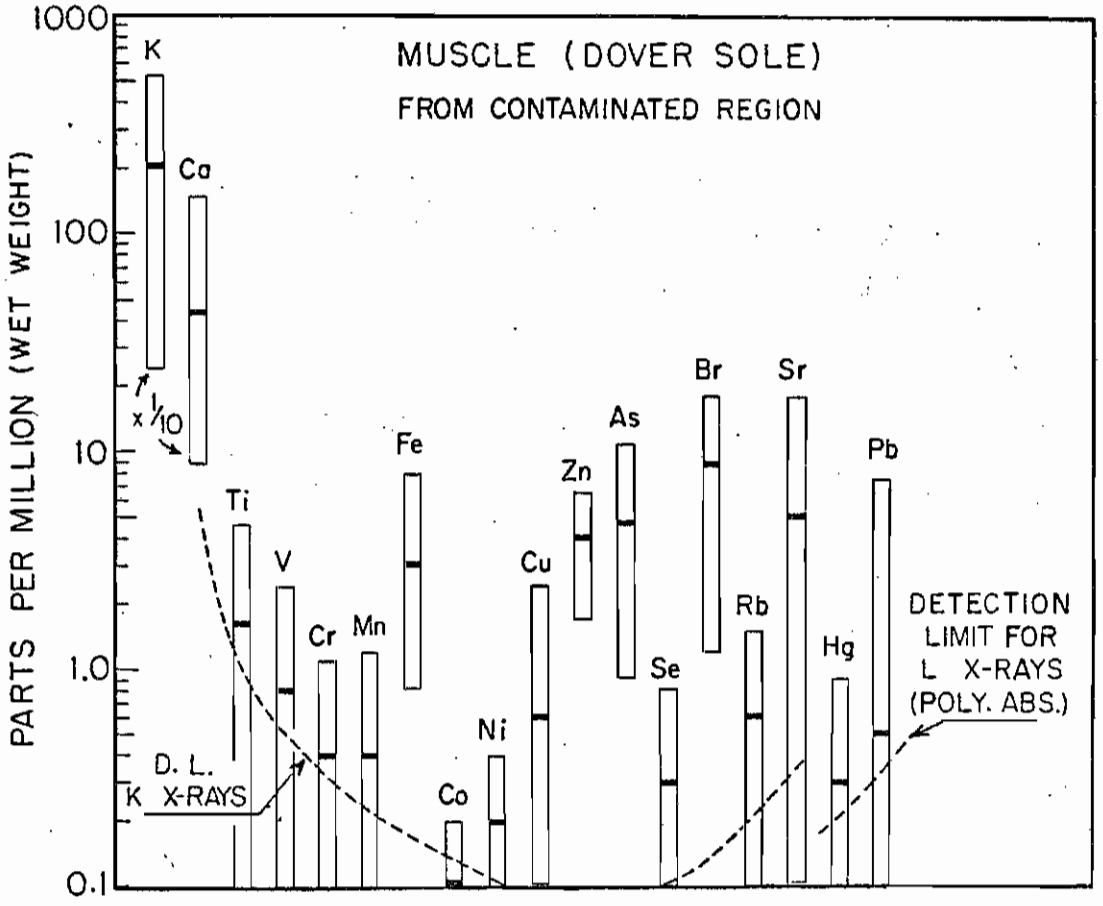
MUSCLE (DOVER SOLE)
FROM CONTAMINATED REGION
PARTS PER MILLION (WET WEIGHT)
1000
100
10
1.0
0.1
K
Ca
x 1/10
Ti
V
Cr
Mn
Fe
Co
Ni
Cu
Zn
As
Se
Br
Rb
Sr
Hg
Pb
D. L.
K X-RAYS
DETECTION
LIMIT FOR
L X-RAYS
(POLY. ABS.)

the As and Se data indicated that these differences were mathematically significant.

Metal levels in the muscle of Dover Sole were generally lower than those observed in crab muscle. Figures 5.14 and 5.15 summarize the data obtained for Dover Sole collected in the control and contaminated regions respectively. Although the PIXE detection limits are quite low (< 1 ppm wet weight for most elements) nearly half of the average abundances shown in Figures 5.14 and 5.15 fall below or within a factor of two of the detection limits. No significant differences were observed between the control and contaminated regions except for As which was approximately 2-fold higher in fish collected from the contaminated region (in contrast to the crab muscle which showed higher levels of As in the control region).

VB.4 Conclusions

To within the order of magnitude variation, this study established the abundance of twelve elements in several marine species. Upper limits were determined for an additional four elements. The presence of As in the range of 2-20 ppm (wet weight) was well established.

It was also determined that there is a large variation in elemental abundances for sections of muscle tissue taken from different regions of the same fish. In addition, we observed large variations for the crab and fish muscles obtained

from the same sampling site. Furthermore, it was not possible because of these variations to correlate the levels of metals observed in these specimens with those existing in the environment, i.e. the bottom sediments of the sampling areas. The surprising similarity in elemental abundances observed in the control and contaminated samples suggests the possibility that some mixing of the control and contaminated populations may have occurred as a result of migration between the two areas.

The results of this study clearly indicate the need for a more controlled experiment and for additional or more extensive baseline studies in order to better understand the inter-sample variations observed. Our work has demonstrated that PIXE is well suited for performing such studies because it is fast and economical for multielemental analysis.

CHAPTER VI

SUMMARY AND CONCLUSIONS

VIA. Advantages and Disadvantages of PIXE

In the seven years since the initial studies of Johansson et al. (1970), PIXE reseachers have made remarkable progress in optimizing the technique, in discovering new areas of application, and in demonstrating to the analytical community that PIXE is a powerful and quantitative tool. Our own studies at Duke have demonstrated the usefulness of PIXE for multielemental analyses of a wide variety of sample types--particularly samples of biological and environmental interest. It is worthwhile at this point to briefly summarize the salient advantages and disadvantages of the PIXE system presently in operation at Duke.

Advantages

1. PIXE is a multielement technique. Typically 10-20 elements in a sample are simultaneously determined.

2. Reasonable sensitivities are obtained over a broad range of elements. In the elemental regions of primary interest ($20 < Z < 40$ and $75 < Z < 90$) interference-free

detection limits typically range between 0.5 and 50 ppm. In terms of absolute abundances, detection limits are commonly at the ng level or lower.

3. PIXE analysis is fast. Total analysis time typically averages less than 10 min per sample, including 5 min of irradiation time and 1-2 min of computer analysis.

4. PIXE is economical for multielemental analysis, although cost estimates are difficult to make as they depend on many considerations. At the present time we would expect that the cost per sample required to support Duke's PIXE system on a continuing basis would be $8 to $10 per sample. Other laboratories report similar figures (Johansson et al., 1976; Cahill, 1975).

5. Sample preparation is minimal in many cases.

6. PIXE analysis is generally non-destructive.

7. PIXE requires a very small amount of sample.

8. Analysis of small sample areas (< 1 mm^2) is possible by using a focused beam.

Disadvantages

1. PIXE requires a well-equipped accelerator facility.

2. Interelement interferences in complex samples can seriously limit PIXE sensitivity and jeopardize the accuracy

and precision of results.

3. Quantitative analysis of thick targets ($\gtrsim$ 1 mg/cm^2) is complicated by matrix effects which are difficult to estimate in some cases. Thin targets yield more quantitative results but in general require more elaborate preparation procedures.

4. In a single irradiation, PIXE can analyze only a small quantity of an unconcentrated sample (< 10 mg). Therefore, to ensure representative sampling one must analyze many targets of the same sample unless the sample is guaranteed to be homogeneous, or employ costly and time-consuming preconcentration techniques such as ashing.

5. Liquid samples must currently be dried prior to irradiation in vacuum.

6. Volatile compounds may be lost in vacuum or during irradiation.

Future modifications to the Duke PIXE system (described in Section VIC) may eliminate the disadvantages (5) and (6) above. In addition, with regards to disadvantage (1), decreased federal funding in recent years for the traditional areas of low energy nuclear research has resulted in greater availability of low-energy Van de Graaff accelerators for PIXE-type studies. Our experiences at Duke indicate that the advantages of PIXE clearly outweigh the disadvantages.

VIB. Comparison to Other X-ray Techniques

The last several years have seen the development of a healthy competition between particle-induced X-ray analysis and X-ray fluorescence analysis (including energy dispersive (EDXRF) and wavelength dispersive (λDXRF) techniques). These techniques share several features in common, e.g.--related physical basis, and similar analytical capabilities and cost per analysis. Because these X-ray methods perform similar analytical tasks it is of interest to evaluate the relative merits and unique capabilities of each method. Such comparisons must be regarded with some caution however since the results can depend strongly on the types of samples analyzed and on how the experimental conditions for each method are optimized.

X-ray fluorescence differs from PIXE in that the exciting source consists of photons rather than charged particles. The incident photon flux can be provided either by radioisotopic sources (Bonner et al., 1973 and 1975) or by an X-ray tube equipped with a transmission anode or secondary fluorescers (Goulding and Jaklevic, 1973; Giauque et al., 1973; Landis et al., 1972). A limiting factor for radioisotopic source excitation is the relatively low photon flux generally provided by such sources. On the other hand, if high intensity radioisotopic sources are used, this type of analysis may be competitive with other X-ray techniques particularly in view of the low cost, high stability, portability,

and simplicity of such a system. (See Cooper, 1972).

The advent of multicrystal wavelength spectrometers with improved efficiency (Wagman et al., 1977; Birks and Gilfrich, 1976) puts wavelength dispersive analysis on a competitive basis with PIXE and EDXRF for analysis of environmental samples. The primary advantage of such a system is the elimination of interelement interferences (owing to the high resolution capabilities) and the resulting simplification in spectrum analysis. The main disadvantages of λDXRF are the relatively low detection efficiencies which must be compensated for by a high power XRF system, and the need for maintaining accurate alignment to ensure a constant detection efficiency. Detection limits for a state-of-the-art multicrystal spectrometer are discussed below.

In order to gain an appreciation of the differences in PIXE and EDXRF, it is useful to compare spectra obtained with both techniques. Figures 6.1-6.4 show spectra of several biological specimens analyzed on an XRF system which was equipped with a Mo secondary fluorescer. (A Ti fluorescer used for low-Z analysis ($Z \leq 20$) and a Sm fluorescer employed for elements in the range $37 \leq Z \leq 55$ were also available but were not used here.) Comparing these spectra with PIXE spectra of the same samples, one observes that the primary difference between EDXRF and PIXE spectra are the respective background shapes. PIXE backgrounds for organic matrices are dominated by secondary electron bremsstrahlung which

Figure 6.1 XRF spectrum from analysis of 23 mg of leaf. A Mo fluorescer was used to obtain the spectrum. Note the coherent and incoherent scatter peaks from the Mo fluorescer in the high energy region of the spectrum.

Figure 6.2 XRF spectrum from analysis of 105 mg of Dover Sole muscle.

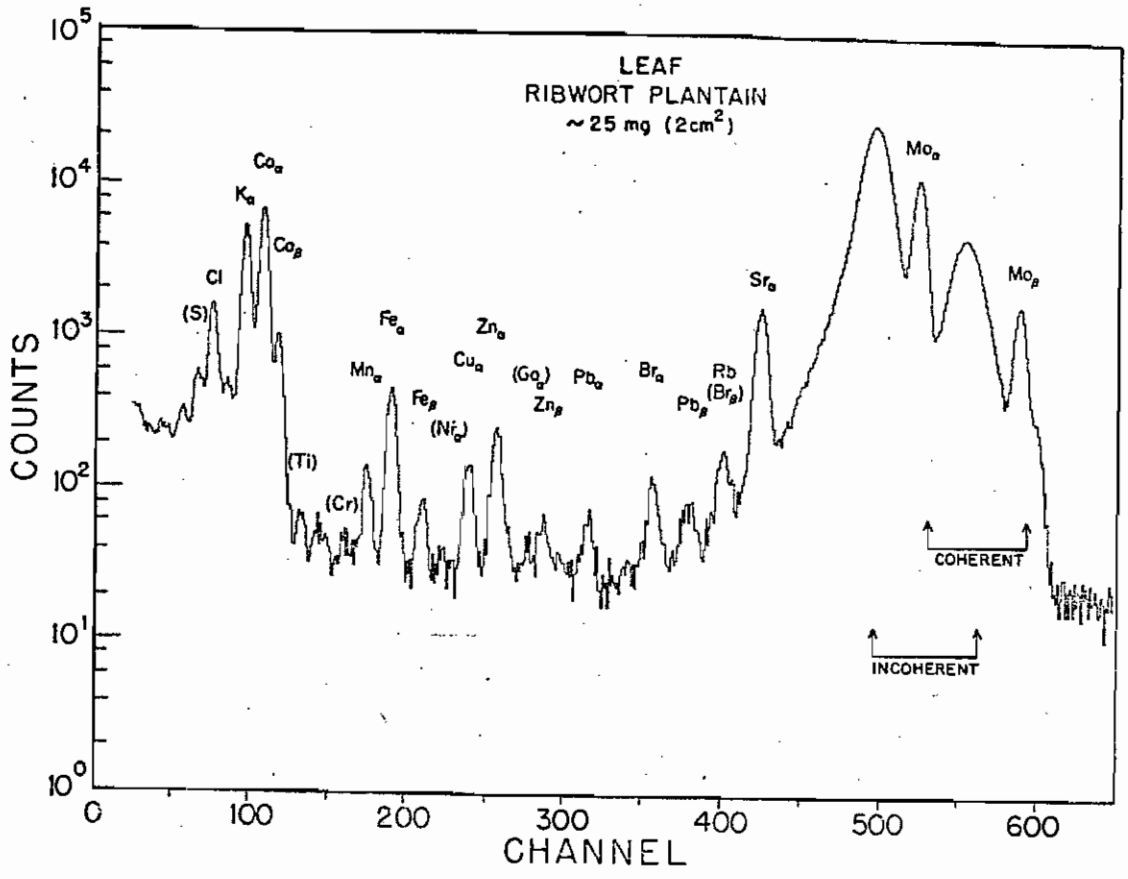
LEAF
RIBWORT PLANTAIN
~25 mg (2cm²)
COUNTS
CHANNEL
(S)
Cl
K_α
Ca_α
Ca_β
(Ti)
(Cr)
Mn_α
Fe_α
Fe_β
(Ni_α)
Cu_α
Zn_α
(Ga_α)
Zn_β
Pb_α
Br_α
Pb_β
Rb
(Br_β)
Sr_α
Mo_α
Mo_β
COHERENT
INCOHERENT

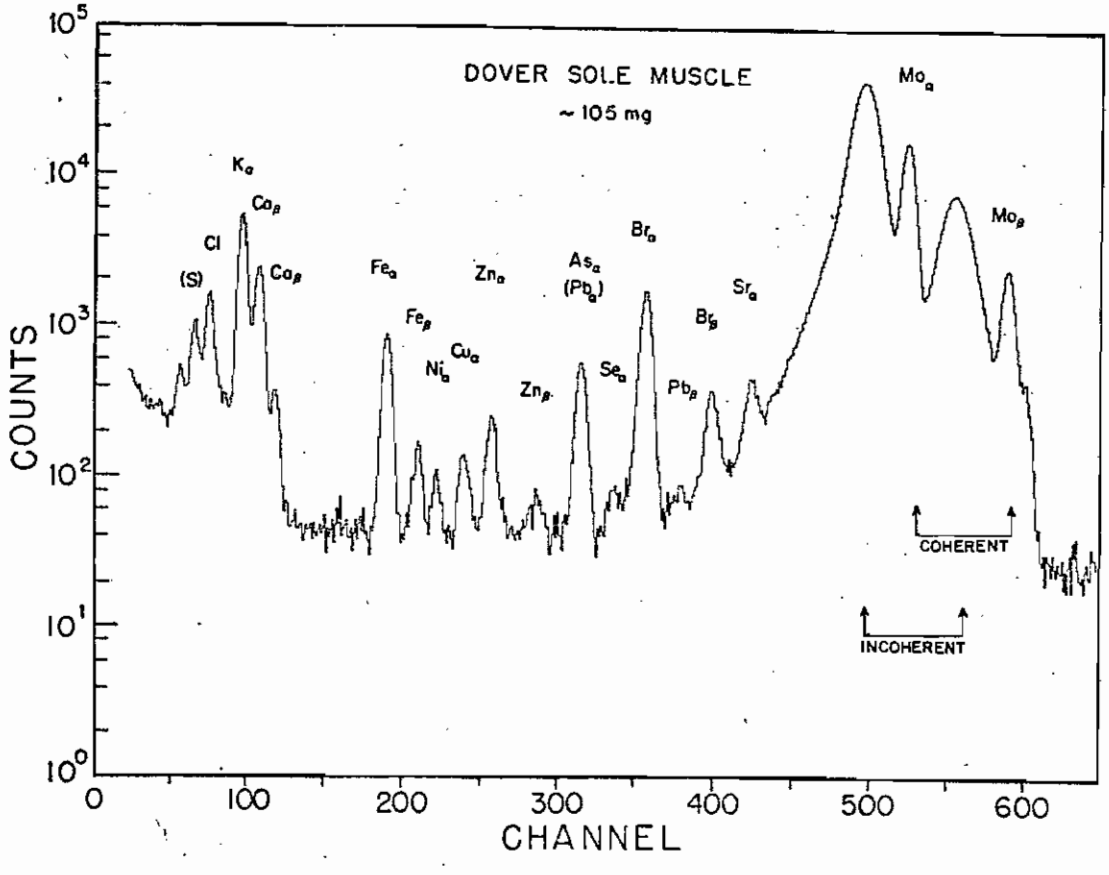
DOVER SOLE MUSCLE
~105 mg
COUNTS
CHANNEL
(S)
Cl
K_α
Ca_β
Ca_β
Fe_α
Fe_β
Ni_α
Cu_α
Zn_α
Zn_β
As_α
(Pb_α)
Se_α
Br_α
Pb_β
Br_β
Sr_α
Mo_α
Mo_β
COHERENT
INCOHERENT

Figure 6.3 XRF spectrum from analysis of 100 mg of pelletized placenta (plain).

Figure 6.4 XRF spectrum from analysis of 100 mg of pelletized placenta (doped in the amounts shown).

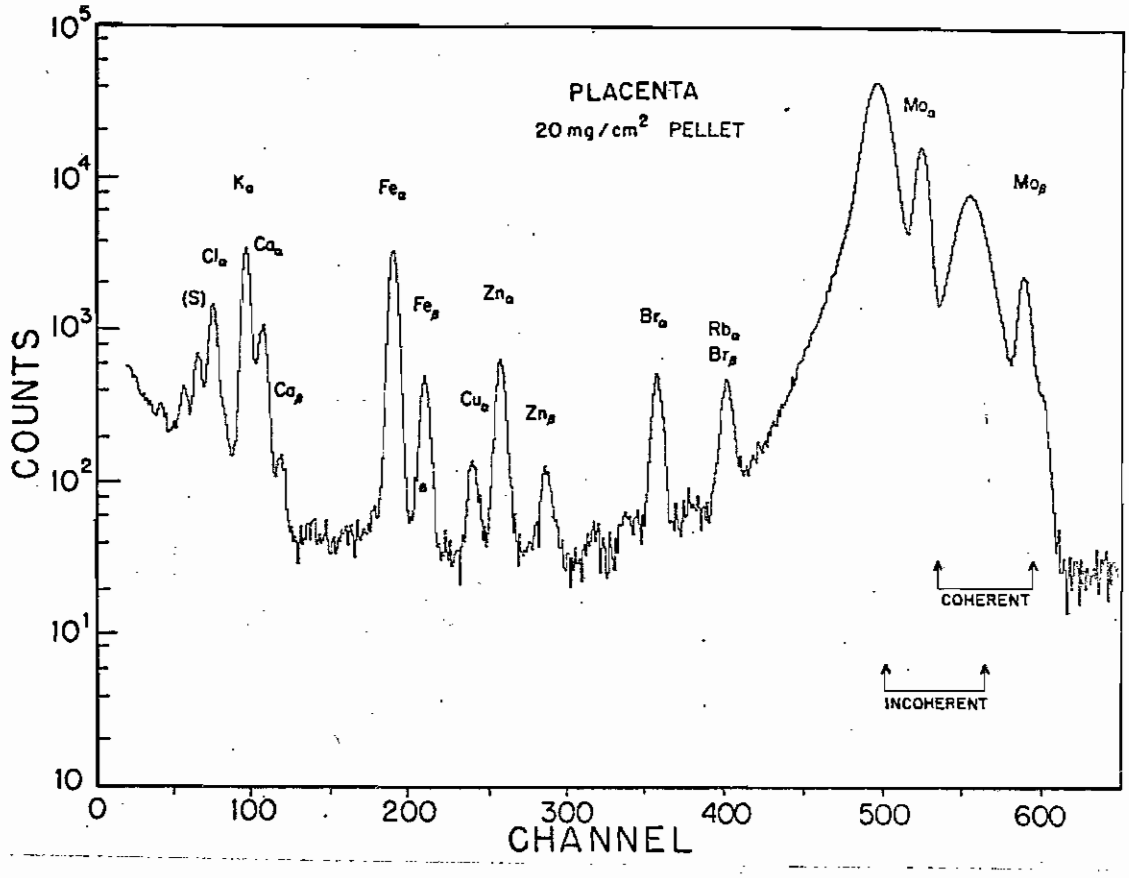
PLACENTA
20 mg/cm² PELLET
COUNTS
CHANNEL
(S)
Cl$_\alpha$
K$_\alpha$
Ca$_\alpha$
Ca$_\beta$
Fe$_\alpha$
Fe$_\beta$
Zn$_\alpha$
Cu$_\alpha$
Zn$_\beta$
Br$_\alpha$
Rb$_\alpha$
Br$_\beta$
Mo$_\alpha$
Mo$_\beta$
COHERENT
INCOHERENT

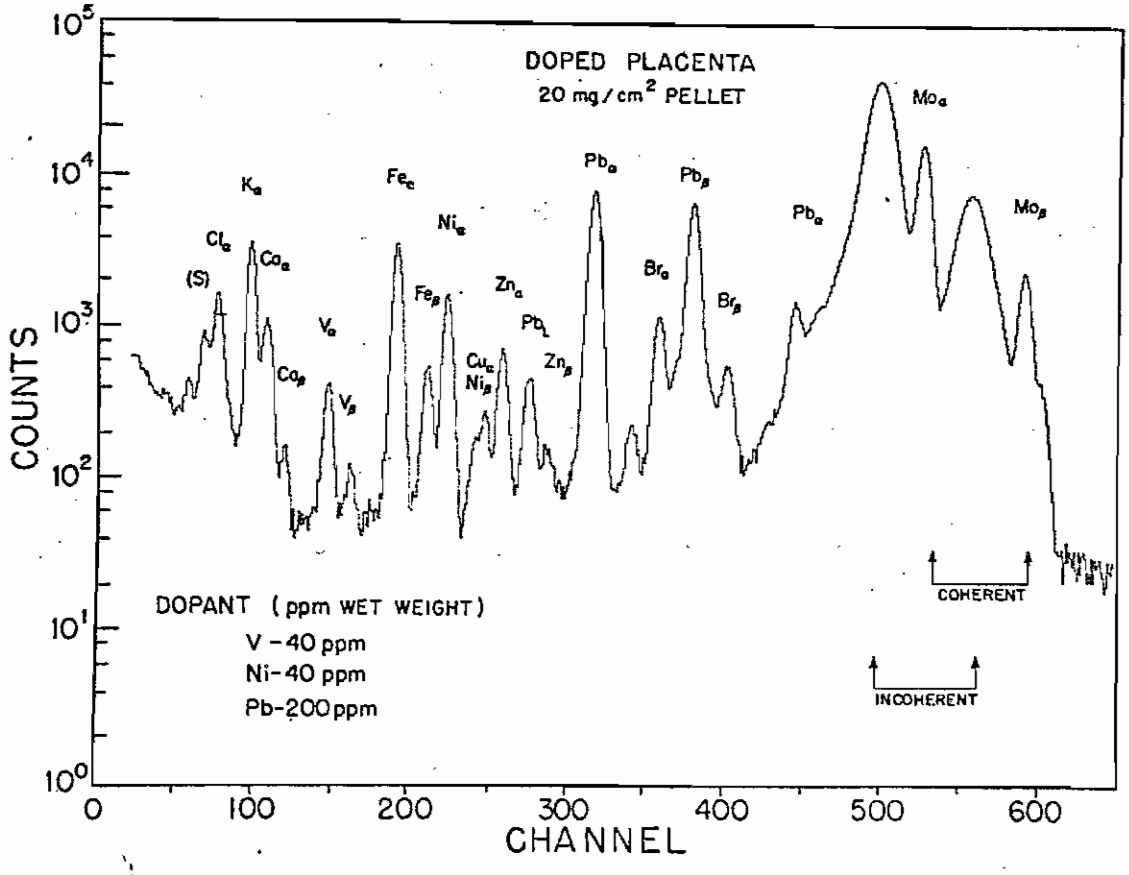
DOPED PLACENTA
20 mg/cm² PELLET
COUNTS
CHANNEL
(S)
Cl$_\alpha$
K$_\alpha$
Ca$_\alpha$
Ca$_\beta$
V$_\alpha$
V$_\beta$
Fe$_\alpha$
Fe$_\beta$
Ni$_\alpha$
Cu$_\alpha$
Ni$_\beta$
Zn$_\alpha$
Pb$_L$
Zn$_\beta$
Pb$_\alpha$
Pb$_\beta$
Br$_\alpha$
Br$_\beta$
Pb$_\alpha$
Mo$_\alpha$
Mo$_\beta$
DOPANT (ppm WET WEIGHT)
V - 40 ppm
Ni - 40 ppm
Pb - 200 ppm
COHERENT
INCOHERENT

peaks in the low energy region. Primary bremsstrahlung produced by the beam itself and Compton scattering of nuclear gamma rays combine to produce a flat or slightly rising background through the X-ray region $E_x \gtrsim 10$ keV. The background shape in XRF spectra on the other hand is dominated by the large peaks caused by Compton (incoherent) and Rayleigh (coherent) scattering of incident photons from the sample into the detector. A plateau (the Compton edge) in the extreme low energy region is caused by the Compton scatter of photons out of the detector. Usually this background feature occurs too low in energy to affect elements of interest. The broadened width of the Compton scatter peaks reflect both the detector resolution and the distribution of scattering angles, and the low-energy tail on the Compton scatter peaks is the result of multiple Compton scatterings in the sample. The region of analytical interest occurs between the low-energy Compton edge and the high-energy scatter peaks. In this region the background is relatively flat and is attributed primarily to escape mechanisms in the detector which are not yet understood (Goulding and Jaklevic, 1977).

A second fundamental difference between PIXE and XRF is the behaviour of the X-ray production cross sections versus atomic number (Figure 2.6 and accompanying discussion). These cross sections are approximately the same order of magnitude for both PIXE and XRF but the former decrease rapidly for higher X-ray energies while the latter increase

rapidly as the X-ray energy approaches but does not exceed the excitation energy. This suggests a potential advantage for XRF in the analysis of heavy elements, and particularly those elements whose absorption edge is immediately below the excitation energy. Optimum sensitivities for XRF analysis can be obtained for selected elemental regions by using a secondary fluorescer of the appropriate material. In an analagous way, PIXE sensitivity can be enhanced in selected elemental regions by use of appropriate X-ray filters and by a suitable choice of bombarding energy (Figure 2.17). (Changes in energy in about 0.5 MeV increments can be made on Van de Graaff accelerators in less than 1 minute.)

Several useful comparisons between XRF and PIXE have been conducted during the past five years, and some results and conclusions of these studies are presented here. One of the better, earlier studies was that of Cooper (1972) who compiled data for various modes of particle and photon-excited energy dispersive analysis. Cooper concluded that although low-energy proton excitation and photon excitation (using Mo X-rays or 100 mCi radioisotopic sources) provided approximately the same sensitivity, practical considerations (e.g. portability, availability, small size) favored photon-excited systems. Furthermore, Cooper concluded that future improvements were likely to benefit XRF more than PIXE. This last conclusion does not appear to have been born out by the progress achieved by both methods in the intervening years.

It is our feeling that Cooper did not give proper recognition to the potential for improvement in PIXE. (For example, significant improvement in PIXE sensitivity can be obtained by using tighter detection geometry as exemplified in current XRF systems, and/or larger beam areas.) Nor did Cooper recognize certain unique capabilities of PIXE--surface analysis, depth-profiling, microscans.

More recently, Goulding and Jaklevic (1977) have presented a hypothetical comparison of EDXRF and PIXE for a specific type of sample. The samples were organic-based and 5 mg/cm^2 thick, and are typical of filter media used in collecting air particulates. PIXE detection limits were estimated for an optimized system having a detector solid angle of $0.003 \times 4\pi$ and 100 nA of beam spread over 1 cm^2. In order to achieve optimum sensitivity over the full elemental range of interest, 200 s analyses at 2 MeV and 4 MeV were assumed. Background levels were estimated from calculations by Folkmann. The optimized XRF system consisted of a pulsed X-ray tube employed 3 secondary fluorescers (Ti, Mo, Sm) and a state-of-the-art Si(Li) detector with guard-ring rejection. Analyses of 100 s each were made with the Ti and Mo fluorescers, and a 200 s analysis was made using the Sm fluorescer so that the total analysis times were the same for both PIXE and XRF.

Results of this comparison indicated that both PIXE and XRF are capable of large-scale analyses at or near the

1 ppm level. The PIXE sensitivities were somewhat better than XRF sensitivities, but this result must be viewed with some caution since no consideration was given to background contributions in the medium and high energy X-ray region due to Compton scattering of nuclear gamma rays, nor to the difficulty in extracting accurate peak areas for low-Z elements whose X-ray signals are superimposed on the intense bremsstrahlung background.

A second recent comparison is made by Scheer et al. (1977) who evaluated the sensitivities of PIXE and XRF for several sample types including: thin organic matrices, moderately thick filter media, and low-Z matrices containing bulk concentrations of higher-Z elements. Because of fundamental differences in X-ray production and background producing processes for PIXE and XRF, PIXE sensitivity shows a relatively strong dependence on sample type, while XRF sensitivity is nearly independent of the sample composition.

The comparison was conducted using pulsed proton beams of 2 and 4 MeV, and an XRF system employing 3 secondary fluorescers. The results indicated approximately the same sensitivities for PIXE and XRF analysis of the thin organic matrix and the moderately-thick filter media although additional considerations in the case of moderately-thick samples may favor the use of XRF. These considerations include beam heating effects and target-thickness correction factors. For the sample containing major concentrations of elements with

Z > 16, Scheer concluded that an optimized XRF system would provide superior sensitivity as a consequence of the more severe pile-up problems with PIXE as well as an increased secondary electron bremsstrahlung background.

In 1973, Gilfrich et al. compared detection limits for air particulate analysis via a number of different excitation modes including wavelength dispersive X-ray analysis. The results indicated that the interference-free detection limits obtained with 5-MeV proton excitation were superior to both energy dispersive and wavelength dispersive XRF. The PIXE results however were obtained on samples which were much thinner than those measured by the XRF systems. Perhaps the most significant conclusion reached by these investigators was that wavelength dispersive analysis using a multicrystal spectrometer was the most practical approach to large-scale analysis of air particulate samples. This conclusion was based largely on the ability of such a system to detect very small concentrations of an element in the presence of much larger concentrations of neighboring elements. Because of interelement interferences, the true detection limits attained with energy dispersive spectrometers can be significantly worse than the reported interference-free detection limits.

Wagman et al. (1977) described the state-of-the-art multicrystal spectrometer used in their analyses of air fil-

ters. The instrument employs 16 fixed monochromators as well as a scanning channel for the determination of any number of additional elements. The system typically analyzes 20 to 30 elements per sample at an estimated cost ranging from $2 to $4 per sample. Minimum detection limits for 100 s analysis time were determined for 30 elements and all but 4 were in the range of 2 to 10 ng/cm^2. Such a system compares very favorably to current PIXE systems.

Our own comparison between PIXE and a secondary fluorescer EDXRF system on five types of samples is summarized by the XRF spectra shown earlier in Figures 6.1-6.4 and the PIXE spectra for like samples which are exhibited in various sections throughout this volume. Basically, these spectra indicate the comparative signal to background ratios and the counting rates for the two methods. The sensitivity levels for these typical types of samples can be seen to be reasonably similar.

Our system was also compared to two EPA XRF systems in an article by Jaklevic and Walter (1977). Here the question was the suitability for measuring particulate aerosol samples collected on nuclepore or mylar membranes. In order of increasing sensitivity the three methods went EDXRF, PIXE and λDXRF. However, the article concluded that all three systems were sufficiently sensitive for aerosol measurements, and because each had distinct advantages, a preference of system type would depend on other factors such as availability,

reliability, competence of personnel, etc.

In conclusion, most studies conducted to date appear to support the view that PIXE and XRF (both wavelength and energy dispersive) provide approximately the same potential sensitivity for biological and environmental analysis. The choice of a particular technique will therefore be based on considerations other than sensitivity. Practical considerations such as availability of an excitation source, simplicity of the system, and portability favor XRF systems. On the other hand if a Van de Graaff accelerator is available, PIXE is a competitive analytical tool which automatically possesses some additional capabilities, e.g., the ability to analyze small sample quantities, the ability to conduct surface analyses and depth profiles, and the scanning capabilities of a focused beam. In terms of overall costs, it appears that PIXE can compete effectively with XRF analysis if a Van de Graaff generator is available.

VIC. Future Improvements

Future developmental work on the Duke PIXE system will be directed toward maximizing the efficiency of the system for routine analyses of large numbers of samples, and extending the applicability of the technique to new types of analysis.

a) Vacuum system: The present design of the vacuum system (Figure 3.1) can be significantly improved by moving both the

vacuum gate value (presently about 1.5 m from the scattering chamber) and the diffusion pump closer to scattering chamber thus minimizing the volume which must be pumped out each time a new target rod is inserted. One should also install a vacuum lock for preevacuating the samples so that they can be inserted into the main chamber without exposing them to air.

b) Triggered beam pulsing: The use of a pulsed beam triggered by a signal from the amplifier provides significant advantages over continuous beam excitation when the counting rate is high. Such a method gives better sensitivity, reduced target damage, and improved performance at high count rates (Thibeau et al., 1973; Koenig et al., 1977). In Cahill's system (Cahill, 1975 and Thibeau et al., 1973), the ion beam passes between two parallel plates, one of which is grounded and the other of which is normally kept at a high voltage. The deflection introduced by these deflecting plates is cancelled by a bending magnet which permits the beam to pass through a pair of slits before striking the target. When an X-ray is detected, a logic pulse from the pulse-processing electronic system triggers the beam deflection circuit nearly grounding the second deflecting plate. The beam is deflected off the target and remains so for the length of time required to process the initial X-ray signal. Such an arrangement drastically reduces the loss of counts to pile-up events and virtually eliminates the need for dead-

time corrections. Since the pulsed beam system operates with essentially zero percent deadtime, unnecessary target damage due to beam heating is minimized. Furthermore, as pointed out by Koenig et al., 1977, it is possible to take advantage of much higher counting rates and better energy resolution than continuous beam excitation can provide.

c) Automatic sample changer: For routine analysis of large numbers of similar samples, it is desirable to automate the sample-changing and positioning process as much as possible. A number of automatic changers have been described in the literature (Cahill, 1975; Bond et al., 1973; Barnes et al., 1973). Cahill's system for air filter analyses can accommodate 102 samples at one time. The samples are merely mounted in conventional 35 mm slide frames.

d) Filtering: Adoption of a single "funny filter" (described in Section IIIB.3) to replace the three filter system currently used could improve the efficient operation of the PIXE system by reducing the analysis time per sample.

e) Improving detection geometry: The sensitivity of the present system could be improved in two ways: (1) by reducing the target-to-detector distance (increasing the solid angle of the detector), and (2) by moving the detector to a backward angle to take advantage of the anisotropic distribution of secondary electron bremsstrahlung. Chu et al., (1977) and Kaji et al., (1977) indicate that a reduction by a factor of nearly two in the secondary electron bremsstrahlung

is possible by moving the detector from its present angle of 90° to a backward angle of 135°. The present target-to-detector distance is about 10 cm. By halving this distance, a factor of $\sqrt{2}$ could be gained in sensitivity (Section IIIF). Sensitivity for low Z elements could be further improved by placing the detector inside the target chamber vacuum eliminating the need for the mylar window of the scattering chamber and the Be window of the detector. The enormous flux of low-energy X-rays into the detector would degrade sensitivity for higher X-ray energies unless some means of filtering were employed.

f) Use of a guard-ring detector: Incomplete charge collection in the detector was discussed in Section IIIB.3 as a source of unwanted background in PIXE spectra. A major factor contributing to the loss of ionizing charge in the detector is poor conduction characteristics along the sides of the detector volume (Goulding and Jaklevic, 1973). Two approaches have been taken to reduce this source of background. The first approach, which is easy to implement and fairly effective, is simply to collimate the detector permitting X-rays to impinge only on the central region of the detector chip. The disadvantages are a reduced solid angle for detection (resulting in degraded sensitivity), and a potential for additional background due to fluorescence of trace impurities in the collimator material by X-rays from the sample. A more elegant approach to improving detector performance is

to use a guard-ring detector as described in the paper by Goulding and Jaklevic (1973). The guard-ring detector provides internal collimation of the detector without sacrificing surface area (or solid angle). A further refinement in the guard-ring detector known as the guard-ring reject system yields even better performance.

It is not clear whether the benefits to be gained by adopting guard-ring detection circuitry for use in PIXE analysis would justify the additional expense of a guard-ring detector, however. The loss of ionizing charge at the sides of the detector occurs predominantly for more energetic X-rays which can penetrate farther into the detector volume. Therefore, the use of a guard-ring detector will be most beneficial for photon-excited systems in which the vast majority (often 90% or more) of the X-rays detected comprise the high-energy scatter peaks of the incident photon beam. Goulding and Jaklevic show that the guard-ring reject circuit can be expected to lower background levels in XRF systems by a factor of 10 over most of the energy range. For PIXE analysis in which most of the X-rays detected are typically below 10 keV, guard-ring detection may provide inconsequential improvements.

g) Use of nuclear scattering processes and nuclear reactions in combination with PIXE: One can make use of nuclear reactions induced in the target by the incident ion beam to extend the analytical capability of the system to atomic numbers

$Z < 13$ (Johansson et al., 1976). Ion-scattering analysis is used in combination with PIXE by Cahill (1975) using alpha particles and by Nelson et al. (1975) using protons. The elastically scattered ions are detected with a solid-state particle detector at an appropriate angle, and the energy loss of the scattered ions can be related to the masses of the target atoms participating in the scattering. Practical limitations to this technique are set by the requirements for mass resolution: in order to resolve a mass difference of 1 atomic mass unit, a combination of high bombarding energy and small target thicknesses must be used. (Nelson et al. have determined that for a target thickness of 1 mg/cm^2, 10 MeV protons are needed in order to resolve Al (M = 27) from Si (M = 28). Such energy requirements restrict this technique to laboratories equipped with larger accelerators than are used by most PIXE analysts.

In addition to elastic scattering to supplement or extend PIXE analysis, nuclear reactions induced in the target nuclei can be used to provide elemental information. The reactions of interest include resonant reactions, inelastic proton scattering $(p,p'\gamma)$ or proton capture reactions $(p,\alpha\gamma)$ and (p,γ), and coulomb excitation processes with subsequent decay by γ-ray emission. Clark et al. (1975) analyzed a standard rock specimen using a combination of PIXE and nuclear reaction techniques: abundances for nine low Z elements between Li and Cl were determined via proton resonance reactions

at bombarding energies between 0.8 MeV and 4.0 MeV; the 4.0 MeV beam was then used to obtain abundances for 19 elements between K and Ba using combined PIXE and coulomb excitation analysis. Similar analyses could be conducted on a conventional PIXE system by including a Ge(Li) (lithium-drifted germanium) detector for γ-ray detection.

h) Wavelength dispersion analysis: The addition of a wavelength spectrometer consisting of one or possibly two scanning crystals to the present energy dispersive system would facilitate the analysis of complex samples. The high resolution capabilities of wavelength dispersion analysis is valuable in resolving interelement interferences observed with the Si(Li) detector, particularly in the region S to Ni. Preliminary feasibility studies with a single crystal scanning spectrometer have been conducted on our system (Willis et al., 1977c) and are reviewed in Appendix B.

i) External beam: By analyzing samples in air, or in a He or N atmosphere rather than in vacuum, several advantages are gained. Target preparation is minimized since samples do not have to be dried prior to irradiation (a procedure which can result in the deterioration of the sample); liquid samples can be analyzed directly and biological specimens can be analyzed in a hydrated state. The mechanics of changing targets are also made easier in atmosphere. Beam heating of targets, though not eliminated is reduced due to heat conduction to the surrounding medium. Lastly, charge accumula-

tion on thick samples is minimized or eliminated since the ionization of the intervening medium by the external beam helps to maintain the target at zero potential. One disadvantage of analyzing samples in air is the resulting presence of a strong argon signal in the X-ray line spectrum. This is eliminated by using a pure He or N atmosphere.

The external beam is typically brought out into atmosphere through a thin film and then collimated immediately before impinging on the sample. Deconninck (1972) used an external beam of 2.0 MeV protons in a He atmosphere to analyze motor oil which was made to flow in front of the beam. Horowitz and Grodzins (1975) have developed a proton microprobe using an external beam for analyzing biological specimens in air. Seaman and Shane (1975) describe an external beam system used to analyze trace elements in wheat flour.

j) Proton microprobe: The proton microprobe is a powerful analytical tool combining the multielemental capability and detection sensitivity of PIXE with spatial resolutions approaching 1 μm. While electron microprobes routinely provide resolutions 10-100 times better (the high-energy protons used in PIXE are more difficult to focus) the sensitivities attainable with the electron microprobe are typically two to three orders of magnitude worse than for proton microprobes.

Several laboratories have developed or are now developing microprobes for microanalysis. Cookson et al. (1972) developed a microbeam system using a special collimator slit

system followed by a series of four quadrupole lenses to produce a beam spot as small as 4 μm. Nobiling et al. (1975) describe a precision collimator system designed to minimize the effects of slit scattering and capable of producing high quality beams of 1 μm diameter and 1 μrad angular divergence. A very simple arrangement for producing a coarser microprobe has been described by Horowitz and Grodzins (1975) who simply collimate the beam by means of a small pinhole (25 μm).

VID. Conclusions

Proton-Induced X-ray Emission (PIXE) has made rapid advances in the seven years since Johansson et al. first demonstrated the feasibility of PIXE. The physical basis for PIXE is well understood, and the optimization of experimental parameters is generally agreed upon. Protons of 2 to 4 MeV have been demonstrated at Duke and other laboratories to provide optimal performance.

The capabilities as well as the limitations of PIXE have been extensively investigated. The greatest strength of PIXE is its ability to determine, rapidly and quantitatively, abundances for 10-20 elements present in a given sample at concentration levels down to 1 ppm on a dry weight basis. The accuracy of the Duke PIXE system is estimated at 10% for thin samples and 15-20% for thick targets, and the precision is estimated at 10-15%. The small mass of material which can be analyzed by PIXE certainly is a

strength of the method; however, it can also constitute a limitation to the method if representative sampling is required. Additional limitations are imposed by interelement interferences which necessitate peak unfolding of X-ray data obtained with Si(Li) detectors. This problem can significantly impair accuracy and sensitivity in certain instances.

Much time and effort has been devoted by PIXE analysts to optimizing sample preparation techniques. The diversity of sample types analyzed at Duke has necessitated a correspondingly wide range of preparation techniques. The ability to obtain quantitative information from moderately thin self-supporting samples such as leaves, and from thick samples (which require minimal sample preparation) has been a particular contribution of the PIXE work at Duke.

PIXE is finding increasing application to areas in which multielement information is desirable: air particulate analysis, biological and medical analyses, and geochemical studies. A major effort has been made at Duke to investigate PIXE's potential in new areas of application. The major studies which have been conducted at Duke--botanical and soil studies, marine toxicity studies, and human lung studies--demonstrate PIXE's particular applicability to large-scale baseline studies and to bioenvironmental studies requiring the analysis of large sample sets.

The future of PIXE will be determined by the need for the kind of multielemental information which PIXE can

provide, and by the ability of PIXE to compete with other analytical techniques performing similar types of analysis. PIXE has so far shown that it can compete well with similar X-ray techniques in terms of cost and analytical capabilities. The availability of Van de Graaff accelerators for future trace element analysis is however not certain as the cost to maintain such a facility will require a sizeable service load to keep the cost per analysis low. However there appears to be a need for and growing interest in trace element studies, and as the value of multielemental information becomes increasingly appreciated, the future usefulness of PIXE should be ensured.

APPENDICES

APPENDIX A: PROGRAM FUDGE

Program FUDGE was written to supplement program TRACE (Section IIID) in analyzing thick targets. The purpose of FUDGE is to calculate correction factors for the reduction in thick target X-ray yields due to proton energy loss and X-ray absorption effects (refer to Figure 3.15).

A. Thin-target calibration

The number of X-ray counts N_Z generated by element Z in a thin target is given by the following relation:

$$N_Z(t) = \sigma_Z(E_0)\,(k\ N_p\ \varepsilon\ \frac{\Omega}{4\pi})\,(\frac{N_0 t n_Z}{M}) \qquad (1)$$

where $\sigma_Z(E_0)$ = x-ray production cross section (cm^2/atom) for incident proton energy E_0

k = relative transition probability

N_p = number of protons which pass through the target

ε = detector efficiency including absorption through windows, air space, and absorbing filter

N_0 = Avogadro's number (molecules/mole)

t = effective target thickness (g/cm^2)

n_z = number of atoms of element Z per molecule of matrix

M = molecular weight of matrix (grams/mole)

$\frac{N_0 t n_z}{M}$ = number of atoms of element Z exposed to beam per cm^2 of beam area ($atoms/cm^2$)

Ω = solid angle subtended by the detector

B. Thick-target calibration

The assumptions implicit in Equation (1) are: (1) that the proton beam suffers insignificant energy loss in penetrating the sample, hence the X-ray production cross section σ_Z is constant throughout the sample, and (2) that the X-rays generated in the target suffer negligible attenuation in the target itself as they exit the sample en route to the detector. These assumptions are valid for target thicknesses $t \lesssim 1$ mg/cm^2. For thicker targets, the variation of σ_Z with proton energy as the beam penetrates the sample must be accounted for, as well as the absorption of X-rays by the target matrix. Accordingly, the thick-target detected X-ray N_Z' is given by:

$$N_Z' = (k\, N_p\, \varepsilon\, \frac{\Omega}{4\pi}) (\frac{N_0 n_z}{M}) \int_{E_0}^{E_f} \frac{\sigma_z(E) T_z(E) dE}{S(E)} \qquad (2)$$

where E_f = energy of the proton beam (keV) as it leaves the target (= 0 for infinitely thick samples)

$\sigma_z(E)$ = X-ray production cross section for element Z at proton energy E (cm^2/atom)

$T_z(E)$ = transmission factor for characteristic X-ray of element Z at depth r(E)

$$= \text{EXP}\left[-\int_{E_0}^{E} U_z \frac{\cot\theta \, dE}{S(E)}\right]$$

where U_z = composite attenuation coefficient (cm^2/g) for characteristic X-rays of element Z in sample matrix. That is,

$U_z = \sum_j \frac{\mu_{zj} c_j}{M}$, where $\sum_j$ represents the sum over all elements in the matrix and

μ_{zj} = attenuation coefficient (cm^2/g) for X-rays of element Z in sample matrix

$\frac{c_j}{M}$ = fraction by weight of element j in matrix

θ = target angle

$S(E)$ = composite stopping power of matrix (keV · cm^2/g)

$$= \sum_j \frac{c_j S_j(E)}{M}$$

$S_j(E)$ = stopping power of matrix element j for protons of energy E (keV · cm^2/g)

C. Thick-target correction factors

The quantities of interest in PIXE analysis are the absolute abundances M_Z (grams) of element Z in the target, and/or the concentration T_Z(ppm) of element Z, where:

$$M_Z(\text{grams}) = C_Z N'_Z / \varepsilon_Z Q \qquad (3)$$

and

$$T_Z(\text{ppm}) = N_Z/\varepsilon_Z Q \bar{M}_Z \ . \qquad (4)$$

Here, ε_Z = thin-target detection efficiency for element Z (counts/μg · μC)

Q = total integrated charge (μC)

C_Z = thick-target yield correction factor

$\bar{M}_Z$ = effective irradiated target mass (grams) based on the detected X-ray yield from element Z.

The values of N_Z', Q, and ε_Z are all known or measured. In order to calculate expected values for M_Z and T_Z, the correction factor C_Z and effective mass $\bar{M}_Z$ must be determined for the given sample.

The correction factor C_Z is defined as the ratio of the thin-target X-ray yield $N_Z(R_p)$ to the detected thick-target yield N_Z':

$$C_Z = \frac{N_Z(R_p)}{N_Z'} = \sigma_z(E_0) \cdot R_p \left[\int_{E_0}^{E_f} \frac{\sigma_z(E) \cdot T_z(E) dE}{S(E)} \right]^{-1} \qquad (5)$$

where $N_Z(R_p)$ is calculated from Equation (1) by assuming a value of t equal to the range of a 3-MeV proton in the thick sample (i.e., the thick target is treated as a thin target by assuming a constant σ_Z and negligible X-ray absorption over the proton range R_p). If the target is only moderately thick so that the beam exits the target with positive energy E_f, then R_p is replaced by the effective target thickness t.

The effective irradiated mass $\bar{M}_Z$ represents the

amount of target mass which would yield the observed number of X-rays of element Z in the thin-target response--i.e., assuming negligible proton energy loss and X-ray absorption. Program FUDGE calculates $\bar{M}_Z$ according to

$$\bar{M}_Z = \frac{\text{irradiated target mass}}{C_Z} \quad \text{(grams)} \tag{6}$$

D. Input data in FUDGE

The calculations contained in Equations (5) and (6) require the following information: (1) X-ray production cross sections for all elements of interest at arbitrary proton energies; (2) X-ray attenuation coefficients for X-ray energies of interest and representative matrices; (3) proton stopping powers for arbitrary proton energies and representative matrices.

Production cross sections at any given proton energy are determined from semiempirical formulae (Equations 2.2 and Table 2.1) developed by Johansson et al. (1976). The tables of attenuation coefficients are comprised of values interpolated from Veigele's tables (1973). Stopping powers are calculated at arbitrary energies from the semiempirical formula used in generating the stopping power tables of Williamson et al. (1966).

In addition to the information above, the program is provided with: tables of X-ray energies for the reference

lines of 22 K-line emitting elements and 6 L-line emitters; the cross-sectional beam area; and the atomic number and atomic weights for 13 elements from which the bulk composition of the target matrix is composed: H, C, N, O, Na, Mg, Al, Si, P, S, K, Ca, and Fe. The following information is input on cards at the time of program execution: (1) the number of layers composing the target; (2) the bulk composition of each layer; (3) the incident proton energy; (4) energy stepsize ΔE; (5) target thickness T; and (6) target angle θ. Several common matrix compositions (mylar, polyethylene, cellulose, and dried tissue) are stored in the program to simplify the card input for these frequently encountered matrices.

E. Numerical calculations

The integration in Equation (5) is carried out stepwise using a finite energy stepsize ΔE selected by the operator. In essence, the thick target is treated as a composite of many thin slabs each of which causes a loss of energy ΔE in the proton beam. The total depth of penetration is calculated at each integration step and compared to the input value for the effective target thickness $t = T/\cos \theta$. The calculation is halted when either of the following occurs: (1) the penetration depth exceeds the effective target thickness (for moderately thick targets), or (2) the calculated energy of the proton beam exiting the current layer is less

than or equal to zero (for infinitely thick targets). The total irradiated mass M_{TOT} (grams) is calculated as the product of the beam area and the penetration depth or effective target thickness, whichever applies.

A useful secondary function of the program is to calculate selected K-shell and L-shell X-ray production and ionization cross sections at arbitrary proton energies. Examples of such calculations are presented in Tables 3 and 4 of Appendix C. One can also calculate proton stopping powers at arbitrarily selected proton energies for typical matrices. The final calculations output by FUDGE include correction factors C_Z for 22 K-line elements (S through Mo) and 6 L-line elements (Ba through Th), effective irradiated masses for these elements, the stopping power of the matrix at the initial proton energy E_0, and the penetration depth of the proton beam. By means of a sense switch interfaced to the computer, the operator can choose to output these calculations at each step of the integration process.

F. Uncertainties

The dominant uncertainties inherent in the FUDGE calculations are attributable to uncertainties in the values assumed for the X-ray production cross sections, the proton stopping powers, and the X-ray attenuation coefficients. Akselsson and Johansson (1974) analyze sources of errors in their own X-ray cross section data and these are probably

representative of cross section data in general (from which Johansson's semiempirical formulae are derived). If all these errors are additive, the total % error would be 6-16.4%. The proton stopping powers taken from Williamson et al. agree well with a recent tabulation by Bichsel (1972) who quotes an uncertainty of 2-10%. Veigele (1973) states that for the region below 10 keV, his attenuation coefficients agree to within 5% with those of Storm and Israel (1970) who themselves quote 10% uncertainty.

The calculations in Equation (5) assume an ideal thick target--i.e., one which has a flat, homogeneous surface exposed to the beam, and which has a known bulk composition. Experimental uncertainties associated with the measurement of real (rather than ideal) thick targets are not included here. These sources of uncertainty are discussed in Section IIIG and include: sample losses due to beam heating, target angle θ, surface irregularities and depth non-uniformities, thick-target enhancement effects, and unknown matrix composition.

A measure of the combined uncertainties in FUDGE calculations and in the measuring process itself can be extracted from numerous analyses conducted at Duke on thick, calibrated standards (Section IIIC.4). These results indicate that for a variety of biological materials, and for elements heavier than Ca, the total analytical uncertainties are typically less than 15-20%.

APPENDIX B: WAVELENGTH DISPERSION ANALYSIS OF PIXE SPECTRA

In a recent publication (Willis et al., 1977c) we reported on the use of a curved crystal spectrometer to observe X-ray spectra generated by proton induced X-ray emission from environmental samples. The primary motivation for these studies was to investigate the potential use of wavelength spectrometers in PIXE analysis--a topic which has received relatively little attention. A discussion of these studies, and some results and conclusions are presented here.

A. Introduction

The primary advantage of a wavelength spectrometer is its high-resolution capability--typically between one and two orders of magnitude better than resolutions attainable by state-of-the-art energy dispersive detectors ($\sim$ 160 eV for the 5.9 KeV Mn K_α line). The use of wavelength dispersive analysis (λDX) virtually eliminates unresolved line interferences and therefore does away with the need for computer routines (moderately complicated and subject to error) to un-

fold overlapping signals. There interelement interferences constitute a major disadvantage of energy dispersive analysis (EDX) and are particularly troublesome in the elemental region S to Ni (where the K_β line from element Z overlaps with the K_α line from element (Z+1) for typical energy dispersive detectors). The advantage of high resolution analysis can be readily appreciated in Figures B1a and B1b which demonstrate the ability of wavelength spectrometers to separate X-ray lines of neighboring elements. The development in recent years of multicrystal spectrometers (Wagman et al., 1977) affording simultaneous multielemental capability puts λDX on a competitive basis with EDX in the analysis of environmental samples.

The major disadvantage of λDX is its low efficiency relative to EDX (which can be easily made 100 times more efficient than λDX). This is primarily because of the much smaller solid angle subtended by the crystal spectrometer as well as reflection losses in the crystal. The efficiency can be significantly improved by using a curved crystal rather than a planar crystal.

B. Apparatus and Experimental Procedure

The experimental arrangement for the studies at Duke is shown in Figure B2. The target, tilted at 40° from the vertical, is irradiated in vacuum by 3-MeV protons. Slits S_1 and S_2 collimate the beam to a diameter of about 1.2 mm on

Figure B1a X-ray spectrum obtained with a scanning crystal spectrometer illustrating the separation of K lines of neighboring elements.

(From Wagman et al., 1977)

Figure B1b Comparison of spectra obtained with energy dispersive and wavelength dispersive analysis of a sample containing K and Ca.

(From Wagman et al., 1977)

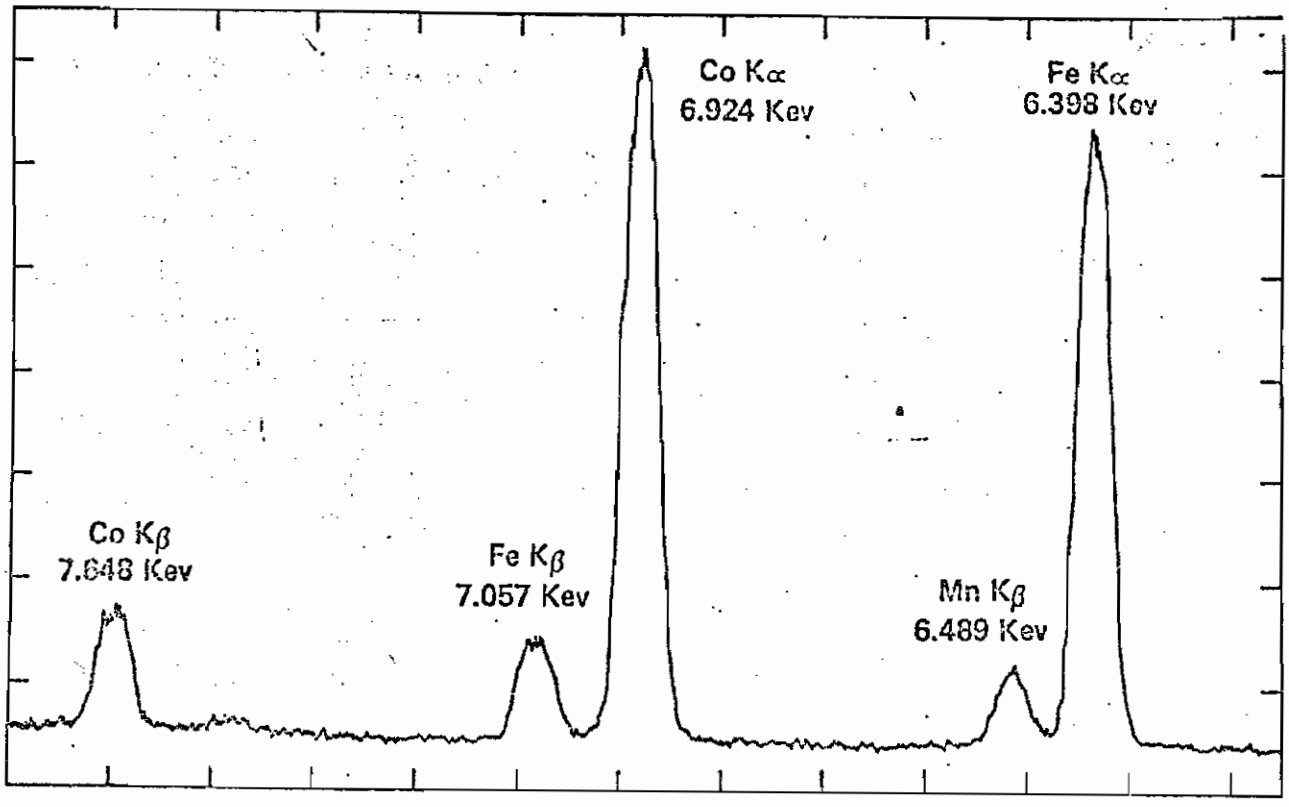
Co Kα
6.924 Kev
Fe Kα
6.398 Kev
Co Kβ
7.648 Kev
Fe Kβ
7.057 Kev
Mn Kβ
6.489 Kev

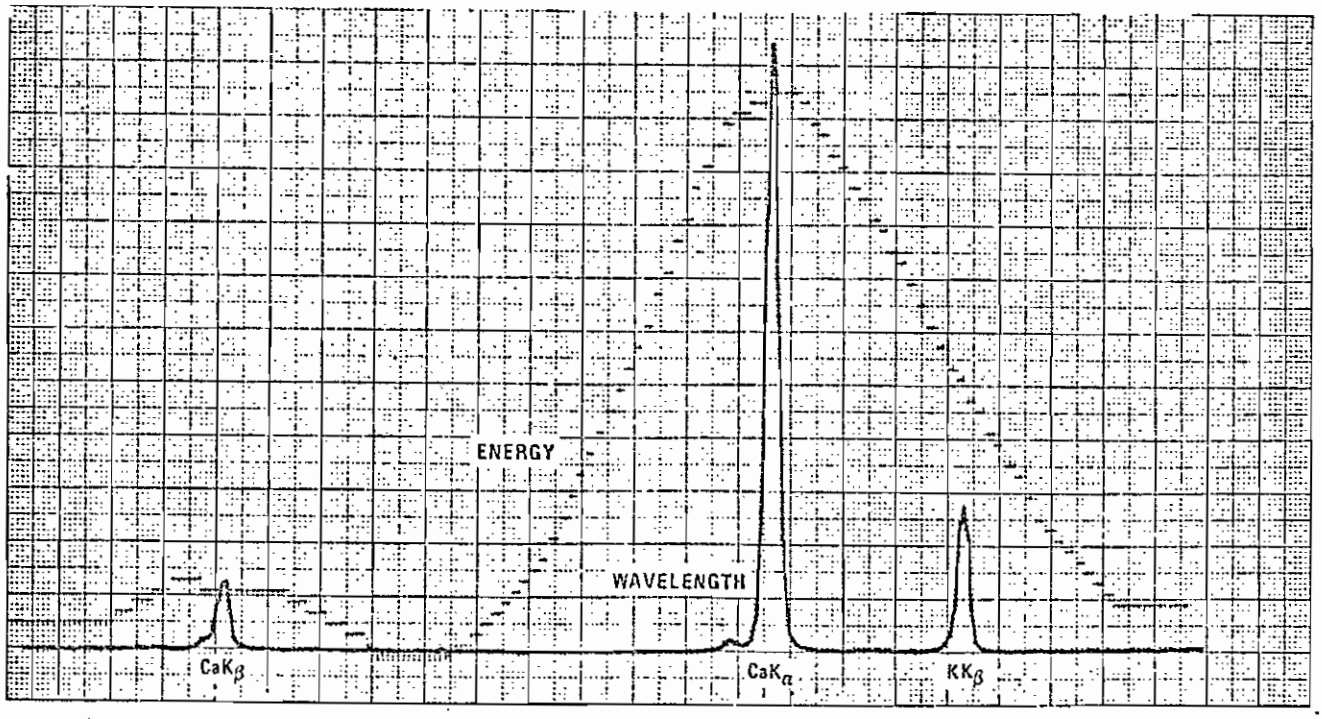
ENERGY
WAVELENGTH
CaKβ
CaKα
KKβ

Figure B2 The experimental arrangement used for wavelength dispersion analysis of proton-induced X-rays.

Figure B3 Calibration of the PET (penta erythritol) crystal spectrometer for K_α X-ray lines observed in first and second order. The index number N corresponds to the dial setting of the spectrometer and is proportional (for a given reflection number n) to the X-ray wavelength.

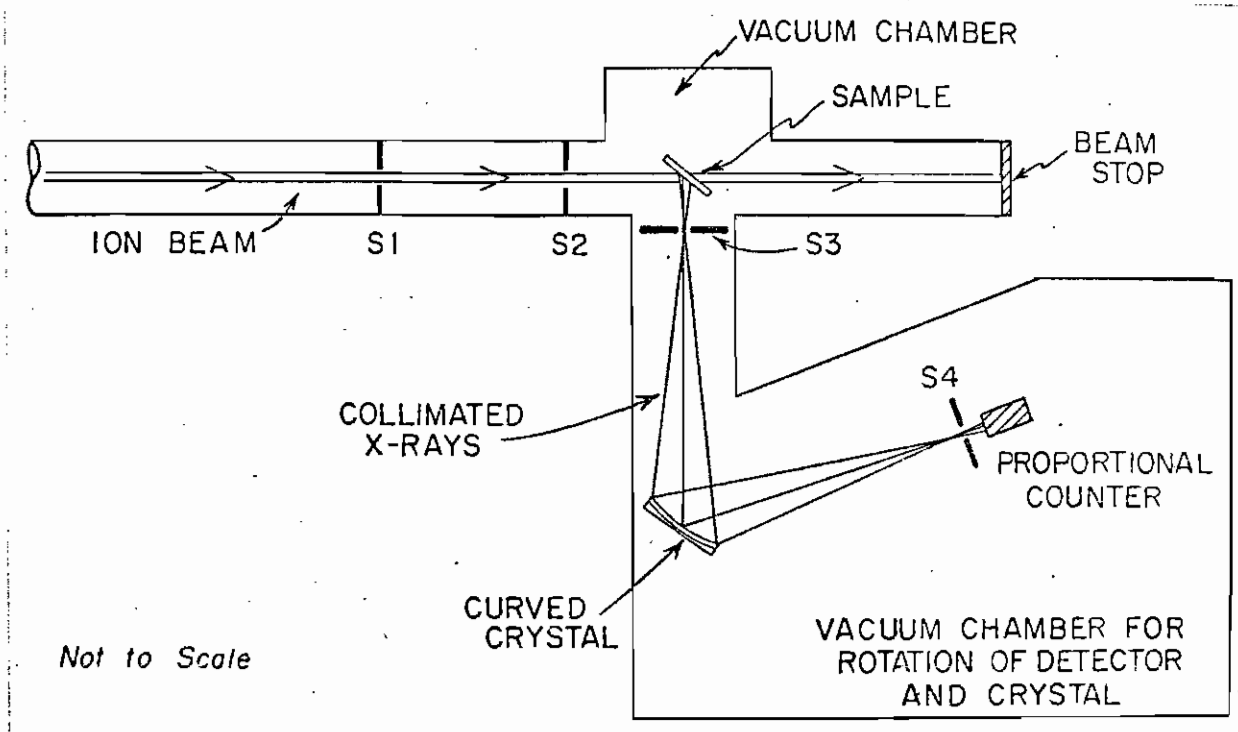

RELATIVE POSITION FOR K_α LINES

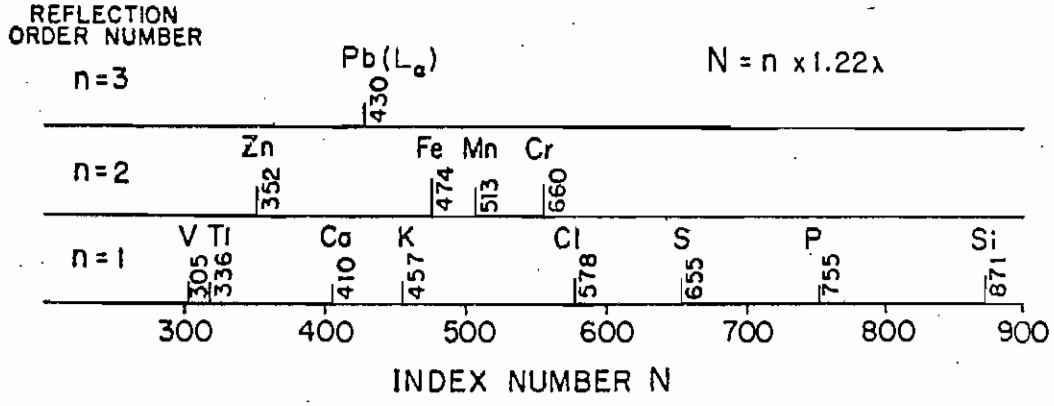

target. Approximately 60 nA of current was maintained on the target for the studies here.

A curved crystal spectrometer (Applied Research Laboratories) with a proportional gas-flow counter was used for the wavelength dispersive analysis. X-rays emitted from the target in the direction of the crystal passed through a 6 μm hostaphan foil (to prevent contaminants from depositing on the crystal) and then through the primary slit S_3. Slit S_3, with a diameter of 0.3 mm, was located 1.6 cm from the target thus giving an acceptance angle of 1.4°. The X-rays were reflected from the crystal and focused at the secondary slit S_4 before entering the proportional counter. The counter and the crystal were coupled together in a Rowland mounting to permit wavelength scanning. This arrangement was then driven by a stepping motor which could be operated in two modes: (1) after a preset amount of charge was collected on the target, the stepping motor would advance the spectrometer automatically to a different wavelength setting; (2) the spectrometer could be advanced by the operator to any desired wavelength setting. (Details of the scanning system are in Doyle, 1976.)

The procedure for the present study was as follows. Selected X-ray lines were scanned in steps of approximately 0.002 Å, and the number of X-rays observed at each wavelength setting was recorded. A logic signal from the current integrator caused the stepping motor to advance to the next wave-

length setting after 0.3 μC of charge had been collected. For 60 nA of beam current, this rate corresponded to approximately one data point every 5 seconds. (Each peak measured for this study required between 20 and 50 data points). After a peak measurement was completed, the spectrometer was advanced to the next X-ray wavelength of interest, thus bypassing regions of the wavelength spectrum which were of no interest.

The detection of X-rays by means of a proportional counter yields output signals whose pulse heights are proportional to the energies of the incident X-rays. By means of a single channel differential discriminator, only those signals corresponding to the desired X-ray energy were accepted and recorded on a scalar.

The particular crystal used for our studies was a PET crystal (penta erythritol) with a 2d spacing of 8.742 Å. The Bragg relation

$$n\lambda = 2d \sin \theta = CN$$

specifies the minimum and maximum observable wavelengths determined by the permitted range of scattering angles θ. Here, n is the reflection order number, N is the dial reading of the scanning spectrometer, and C is a calibration factor for the PET crystal. For our spectrometer, the approximate range of wavelengths observed in first order is given by $2.5 \text{ Å} \lesssim \lambda \lesssim 10 \text{ Å}$ corresponding to the K_α X-ray lines for elements between Al and V. An early calibration of the

PET crystal is shown in Figure B3 indicating the elements which can be potentially detected in the first three reflection orders. By using different crystals with appropriate 2d spacings it is possible to cover a much larger elemental region in first order, but this procedure was not used in these initial studies.

C. Results and Conclusions

Five samples of environmental interest were analyzed with the crystal spectrometer. These included thick pellets pressed from NBS orchard leaf (SRM #1571) and coal (SRM #1632), two aerosol samples collected on 1.1 mg/cm^2 nuclepore, and one blank nuclepore. The aerosol samples represented particulates below 10 μm collected in a 24-hour air sampling device.

Resulting spectra for the orchard leaf sample and one of the aerosol samples are shown in Figures B4 and B5 respectively. For comparison, a PIXE spectrum of orchard leaf collected with the energy dispersive system is shown in Figure B6. The superior capability of wavelength dispersion analysis to separate the K_α lines of neighboring light elements is clearly evidenced in a comparison of the two orchard leaf spectra. Each data point in the λDX spectra represents the sum of the X-ray yields measured at 5 separate wavelength settings--for a total of 1.5 μC of charge per data point (approximately 25 sec). Figure B7 shows the actual

Figure B4 Results obtained for wavelength dispersive analysis of an NBS orchard leaf pellet irradiated with 3-MeV protons. Each data point represents the sum of data obtained at 5 wavelength settings. Regions between the peaks were not analyzed.

Figure B5 Results obtained for wavelength dispersive analysis of an aerosol sample collected on 1.1 mg/cm^2 nuclepore and irradiated with 3-MeV protons. The Fe line, observed in second order, was actually measured on another air filter, as the sample shown here had relatively little Fe.

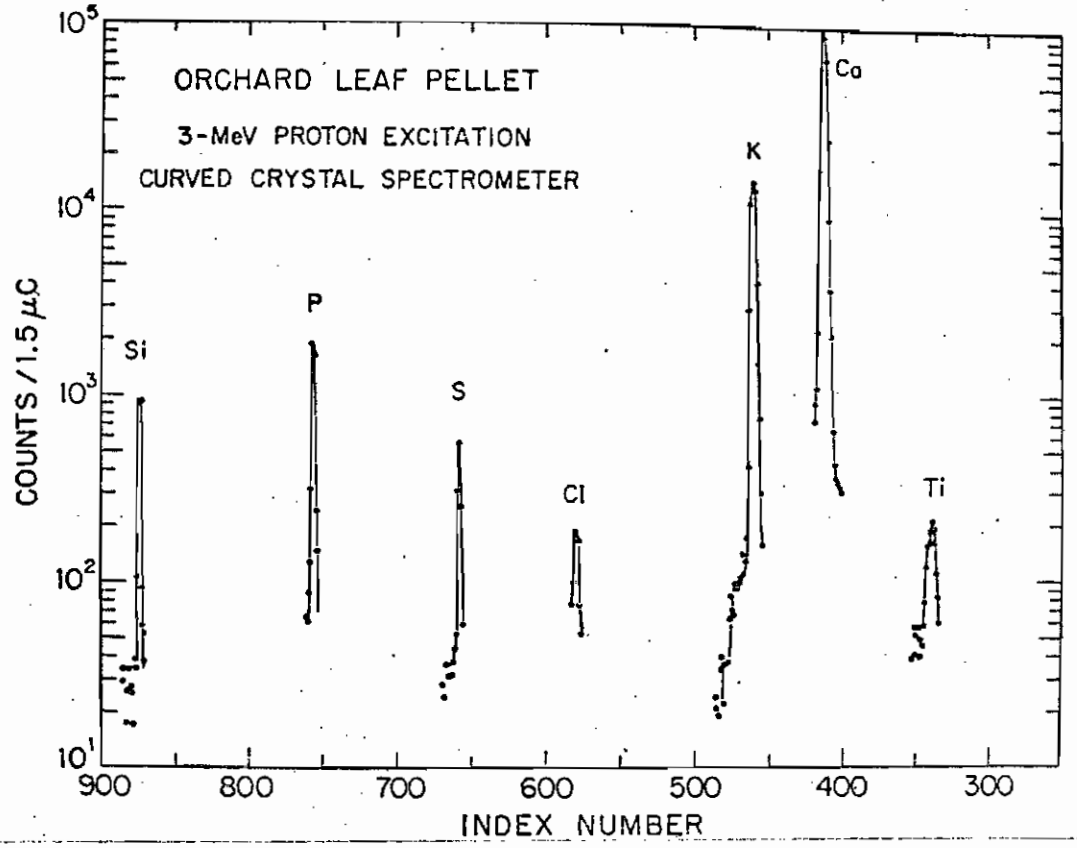
ORCHARD LEAF PELLET
3-MeV PROTON EXCITATION
CURVED CRYSTAL SPECTROMETER
COUNTS / 1.5 μC
INDEX NUMBER
Si
P
S
Cl
K
Ca
Ti

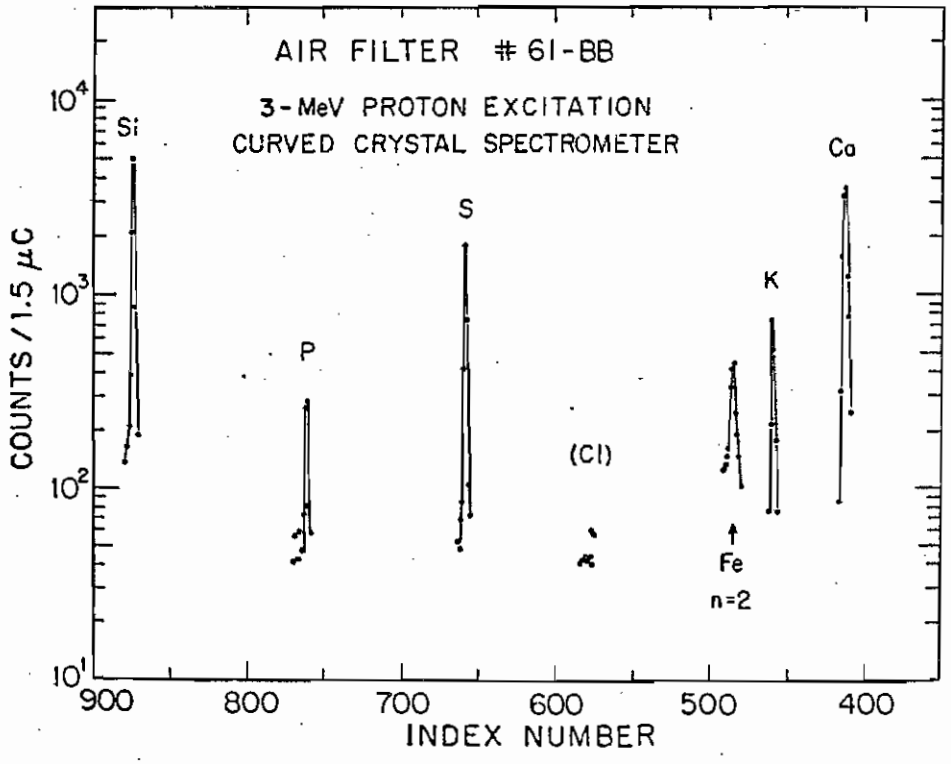
AIR FILTER #61-BB
3-MeV PROTON EXCITATION
CURVED CRYSTAL SPECTROMETER
COUNTS / 1.5 μC
INDEX NUMBER
Si
P
S
(Cl)
Fe
n=2
K
Ca

Figure B6 Typical PIXE spectrum of an NBS orchard leaf pellet for comparison with Figure B4. The spectrum was collected using an energy dispersive Si(Li) detector with a resolution of about 170 eV FWHM for the Mn K_α line (5.898 keV). Note the lack of separation between the K K_α and Ca K_α lines.

Figure B7 Expanded view of the Si and Ca region shown previously in Figure B4 obtained by wavelength dispersive analysis. Note that the resolution of the crystal spectrometer is approximately 2 eV for Si K_α and 30 eV for Ca K_α.

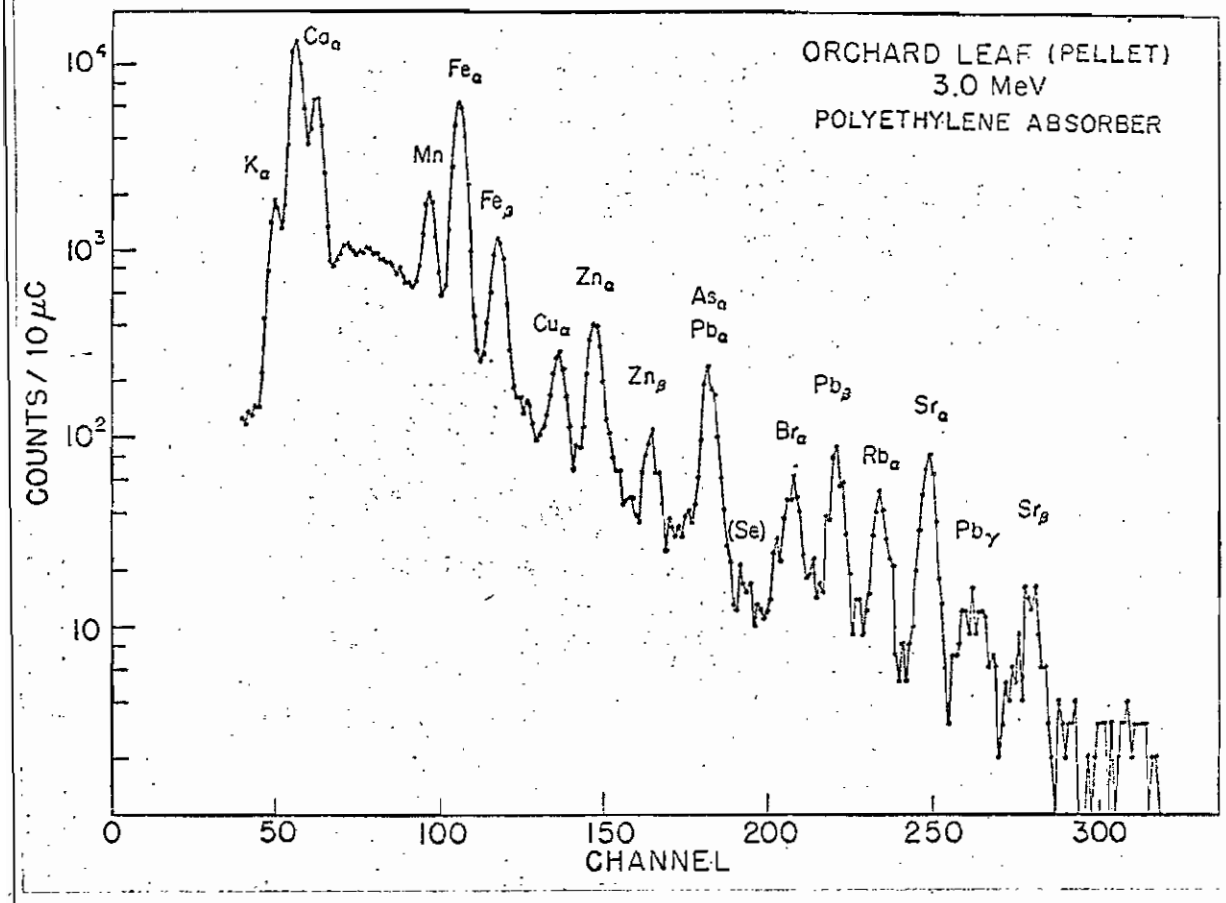
ORCHARD LEAF (PELLET)
3.0 MeV
POLYETHYLENE ABSORBER
COUNTS / 10 μC
CHANNEL
Ca$_\alpha$
Fe$_\alpha$
K$_\alpha$
Mn
Fe$_\beta$
Zn$_\alpha$
Cu$_\alpha$
As$_\alpha$
Pb$_\alpha$
Zn$_\beta$
Pb$_\beta$
Sr$_\alpha$
Br$_\alpha$
Rb$_\alpha$
(Se)
Pb$_\gamma$
Sr$_\beta$

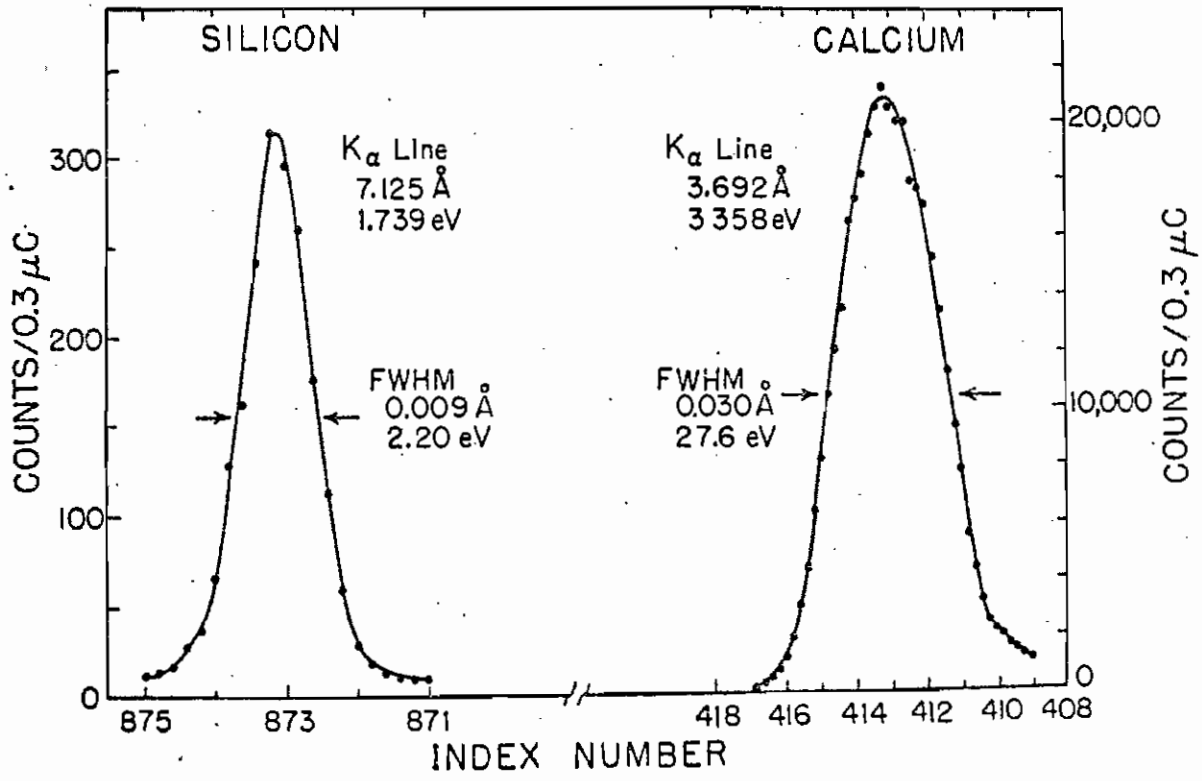
SILICON
CALCIUM
K$_\alpha$ Line
7.125 Å
1.739 eV
FWHM
0.009 Å
2.20 eV
K$_\alpha$ Line
3.692 Å
3358 eV
FWHM
0.030 Å
27.6 eV
COUNTS/0.3 μC
INDEX NUMBER

data for the Si and Ca peaks of the orchard leaf spectrum. The resolutions obtained by the crystal spectrometer for these two peaks are approximately 2 eV and 30 eV respectively compared to 170 eV for the energy dispersive Si(Li) detector.

One major disadvantage of using a scanning, single crystal spectrometer is the relatively poor efficiency for multielemental analysis. In the samples analyzed, only selected elements among those observable in first order (Si to V) were detected with any reasonable efficiency. The abundant Fe concentration (300 ppm) in orchard leaf could not be detected above background using the second order reflection.

The analytical efficiency (counts/μg · μC) of the crystal spectrometer used in these studies is not yet determined, thus making it difficult to compare the sensitivities of wavelength and energy dispersive analyses. Some feeling for the system's efficiency can be obtained by comparing selected peak areas of Figure B4 with the NBS abundances shown in Table 3.5. (The values in parentheses are not certified.) A relative efficiency curve for the PET crystal as a function of X-ray energy has been measured and is shown in Figure B8. At low X-ray energies, the efficiency is strongly affected by absorption losses in the thin window of the proportional counter and in the protective layer of hostaphan at the entrance to the spectrometer. The efficiency curve is also influenced by the reflectivity of the crystal

Figure B8 Relative efficiency of the PET crystal versus X-ray energy for first order reflection. See text for discussion.

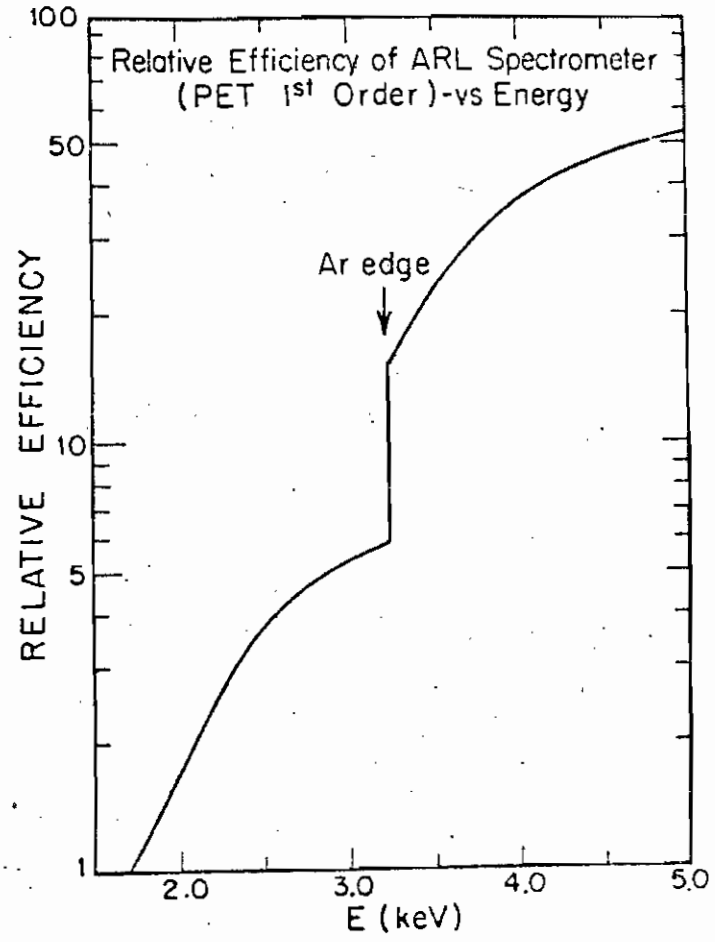
Relative Efficiency of ARL Spectrometer
(PET 1st Order)-vs Energy
Ar edge
RELATIVE EFFICIENCY
100
50
10
5
1
2.0
3.0
4.0
5.0
E (keV)

which increases for larger Bragg angles θ. The discontinuity in the relative efficiency curve at the Ar absorption edge is due to the gas mixture (90% Ar) contained in the proportional counter.

The results of our studies indicate that wavelength dispersion analysis can be a useful supplement to energy dispersive systems. The high resolution capabilities of λDX would make it particularly helpful in resolving inter-element interferences observed in energy dispersive spectra--especially in the region S to Ni.

A major factor limiting the effectiveness of a single scanning crystal is its relatively poor efficiency for multielemental analysis. The λDX system at Duke has not been optimized for analytical applications and it is difficult therefore to estimate the ultimate sensitivity of such a system. Modifications yielding improved sensitivity would include raising the proton energy and beam current, counting for longer times, and optimizing the proportional counter through adjustments in the gas pressure and mixture. The ultimate sensitivities for multielement λDX are achieved by using an arrangement of multiple crystals optimized for specific X-ray lines. Such a system can provide interference-free detection limits which are about the same as energy dispersive systems, but with much better precision for multielement analysis where spectral unfolding is necessary (Birks and Gilfrich, 1976).

APPENDIX C: USEFUL TABLES

Table C.1

X-Ray Critical-Absorption and Emission Energies in keV

Atomic Number	Element	K series					L series							
		K_{ab}	$K_{\beta 2}$	$K_{\beta 1}$	$K_{\alpha 1}$	$K_{\alpha 2}$	L_{Iab}	L_{IIab}	L_{IIIab}	$L_{\gamma 1}$	$L_{\beta 2}$	$L_{\beta 1}$	$L_{\alpha 1}$	$L_{\alpha 2}$
1	Hydrogen	0.0136												
2	Helium	0.0246												
3	Lithium	0.055			0.052									
4	Beryllium	0.116			0.110									
5	Boron	0.192			0.185									
6	Carbon	0.283			0.282									
7	Nitrogen	0.398			0.392									
8	Oxygen	0.531			0.523									
9	Fluorine	0.687			0.677									
10	Neon	0.874			0.851		0.048	0.022	0.022					
11	Sodium	1.08		1.067	1.041		0.055	0.034	0.034					
12	Magnesium	1.303		1.297	1.254		0.063	0.050	0.049					
13	Aluminum	1.559		1.555	1.487	1.486	0.087	0.073	0.072					
14	Silicon	1.838		1.833	1.740	1.739	0.118	0.099	0.098					
15	Phosphorus	2.142		2.136	2.015	2.014	0.153	0.129	0.128					
16	Sulphur	2.470		2.464	2.308	2.306	0.193	0.164	0.163					
17	Chlorine	2.819		2.815	2.622	2.621	0.238	0.203	0.202					
18	Argon	3.203		3.192	2.957	2.955	0.287	0.247	0.245					
19	Potassium	3.607		3.589	3.313	3.310	0.341	0.297	0.294					
20	Calcium	4.038		4.012	3.691	3.688	0.399	0.352	0.349			0.344	0.341	
21	Scandium	4.496		4.460	4.090	4.085	0.462	0.411	0.406			0.399	0.395	
22	Titanium	4.964		4.931	4.510	4.504	0.530	0.460	0.454			0.458	0.452	
23	Vanadium	5.463		5.427	4.952	4.944	0.604	0.519	0.512			0.519	0.510	
24	Chromium	5.988		5.946	5.414	5.405	0.679	0.583	0.574			0.581	0.571	
25	Manganese	6.537		6.490	5.898	5.887	0.762	0.650	0.639			0.647	0.636	
26	Iron	7.111		7.057	6.403	6.390	0.849	0.721	0.708			0.717	0.704	
27	Cobalt	7.709		7.649	6.930	6.915	0.929	0.794	0.779			0.790	0.775	
28	Nickel	8.331	8.328	8.264	7.477	7.460	1.015	0.871	0.853			0.866	0.849	
29	Copper	8.980	8.976	8.904	8.047	8.027	1.100	0.953	0.933			0.948	0.928	
30	Zinc	9.660	9.657	9.571	8.638	8.615	1.200	1.045	1.022			1.032	1.009	
31	Gallium	10.368	10.365	10.263	9.251	9.234	1.30	1.134	1.117			1.122	1.096	
32	Germanium	11.103	11.100	10.981	9.885	9.854	1.42	1.248	1.217			1.216	1.186	
33	Arsenic	11.863	11.863	11.725	10.543	10.507	1.529	1.359	1.323			1.317	1.282	
34	Selenium	12.652	12.651	12.495	11.221	11.181	1.652	1.473	1.434			1.419	1.379	
35	Bromine	13.475	13.465	13.290	11.923	11.877	1.794	1.599	1.552			1.526	1.480	
36	Krypton	14.323	14.313	14.112	12.648	12.597	1.931	1.727	1.675			1.638	1.587	
37	Rubidium	15.201	15.184	14.960	13.394	13.335	2.067	1.866	1.806			1.752	1.694	1.692
38	Strontium	16.106	16.083	15.834	14.164	14.097	2.221	2.008	1.941			1.872	1.806	1.805
39	Yttrium	17.037	17.011	16.736	14.957	14.882	2.369	2.154	2.079			1.996	1.922	1.920
40	Zirconium	17.998	17.969	17.666	15.774	15.690	2.547	2.305	2.220	2.302	2.219	2.124	2.042	2.040
41	Niobium	18.987	18.951	18.621	16.614	16.520	2.706	2.467	2.374	2.462	2.367	2.257	2.166	2.163
42	Molybdenum	20.002	19.964	19.607	17.470	17.373	2.884	2.627	2.523	2.623	2.518	2.395	2.293	2.290
43	Technetium	21.054	21.012	20.585	18.410	18.328	3.054	2.795	2.677	2.792	2.674	2.538	2.424	2.420
44	Ruthenium	22.118	22.072	21.655	19.278	19.149	3.236	2.966	2.837	2.964	2.836	2.603	2.558	2.554
45	Rhodium	23.224	23.169	22.721	20.214	20.072	3.419	3.145	3.002	3.144	3.001	2.834	2.696	2.692
46	Palladium	24.347	24.297	23.816	21.175	21.018	3.617	3.329	3.172	3.328	3.172	2.990	2.838	2.833
47	Silver	25.517	25.454	24.942	22.162	21.988	3.810	3.528	3.352	3.519	3.348	3.151	2.984	2.978
48	Cadmium	26.712	26.641	26.093	23.172	22.982	4.019	3.727	3.538	3.716	3.528	3.316	3.133	3.127
49	Indium	27.928	27.859	27.274	24.207	24.000	4.237	3.939	3.729	3.920	3.713	3.487	3.287	3.279
50	Tin	29.190	29.106	28.483	25.270	25.042	4.464	4.157	3.928	4.131	3.904	3.662	3.444	3.435
51	Antimony	30.486	30.387	29.723	26.357	26.109	4.697	4.381	4.132	4.347	4.100	3.843	3.605	3.595
52	Tellurium	31.809	31.698	30.993	27.471	27.200	4.938	4.613	4.341	4.570	4.301	4.029	3.769	3.758
53	Iodine	33.164	33.016	32.292	28.610	28.315	5.190	4.856	4.559	4.800	4.507	4.220	3.937	3.926
54	Xenon	34.579	34.446	33.644	29.802	29.485	5.452	5.104	4.782	5.036	4.720	4.422	4.111	4.098
55	Cesium	35.959	35.819	34.984	30.970	30.623	5.720	5.358	5.011	5.280	4.936	4.620	4.286	4.272
56	Barium	37.410	37.255	36.376	32.191	31.815	5.995	5.623	5.247	5.531	5.156	4.828	4.467	4.451
57	Lanthanum	38.931	38.728	37.799	33.440	33.033	6.283	5.894	5.489	5.789	5.384	5.043	4.651	4.635
58	Cerium	40.449	40.231	39.255	34.717	34.276	6.561	6.165	5.729	6.052	5.613	5.262	4,840	4.823
59	Praseodymium	41.990	41.772	40.746	36.023	35.548	6.846	6.443	5.968	6.322	5,850	5.489	5.034	5.014
60	Neodymium	43.571	43.298	42.269	37.359	36.845	7.144	6.727	6.215	6.602	6.000	5.722	5.230	5.206

Table C.1

X-Ray Critical-Absorption and Emission Energies in keV

Atomic Number	Element	K series					L series							
		K_{ab}	$K_{\beta 2}$	$K_{\beta 1}$	$K_{\alpha 1}$	$K_{\alpha 2}$	L_{Iab}	L_{IIab}	L_{IIIab}	$L_{\gamma 1}$	$L_{\beta 2}$	$L_{\beta 1}$	$L_{\alpha 1}$	$L_{\alpha 2}$
61	Promethium	45.207	44.955	43.945	38.649	38.160	7.448	7.018	6.466	6.891	6.336	5.956	5.431	5.400
62	Samarium	46.846	46.553	45.400	40.124	39.523	7.754	7.201	6.721	7.180	6.587	6.206	5.636	5.609
63	Europium	48.515	48.241	47.027	41.529	40.877	8.069	7.624	6.983	7.478	6.842	6.456	5.846	5.816
64	Gadolinium	50.229	49.961	48.718	42.983	42.260	8.393	7.940	7.252	7.788	7.102	6.714	6.059	6.027
65	Terbium	51.998	51.737	50.391	44.470	43.737	8.724	0.258	7.519	8.104	7.368	6.979	6.275	6.241
66	Dysprosium	53.789	53.491	52.178	45.985	45.193	9.083	8.621	7.850	8.418	7.638	7.249	6.495	6.457
67	Holmium	55.615	55.292	53.934	47.528	46.686	9.411	8.920	8.074	8.748	7.912	7.528	6.720	6.680
68	Erbium	57.483	57.888	55.690	49.099	48.205	9.776	9.263	8.364	9.089	0.188	7.810	6.948	6.904
69	Thulium	59.335	58.969	57.576	50.730	49.762	10.144	9.628	8.652	9.424	8.472	8.103	7.181	7.135
70	Ytterbium	61.303	60.959	59.352	52.360	51.326	10.486	9.977	8.943	9.779	8.758	8.401	7.414	7.367
71	Lutecium	63.304	62.946	61.282	54.063	52.059	10.867	10.345	9.241	10.142	9.048	0.708	7.654	7.604
72	Hafnium	65.313	64.936	63.209	55.757	54.579	11.264	10.734	9.556	10.514	9.346	9.021	7.898	7.843
73	Tantalum	67.400	66.999	65.210	57.524	56.270	11.676	11.130	9.876	10.892	9.649	9.341	8.145	8.087
74	Tungsten	69.508	69.090	67.233	59.310	57.973	12.090	11.535	10.198	11.283	9.959	9.670	8.396	8.333
75	Rhenium	71.662	71.220	69.298	61.131	59.707	12.522	11.955	10.531	11.684	10.273	10.008	8.651	8.584
76	Osmium	73.860	73.393	71.404	62.991	61.477	12.965	12.383	10.869	12.094	10.596	10.354	8.910	8.840
77	Iridium	76.097	75.605	73.549	64.886	63.278	13.413	12.819	11.211	12.509	10.910	10.706	9.173	9.098
78	Platinum	78.379	77.866	75.736	66.820	65.111	13.873	13.268	11.559	12.939	11.249	11.069	9.441	9.360
79	Gold	80.713	80.165	77.968	68.794	66.980	14.353	13.733	11.919	13.379	11.582	11.439	9.711	9.625
80	Mercury	83.106	82.526	80.258	70.821	68.894	14.841	14.212	12.285	13.828	11.923	11.823	9.987	9.896
81	Thallium	85.517	84.904	82.558	72.860	70.820	15.346	14.697	12.657	14.288	12.268	12.210	10.266	10.170
82	Lead	88.001	87.343	84.922	74.957	72.794	15.870	15.207	13.044	14.762	12.620	12.611	10.549	10.448
83	Bismuth	90.521	89.833	87.335	77.097	74.805	16.393	15.716	13.424	15.244	12.977	13.021	10.836	10.729
84	Polonium	93.112	92.386	89.809	79.296	76.868	16.935	16.244	13.817	15.740	13.330	13.441	11.120	11.014
85	Astatine	95.740	94.976	92.319	81.525	78.956	17.490	16.784	14.215	16.248	13.705	13.873	11.424	11.304
86	Radon	98.418	97.616	94.877	83.800	81.090	18.058	17.337	14.618	16.768	14.077	14.316	11.724	11.597
87	Francium	101.147	100.305	97.483	86.119	83.243	18.638	17.904	15.028	17.301	14.459	14.770	12.029	11.894
88	Radium	103.927	103.048	100.136	88.495	85.446	19.233	18.481	15.442	17.845	14.039	15.233	12.338	12.194
89	Actinium	106.759	105.838	102.846	90.894	87.691	19.842	19.078	15.865	18.405	15.227	15.712	12.650	12.499
90	Thorium	109.630	108.671	105.592	93.334	89.942	20.460	19.688	16.296	18.977	15.620	16.200	12.966	12.808
91	Protactinium	112.581	111.575	108.408	95.851	92.271	21.102	20.311	16.731	19.559	16.022	16.700	13.291	13.130
92	Uranium	115.591	114.549	111.289	98.428	94.648	21.753	20.943	17.163	20.163	16.425	17.210	13.613	13.438
93	Neptunium	118.619	117.533	114.181	101.065	97.023	22.417	21.596	17.614	20.774	16.837	17.740	13.945	13.758
94	Plutonium	121.720	120.592	117.146	103.653	99.457	23.097	22.262	18.066	21.401	17.254	18.278	14.279	14.082
95	Americium	124.876	123.706	120.163	106.351	101.932	23.793	22.944	18.525	22.042	17.677	18.829	14.618	14.411
96	Curium	128.088	126.875	123.235	109.098	104.448	24.503	23.640	18.990	22.699	18.106	19.393	14.961	14.743
97	Berkelium	131.357	130.101	126.362	111.896	107.023	25.230	24.352	19.461	23.370	18.540	19.971	15.309	15.079
98	Californium	134.683	133.383	129.544	114.745	109.603	25.971	25.080	19.938	24.056	18.980	20.562	15.661	15.420
99	Einsteinium	138.067	136.724	132.781	117.646	112.244	26.729	25.824	20.422	24.758	19.426	21.166	16.018	15.764
100	Permium	141.510	140.122	136.075	120.598	114.926	27.503	26.584	20.912	25.475	19.879	21.785	16.379	16.113

Table C.2

X-Ray Line Identification Chart

EACH CHANNEL = 20 eV. (FIVE HIGH RESOLUTION RANGES – 1000 CHANNEL ANALYSIS)

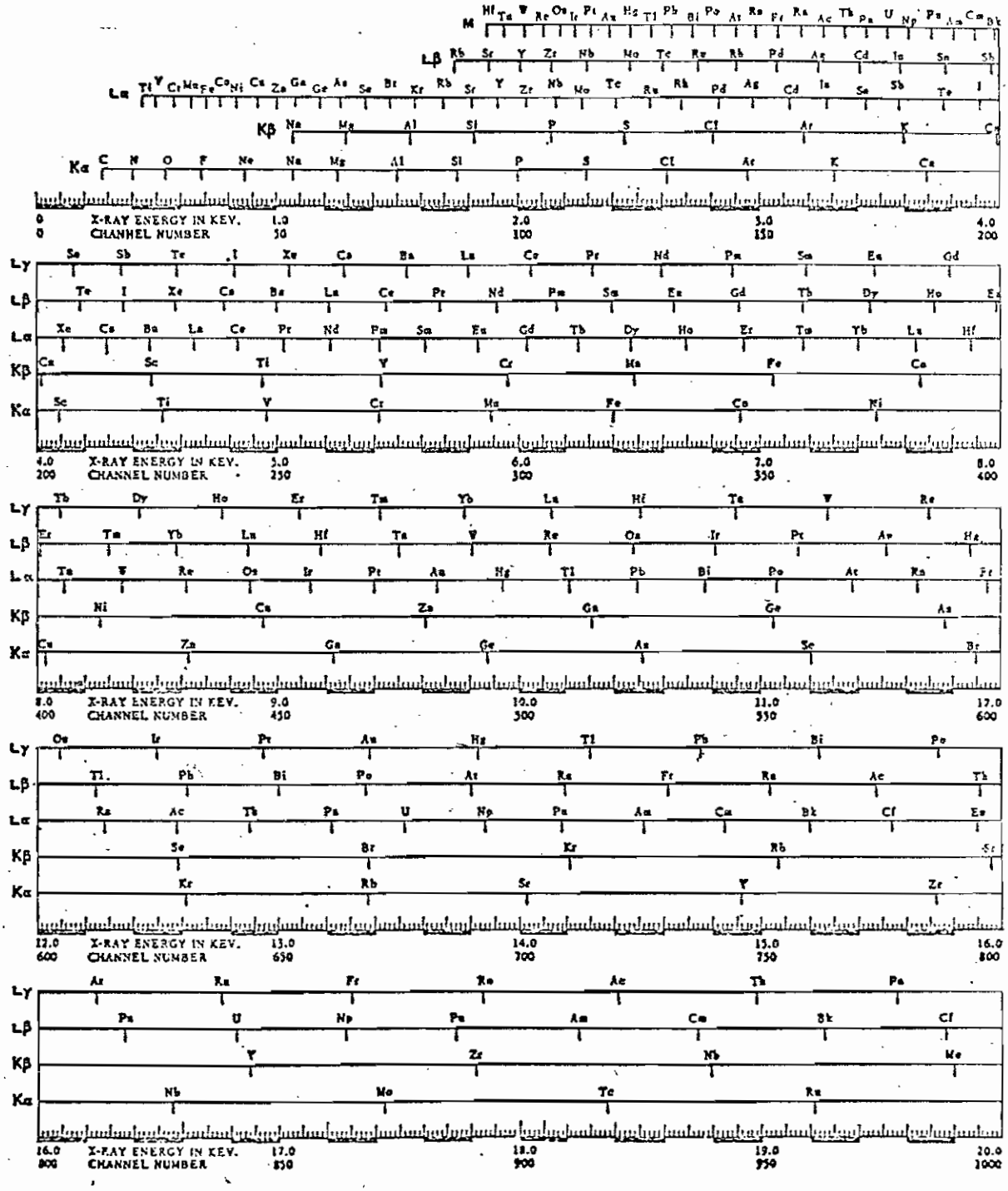

Table C.3

K_α X-ray production cross sections (barns) as calculated by Equation 2.2

	Proton Energy (MeV)												
Element	0.5	1.0	1.5	2.0	2.5	3.0	3.5	4.0	4.5	5.0	6.0	8.0	10.0
S	68.1720	285.572	472.49	638.15	755.51	831.72	876.5	898.6	904.9	900.4	872.6	792.2	717.1
CL	46.6403	197.713	371.91	523.94	641.43	725.66	782.2	817.2	836.1	843.1	834.3	776.6	710.2
K	21.9333	108.295	224.88	341.72	444.72	529.29	595.4	645.2	681.1	705.8	729.8	720.1	679.8
CA	15.1685	80.272	174.11	273.60	365.97	445.72	511.4	563.7	604.1	634.2	670.2	682.1	656.5
TI	7.5163	45.212	105.93	176.61	248.00	314.79	374.3	425.7	468.9	504.5	555.9	601.5	603.2
V	5.3265	34.052	82.61	141.43	203.00	262.51	317.3	366.0	408.4	444.5	499.5	556.9	570.3
CR	3.7919	25.736	64.51	113.21	165.83	218.23	267.8	313.2	353.7	389.2	445.7	511.6	535.1
MN	2.6709	19.226	49.74	89.35	133.42	178.49	222.2	263.2	300.7	334.4	390.0	460.5	491.8
FE	1.8988	14.489	38.62	70.91	107.80	146.44	184.8	221.5	255.9	287.3	341.0	413.7	451.0
CO	1.3533	10.946	30.03	56.29	87.03	119.95	153.3	185.9	216.9	245.9	296.6	369.6	410.9
NI	0.9609	8.243	23.25	44.47	69.86	97.61	126.2	154.8	182.4	208.6	255.7	326.7	370.4
CU	0.6830	6.214	18.01	35.11	55.99	79.26	103.7	128.4	152.7	176.1	219.2	286.9	331.5
ZN	0.4845	4.683	13.95	27.68	44.61	64.21	84.9	106.2	127.4	148.2	187.1	250.8	295.2
GA	0.3410	3.505	10.72	21.66	35.56	51.57	68.9	87.0	105.3	123.4	157.9	216.6	259.5
AS	0.1679	1.959	6.31	13.21	22.27	33.02	45.0	57.8	71.0	84.5	111.0	158.8	196.9
SE	0.1181	1.471	4.87	10.35	17.68	26.49	36.4	47.1	58.4	69.9	93.0	135.7	171.0
BR	0.0829	1.103	3.75	8.11	14.01	21.20	29.4	38.3	47.8	57.6	77.5	115.4	147.7
RB	0.0405	0.620	2.22	4.96	8.78	13.55	19.1	25.3	32.0	39.0	53.6	82.8	109.1
SR	0.0283	0.466	1.71	3.89	6.97	10.86	15.4	20.5	26.1	32.1	44.6	70.0	93.5
Y	0.0198	0.350	1.32	3.06	5.54	8.70	12.4	16.7	21.4	26.4	37.0	59.1	80.1
ZR	0.0138	0.264	1.02	2.40	4.40	6.98	10.0	13.6	17.5	21.7	30.7	49.9	68.5
MO	0.0097	0.199	0.62	1.49	2.80	4.52	6.6	9.0	11.7	14.7	21.2	35.5	50.0

Table C.4

L-shell X-ray production cross sections (barns) as calculated by Equation 2.2

	Proton Energy (MeV)												
Element	0.5	1.0	1.5	2.0	2.5	3.0	3.5	4.0	4.5	5.0	6.0	8.0	10.0
BA	14.9699	83.230	184.75	299.95	418.05	533.31	642.7	744.9	839.3	925.9	1076.3	1298.8	1440.7
W	0.9820	9.540	27.53	52.89	83.38	117.25	153.1	190.1	227.6	264.8	337.7	471.3	585.4
AU	0.4208	4.804	14.92	29.98	48.83	70.40	93.8	118.5	144.0	169.8	221.5	320.1	408.4
HG	0.3561	4.202	13.24	26.87	44.04	63.82	85.4	108.3	131.9	156.0	204.3	297.3	381.4
PB	0.2616	3.301	10.72	22.15	36.79	53.85	72.6	92.7	113.6	135.0	178.5	263.3	341.2
PB	0.2616	3.301	10.72	22.15	36.79	53.85	72.6	92.7	113.6	135.0	178.5	263.3	341.2
TH	0.0664	1.104	4.05	9.03	15.80	24.08	33.5	44.0	55.2	66.9	91.5	142.2	191.9

REFERENCES

LIST OF REFERENCES

M. Ahlberg, R. Akselsson, D. Brune, and J. Lorenzen, Nucl. Instrum. Methods 123 (1975) 385.

M. Ahlberg, Thesis, (Department of Nuclear Physics, Lund Institute of Technology, Lund, Sweden, 1975).

M. Ahlberg and R. Akselsson, Int. J. Appl. Radiat. Isotopes 27 (1976) 279.

M. Ahlberg, Nucl. Instrum. Methods 142 (1977) 61.

J. Antonovics, A. D. Bradshaw, and R. G. Turner, Advances in Ecological Research, 7 (1971) 1.

F. Arinc, L. Wielopolski, and R. P. Gardner, X-Ray Fluorescence Analysis of Environmental Samples, ed. T. G. Dzubay (Ann Arbor Science, Ann Arbor, 1977) 227.

W. Bambynek, B. Crasemann, R. W. Fink, H. U. Freund, H. Mark, C. D. Swift, R. E. Price, and P. V. Rao, Rev. Mod. Phys. 44 (1972) 716.

J. Bang and J. M. Hansteen, Kgl. Dan. Vidensk. Selsk. Mat. Fys. Medd. 31 (1959) no. 13.

B. K. Barnes, L. E. Beghian, G. H. R. Kegel, S. C. Mathur, and P. W. Quinn, Bulletin of the American Physical Society, 18 (1973) 636.

M. Barrette, G. Lamoureux, E. Lebel, R. Lecompte, P. Paradis, and S. Monaro, Nucl. Instrum. Methods 134 (1976) 189.

G. Basbas, W. Brandt, and R. Laubert, Phys. Rev. A7 (1973)983.

R. M. Baum, W. F. Gutknecht, R. D. Willis, and R. L. Walter, Anal. Chem. 47 (1975) 1727.

R. Baum, W. F. Gutknecht, R. D. Willis, and R. L. Walter, Anal. Chim. Acta 85 (1976) 323.

R. M. Baum, R. D. Willis, R. L. Walter, W. F. Gutknecht, and A. R. Stiles, X-Ray Fluorescence Analysis of Environmental Samples, ed. T. G. Dzubay (Ann Arbor Science, Ann Arbor, 1977) 165.

P. R. Bevington, Data Reduction and Error Analysis for the Physical Sciences (McGraw-Hill, New York, 1969) 237.

H. Bichsel, American Institute of Physics Handbook (McGraw-Hill, New York, 1972) p. 8.

L. S. Birks and J. V. Gilfrich, Anal. Chem. 48 (1976) 273R.

C. D. Bond, L. S. August, P. Shapiro, C. M. Davisson, and W. I. McGarry, Bulletin of the American Physical Society, 18 (1973) 636.

N. A. Bonner, F. Bazan, and D. C. Camp, UCRL - 51388 (1973).

N. A. Bonner, F. Bazan, and D. C. Camp, Chem. Instrumentation 6 (1975) 1.

H. J. M. Bowen, Trace Elements in Biochemistry (Academic, New York, 1966).

H. R. Bowman, E. K. Hyde, S. G. Thompson, and R. C. Jared, Science 151 (1966) 562.

T. A. Cahill, Report to the California Air Resources Board and Project Clean Air, University of California, Riverside, Report No. UCD-CNL 162, October, 1972.

T. A. Cahill, R. G. Flocchini, P. J. Feeney, and D. J. Shadoan, Nucl. Instrum. Methods 120 (1974) 193.

T. A. Cahill, New Uses of Ion Accelerators, ed. J. F. Ziegler (Plenum, New York, 1975) p. 1.

J. A. Cavins, A. D. Marwick, and I. V. Mitchell, Thin Solid Films 19 (1973) 91.

D. C. Camp, A. L. Van Lehn, J. R. Rhodes, and A. H. Pradzynski, X-ray Spectrometry 4 (1975) 123.

J. L. Campbell, A. W. Herman, L. A. McNelles, B. H. Orr, and R. A. Willoughby, Advan. X-Ray Anal. 17 (1974) 457.

J. L. Campbell, B. H. Orr, A. W. Herman, L. A. McNelles, J. A. Thompson, and W. Brian Cook, Anal. Chem. 47 (1975) 1542.

J. F. Chemin, I. V. Mitchell, and F. W. Saris, J. Appl. Phys. 45 (1974) 532 and 537.

T. C. Chu, V. R. Navarrete, H. Kaji, G. Izawa, T. Shiokawa, K. Ishii, S. Morita, and H. Tawara, J. Radioanal. Chem. To be published.

P. J. Clark, G. F. Neal, and R. O. Allen, Anal. Chem. 47 (1975) 650.

J. A. Cookson, A. T. G. Ferguson, and F. D. Pilling, J. Radioanal. Chem. 12 (1972) 39.

J. A. Cookson and F. D. Pilling, Phys. Med. Biol. 20 (1975) 1015.

J. A. Cooper, Battelle Northwest Laboratories Report BNWL-SA-4304 (1972).

J. A. Cooper, Battelle Northwest Laboratories Report BNWL-SA-4690 (1973).

L. A. Currie, Anal. Chem. 40 (1968) 586.

G. Deconninck, J. Radioanal. Chem. 12 (1972) 157.

G. Deconninck, G. Demortier, and F. Bodart, Atomic Energy Review 13 (1975) 367.

B. L. Doyle, Thesis, (University of North Carolina, 1976).

T. G. Dzubay, P. J. Lamothe, and H. Yasuda, Advan. X-Ray Anal. 20 (1977) 411.

U. Fano and W. Lichten, Phys. Rev. Lett. 14 (1965) 627.

R. G. Flocchini, P. J. Feeney, R. J. Sommerville, and T. A. Cahill, Nucl. Instrum. Methods 100 (1972) 397.

F. Folkmann, C. Gaarde, T. Huus, and K. Kemp, Nucl. Instrum. Methods 116 (1974a) 487.

F. Folkmann, J. Borggreen, and A. Kjeldgaard, Nucl. Instrum. Methods 119 (1974b) 117.

F. Folkmann, J. Phys. E 8 (1975) 429.

F. Folkmann, Ion Beam Surface Layer Analysis, eds. O. Meyer, G. Linker, and F. Käppeler (Plenum, New York, 1976a) vol. 2, p. 695.

F. Folkmann, Ion Beam Surface Layer Analysis, eds. O. Meyer, G. Linker, and F. Käppeler (Plenum, New York, 1976b) vol. 2, p. 747.

F. Folkmann, Material Characterization Using Ion Beams, ed. A. Cachard and J. P. Thomas (Plenum, New York, 1977).

B. A. Fowler, R. C. Fay, R. L. Walter, R. D. Willis, and W. F. Gutknecht, Environm. Health Perspectives 12 (1975) 71.

J. Freedman, ed., Trace Element Geochemistry in Health and Disease (Geological Society of America, 1975), Special paper 155.

J. D. Garcia, Phys. Rev. A1 (1970) 1402.

J. D. Garcia, R. J. Fortner, and T. M. Kavanagh, Rev. Mod. Phys. 45 (1973) 111.

R. D. Giauque, F. S. Goulding, J. M. Jaklevic, and R. H. Pehl, Anal. Chem. 45 (1973) 671.

J. V. Gilfrich, P. G. Burkhalter, and L. S. Birks, Anal. Chem. 45 (1973) 2002.

T. T. Gorsuch, The Destruction of Organic Matter (Pergamon Press, Elmford, New York, 1970).

F. S. Goulding and J. M. Jaklevic, Ann. Rev. of Nuclear Sci. 23 (1973) 45.

F. S. Goulding and J. M. Jaklevic, Nucl. Instrum. Methods 142 (1977) 323.

J. M. Hansteen, Advances in Atomic and Molecular Physics, eds. D. R. Bates and B. Bederson (Academic, New York, 1975) vol. 11, p. 299.

J. F. Harrison and R. A. Eldred, Advan. X-Ray Anal. 17 (1974) 560.

I. Hasselmann, W. Koenig, F. W. Richter, V. Steiner, V. Wätjen, J. C. Bode, and W. Ohta, Nucl. Instrum. Methods 142 (1977) 163.

A. W. Herman, L. A. McNelles, and J. L. Campbell, Int. J. Appl. Radiat. Isot. 24 (1973) 677.

P. Horowitz and L. Grodzins, Science 189 (1975) 795.

P. Horowitz, M. Aronson, L. Grodzins, W. Ladd, J. Ryan, G. Merriam, and C. Lechene, Science, 194 (1976) 1162.

K. Ishii, S. Morita, and H. Tawara, Phys. Rev. A13 (1976) 131.

J. M. Jaklevic and R. L. Walter, X-Ray Fluorescence Analysis of Environmental Samples, ed. T. G. Dzubay (Ann Arbor Science, Ann Arbor, Mich., 1977) 63.

S. A. E. Johansson and T. B. Johansson, Nucl. Instrum. Methods 137 (1976) 473.

T. B. Johansson, R. Akselsson, and S. A. E. Johansson, Nucl. Instrum. Methods 84 (1970) 141.

T. B. Johansson, R. Akselsson, and S. A. E. Johansson, Advan. X-Ray Anal. 15 (1972) 373.

T. B. Johansson, R. E. Van Grieken, J. W. Nelson, and J. W. Winchester, Anal. Chem. 47 (1975) 855.

H. Kaji, T. Shiokawa, K. Ishii, S. Morita, M. Kamiya, K. Sera, and H. Tawara, Nucl. Instrum. Methods 142 (1977) 21.

H. C. Kaufmann and R. Akselsson, Advan. X-Ray Anal. 18 (1975) 353.

W. Koenig, F. W. Richter, U. Steiner, R. Stock, R. Thielmann, and U. Wätjen, Nucl. Instrum. Methods 142 (1977) 225.

D. A. Landis, F. S. Goulding, and B. V. Jarrett, Nucl. Instrum. Methods 101 (1972) 172.

C. H. Lochmüller, J. W. Galbraith, and R. L. Walter, Anal. Chem. 46 (1974a) 440.

C. H. Lochmüller, J. Galbraith, R. L. Walter, and R. D. Willis, Anal. Biochem. 57 (1974b) 618.

D. H. Madison and E. Merzbacher, Atomic Inner-Shell Processes, ed. B. Crasemann (Academic, New York, 1975) vol. 1, p. 1.

E. Merzbacher and H. W. Lewis, Handbuch der Physik, ed. S. Flügge (Springer-Verlag, Berlin, 1958) vol. 34, p. 166.

G. Middleton and R. E. Stuckey, Analyst 79 (1954) 138.

C. F. Moore, M. Senglaub, B. Johnson, and P. Richard, Phys. Lett. A40 (1972) 107.

H. Moseley, Phil. Mag. 26 (1913) 1024.

H. Moseley, Phil. Mag. 27 (1914) 703.

J. W. Nelson and D. L. Meinert, Advan. X-Ray Anal. 18 (1975) 598.

R. Nobiling, Y. Civelekoglu, B. Povk, D. Schwalm, and K. Traxel, Nucl. Instrum. Methods 130 (1975) 325.

S. K. Perry and F. P. Brady, Nucl. Instrum. Methods 108 (1973) 389.

P. Richard , Atomic Inner-Shell Processes, ed. B. Crasemann (Academic, New York, 1975) vol. 1, p. 74.

S. I. Salem, S. L. Panossian, and R. Krause, At. Data and Nucl. Data Tables 14 (1974) 91.

J. Scheer, L. Voet, U. Wätjen, W. Koenig, F. W. Richter, and U. Steiner, Nucl. Instrum. Methods 142 (1977) 333.

J. H. Scofield, Phys. Rev. A9 (1974) 1041.

G. G. Seaman and K. C. Shane, Nucl. Instrum. Methods 126 (1975) 473.

R. W. Shaw, Jr. and R. D. Willis, Proceedings of the Symposium on Electron Microscopy and X-Ray Applications to Environmental and Occupational Health Analyses (Ann Arbor Science, Ann Arbor, Mich.). To be published.

J. M. Stanford, R. D. Willis, R. L. Walter, W. F. Gutknecht, and J. Antonovics, Rad. and Environm. Biophys. 12 (1975) 175.

A. R. Stiles, T. G. Dzubay, R. M. Baum, R. L. Walter, R. D. Willis, L. J. Moore, E. L. Garner, J. W. Gramlich, and L. A. Machlan, Advan. X-Ray Anal. 19 (1976) 473.

E. Storm and H. I. Israel, Nucl. Data Tables 7 (1970) 565.

H. Thibeau, J. Stadel, W. Cline, and T. A. Cahill, Nucl. Instrum. Methods 111 (1973) 615.

C. J. Umbarger, R. C. Bearse, D. A. Close, and J. J. Malanify, Advan. X-Ray Anal. 16 (1973) 102.

E. J. Underwood, Trace Elements in Human and Animal Nutrition (Academic, New York, 1971).

V. Valković, D. Miljanić, R. M. Wheeler, R. B. Liebert, T. Zabel, and G. C. Phillips, Nature 243 (1973) 543.

V. Valković, R. B. Liebert, T. Zabel, H. T. Larson, D. Miljanić, R. M. Wheeler, and G. C. Phillips, Nucl. Instrum. Methods 114 (1975) 573.

W. J. Veigele, At. Data Tables 5 (1973) 51.

J. Wagman, R. L. Bennett, and K. T. Knapp, X-Ray Fluorescence Analysis of Environmental Samples, ed. T. G. Dzubay (Ann Arbor Science, Ann Arbor, Mich., 1977) 35.

R. L. Walter, R. D. Willis, W. F. Gutknecht, and J. M. Joyce, Anal. Chem. 46 (1974) 843.

R. L. Walter, R. D. Willis, W. F. Gutknecht, and R. W. Shaw, Jr., Nucl. Instrum. Methods 142 (1977) 181.

R. L. Watson, C. J. McNeal, and F. E. Jenson, Advan. X-Ray Anal. 18 (1975) 288.

C. F. Williamson, J. P. Boujot, and J. Picard, CEA Report 3042 (1966).

R. D. Willis, R. L. Walter, R. W. Shaw, Jr., and W. F. Gutknecht, Nucl. Instrum. Methods 142 (1977a) 67.

R. D. Willis and R. L. Walter, Nucl. Instrum. Methods 142 (1977b) 231.

R. D. Willis, R. L. Walter, B. L. Doyle, and S. M. Shafroth, Nucl. Instrum. Methods 142 (1977c) 317.

R. Woldseth, X-Ray Energy Spectrometry (Kevex, Burlingame, 1973).

L. Wu and J. Antonovics, Ecology 57 (1976) 205.

R. Zeisler, J. B. Cross, and E. A. Schweikert, Anal. Chem. 48 (1976) 2124.

BIOGRAPHY

Robert Dalton Willis

Born: April 23, 1948, Independence, Missouri

Education: B. S. in Physics, Denison University, 1970

Positions: N.D.E.A. Fellow, Duke University, 1971-1973

Research Assistant, Duke University, 1973-1976

Memberships: American Physical Society

American Association of Physics Teachers

Phi Beta Kappa

Sigma Xi

Publications:

Metal-Ion Distribution in Metalloproteins by Proton-Induced X-Ray Emission Analysis, C. H. Lochmuller, J. Galbraith, R. L. Walter, and R. D. Willis, Anal. Biochem. 57, 618-622 (1974).

Analysis of Biological, Clinical, and Environmental Samples Using Proton-Induced X-Ray Emission, R. L. Walter, R. D. Willis, W. F. Gutknecht, and J. M. Joyce, Anal. Chem. 46, 843-855 (1974).

Proton-Induced X-Ray Emission Analysis - A Promising Technique for Studying the Metal Content of Plants and Soils, J. M. Stanford, R. D. Willis, R. L. Walter, W. F. Gutknecht, and J. Antonovics, Rad. and Environm. Biophys. 12, 175-180 (1975).

Levels of Toxic Metals in Marine Organisms Collected from Southern California Coastal Waters, B. Fowler, R. L. Walter,

W. F. Gutknecht, and R. D. Willis, Environmental Health Perspectives, 12, 71-76 (1975).

Preparation of Standard Targets for X-Ray Analysis, R. Baum, W. F. Gutknecht, R. D. Willis, and R. L. Walter, Anal. Chem. 47, 1727 (1975).

Trace Element Studies in Bioenvironmental Samples Using 3-MeV Protons, R. L. Walter, R. D. Willis, and W. F. Gutknecht, in J. L. Duggan, ed., Application of Small Accelerators, Vol. 1, 189 (1975).

Calibration of an EDXRF Spectrometer, A. R. Stiles, T. G. Dzubay, R. M. Baum, R. L. Walter, R. D. Willis, L. J. Moore, E. L. Garner, J. W. Gramlich, and L. A. Machlan, in C. O. Rudd, ed., Advances in X-Ray Analysis, vol. 19 (Plenum, New York, 1976), p. 473.

Proton-Induced X-Ray Emission Analysis of Metals Extractable from Soils Using Buffer Solutions of Varying Type and pH, R. Baum, W. F. Gutknecht, R. D. Willis, and R. L. Walter, Anal. Chim. Acta, 85, 323-329 (1976).

Solution-Deposited Standards Using a Capillary Matrix and Lyophilization, R. Baum, R. L. Walter, W. F. Gutknecht, A. R. Stiles, and R. D. Willis, in T. G. Dzubay, ed., X-Ray Fluorescence Analysis of Environmental Samples (Ann Arbor Science, Ann Arbor, 1977), p. 165.

TRACE-A Least Squares Fitting Program for PIXE Spectra, R. D. Willis, A. B. Baskin, and R. L. Walter, in T. G. Dzubay, ed., X-Ray Fluorescence Analysis of Environmental Samples (Ann Arbor Science, Ann Arbor, 1977), p. 259.

Proton-Induced X-Ray Emission Analysis of Thick and Thin Targets, R. D. Willis, R. L. Walter, R. W. Shaw, Jr., and W. F. Gutknecht, Nucl. Instr. Methods, 142, 67 (1977).

The Application of Proton-Induced X-Ray Emission to Bioenvironmental Analyses, R. L. Walter, R. D. Willis, W. F. Gutknecht, and R. W. Shaw, Jr., Nucl. Instr. Methods, 142, 181 (1977).

Computer Analysis of Proton Induced X-ray Emission Spectra, R. D. Willis and R. L. Walter, Nucl. Instr. Methods, 142, 231 (1977).

Wavelength-Dispersion Analysis of PIXE Spectra, R. D. Willis, R. L. Walter, B. L. Doyle, and S. M. Shafroth, Nucl. Instr. Methods, 142, 317 (1977).

Particle Induced X-Ray Emission Analysis--PIXE, R. L. Walter, and R. D. Willis, in L. S. Birks and H. K. Herglotz, eds., Practical Spectroscopy Series, Vol. 3 (Marcel Dekker, Inc., New York), Chapter 7. To be published.

X-Ray Emission Analysis: Sample Losses During Excitation, R. W. Shaw, Jr. and R. D. Willis, in Proc. of the Symposium on Electron Microscopy and X-Ray Applications to Environmental and Occupational Health Analyses (Ann Arbor Science, Ann Arbor). To be published.

Particle Induced X-Ray Emission--PIXE, R. L. Walter, W. F. Gutknecht, and R. D. Willis, (Plenum, New York). To be published.